Development and Characterisation of Halide Perovskite Visible Light and X-Ray Detection Devices

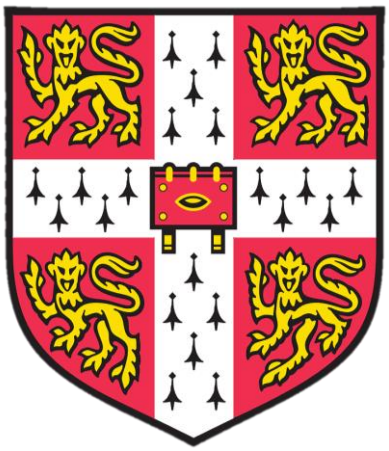

Oliver D.I. Moseley

Department of Physics

University of Cambridge

This thesis is submitted for the degree of

Doctor of Philosophy

Fitzwilliam College

October 2022

Declaration

This thesis is the result of my own work and includes nothing which is the outcome of work done in collaboration except as declared in the Preface and specified in the text. I further state that no substantial part of my thesis has already been submitted, or, is being concurrently submitted for any such degree, diploma or other qualification at the University of Cambridge or any other University or similar institution except as declared in the Preface and specified in the text. It does not exceed the prescribed word limit for the relevant Degree Committee.

Oliver D.I. Moseley

October 2022

Development and Characterisation of Halide Perovskite Visible Light and X-Ray Detection Devices

Oliver D.I. Moseley

Sending and receiving information with electromagnetic radiation is fundamental to imaging and communications. Humankind's ability to utilise this radiation is dependent on how efficiently we can detect it, and improving detectors will advance these technologies. Visible light and X-rays make up two regions of the electromagnetic spectra, both key bands for imaging in different modalities. The visible spectrum represents the energies we can detect with our eyes, while X-rays are highly penetrative and allow the inside of opaque objects to be imaged. While their applications are highly complementary, their detector technologies also share commonalities, allowing the development of both simultaneously. In this thesis, the unique properties of metal halide perovskites are utilised to advance both visible light and X-ray detectors. However, other properties of perovskites, such as ion migration, can provide challenges when characterising performance, and so techniques to accurately measure their detecting ability are also developed.

Metal halide perovskites are exploited to design two new detector device structures, increasing the functionality of photodetectors and overcoming the existing limitations of direct X-ray detectors. A unique photodetector, utilising the band gap tunability of perovskites, is developed to produce a multiband response that can controllably detect different regions of the visible spectrum. The resulting device is employed in a method to send communications with added encryption. Additionally, a concept for a novel X-ray detecting device is developed, using the ability of perovskites to retain impressive properties after low-temperature solution deposition. The device structure decouples the dimensions of photon absorption and charge carrier collection to retain performance across the X-ray spectrum, overcoming the limitations currently preventing the commercial success of direct X-ray detectors.

The potential of perovskites as scintillators for indirect X-ray detection is investigated. The published performances are contextualised with a detailed analysis of the operating mechanism. This mechanistic insight highlights the advantages this material could bring, and we propose the applications that would benefit most from perovskite scintillators, as well as the origins of the remaining limitations. The concurrent understanding of perovskites in other optoelectronic devices is utilised to suggest pathways to overcome the remaining challenges and bring the material closer to commercialisation. These suggestions are applied, and impressive scintillation performance is demonstrated from an emerging Cs_2ZrBr_6 nanocrystal scintillator system.

This work also highlights the specific considerations required when characterising perovskite-based detectors. The large defect density in these materials is shown to be a double-edged sword; making measurements under low light intensities prone to errors, but also acting as another lever to control detection performance. The challenges of characterising direct X-ray detectors are also discussed, alongside the development of experimental procedures to robustly measure halide perovskite devices.

Overall, this thesis utilises the unique properties of perovskites to develop detectors with new functionality, whilst ensuring the same properties do not reduce the accuracy when characterising their performance. The work brings perovskite detectors one step closer to a commercial reality.

Acknowledgements

I owe so much to so many who enabled the completion of this thesis, to whom I'll always be grateful. Firstly, to my supervisor, Sam Stranks. Thank you for giving me the perfect blend of freedom and guidance during my PhD. I have been able to follow my scientific passions with access to facilities most researchers can only dream of, and I realise how lucky I am to have experienced this. Thank you also for creating such a stimulating research environment. Your desire to overcome the traditional barriers to becoming a scientist has created the most inspiring and welcoming group of people. I will never forget the excitement I felt in my first StranksLab group meeting back in September 2018. While the group has changed a lot since then, this feeling never left me, and it made my PhD such an enjoyable experience.

So much of this thesis was only possible thanks to the unrelenting support of Bart Roose, my super-domestique, who devoted so much of his time and effort to get me over the mountains of academic research. And to every member of StranksLab, thank you for all your ideas, discussions and advice throughout my time at Cambridge. Undertaking this PhD coincided with many concerning world events. Reminders that there are people so determined to make a positive change were invaluable. I should thank Miguel, Beth and Szymon in particular, for putting up with my constant questioning and messages at unholy hours. Your support and expertise were instrumental to this work.

To my parents, Jody and Aron, thank you for always trusting me and supporting me with whatever I wanted to do. I would never have achieved this without you. To the rest of my family, you will be glad to know I have finally left *school*.

Lastly, to Katie. Four years ago, I asked you to completely uproot your life and come to Cambridge. I asked you to close your eyes and jump into this unknown with me. Without hesitating, you grabbed my hand and we leapt together. You experienced all the highs and all the lows of the last four years. You were there after every interesting finding and every failed experiment, every paper acceptance and every rejection. You were always there for me, whenever I needed you. I owe you so much.

Research Output

Publications

Published

O. D. I. Moseley, T. A. S. Doherty, R. Parmee, M. Anaya and S. D. Stranks, *Halide Perovskite Scintillators: Unique Promise and Current Limitations*, Journal of Materials Chemistry C, 2021, **9**, 11588.

O. D. I. Moseley*, B. Roose*, S. J. Zelewski, S. Kahmann, K. Dey and S. D. Stranks, *Tuneable Multiband Halide Perovskite Tandem Photodetectors with Switchable Response*, ACS Photonics, 2022, **9**, 3958-3966

** Authors contributed equally*

Under Review

O. D. I. Moseley, B. Roose, S. J. Zelewski and S. D. Stranks, *Identification and Mitigation of Transient Phenomena that Complicate the Characterisation of Halide Perovskite Photodetectors,* **under review**.

Patents

UK patent application filed, application number 2215731.7.

Nomenclature

BGO	Bismuth germinate ($Bi_2Ge_3O_9$)
CCN	Charge collection narrowing
CT	Computed tomography
CW	Continuous wave
CZT	Cadmium zinc telluride
DMF	N,N-dimethylformamide
DMSO	Dimethyl sulfoxide
DOI	Depth-of-interaction
EQE	External quantum efficiency
ETL	Electron transport layer
FA	Formamidinium
FF	Fill-factor
FWHM	Full-width-half-maximum
GOS	Gadolinium oxysulfide (Gd_2O_2S)
HTL	Hole transport layer
IR	Infrared
IV scan	Current-voltage scan
J_{sc}	Short-circuit current
JV scan	Current density-voltage scan
LDR	Linear dynamic range
LED	Light emitting diode
LoD	Limit of detection
LYSO	Lutetium-yttrium oxyorthosilicate ($Lu_{2(1-x)}Y_{2x}SiO_5$)
MA	Methylammonium
MTF	Modulation transfer function
NEP	Noise equivalent power

NIR	Near-infrared
PCE	Power conversion efficiency
PET	Positron emission tomography
PL	Photoluminescence
PLQE	Photoluminescence quantum efficiency
PMT	Photomultiplier tube
RL	Radioluminescence
RLQE	Radioluminescence quantum efficiency
RPM	Revolutions per minute
SEM	Scanning electron microscopy
SMU	Source-measure unit
SPECT	Single photon emission computed tomography
TOF	Time-of-flight
TPD	Two-terminal tandem photodetector
UV	Ultraviolet
V_{oc}	Open-circuit voltage
XRD	X-ray diffraction

List of Figures

List of Tables

Table of Contents

Chapter 1

Introduction

Humans were limited to seeing with just visible light for millennia, but advancements in detector technologies have expanded our vision across the whole electromagnetic spectra. Radio telescopes allow us to image galaxies in new ways, fundamental to detecting the cosmic microwave background radiation that underpins the Big Bang theory of the origins of the universe. Wilhem Röntgen discovered that detecting X-rays which have penetrated through the skin allow us to see inside our bodies, revolutionising modern medicine.[1] The limitations of our eyes did not only restrict imaging. Long distance communication, once restricted to semaphores and smoke signals, now utilises energies we cannot see, and has transformed the way we talk and send information. The detection and transmission of radio waves, microwaves and infrared light underpins modern telecommunications, enabling the development of mobile phones, television and the internet. Improving our ability to detect electromagnetic radiation will allow these technological advancements to continue.

The importance of detectors has never been greater. We are living in the information age where data and its communication are fundamental to civilisation. It is detectors that generate much of this data, and enable its transmission and communication. The development of the internet of things, an interconnected network of sensors and technologies, and the shift towards autonomous vehicles will further the need for detectors.[2,3] It is estimated that sensors alone in driverless cars generate up to 40 terabytes of data per hour.[4]

Photodetectors are used to sense visible photons, termed *visible* as these are the photons the receptors in our eyes can detect. This importance of visible light to humans makes photodetectors ubiquitous in modern society. Streetlights turn on at night, your smart watch measures your heart rate, and we take pictures, using photodetectors. The list is almost endless, covering applications in home electronics, hospitals, and scientific research. Communications using visible light are a candidate to overcome the crowded spectral regions already in use, and

as ‘smart’ consumer technologies are continually developed, this will become more important.[5] This has led to the development of Li-Fi, a Wi-Fi alternative exploiting the visible portion of the electromagnetic spectrum.[6] Commercial photodetectors are monopolised by traditional inorganic semiconductors, with mature fabrication and well-understood properties. However, developing new detector materials may advance functionality beyond what is currently feasible and allow new technologies to be developed.

X-ray detectors, as the name suggests, sense X-ray photons. The ability to penetrate objects opaque to visible light allows X-rays to image the inside of objects. Since its discovery in the late 19th century, X-ray imaging has developed rapidly, and the introduction of tomographic techniques now enables 3D scanning.[7] These techniques have revolutionised medicine and materials inspection, allowing diseases or material flaws to be identified before they can manifest and cause harm. In 2017, 23 million medical radiographs and 5 million computed tomography (CT) scans were performed in the UK alone.[8] However, the use of ionising radiation in medicine comes with a caveat; it is carcinogenic,[9] and the usefulness of the procedure must be balanced against this risk.[10] Improving the performance of X-ray detectors will provide more diagnostic information per scan, whilst simultaneously reducing radiation doses administered. This will help tip the balance of risk versus reward, and allow greater use without the concern of side effects.

In this thesis, we develop photo- and X-ray detectors employing metal halide perovskites. By exploiting the unique properties of this material, we design and develop new device structures that overcome the traditional limits of detection. This allows improved performance and introduces detector functionality that is unachievable with existing technologies. Additionally, as the commercialisation of new detector technologies requires a detailed understanding of their performance under operating conditions, we highlight the challenges perovskite detectors face when characterising their detection ability, and propose methods for accurately measuring these devices.

In the first experimental chapter, Chapter 4, metal halide perovskite photodiodes are utilised to detect visible light. We introduce how some properties of this emerging material, namely its significant and mobile defect density, can generate transient detector performance, and subsequently, additional care is required when characterising detection under low light intensities. Furthermore, the engineering of these defects is shown to act as a lever on final device behaviour, providing an additional point of control over detector performance and enabling optimisation to specific application requirements.

The next chapter, Chapter 5, introduces a unique photodetector device structure that employs two separate light absorbers. The ability for metal halide perovskites to be solution processed, combined with the precise band gap control through compositional engineering, makes them ideal candidates for the absorber layers in this device. The photodetector exhibits selective and switchable detection of multiple photon bands which could open up new applications, and we demonstrate usage in visible light communications with added security.

Chapter 6 discusses the promise of metal halide perovskites as scintillators for indirect X-ray detection. The mechanistic origins of the bright and ultrafast emission are introduced, along with suggestions to overcome the remaining discrepancy between theoretical and published light yields. We utilise the self-trapping of excitons in Cs_2ZrBr_6 nanocrystals to reinforce the requirement of Stokes shifts to achieve efficient radioluminescence. Finally, we conclude by highlighting the detector applications where the performance of perovskite scintillators will bring the most benefits.

In Chapter 7, the final experimental chapter, we demonstrate how the inherent limitations of existing direct X-ray detectors can be overcome with the design of new device structures. We utilise metal halide perovskites as the X-ray sensitive material, and begin by using the device as a photodetector. The theoretical advantages for X-ray detection, a result of decoupling the dimensions of photon absorption and charge collection, are then described, as well as proposals for the device design. This work is combined with the development of experimental techniques to accurately measure the performance of direct perovskite X-ray detectors.

Chapter 2

Background

This chapter introduces the scientific topics fundamental to the research in this thesis. The principles of detecting photons are explained, highlighting the specific challenges relating to photo- and X-ray detection. The main detection mechanisms are presented, establishing the importance of the device structure on the detector performance. Finally, the advantageous properties of metal halide perovskites for detection applications are discussed, along with the key findings already published.

A portion of the text in this chapter was adapted from O. D. I. Moseley et. al, Halide Perovskite Scintillators: Unique Promise and Current Limitations, *J. Mater. Chem. C*, 2021, **9**, 11588-11604.[11]

2.1 Visible and X-Ray Photons

Electromagnetic radiation is a form of energy comprised of oscillating electric and magnetic fields travelling at a constant speed through a medium. In a vacuum, this is the speed of light, *c*. The constant speed requires the energy of the radiation to be a function of its wavelength or frequency, generating the electromagnetic spectrum (Figure 2.1). For convenience, this spectrum is categorised into bands based on differences in their generation, interactions with matter, and applications. From low to high energy, these bands are radio waves, microwaves, infrared (IR), visible, ultraviolet (UV), X-rays and γ-rays. The boundaries between these bands are not precisely defined, and adjacent regions blur into each other.

The lower energy electromagnetic bands, from radio waves to infrared, mainly interact with matter through molecular vibrations and rotations, or charge oscillations. However, the visible spectrum, with photons approximately 1.6 – 3.0 eV, represents the onset where electrons in atoms and molecules begin absorbing radiation, and these photoexcited electrons can then be

used to do work. Retinal molecules in our eyes can absorb visible photons, the beginning of the signal cascade that enables human vision and, subsequently, the visible spectrum is defined as the photons we can see. The absorption of visible light by chlorophyll allows plants to convert light into chemical energy via photosynthesis. It is no coincidence that the emission from the sun covers the visible spectrum, and its peak energy is in this region. Being the light we can see, the visible spectrum is vital to humans, but it has other uses beyond imaging. As many electronic transitions in atoms fall under this energy band, optical spectroscopy allows us to study molecules. Absorption and emission spectroscopy led to the discovery of helium, and is still commonplace in research labs today. Moreover, the visible band is utilised in communications, where optical signals are modulated to send information at the speed of light.

As you reach the X- and γ-ray regions of the electromagnetic spectrum the energy given to electrons is above the ionisation energy, and they are emitted from their atoms. The distinction between X-rays and γ-rays, the most energetic regions of the electromagnetic spectra, is subtle. They are often differentiated by their generation source, with γ-radiation originating from the radioactive decay of atomic nuclei. However, by this definition, their energies overlap, and in this thesis the two are instead distinguished based on their applications. Herein, due to a focus on imaging, the term X-rays denotes radiation of energies from 0.15 keV up to the 511 keV used in positron emission tomography (PET).

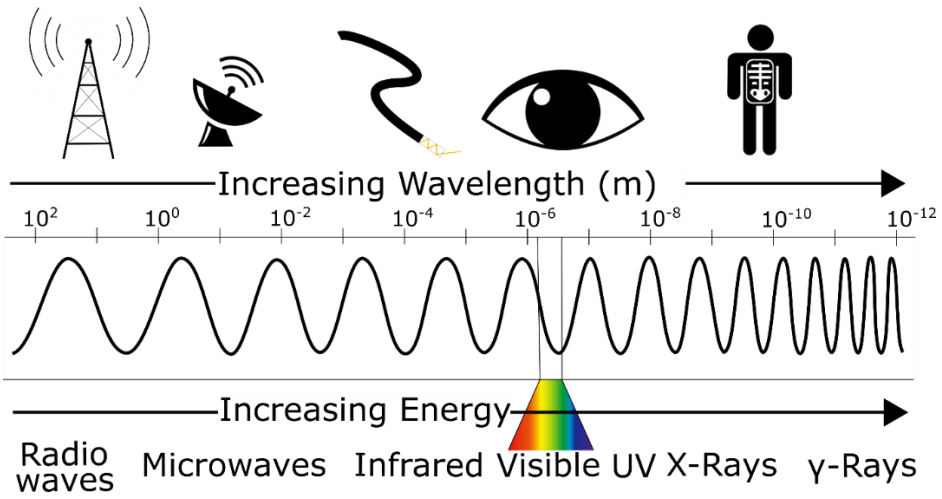

Figure 2.1: The Electromagnetic Spectrum.

The high energies of X-rays interact with matter via the photoelectric effect and Compton scattering, and as detailed later, these processes are inefficient in most materials. Therefore, X-rays can travel through materials without being fully attenuated, and exhibit long penetration depths. The extent of the interaction of an X-ray with matter depends on the material's

elemental composition and density. As a result, X-rays that have transmitted through objects contain information on the materials it has encountered, and the radiation can be used to produce internal images. Non-destructive internal imaging is vital to modern medicine, security and industrial inspection, and is the most common use of X-rays. In addition, as the wavelength of X-rays are on the same order of magnitude as atomic spacings in materials ($\sim 10^{-10}$ m), they are used to study atomic structure with X-ray crystallography, a technique which has advanced our understanding of chemical bonding.

Visible light can be generated by a variety of mechanisms. Heating an object will cause it to emit as a function of its temperature, which can produce light in the visible spectrum. The process of light emission from heat is called incandescence, and covers sources such as the sun, flames, and traditional light bulbs. The overlap of the visible spectrum with outer shell electronic transitions in atoms and molecules means light energy can be emitted when excited electrons lose their energy. This emission can be stimulated by various means, for example electrically, which forms the basis of light emitting diodes (LEDs) and lasers. The higher energies of X-rays make their production more difficult. The main mechanisms for their generation are the deceleration of high-energy electrons, characteristic X-ray generation from atomic transitions, and radioactive decay. Synchrotrons and X-ray tubes both exploit the deceleration of high-energy electrons. However, although intense and coherent sources of radiation, synchrotrons require large particle accelerators, restricting their use to a handful of worldwide facilities. In contrast, X-ray tubes are widely used generators of radiation, utilised in hospitals and airports. By colliding high-energy electrons with a target material, X-ray tubes generate a spectrum of radiation, as well as characteristic X-ray peaks if core electron transitions occur in the target (see Chapter 7 for more detail on X-ray generation).

Whilst the energy differences between visible and X-ray photons leads to differences in their production and application, detectors of these spectral bands share many similarities in their design and mechanism. The detecting materials also have common requirements, and the properties which make a good photodetector are also beneficial to X-rays (and vice versa), allowing the development of both in parallel. The remainder of the background section explains the operation of these detectors, discussing the working mechanisms and requirements for applications, before introducing metal halide perovskites as an ideal candidate for both types of device.

2.2 Introduction to Detectors

Detectors are devices used to sense stimuli by converting them into a measurable signal. By measuring the presence of a physical quantity, detectors provide information about their environment. Light, chemicals, sound and touch can all be sensed, and what detectors of all these phenomena have in common is the process of converting one form of energy (the stimulus) into a different – and usually electronic – form (the detector output). The detection of electromagnetic energy is a common application of sensors. Detecting electromagnetic radiation allows us to see, by producing images, and is vital to our ability to communicate. We send messages at the speed of light, through the air or cables, by modulating this radiation, and this requires the energy to be detected at the receiver.

The ability of a detector to sense the relevant photons can be quantified with a range of metrics. Each application will have different requirements for the performance of its detector, and as such, there is no one-size-fits-all material or device structure. For a detector to resolve a stimulus, its response must be distinguishable from the noise of the device, which makes a large response and a low noise a requirement. The noise of a device originates from the fluctuations of a detector's output, and these have various sources – some avoidable and some unavoidable. Other key features of a detector are how quickly it can respond to a signal and its ability to resolve repeated signals, and these are both determined by the response speed. Applications such as communications require rapid detection (>MHz) to enable more information to be sent. Imaging at fast repetition rates, such as tomographic applications, also requires a quick response to prevent imaging artefacts between frames.

An important property of a detector is its spectral bandwidth, defined as the range of photon energies that generate a response. Detectors that sense a wide range of energies, such as the whole visible spectrum, are known as broadband. Most detectors have a broadband response, as they absorb a range of photon energies. However, by carefully engineering the device design, detectors can generate a selective response to specific bands of photons without the need for additional filters. Narrowband detectors respond selectively to only a narrow range of photon energies, which allows the detection of individual colours of visible light.

Detecting photons is possible through a range of mechanisms. Our eyes detect visible photons chemically using photoreceptor cells (rods and cones), whereby a trans-cis isomerisation occurs on light detection that results in electrical signals being sent to the brain. Chemical detection also form the basis of original photographic films, which use light-induced redox

chemistry of silver halide crystals to generate an image. Furthermore, the energy of photons can also be detected by conversion to heat in a detector, such as in bolometers, or by generating photoelectrons, the foundations of photomultiplier tubes.

The importance of a digital output, and the improved detector performance, make detectors that convert photons into electronic signals the most useful. Semiconductors have manipulatable electrical properties that can be altered by incident radiation. Detectors utilising semiconductors offer compact, cheap and rugged devices, and piggybacking the development of semiconductor electronics through the second half of the 20th century, makes them the standard in commercial detectors.

The detection of photons by a semiconductor occurs in two steps. First, the incident photons must be absorbed by the semiconductor, and second, the energy of these photons must be converted into a signal. X-ray and optical photons interact with matter by different processes, making the absorption step where the largest differences in these detectors originates. The result of photon absorption is the generation of excited charge carriers, and it is the collection of these charges that forms the electronic signal. The mechanisms of these steps are now discussed in turn, with any differences between the processes in visible light and X-ray detectors highlighted.

2.3 Absorption of Photons

The absorption of photons in detectors is the first step in converting the stimulus into an electrical signal. The higher energy of X-rays compared to visible light means the absorption of X-ray and visible photons occurs via different processes. This results in X-rays having longer penetration depths and generating more carriers per incident photon compared to visible light. While the penetrating ability of X-rays gives rise to its ability to internally image opaque objects, it also imposes challenges on detectors and is the source of the main design differences between X-ray and photodetectors.

Semiconductors, treading the line between insulators and conductors, possess a valence band containing electrons, and an empty conduction band. The energetic difference between these bands, the band gap, is vital to the definition of a semiconductor, wide enough to prevent significant thermal occupation of the conduction band at room temperature, but not so wide that the occupation of the conduction band is too difficult. Materials with band gaps between 0.5 and 3 eV are often defined as semiconductors.[12] This energy overlaps with the visible

spectrum (~1.5 to 3 eV), which allows visible photons to excite electrons from the valence to the conduction band in such materials. This process also leaves behind an electron vacancy, referred to as a hole, in the valence band. Photons with energies below the band gap are not absorbed, and instead are transmitted through the semiconductor without generating a response. The band gap of the material therefore controls the absorption onset of photons and the spectral bandwidth. For visible photons with energy greater than the band gap, electrons are excited deeper into the conduction band. The hot carriers then rapidly decay via vibrational states to the conduction band edge, at which point the extra energy they possess can be converted into a signal.

Attenuation of X-ray photons occurs by the photoelectric and Compton effects. The Compton effect is the inelastic scattering of an X-ray photon with an electron, resulting in the transfer of a portion of its energy. Greater scattering angles result in more energy being transferred to the electron and absorbed by the detector. Absorption via the photoelectric effect occurs when X-ray photons are above the binding energy of core electrons in the atoms of detector materials. The entire photon energy is transferred to a core electron, which is emitted from the atom as a photoelectron, with kinetic energy equal to photon energy minus the binding energy. Both the photoelectric and Compton processes generate a high-energy electron and hole, which go on to produce more excited charge carriers via secondary X-ray emission, Auger events and further scattering. Once the energies of the excited carriers drops below the threshold for further ionisation, they thermalise to the band edge,[13] and this cascade allows multiple charge carriers to be generated per incident photon. The total number of generated charge carriers can be estimated by dividing the X-ray energy by the electron-hole pair creation energy, $W_{\pm}$, a material specific quantity. The Klein rule approximates $W_{\pm} \approx 3\ E_{BG}$ for crystalline semiconductors, resulting in ~10^3 – 10^4 excited charge carriers per X-ray photon.[14] In contrast, visible photon absorption is usually limited to one excited charge carrier pair per photon. The generation of a quantity of charge carriers that is proportional to the photon energy allows X-ray detectors to provide a measure of the incident photon energy, adding energy resolution information to its output signal.

The photon absorption efficiency of a material is quantified by its absorption coefficient. For the electronic transitions resulting from visible light absorption, the absorption coefficient measures the overlap integral between the ground and excited state wave functions combined with the density of states available for the transition. This is known as Fermi's golden rule.[15] The more quantum mechanically allowed a transition is, the greater this overlap, which can be

qualitatively represented by selection rules for the absorption process.[16] If these selection rules are obeyed, as is the case for III-V semiconductors (e.g. gallium arsenide), the absorption coefficient can exceed 10^5 cm^{-1}. The attenuation of light through materials is calculated using the Beer-Lambert law,

$$log_{10}\left(\frac{I_o}{I}\right) = \alpha\, d \qquad (2.1),$$

where I_0 and I are the initial and transmitted light intensities, α is the absorption coefficient, and d is the material thickness, which results in less than a few micrometres to absorb the majority of visible photons in semiconductors (Figure 2.2a).[17]

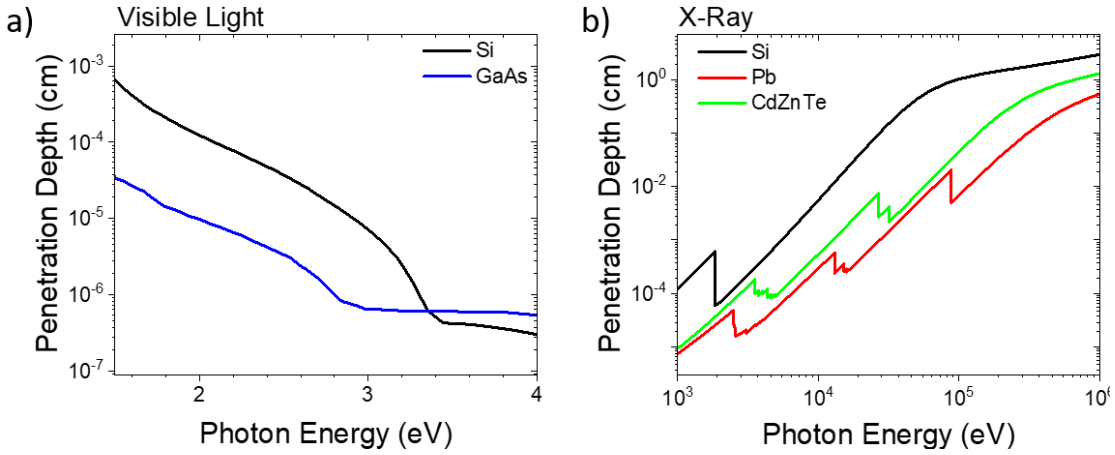

Figure 2.2: Penetration Depth of Visible and X-Ray Photons. *Penetration depth is the thickness required to absorb 1/e of the incident intensity. a) Visible photons (~300 − 850 nm), using data obtained from* [18]*. GaAs = gallium arsenide. b) X-ray photons, calculated using data obtained from the XCOM cross-section database from the NIST website.*[19]

For X-ray absorption, the probability of photoelectric absorption scales approximately as a function of $\rho Z^3/E_{in}^3$ and Compton scattering ρ/E_{in}, where Z is the atomic number, ρ is the material mass density and E_{in} the X-ray energy.[13,20] The photoelectric effect has clear absorption edges, when the incident X-ray are of similar energy to the core electron binding energy, and at these points the absorption efficiency spikes. These equations show that X-ray absorption is greater for materials with large densities and high atomic number constituents, but becomes less efficient as X-ray energy increases. The absorption coefficients are highly material dependent and for low density and low atomic number materials this can be below 1 cm^{-1}, making X-rays a highly penetrating radiation. Indeed, the advantages of X-rays arise due to their penetrating ability, which allows them to pass through objects, but it also brings challenges to their detection. Detectors must efficiently attenuate the radiation, a requirement

that limits the suitable materials to those with high atomic numbers and high mass densities. Even optimal materials require very large thicknesses to absorb X-rays, and Figure 2.2b shows that 0.2 mm of lead are needed to sufficiently stop 150 keV photons. As detailed in the next section, this can put challenges on the subsequent step of directly converting the generated charge carriers into an electrical signal in X-ray detectors.

2.4 Direct Signal Generation

Once the absorbing semiconductor has converted the incident photons into excited electrons and holes, energetically separated across its band gap, it must convert these charge carriers into an electronic signal. This can be done *directly*, by extracting the generated charges out of the semiconductor to produce a current or voltage. The performance of a direct detector depends on two primary features: its ability to convert incident photons into charge carriers, and its ability to convert these charge carriers into a signal. While both these processes are dependent on the properties of the semiconductor material, the latter also depends on the detector device structure, as this affects the charge collection mechanism.

2.4.1 Device Structures

The device structure in direct detectors influences the mechanism of charge carrier collection and, as a result, it affects the detection performance. There exists a range of possible device structures, each with inherent advantages in their detection performance, with the photodiode and photoconductor the most common. The prefix *photo-* does not make them unique to visible photons, and the same structures can be applied to extract the charge carriers generated in X-ray detectors. Photoconductors are the simplest direct detecting devices, consisting of a metal-semiconductor-metal architecture (Figure 2.3a). As most metals used in devices are opaque to visible photons, photoconductors are commonly produced in lateral structures. The absorption of photons and generation of free charge carriers increases the conductivity of the semiconductor, which in turn modulates the electrical response from the detector. With no external bias, the response from a photoconductor is zero, as there is no driving force to collect the generated charges. However, applying a bias allows the charges to be collected, and current flows through the device. A higher incident light intensity generates more charge carriers in the device, which in turn produces more current. The response of a photoconductor is symmetrical due to inherent symmetry in the device structure, and the current as a function of both bias and light intensity is shown in the current-voltage (IV) curves in Figure 2.3b.

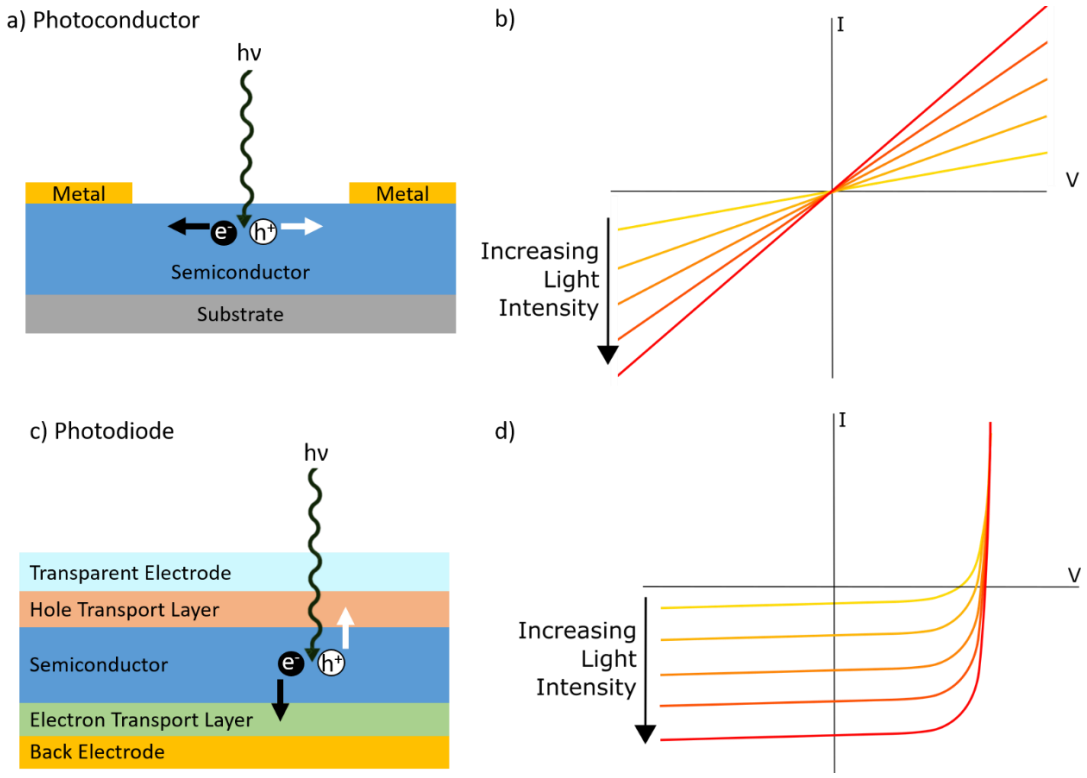

Figure 2.3: Photodetector Structures and IV Curves. *a) Photoconductors, with the corresponding IV curves as a function of light intensity (b). c) p-i-n photodiodes, again with expected IV curves in (d).*

Another direct detector structure is the photodiode. Photodiodes, like diodes, are asymmetric, possessing a p-n or p-i-n semiconductor architecture (Figure 2.3c). The p- and n-type regions are semiconductors doped with additional holes or electrons, respectively. These materials act to selectively transport holes (p-type), or electrons (n-type), and hence are often referred to as hole or electron transport layers (HTLs and ETLs, respectively). Combining these semiconductor materials together forms a junction, which in turn creates a depletion region within the device and an in-built electric field. If photons are absorbed in, or close to, this depletion region, the generated electron and hole are separated across the p-n junction by the electric field, after which they can be extracted out of the device to produce current. This allows self-powered operation, as a photocurrent is generated by the device without an external bias. If the photodiode is placed in a circuit with a load resistance, the generation and separation of charge carriers produces a voltage, in a process known as the photovoltaic effect. This ability to produce electrical power allows photodiodes to also be used as solar cells, a complementarity that will be utilised in this thesis. Photodiodes in the role of detectors are more commonly operated under reverse bias, due to improved detection performance in these conditions. IV curves of a photodiode are shown in Figure 2.3d.

As the device structure dictates the mechanism of charge carrier collection and signal generation in a detector, selecting a structure requires consideration of the required performance for the end application. The performance of a photodetector is quantified by several figures of merit, defined in Table 2.1, and the influence of the photodetector structure on these metrics is now introduced.

Table 2.1: Figures of Merit for Direct Detectors.

Figure of Merit	Description
Sensitivity	A measure of detector response amplitude at a given incident intensity. Quantified by the responsivity, *R*, for photodetectors and sensitivity, *S*, for X-ray detectors (A W^{-1} (*R*), C Gy_{air}^{-1} cm^{-2} (*S*)).
Gain	A measure of the amplification of detector response beyond contributions of purely photogenerated charge carriers. Quantified by the gain factor, *G* (unitless), where unity *G* values are equivalent to 100% EQE.
Noise	A measure of the random fluctuations of a detector output, from which the response signal must be distinguishable. (A $Hz^{-1/2}$).
LDR	The range of incident powers between which the detector maintains a constant sensitivity. (dB).
Detection Limit	A measure of the lowest incident signals which can be distinguished from the noise. Noise equivalent power (NEP, W $Hz^{-1/2}$) and Detectivity (*D**, Jones) are used for photodetectors, and limit of detection (LoD, Gy s^{-1}) are used for X-ray detection.
Spectral Bandwidth	Specific to photodetectors, the range of photon energies that can be detected.
Rise/Fall Times	One measure of response speed, the time taken for a detector to respond to a stimulus. ($t_{rise/fall}$, s).
Bandwidth	Another measure of response speed, representing the frequencies of pulsed light that a detector can resolve. (f_{-3dB} , Hz).
Energy Resolution	Specific to X-ray detectors, a measure of the ability to resolve the energy of an incident X-ray photon. Quantified by the width of the detector photopeak divided by the original photon energy. (%).

A key parameter of a detector is how large a signal it outputs in response to a given stimulus. Nomenclature and units convenient to the applications of X-ray and visible photons mean their detectors are quantified using different metrics, but essentially they represent a quantity of electrical response per incident light intensity. Photodetectors are quantified by responsivity, *R* (units A W^{-1}), whereas X-ray detectors measure in terms of sensitivity, *S* (units μC Gy^{-1}_{air}).

The responsivity is calculated using Equation 2.2, where I_{light} and I_{dark} are the detector currents under illumination and in the dark respectively, and P_{in} is the incident power. Equation 2.3 quantifies an X-ray detector's sensitivity, where Q is the amount of charge collected per unit of X-ray dose, D.

$$R = \frac{I_{light} - I_{dark}}{P_{in}} \quad (2.2).$$

$$S = \frac{Q}{D} \quad (2.3).$$

The structure of a photodetecting device can amplify its response signal, increasing the sensitivity. This phenomenon occurs in photoconductor devices by a mechanism known as gain, whereby excited charge carriers can recirculate through a device several times, continually contributing to the response. For gain to occur, charges must be able to travel through the circuit more than once, and two criteria are required for this to occur: an ohmic interface between the electrode and semiconductor to allow charge injection, and charge carrier lifetimes must exceed carrier transit times through the device ($\tau_{lifetime} > \tau_{transit}$). Once these are fulfilled, photogenerated carriers can contribute to photocurrent more than once and increase the response. Gain is quantified by the gain factor, G, which represents the number of times a detector's response is amplified above unity. G can be calculated from the ratio of carrier lifetime and transit times, where h is Planck's constant, c is the speed of light, q is the elementary charge, R is the responsivity and λ is the wavelength of incident light.

$$G = \frac{h\,c\,R(\lambda)}{\lambda\,q} = \frac{\tau_{lifetime}}{\tau_{transit}} \quad (2.4).$$

The gain factor is related to the external quantum efficiency (EQE), the ratio of photons incident on a detector to charge carriers collected, and $G = 1$ is equivalent to 100% EQE. The cascade of photocarrier generation means X-ray detectors already generate many charge carriers per photon, producing EQEs well in excess of 100%, and the signal can be amplified further by a device gain mechanism.

Photodiode type detectors, similar to photovoltaic devices, are often limited to a maximum of one photogenerated electron per incident photon, thus EQE and G values are below unity. The rectifying barriers at each semiconductor-transport layer interface prevent charge circulation and limit photocurrent to contributions from photogenerated carriers only. Amplification of

response is important with low incident photon intensities, where larger signals are needed in order to be distinguishable from the detector noise.

A desirable feature of a device sensitivity is for it to remain unchanged with incident intensity. The linear dynamic range (LDR) represents the extent of this linear response, as quantified by Equation 2.5, where P_{max} and P_{min} are the maximum and minimum incident power bounds of linear response. As the amount of gain is often a function of incident light intensity, photoconductors show reduced linear dynamic ranges, often below 100 dB[21] whereas photodiodes can exceed 250 dB.[22,23]

$$LDR = 10 \times log \frac{P_{max}}{P_{min}} \tag{2.5}.$$

In addition to large signal amplitudes, the detection of low light intensities also requires low detector noise. Noise is the random fluctuations of the detector output, and the response signal must be distinguishable from this for a stimulus to be registered. There are many individual sources of noise in a detector, often defined by their frequency dependence. White noise sources are independent of frequency whereas some noise sources increase at lower frequencies.[24] Shot noise is a source of white noise that arises due to the discrete nature of both photons and electrical charge, therefore described by Poisson statistics. In detectors, the flow of current contributes to the device shot noise, which can be defined as:

$$i_{shot} = \sqrt{2qI\Delta f} \tag{2.6},$$

where q is the elementary charge, I is the current and Δf is the measurement bandwidth. It is frequently assumed in the literature that detectors are limited by the dark current shot noise, and this value can provide an estimate for the total noise of the system.[25–30] However, this is often not the case, which leads to underestimations of the true noise value. The random thermal motion of charge carriers contributes to the device noise. This is referred to as Johnson noise, which like shot noise, has a white frequency dependence. It is defined as:

$$i_{Johnson} = \sqrt{\frac{4kT\Delta f}{R}} \tag{2.7},$$

where k is the Boltzmann constant, T is the temperature and R is the device resistance. Low frequency noise arises from *1/f* noise sources. The origin of *1/f* noise is not well understood,

but is associated with processes such as generation and recombination, and carrier tunnelling. Its magnitude increases at lower frequencies and, as a result, it is referred to as pink noise.[31]

The total noise in a photodetector is the sum of the individual noise sources. The contribution of dark current to shot noise makes it a target to lower the total noise from a device. Dark current refers to the current that flows through a detector in the absence of illumination, and there are two main contributions to this current. Carriers can occupy the conduction band from thermal excitation, and generate a dark current. This is an unavoidable contribution and its magnitude is a function of temperature and band gap, which is why narrow band gap IR detectors require cooling to reduce the thermally induced dark current. The other contribution arises from electron or hole injection into the semiconductor.[32] In photoconductors, there is often no barrier to this injection, due to ohmic metal-semiconductor contacts, meaning the current flow in the dark, and associated shot noise, is high. In contrast, the transport layers in p-i-n photodiodes can be engineered to possess a wide band gap to act as a blocking layer for charge injection into the semiconductor. This decreases the dark current in photodiodes, and as a result, they often possess lower noise than photoconductor structures.

The ability of a detector to measure small light signals is defined by the noise equivalent power (NEP) for photodetectors and the limit of detection (LoD) in X-ray detectors. The NEP is the optical power required to generate a signal equal to the noise current, calculated by:

$$NEP = \frac{i_{noise}}{R} \tag{2.8},$$

where R is the responsivity. As noise is dependent on detector area, A, and measurement bandwidth, Δf, the detectivity (D^*) is often used as an ultimate measure of a visible light detector sensitivity, allowing fairer comparisons between detectors with different designs. The units of detectivity are cm $Hz^{½}$ W^{-1}, commonly simplified to *Jones*.

$$D^* = \frac{\sqrt{A\Delta f}}{NEP} \tag{2.9}.$$

Similar to the NEP, the LoD for X-ray detectors is determined from the device response and noise. However, it is much less rigorously defined, with various methods being used for its calculation.[33] A more detailed discussion on this parameter is included in Chapter 7. The LoD of an X-ray detector is particularly important in medical imaging as it impacts the dose rates

exposed to patients during scans. Typical dose rates used in diagnostic radiology are below 5.5 μGy s^{-1} and lower LoDs in detectors may enable this to be reduced.[34,35]

Detectors are often required to sense light signals that vary with time, and the speed of response is a key figure of merit. The speed of response represents the time taken for a detector to generate and collect charge carriers, and output a signal from the device. The response speed can be quantified in terms of time or frequency. The response time is typically represented as the rise and fall times, t_{rise} and t_{fall}, the time taken for the signal go from 10% to 90% of the peak response. The frequency dependence is defined by the cut-off frequency (f_{-3dB}), the point where the response drops to 3 dB of the initial value. The cut-off frequency is also known as the detector bandwidth (not to be confused with spectral bandwidth, the range of photon energies a device can detect).

$$t_{rise/fall} = t_{90\%} - t_{10\%} \tag{2.10}.$$

The response speed is made up of two contributions, one relating to the resistance-capacitance (*RC*) constant of the detector, and another relating to the transit time ($\tau_{transit}$) of carriers through the device. The overall contributions of these factors to the response speed is shown in Equation 2.11, with one component usually limiting the overall response speed of a detector. In X-ray detectors, the large thicknesses required means they will always be limited by the transit time of the carriers. However, the case for photodetectors is less predefined, and optimisation of response speed aims to make their contributions equal. Optimising response speed through device design involves reducing the device capacitance, tuning the thickness of the absorbing layer, and removing any slow transit components.[36]

$$f_{-3dB}^2 \approx \left(\frac{3.5}{2\pi\tau_{transit}}\right)^2 + \left(\frac{1}{2\pi RC}\right)^2 \tag{2.11}.$$

Reducing the transit time of carriers through the device can be achieved by employing thinner absorption layers, which lowers the distance for charge carriers to travel. In addition, transit times can be improved by operating under a reverse bias, as this increases carrier drift velocities. The effect of thickness (*d*) and bias (*V*) on transit times is shown in Equation 2.12:

$$\tau_{transit} = \frac{\mu V}{d^2} \tag{2.12},$$

where μ is carrier mobility. Reducing the device capacitance will also improve response speeds. For p-n junction photodiodes, applying a reverse bias has the additional improvement on speed beyond decreasing transit times, by widening the depletion region to reduce the device capacitance. In p-i-n devices, this effect is minimised as the depletion region is fixed by the width of the intrinsic absorber. Instead, in p-i-n structures, using thicker semiconductors will reduce this capacitance. Therefore, there is a trade-off between transit time and capacitance when selecting the absorber thickness. The area of the photodetector can also be reduced to minimise the device capacitance, which improves response speeds.[37] The contribution of thickness (d) and area (A) to capacitance can be seen in Equation 2.13, where ε_o is the permittivity of free space:

$$C = \frac{\varepsilon_0 A}{d} \quad (2.13).$$

Although photoconductors displaying gain have large response amplitudes, they suffer from slow detection speeds, as the recirculation of charge carrier results in a slow build up in response signals. The gain-bandwidth trade-off is a consideration when selecting a device structure, balancing the photocurrent amplification of photoconductors ($G > 10^4$)[38], with the response speed of their photodiode counterparts (typically hundreds of microseconds vs hundreds of nanoseconds)[37,39]. A summary of the advantages of each structure is included in Table 2.2. The range of device mechanisms leads to a choice when it comes to designing a photodetector. The desired application dictates the structure chosen, to optimise its detection properties to the task in hand.

Table 2.2: Advantages of Direct Detection Device Structures.

Photoconductor	Photodiode
• High responsivity (gain) • Simple structure	• Low dark current • Self-powered operation • Fast response • Large linear dynamic range

2.4.2 Material Requirements

To ensure the generated charges are collected in direct detectors, high mobilities and long lifetimes of excited charge carriers are required properties of semiconductor materials. These

features enable large diffusion lengths and mobility-lifetime products, which represent on average how far carriers can diffuse or drift before recombining. Transport length scales must be above the order of semiconductor thickness to efficiently generate a response. Photodetectors, needing sub-micrometre thicknesses to absorb visible light, are well within the transport capabilities of many semiconductors (values of specific detector materials are discussed in the context of metal halide perovskites in Section 2.6.2.), and light can be efficiently detected. However, as thicknesses in X-ray detectors can exceed millimetres, semiconductors with long transport lengths are essential.

Photodetectors are monopolised by traditional inorganic semiconductors, due to the low cost, mature fabrication, and well-understood properties. Silicon has a band gap of 1.1 eV and is utilised for visible light applications, while germanium (E_{BG} = 0.66 eV) is used for infrared detection. Silicon has an unfavourable indirect band gap, requiring additional phonon interactions in order to absorb light. This reduces silicon's absorption efficiency, and thicker (>100 μm) silicon layers are needed, but the excellent semiconducting properties compensate for this. Alternatives to silicon, such as III-V and other alloyed semiconductors, may have advantages in specific applications. For example, gallium arsenide has higher electron mobilities than silicon, allowing faster response speeds.[40–42] In addition, the alloying of materials allows tuning of the band gap and subsequent control over the spectral bandwidth. However, the cheap production from abundant precursors, and corresponding economies of scale of such a widely used material, make silicon the workhorse photodetector material.

The long penetration depth of X-rays generates inherent challenges to their direct detection. Detectors are required to be thick in order to absorb the radiation, often above millimetres, but this puts constraints on the charge carrier collection, with charges likely to recombine before extraction. A thickness trade-off exists, balancing absorbing as many photons and collecting as many charges as possible. Detector materials are required to be highly attenuating, to reduce the distances charges need to travel, and have long carrier transport distances. This combination of properties is extremely rare and, as a result, commercial direct detectors are not common. Additionally, as the required detector thickness increases with X-ray energy, most direct detectors are restricted to the lower energy region of the spectrum before carrier transport becomes inefficient. Long carrier transit distances also increase their collection time, making direct detectors slow at responding (hundreds of microseconds up to milliseconds, depending on the electric field and thickness).[43] This can be problematic for tomographic applications,

which take with up to 1000 images per second,[44] as well as energy resolution applications, where photons must be processed individually before the next one arrives.

There exists some commercial applications of direct X-ray detectors. Despite their low attenuation, silicon X-ray detectors do exist, for example in silicon drift detectors (SDDs), however a low attenuation means they are rarely used in imaging applications.[45,46] The higher atomic number elements in cadmium zinc telluride (CZT, Cadmium Z = 48, Telluride Z = 52) results in better stopping power, and it is emerging as an X-ray detector material, especially for photon counting applications.[47,48] Amorphous selenium (a-Se) detectors are the most common direct X-ray detector, used in mammographic imaging applications where the sub-40 keV photons can still be efficiently detected.[49,50] To advance the use of direct X-ray detectors, semiconductors with improved carrier collection properties and higher attenuation efficiencies need to be developed. Otherwise, a solution to the limitations on direct detector performance comes by indirectly detecting the incident X-rays via an additional light emission step.

2.5 Indirect Detection

Indirect X-ray detectors involve a radiation-sensitive material that down-converts the incident beam into visible light, which is then collected by a sensitive photodetector, such as p-i-n photodiode arrays or photomultiplier tubes. The absorption process is the same as direct detectors, generating a cascade of carriers per X-ray photon. However, instead of collecting the generated charge carriers as electrical current, they are re-emitted as optical photons that are more easily detected by a separate photodetector. This emissive material is known as a scintillator, and the light produced from ionising radiation excitation is known as radioluminescence (RL). Given there are no long-range charge collection requirements, scintillators can retain detection properties when the material thickness exceeds millimeters, enabling use across the whole X- and γ-ray spectrum. As a result, indirect detectors dominate applications from medical radiography to particle collider calorimeters.

Decoupling the X-ray detection process into two distinct steps permits each to be optimised separately. The requirements of a photodetector to detect the scintillated light are within the capabilities of current performance, exploiting decades of development of this technology. Therefore, advancements in indirect detection rely on improvements in the performance of the scintillator itself. A summary of the figures of merit of a scintillator material are included in Table 2.3. Two essential performance attributes are bright and fast emission. The emission

from a scintillator is quantified by its light yield, i.e., the number of photons emitted per MeV of incident radiation. Like the responsivity for photodetectors, this quantifies the sensitivity. Emissive commercial materials CsI:Tl and GOS:Tb (GOS = gadolinium oxysulfide, Gd_2O_2S) both have light yields exceeding 60,000 photons MeV^{-1}, [51] allowing sensitive detection. Fast emission is a requirement in many applications, particularly high frame rate imaging (tomography) and time-of-flight systems. Fast emission is offered by the 5d-4f transition in lanthanides (Ce^{3+}, Pr^{3+}, Eu^{2+})[52,53], which offer decay times on the nanosecond scale whilst maintaining high emission yields, for example LSO:Ce, LYSO:Ce and $LaBr_3$:Ce. It is also important to consider the indirect detection system as a combination of the scintillator with the photodetector and signal processing electronics. The emission from the scintillator must be detected by the photodetector, which requires efficient spectral overlap of the RL and the photodetector quantum efficiency, and appropriate optical coupling between the two devices.

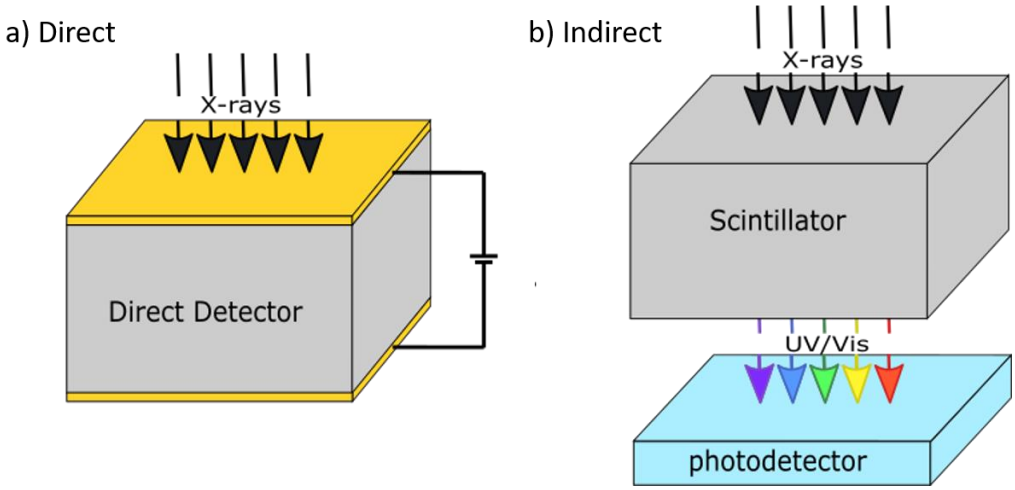

Figure 2.4: X-Ray Detection Mechanisms. *a) Direct detection. b) Indirect detection. Reproduced from Ref. 11 with permission from the Royal Society of Chemistry.*

The use of ionising radiation to generate images is a key application of detectors, requiring high spatial resolution, linear response with incident intensity, and low afterglow. In general, the spatial resolution of indirect detectors is fundamentally limited compared to direct detectors, due to light scattering in the scintillation step. To mitigate these losses, CsI:Tl can be evaporated into large needle like structures that allow waveguiding to improve spatial resolution. Such detectors typically use a fibre-optic plate as a supporting structure, which has the added advantage of attenuating the primary X-ray beam, providing protection to the optical sensor. In addition, high light yields (~60,000 photons MeV^{-1}) and mature fabrication techniques make CsI:Tl common in flat-panel imagers for medical radiography. Linear

responses to incident intensity is important as it allows intensity discriminations between small differences in tissue density, and it is primarily implemented by computed tomography (CT), which has the added benefit of consolidating large image sets, thereby reducing noise. Finally, a key requirement for imaging is low afterglow levels, which otherwise distorts image quality and reduces the modulation transfer function (MTF), especially in high frame-rate applications. Afterglow in CsI:Tl is high,[54] with >2% emission remaining at 3 ms,[55] limiting its use to longer integration times.

Table 2.3: Figures of Merit for Indirect X-Ray Detectors.

Figure of Merit	Description
Light Yield	The number of photons emitted by the scintillator per photon of set energy. (photons MeV^{-1}).
Response Speed	Assesses the temporal response of the device and can be quantified by the decay time of the scintillator emission. (ns).
Afterglow	Measures the residual light emission intensity a set time after excitation. Often caused by trapping and detrapping of charges before reaching luminescent centres and represented by the percent of total emission at a certain time after excitation. (e.g. % at 10 ms).
Emission Spectra	The spectrum of the scintillator emission. Ideally, this is tuned to the most suitable photodetector for the application, e.g. PMTs.
Dose Linearity	Represents the radiation dose range for which the scintillator response is linear. Particularly important in imaging applications.
Energy Linearity	Represents the photon energy range for which scintillator response is linear. Particularly important in photon counting modes for energy resolution.
Spatial Resolution	Measures the smallest object that can be resolved by an imager. The modulation transfer function (MTF) is used in radiology applications, which quantifies the level of detail in an object that is retained by the image.
Detector Quantum Efficiency	Detector quantum efficiency (DQE), quantifies the imaging ability of a detector. It is more all-encompassing than MTF by containing the signal contrast as well as the noise of the system.

X-rays generate a charge carrier generation cascade in detectors due to their large energies relative to the detector band gap. The number of carriers generated is proportional to the photon energy and, as a result, X-ray detectors can be used to resolve the energy of the incident photons. Energy resolution information is utilised in spectroscopy, high-energy physics, and security applications, and requires operating the detector in photon counting mode. The response of the scintillator is required to be proportional to the incident photon energy, and

each photon must be analysed before the next one arrives, necessitating scintillator detectors with fast emission and fast processing electronics. The resolving ability of a scintillator is quantified by its energy resolution and an ideal indirect detector would be able to resolve closely spaced photons, such as the 604 and 662 keV emission of caesium isotopes.[56] This requirement is particularly important in security applications and is fulfilled by NaI:Tl, with an energy resolution around 7% and a large light output of 43,000 photons MeV^{-1},[57] along with the ability to be fabricated in large dimensions.

Table 2.4: X-Ray Detector Applications and Material Requirements.

Application	Energy Range (keV)	Typical Material	Current Performance [Ref.]			Application Specific Requirements
			Light Yield (photons/MeV)	Decay Time (ns) (afterglow)	λ Max. (nm)	
Radiography (Medical)	60-120	CsI:Tl	60,000 [58]	1000 (0.5% at 3 ms) [58]	550	● Spatial resolution ● Linear response with dose
Radiography (Industrial)	10-120	GOS:Tb	60,000 [59]	600,000 (< 0.1% at 3 ms) [44]	545	● Scalable to large dimensions to image large objects ● Emission wavelength suitable to silicon imagers ● Low-cost
Computed Tomography (Medical)	80-140	$CdWO_4$	20,000 [60]	2000 (0.05% at 3 ms) [61]	495	● < 0.1% $^{o}C^{-1}$ temperature coefficient from beam induced heating ● Afterglow < 0.1% at 3 ms ● Decay Times below 10 μs ● > 20,000 photons MeV^{-1}
Mammography (Medical)	20-40	a-Se (direct detection)	n/a	n/a	n/a	● Spatial resolution ~100s μm (to detect low-contrast tumours)
PET (Medical)	511	LSO:Ce	40,000 [62]	40 [62]	420	● Spatial resolution to accurately determine line of response ● Energy resolution to reject scattered events ● Short emission decay times to reduce coincidence gate
TOF-PET (Medical)	511	$LaBr_3$:Ce	61,000 [63]	35 [63]	358	● Timing resolution of 10 ps
Astronomy	3-79 (NuSTAR)	CdZnTe (direct detection)	n/a	n/a	n/a	● Energy resolution of ~1.5 % at 60 keV
Calorimetry (High-Energy Physics)	Photons and electrons	Many: $PbWO_4$ (LHC Calorimetry)	140 [64]	Several components: <10ns, 20-200 ns, >500 ns [64]	475	● Energy resolution ● Large area fabrication 2x2x20 cm ● Sensitive to high energy photons
Spectroscopy (Nuclear Security)	10 – 10,000	NaI:Tl	43,000 [65]	230 [66]	415	● Energy resolution to resolve isotopes <7% 662 keV ● Low-cost for large areas

As indirect detectors retain their performance when of suitable thicknesses to absorb X-rays, they are more common commercially than direct systems. However, the introduction of the additional step can introduce inefficiencies that reduce detector performance. X-ray energy can be lost in this extra step from low RL light yields, and emitted light can spread to lower image resolution. This is where the simplicity of direct detectors is advantageous, but more work is

required to improve their performance. X-rays are utilised in a wide range of applications, each with unique requirements for the detector. As a result, the choice of X-ray detection mechanism and material is highly specific to each situation. In contrast to visible detectors where silicon devices prevail, many different X-ray detector materials are used commercially. A summary of the application specificity of X-ray detectors is included in Table 2.4.

2.6 Metal Halide Perovskites

Perovskites are a class of material that crystallise into the ABX_3 structure of the perovskite mineral, $CaTiO_3$. Metal halide perovskites represent a subcategory of perovskites, utilising a halide ion in the X-site, a B-site metal (most commonly Pb^{2+}), and an A-site cation often containing an organic component. The properties of these materials are a hybridisation of their organic and inorganic components, offering the low-cost, solution-based processing, and tunability associated with organic semiconductors, whilst retaining the ideal semiconductor properties expected from an inorganic material. In this thesis, the term perovskite is used to refer specifically to the metal halide variety.

2.6.1 Structure and Composition

The perovskite unit cell is shown in Figure 2.5. The extended structure shows divalent B-site cations surrounded by six monovalent X-site anions to form corner sharing $[BX_6]^{2-}$ octahedra, with monovalent A-site cations filling the interstitial sites. Various combinations of ions can form the perovskite structure, and provided they have the correct oxidation state, the size of the ions determines whether a perovskite structure can be formed. The Goldschmidt tolerance factor, *t*, predicts the lattice stability based on the ionic radii (*r*) of each site:

$$x = \frac{r_A + r_X}{\sqrt{2}(r_B + r_X)} \tag{2.14}.$$

Tolerance factors $0.8 \leq t \leq 1$ would be expected to form the perovskite structure. Cubic lattices form when *t* is close to unity, $0.9 \leq t \leq 1$, whereas lower symmetry tetragonal or orthorhombic formations arise when $0.8 \leq t \leq 0.89$ in order to accommodate the ions.[67,68]

While many ions can be utilised, there are several key compositions which have already gained success in applications. Methylammonium ($CH_3NH_3^+$, MA), formamidinium ($CH(NH_2)_2^+$, FA) or Cs^+ cations, or alloys thereof, represent typical A-site components. Lead, Pb^{2+}, occasionally partially or fully substituted with tin, Sn^{2+}, occupy the B-site. Finally, chloride, bromide and

iodide (Cl^-, Br^- and I^-) fulfil the X-site. Combinations of ions in these sites can tailor the structural stability, ensuring perovskite structures form, and allow control of their optoelectronic properties.[69]

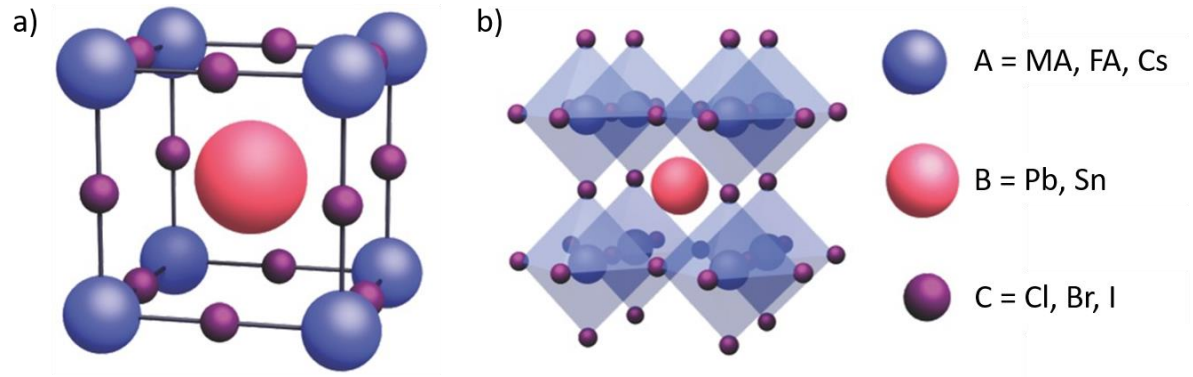

Figure 2.5: The Perovskite Structure. *a) Unit cell. b) Extended structure, with common ions for metal halide perovskites. Adapted with permission from Ref. 70.*

2.6.2 Optoelectronic Properties

Absorption

The band structure of a semiconductor determines its visible light absorption coefficient and its band gap, which in turn controls the energies of photons it can detect. Perovskites have a direct band gap, and subsequently possess high absorption coefficients around $10^5\ cm^{-1}$ across most of the visible spectrum.[71] Their absorption onset is sharp, with Urbach energies comparable to silicon (~10 meV), indicating an ordered semiconductor.[72] The valance band maximum is an antibonding hybrid of B-site *s* orbitals and X-site *p* orbitals, and the conduction band minimum is a mostly nonbonding combination of B-site *p* orbitals with some X-site *p* nature.[73] Therefore, changing the elements in the $[BX_6]^{4-}$ octahedra can alter the band gap of the material. The effect of A-site cations, whilst not directly contributing to the band edge states, play a smaller role on the band gap. By causing lattice contractions and tilting, different sized A-site cations will influence the overlap of the B- and X-site orbitals, changing the band structure.[74] A-site cations are more important to stabilising the crystal structure itself.[69] Compositional tuning allows control of the band gap from 1.2 to 3.1 eV.[75] The specific synthesis of reduced dimensionality structures, such as perovskite nanocrystals, provides further control of band gap, increasing values with quantum confinement effects.[76]

Perovskites are also highly suited to absorbing X-rays due to the presence of lead (Z = 82), the second highest non-radioactive element behind bismuth. Incorporations of fractions of caesium

(Z = 55) and iodine (Z = 53), along with suitable densities around 4 g cm^{-3} ($MAPbI_3$) further improve X-ray absorption.[54] As a result of the efficient attenuation, thinner perovskite layers are required compared to conventional detector materials: 0.36 mm of $MAPbI_3$ is needed to sufficiently stop 100 keV, compared to 10 mm, 1.6 mm and 0.46 mm, for Si, Se and CZT, respectively.[19]

Collection of Charge Carriers

The absorption of light generates an electron in the conduction band and leaves behind a hole in the valence band, and these particles are electrostatically attracted to one another. If this interaction, which is quantified by the binding energy, is high enough, it can lead to the generation of quasi-particle known as an exciton. Room-temperature binding energies are reported to be below 10 meV in perovskites, making free electrons and holes the dominant species. As a result, additional considerations of exciton separation are not required in device design.[77] This makes perovskites suitable as a light harvesting material for solar cells and detectors.

The ability to collect charges relies on the diffusion length, L, how far a charge carrier will travel before recombining. In turn, the diffusion length depends on the carrier mobility, μ, how fast it moves in an electric field, and the lifetime, τ:

$$L = \sqrt{D\tau} \tag{2.15},$$

$$D = \frac{\mu k_B T}{q} \tag{2.16},$$

where D is the diffusion coefficient k_B is the Boltzmann constant, T is the temperature and q is the elementary charge. The use of electric fields to aid charge collection in detectors makes the mobility-lifetime product, how far a carrier will move in a given electric field, a useful metric.[35] As a result, long lifetimes and high mobilities are desirable to collect charge carriers in detectors, especially X-ray detectors, with large electrode spacings.

Values of perovskite mobility in the literature vary, due to the dependence on variables such as material composition, processing conditions, and measurement technique. High-quality single crystals can exceed 100 $cm^2\ V^{-1}\ s^{-1}$, and values generally decrease for polycrystalline films.[78–81] Traditional semiconductors possess mobilities an order of magnitude higher, exceeding 1000 $cm^2\ V^{-1}\ s^{-1}$,[82] and the limitations to perovskite mobility have been attributed to Fröhlich scattering from optical phonons.[83] Instead, impressive diffusion lengths and

mobility-lifetime products are due to the long lifetime of charge carriers in perovskites, exceeding tens of microseconds.[79,84,85] The long lifetimes are in part due to low levels of deep traps, though could be further influenced by long lived carriers in shallow trap states,[86] polaron formation[87] and the Rashba effect.[88,89] The long drift and diffusion lengths of charges in perovskites results in efficient carrier collection, making them a suitable material for direct detector applications.

Recombination of Charge Carriers

If not collected, excited charge carriers in a semiconductor recombine, and this process can be described with the following rate equation:

$$-\frac{dn}{dt} = k_1 n + k_2 n^2 + k_3 n^3 \qquad (2.17),$$

where n is the carrier concentration, k_1 is the Shockley Read Hall recombination rate constant, k_2 is the band-to-band rate constant and k_3 is the Auger rate constant. The processes represented by k_1 and k_3 are non-radiative, and do not result in the emission of a photon. Instead, radiative recombination between electrons and holes occurs from the bimolecular k_2 process. The dominant recombination process in a semiconductor is dictated by the charge carrier density. Non-radiative recombination via a trap-assisted Shockley Read Hall mechanism dominates in perovskites at low excitation fluences, where carrier concentrations are below the density of trap states in the material. Trap densities in perovskites range from 10^{11} to 10^{16} cm^{-3} depending on processing conditions.[90,91] Radiative recombination dominates when excitation densities can exceed the trap states densities, and this regime is desired for efficient light emission in scintillators (and, indeed, for efficient carrier collection in direct detectors, where non-radiative processes result in charge carrier losses). The efficiency of the emission processes following optical and X-ray excitation are photoluminescence and radioluminescence quantum efficiencies, respectively (PLQE and RLQE). Increasing the efficiency of these radiative processes involves decreasing the prevalence of the competing non-radiative loss pathways. For example, the reduction of trap state densities by passivation increases emission quantum efficiencies, by decreasing the rate of Shockley Read Hall recombination.[92–94]

Introducing perovskite structures with quantum confinement leads to an increase in the exciton binding energy, as the electrostatic interaction between the electron and hole is no longer screened in all three dimensions.[95] Quantum confinement can be introduced by replacing the A-site cation with long chain organic molecules, such as butylammonium, which act as spacers

between sheets of BX_6 octahedra. Precise stoichiometric control of the amount of organic spacer can allow dimensionality tuning, allowing 1 and 2D structures to form.[96] Additionally, colloidal synthesis can produce 0D nanocrystal structures. The increase in exciton binding energy in these confined systems can mean free electrons and holes are no longer the dominant species, and instead excitons can form. The lack of free charge carriers, combined with the insulating effect of any organic material, is detrimental to charge collection applications.[97] However, it increases the probability the exciton will recombine radiatively, and emit photons. This is desirable in light emission applications, such as LEDs and scintillators, and reduced dimensionality perovskites are common in these applications.[98–100]

2.6.3 Processing

A key advantage of perovskite semiconductors compared to traditional inorganic materials is their ability to be produced using solution processing methods. This enables low-temperature perovskite deposition without the need for sophisticated equipment, reducing production costs. Depositing the correct stoichiometry of precursor salts (for example, methylammonium iodide and lead(II) iodide for $MAPbI_3$), followed by annealing to remove remaining solvent (~100 ^oC), forms the perovskite structure. The fabrication process dictates the properties of the perovskite film, as well as its material morphology and crystallinity. An important feature of the deposition procedure for detectors is the perovskite thickness, which must be adequate to absorb the incident photons. Other requirements are uniformity and being free of pinholes.

Solution deposition, while advantageous for low-cost production, usually produces semiconductors with significant disorder and high defect densities. Classical semiconductor theory correlates defect density with inferior properties, lowering mobilities and lifetimes, and promoting non-radiative decay. As a result, solution processed defective films are expected to show poor performance.[101,102] Defect densities in these perovskite films are on the order of 10^{15} cm^{-3}, [81,103,104] two orders of magnitude above polycrystalline silicon.[105] However, the properties of perovskites, introduced above, are indicative of a high performance semiconductor, demonstrating a remarkable tolerance to these defects. This tolerance is in part due to the antibonding nature of the band edge states, whereby defects involving the breaking of bonds will not reside within the band gap.[106] It has also been found that the low formation energy of defects produces shallow intraband traps, or traps not within the band gap at all, whereas detrimental deep trap states have a high formation energy.[107] This prevents the short recombination lifetimes and Shockley-Read-Hall recombination that can diminish the optoelectronic properties of a material.

Spin coating, a fabrication method whereby precursor solutions are deposited onto a substrate followed by spinning at several thousand revolutions per minute (rpm), generates uniform and compact thin films. Its simplicity and inexpensive equipment make it a workhorse of the perovskite research community. Precursor solution concentration and spin parameters provide points of control over the deposition. However, a disadvantage of this method comes from its lack of scalability. Film production is only possible on small substrates (on the scale of a few cm^2) and it is a batch process. Commercial production of perovskites would require a higher throughput, with a roll-to-toll deposition process. Blade coating and inkjet printing would fulfil this requirement, but currently state-of-the-art perovskite device performance still relies on spin coated films.[108–111] Spin coating also favours thin films, up to ~1 μm, which suits the absorption depth of optical photons, but not X-rays, so thicker deposition methods are needed for X-ray detectors.

Solution processing of perovskites generates polycrystalline films, with visible grains separated by grain boundaries. Adjacent perovskite grains have shown differences in performance, an example of heterogeneity in perovskite films.[112] The boundaries between grains have also shown to be detrimental to performance, promoting non-radiative decay and acting as ion-migration channels and degradation pathways.[113–115] Growing single crystals, with no grain boundaries visible under microscopy, is one pathway to improve performance over polycrystalline films. Single crystals can also be produced with controllable thicknesses exceeding centimetres, suiting X-ray detection, and offer trap densities below 10^{10} cm^{-3}.[23,116,117]

Classically, the growth of single crystals is time consuming. After dissolving precursors into a heated solution, the temperature must be slowly decreased to induce supersaturation and a low density of perovskite nucleation events. Crystal growth rate is on the order of millimetres per day, taking weeks to months to reach the sizes needed for devices.[118,119] However, perovskites show an unusual solubility in some solvents, whereby they become less soluble as temperature increases. This allowed the development of an inverse temperature crystallisation method, able to grow sizable crystals in just a few hours.[120,121] Another traditional disadvantage of crystal growth is it offers no control over their shape, which is impractical to device integration. The growth occurs in all three dimensions, which means that controlling thickness also limits the lateral sizes of the device. It was discovered that the shape of perovskite single crystals could be controlled by confining the space in which it grows.[121] Subsequently, large area and thin

single crystals are now possible, which are much more appealing to devices and applications.[122,123]

2.6.4 Optoelectronic Devices

A unique combination of properties have allowed perovskites to be successfully deployed in a wide range of optoelectronic devices. The interest in the material surged following demonstrations as a sensitiser in solar cells in 2009, and perovskite photovoltaics have since developed dramatically.[124] Ambipolar transport of elections and holes enables planar device structures, and power conversion efficiencies (PCEs) now approach 26%.[124–126] The band gap tunability and facile processing has allowed tandem solar cells to also flourish. Tandem devices employ two light absorbers, absorbing complementary regions of the spectrum, to overcome the thermodynamic limitations of single junction solar cells.[127] All-perovskite tandems, involving perovskites with a wide and narrow band gap, now exceed the efficiencies of single junctions.[128] More immediate commercialisation may come from perovskite-silicon tandems, which piggyback on the maturity of silicon photovoltaics, and now exceed 30% efficiency.[124,129]

While perovskite solar cells can efficiently convert light into electricity, LEDs perform the opposite function. Perovskite LEDs exploit the high emission quantum yields and band gap tunability to efficiently emit light with high colour purity, which could enable low-cost and energy efficient lighting and displays.[130–132] Lasers,[133–135] memristors,[136–138] and transistors[139–141] have also all been demonstrated with perovskites, highlighting the versatility of this material.

Photodetectors

The exceptional light harvesting ability of perovskites make them ideal photodetector candidates, and the development of perovskite photodetectors followed their successful deployment in solar cells. Initial devices exploited the simplicity of metal-semiconductor-metal devices, and perovskite photoconductors emerged in 2014.[142,143] Photodiodes were developed later the same year,[37,144] and impressive detection was achieved within the first wave of devices.

Initial devices utilised simple $MAPbX_3$ perovskites (X usually iodide), and the detection performance was quick to outperform existing commercial detectors. Engineering of the transport layers was an early target to improve performance, and allowed perovskite

photodiodes to exceed the responsivity of silicon devices, with 0.4 A W^{-1} at 600 nm.[145] Composite Al_2O_3 and PCBM ([6,6]-phenyl-C_{61}-butyric acid methyl ester) interfacial layers enabled this responsivity, also suppressing the dark current compared to reference devices. The thickness optimisation of PCBM and C_{60} for transport layers in photodiodes was separately developed. The benefits of a thick interlayer, reducing dark current injection and shunt pathways, was balanced against the low mobility of the organic molecules to prevent space charge regions forming to maintain LDRs and response speeds.[22] LDRs above 200 dB were displayed, exceeding the commercial Si and InGaAs detectors (120 dB and 66 dB, respectively).[37] Transport layers were also shown to influence the perovskite interface, and the passivation effect of fullerene layers alongside the injection blocking of a crosslinked organic polymer reduced dark currents, enabling the resolution of low light intensities below 1 pW cm^{-2}.[146] Additionally, the amplification of photocurrents through developing devices with photoconductive gain was shown in the first wave of published perovskites detectors, which combined with a low dark current would further enhance low-light detection.[38,104,144]

Through combining the reductions in dark currents with the ideal light harvesting properties of perovskites, the initial developments produced detectivities above 10^{12} Jones, surpassing the sensitivity of silicon devices.[22,145,146] In some cases, 10^{13} Jones was exceeded. However, these claims relied on unproved assumptions that the noise current was limited by the dark current shot noise.[37,38] Also, photodiodes optimised for fast responses were developed, by reducing perovskite thickness and device active areas, reaching 2.8 MHz cut-off frequencies.[37] The impressive performance of this initial wave of perovskite photodetectors highlights the suitability of perovskites to light detection.

With initial performance already comparable to, or exceeding, commercial levels, photodetector development focused on producing devices with greater functionality. The unique properties of perovskites allow detector features that are not possible with traditional inorganic semiconductor devices. Low-temperature and solution deposition is compatible with flexible substrates, which enables perovskite detectors that bend and conform to surfaces. Polymer (PET and PEN) and carbon cloth based substrates were utilised to give flexibility, and performance was maintained after hundreds of 180º bending cycles.[143,147–149] Flexibility was not restricted to simple photoconductive structures either, with flexible photodiodes also demonstrated, impressively maintaining the high detectivities of rigid devices.[30,150] Additionally, perovskites have been combined with plasmonic structures to enhance absorption and photocurrent, with ~250% improvements in responsivity shown.[151–154]

The ability to tune the band gap in perovskites offers control over the regions of the spectrum absorbed by the detector, allowing manipulation of the spectral bandwidth. By varying the perovskite composition, bandwidths were shifted deeper into the IR with the addition of tin alloys.[155–157] Spectral selectivity was introduced by developing wide band gap perovskites, through chloride additions or quantum confined perovskite structures, which exclusively detect UV light, remaining blind to visible light.[158–161]

Spectral selectivity was advanced further by introducing detectors with a highly narrowband response that is sensitive to only a small band of photon energies (Figure 2.6a). This is vital for colour imaging and applications including robotic vision, communications, and spectroscopy. Traditionally, colour selectivity is obtained through the addition of filters onto broadband detectors, which add bulk, cost and complexity to the detector, whilst also being susceptible to side-peaks and damage. Filterless detectors, with in-built narrowband responses, would therefore improve colour selective performance. Narrowband perovskite detectors were shown using a charge collection narrowing mechanism (sometimes referred to as CCN) introduced by Armin et al..[162] Charge collection narrowing is a method to manipulate the internal quantum efficiency of different energy photons, by employing thick absorber layers (Figure 2.6b). Photons of high energy, above the absorber band gap, are efficiently absorbed by the perovskite close to the surface. The resulting imbalanced carrier transport distances for the generated electrons and holes leads to low collection efficiencies. Lower energy photons, of approximately the same energy as the perovskite band gap, are absorbed much more uniformly across the whole absorber thickness, and as a result have much higher collection efficiencies. This leads to only a select band of photons being detected by the device, and by tuning the perovskite band gap, the peak response can be shifted throughout the spectrum. This mechanism has been successful for perovskite detectors, offering spectral control and high selectivity, with full-width-half-maxima (FWHM) as low as 12 nm.[163–168] However, the thick active layers in these devices, while responsible for the selectivity, can detract from other detection metrics. Slow response speeds, low responsivity of the narrowband peak, and the requirement of external biases, all result from charge collection narrowing. This was overcome by exploiting a self-filtering mechanism, whereby an ‘optically active, electronically dead’ perovskite layer was used as a filter, allowing narrowband response from thin perovskite layers which retained fast response speeds of 100 ns (Figure 2.6c).[169]

Recently, greater spectral functionality has been offered from dualband photodetectors, which have two separate response windows in a single device, and these bands can be switched in-

situ. Originally, these devices were only possible via complicated and expensive lithographic processes on inorganic semiconductors, limiting applications to military use.[170–172] Lowering the cost of multiband detectors, by using the unique properties of perovskites, will enable more affordable devices and lead to new applications. Dualband detection has been developed with perovskites through several intelligent device structures.[173–176] These devices allow switchable performance, often with bias polarity[177,178] or illuminating different sides of the device[179]. However, to date, only two separate modes of operation have been achieved. Enhanced functionality will be presented in Chapter 5.

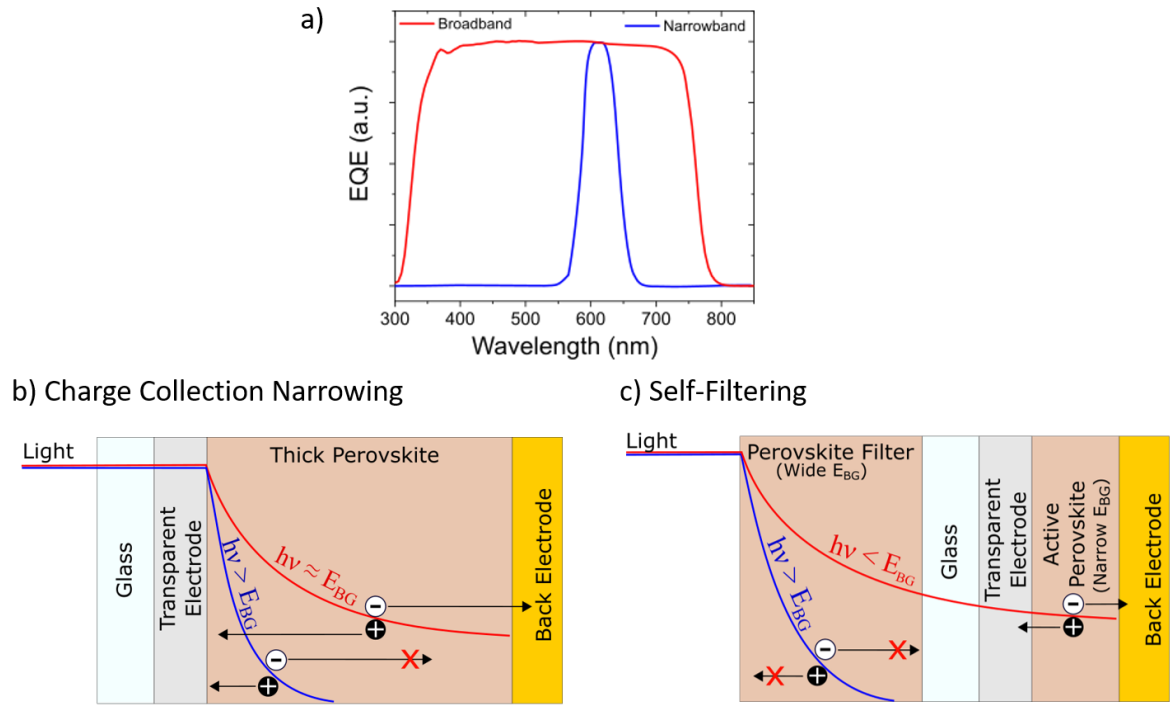

Figure 2.6: Narrowband and Broadband Photodetector Response. *a) Response Spectrum of a narrow and broadband photodetector. b) Mechanism of charge collection narrowing to achieve filterless narrowband response. c) Self-filtering narrowband detection mechanism, using a wide band gap perovskite filter.*

Direct X-Ray Detectors

A combination of efficient X-ray attenuation from high atomic number components with excellent charge transport makes perovskites the ideal material for direct X-ray detectors. However, as most applications of perovskites require sub-micrometre films, the first challenge facing perovskites in this role was producing thick enough layers to absorb radiation. Single crystals overcame this hurdle, enabling millimeter thicknesses, and the first X-ray induced currents were reported in $CsPbBr_3$ and $MAPbI_3$ crystals.[80,180] The importance of long carrier

drift lengths to collect carriers across the large thicknesses, led to a focus on optimising the mobility-lifetime product in perovskite X-ray detectors. $MAPbI_3$, $MAPbBr_3$ and $CsPbBr_3$ single crystals all exhibit mobility-lifetime products around 10^{-2} cm^2 V^{-1}, and allowed sensitivities to reach of 80 μC Gy_{air}^{-1} cm^{-2}, four times greater than a-Se devices.[78,181–183] Unlike photodetectors and solar cells, which grow perovskite directly onto substrates, crystal production produces freestanding perovskites, which need to be incorporated into devices after growth. By modifying a silicon wafer with a self-assembled monolayer, $MAPbBr_3$ was grown directly onto substrates, simplifying device fabrication. This monolayer also reduced dark currents, and led to sensitivities of 2.1 x10^4 μC Gy_{air}^{-1} cm^{-2}. One caveat to this result is the optimisation of device thickness to 8 keV X-rays, requiring only 150 μm of perovskite to absorb the soft X-rays. Once thickness increased to 2 mm, suitable for 50 kV radiation, sensitivities lowered to 322 μC Gy_{air}^{-1} cm^{-2}.[184] This provides an example of the transparency required when reporting the performance of X-ray detectors, discussed further in Chapter 7.

New fabrication methods were developed, aiming to create thick perovskite films whilst offering more control over shape, size and device integration. Pressing of perovskite microcrystals generated thick perovskite wafers suitable for X-ray detection. The increase in the number of boundaries between grains lowered mobility-lifetime products to 10^{-4} cm^2 V^{-1}, but sensitive detection of 2500 μC Gy_{air}^{-1} cm^{-2} for 70 kV tube voltages was maintained.[185–188] Integration of similar perovskite wafers onto transistor arrays allowed X-ray images to be produced, a significant step towards commercialisation, but spatial resolution was below the level of a-Se.[189] A hot-pressing fabrication method, whereby $CsPbBr_3$ powders are melted and slowly cooled, allowed record sensitivities of 5.5 x10^4 μC $Gy_{air}^{-1}cm^{-2}$.[190] Elsewhere, the simplicity of perovskite deposition has also allowed the development of a unique method to deposit precursors within a membrane scaffold structure, leading to mechanical properties which can be controlled with the scaffold material. A nylon membrane, filled with $MAPbI_3$ by a vacuum pumping method, produced a flexible detector which maintains sensitivity of 14,400 μC $Gy_{air}^{-1}cm^{-2}$ (100 keV X-rays).[191] Flexible detectors that can conform to objects can improve imaging by reducing any vignetting associated artefacts.[192]

The ability of X-ray photons to generate a response proportional to their energy allows energy resolution information from X-ray detectors. Resolving photon energies requires individual photons to be fully absorbed by a detector, followed by an efficient conversion and collection of the resulting charge carriers. In addition, photons must be processed one by one, to enable the full signal to be collected before the next photon arrives. This is known as photon counting

mode, and is utilised in spectroscopy and nuclear reaction applications, often detecting the emission of radioactive nuclei (hence also referred to as γ-mode). Most imaging applications instead use the current integration mode discussed above.[193] Photon counting performance is quantified by the energy resolution, which measures the ability to resolve the monoenergetic emission of radioisotope decay (e.g. 122 keV photons from ^{57}Co and 662 keV photons from ^{137}Cs isotopes). Energy resolutions of commercial materials (CZT and Ge) are below 1% (lower values represent higher resolution). The attenuation and carrier transport properties of perovskites make them ideal for this application, and initial reports have displayed high resolution.[181–183,194–196] $CsPbBr_3$ devices have shown the best performance to date, 1.4% resolution of 662 keV photons, approaching commercial values, whilst also demonstrating a scalable ingot production method.[197]

The long transport distance in direct detectors requires large external biases in order to maintain suitable detection efficiencies and response times. However, external biases increase the dark current through increased charge injection, and make it susceptible to charge drifting. The drifting of dark current changes the baseline of a detector, causing repeat scans to provide different readings, which generates imaging artefacts. Ion migration within the perovskite layer has been reasoned to cause the drift, with ions moving towards interfaces to set up an internal electric field which opposes the external bias.[198–200] The soft nature of the perovskite lattice, with an abundance of defects and grain boundaries, have made ion migration a common issue in all perovskite device applications (see Chapter 4 for a study on the impact of ion migration on perovskite photodetectors).[201–203] Efforts to decrease the variation in dark current with time will improve device operation, while targeting the magnitude of dark current will reduce the device noise to enable lower LoDs. Removing the charge injection pathways that contribute to dark current has been attempted by reducing the perovskite defect density,[204,205] optimising the perovskite interfaces energetics, and developing devices that can operate without an external bias.[206–208] Lower dimensionality structures show reduced current drifts, with increased energetic barriers to ion migration[208–211] The low and stable dark current in these devices allows LoDs below 100 $nGy_{air}\ s^{-1}$.[212,213] More fundamental improvements may be possible by redesigning the detector structure, to overcome the requirements of long transport lengths and large biases, as proposed in Chapter 7.[214,215]

Indirect X-Ray Detectors

Perovskites were first proposed as scintillators in the 1990s.[216–219] This application has been revived in the last few years following the great success of perovskites as light emitters with

high PLQEs and colour control from band gap and dimensionality tuning. Recently, scintillation has been demonstrated from a range of perovskites, from bulk crystals to nanocrystals.[98,99,220] They remain an exciting prospect to offer sub-nanosecond emission with high light yields, from a material that can be synthesised inexpensively and at low temperatures.

Initial research into perovskite scintillators focused on 2D structures. These perovskites contain sheets of lead halide octahedra separated by large organic spacer cations, and (Phe)$PbBr_4$ ($(C_6H_5(CH_2)_2NH_3)_2PbBr_4$) displayed light yields of 10,000 photons MeV^{-1} with impressive decay times of 9.6 ns.[54,218,221] These systems were continually developed, and a study of 11 similar compounds reached a peak performance of 40,000 photons MeV^{-1} and 5.3 ns decay times using $(BA)_2PbBr_4$ (BA = butylammonium).[222] The ultrafast emission of 2D materials is promising, exceeding the speed of fast commercial materials such as LYSO:Ce (33 ns)[223] and $LaBr_3$:Ce (15 ns)[63], which may enable new timing resolution functionality in detectors. Decay times were developed further by doping with lithium.[224,225] A 4% Li:Pb ratio in a PEA_2PbBr_4 system (PEA = phenethylammonium) increased light yields by removing competing non-radiative pathways. 13% improvements in light yields produced over 20,000 photons MeV^{-1}, with timing resolutions below 100 ps possible.[226] This doping technique was expected to be universally beneficial, and could find success in other 2D perovskite scintillators.

$CsPbX_3$ nanostructures are a promising class of scintillator materials. $CsPbBr_3$ nanocrystals exceed the X-ray to light conversion efficiency of commercial GOS and exhibited fast decay times of 44 ns.[98,99] $CsPbBr_3$ nanosheets demonstrated a light yield of 21,000 photons MeV^{-1}, in a blade coating deposition that enables large area fabrication (72 cm^2).[227] Further improvements in emission were seen by embedding $CsPbBr_3$ nanocrystals inside a Cs_4PbBr_6 host matrix. Passivation effects of the host material enabled light yields of 64,000 photons MeV^{-1}, matching CsI:Tl.[228,229] Incorporating nanocrystals inside various materials has since become a successful strategy to overcome the radiation induced aggregation of the material and improve mechanical properties, with examples of flexible scintillator composites.[230–234] This strategy was taken further by designing perovskite nanocrystal-polymer combinations, whereby the perovskite acts as an X-ray sensitiser for the organic emitter.[235] These systems have allowed rapid RL decays of 3.4 ns.[236]

Aiming to reduce the toxicity of scintillators, lead-free perovskites have also been utilised. Replacing lead with different size and oxidation state cations, can open up new materials and structures. Double perovskites, containing ordered arrangements of mono- and trivalent B-site

metals, have demonstrated impressive RL properties. $Cs_2Ag_{0.6}Na_{0.4}In_{1-y}Bi_yCl_6$ scintillators allow the X-ray attenuation to be tuned through additions of bismuth, the most attenuating non-radioactive element, and optimal stoichiometries displayed a light yield of 39,000 photons MeV^{-1}.[237] Similarly, $Cs_2NaLnCl_6$, (Ln = Tb or Eu) have reached 46,600 photons MeV^{-1}.[238,239] However, the Laporte forbidden f-f orbital transition from the lanthanide contribution slows the response speed, with decay times exceeding milliseconds, which would generate imaging aretefacts.[239]

The most impressive light yields to date originate from low-dimensional organic metal halides. These materials do not form the perovskite structure, but do contain metal halide moieties, and are often categorised with perovskite scintillators. $Cs_3Cu_2I_5$, forming a 0D structure, is a promising example of these materials, demonstrating light yields of 79,000 photons MeV^{-1}.[240–243] This material has also been developed into 400 cm^2 flexible films, suitable for commercial applications.[244] Similarly, $(C_{38}H_{34}P_2)MnBr_4$ and Cs_4EuBr_6 form 0D structures, emitting 80,000 and 78,000 photons MeV^{-1}, respectively.[245,246] State-of-the-art light yields have been realised with 1D Rb_2CuBr_3, emitting 91,000 photons MeV^{-1}.[247] These structures are all in excess of the brightest commercial materials, with CsI:Tl and GOS both emitting ~60,000 photons MeV^{-1},[58,59] which could enable more sensitive X-ray detectors once combined with photodetectors in complete systems. However, while these structures produce the highest light yields, there are concerns on their response times and afterglow. Emission commonly originates from self-trapped structures, which can produce slow decay times. Rb_2CuBr_3 in particular exhibits significant afterglow, with 2.7% emission remaining 20 ms after irradiation. [247]

Despite a short period of development, perovskite scintillators have already been incorporated in full indirect detection systems, displaying impressive performance. Nanocrystal based perovskite imagers have produced high spatial resolution, quantified by the MTF, due to reduced internal light scattering compared to bulk films and single crystals. The resulting reduction in optical cross-talk is promising for high-resolution imaging applications. MTF values of 9.81 lp mm^{-1} (MTF=0.2)[99] and MTF=0.72 at 2 lp mm^{-1} [98] have been reported in $CsPbBr_3$ NCs, exceeding the performance of GOS and CsI:Tl reference devices, respectively. The short decay times of the $Cs_2Ag_{0.6}Na_{0.4}In_{1-y}Bi_yCl_6$ double perovskite enabled a dynamic image of a bending finger to be produced, possible at low incident doses of 47.2 μGy s^{-1}.[237] However, an initial resolution of 4.3 $lpmm^{-1}$ (MTF=0.2) dropped to 1.4 $lpmm^{-1}$ as the perovskite wafer thickness increased from 0.1 to 0.6 mm, due to increased light scattering within the scintillator, highlighting the inherent limitations to indirect detection. Wide linear

responses between 30 – 550 μGys^{-1}, the limits of the X-ray source utilised in the study[247], have been presented, as well as linearity down to 13 nGys^{-1}, an encouraging result for low-dose imaging.[98] Apart from self-trapped perovskite emission, reports on perovskites have displayed virtually no afterglow (5 ppm at 20 ms[248]), offering levels similar to commercial bismuth germinate (BGO, $Bi_2Ge_3O_9$) and cadmium tungstate ($CdWO_4$). Combined with the short decay times, this may enable faster frame rates than is currently possible.

There have also been reports of energy resolution from perovskite scintillator spectroscopic systems. For example, (Phe)$PbBr_4$ crystals exhibited an energy resolution of 35 ± 5% (662 keV) with a linear response over the 122 − 662 keV range,[248] and a similar lithium-doped $(PEA)_2PbBr_4$ system presented improved resolution of 12.4% (662 keV).[224] In addition, $MAPbBr_{0.05}Cl_{2.95}$ demonstrated an improved value of 10.5 ± 0.4% (662 keV)[249]. A $CsPbBr_3$:Cs_4PbBr_6 powder presented the best energy resolution values in perovskite scintillators to date, reaching 3.0 ± 0.1% (59.6 keV), emphasising the promise in this application.[229] Overall, although current performance falls short of optimised energy resolving detectors, such as Silicon Drift Detectors (SDDs), the energy resolution of perovskites scintillators is largely unexplored and represents an exciting area for further development.

Overall, the combination of excellent semiconductor properties and efficient X-ray attenuation make perovskites uniquely placed to advance photodetectors, direct X-ray detectors and scintillators. These ideal properties not only enable perovskite detectors to outperform established materials, but offer the chance to introduce new detector functionality. This could lead to improved detectors that can enhance existing applications and open up new technologies for visible and X-ray photons.

Chapter 3

Experimental Methods

In this chapter, experimental details on detector fabrication are outlined as well as the resulting techniques to assess perovskite quality and device performance. The development process of photo- and X-ray detector characterisation methods are included in Chapters 4 and 7, respectively, with a summary of the established procedures included here. The cases where experiments were performed by colleagues, or were collaborative, are clearly stated.

3.1 Device Fabrication

3.1.1 Optical Photodetectors

n-i-p Photodiodes – Bart Roose

Fluorine doped tin oxide (FTO, Sigma Aldrich) coated glass was cleaned by sonication in 2% Hellmanex III (Helma) solution (in deionised water) for 15 minutes, then rinsed with deionised water, followed by sonication in isopropanol (IPA, Sigma Aldrich) for 15 minutes. Substrates were dried and transferred to a hotplate and heated to 450 ^{o}C. Compact titanium(IV) oxide (c-TiO_2) was deposited by spray pyrolysis of a solution containing 9 mL ethanol, 0.6 mL titanium(IV) diisopropoxide bis(acetylacetonate) (Sigma Aldrich) and 0.4 mL acetylacetone (Sigma Aldrich). Substrates were cooled to room temperature before the mesoporous TiO_2 (m-TiO_2, 150 mg mL^{-1} paste in ethanol, Greatcell Solar Materials) was deposited by spin coating (4000 rpm, 10 seconds, 2000 rpm ramp). After spin coating, the substrates were transferred to a hotplate preheated at 125 ^{o}C and the following protocol was used for annealing: 10 minutes at 125 ^{o}C, 15 minute ramp and 5 minute dwell at 325 ^{o}C, 5 minute ramp and 5 minute dwell at 375 ^{o}C and 5 minute ramp and 30 minutes dwell at 450 ^{o}C. Substrates were then allowed to cool to 150 ^{o}C, after which they were transferred to a nitrogen-filled glovebox for perovskite deposition. Perovskite films were deposited from a precursor solution containing,

formamidinium iodide (FAI, 1 M, Greatcell Solar Materials), lead(II) iodide (PbI_2, 1.1 M, TCI), methylammonium bromide (MABr, 0.2 M, Greatcell Solar Materials), lead(II) bromide ($PbBr_2$, 0.22 M, TCI), and caesium iodide (CsI, 0.075 M, Sigma Aldrich) in anhydrous N,N-dimethylformamide and dimethylsulfoxide (DMF:DMSO, both Sigma Aldrich) 4:1 (v/v). The perovskite solution was spin coated in a two-step program at 1000 and 6000 rpm for 10 and 20 seconds respectively. During the second step, 100 μL of anhydrous chlorobenzene (Sigma Aldrich) was poured onto the spinning substrate 5 seconds prior the end of the program. The substrates were then transferred to a hotplate preheated to 100 ^{o}C and annealed for 60 min. After cooling down to room temperature, spiro-OMeTAD (0.07 M, Lumtech) in chlorobenzene, doped with t-butylpyridine (3.3 mol mol^{-1}, referring to per mol of spiro-OMeTAD, Sigma Aldrich), bis(trifluoromethane)sulfonamide lithium (0.5 mol mol^{-1}, Sigma Aldrich), and tris(2-(1H-pyrazol-1-yl)-4-tertbutylpyridine) cobalt(III) tris(bis(trifluoromethylsulfonyl)imide) (0.05 mol mol^{-1}, Sigma Aldrich) was deposited by spin coating (4000 rpm, 20 seconds). Devices were finished by thermal evaporation of 80 nm of gold. Device pixel areas were defined by the evaporation mask to be 0.1 cm^2. Devices were stored in a desiccator cabinet, with <10% relative humidity maintained by silica beads and nitrogen purging.

p-i-n Photodiodes – Bart Roose

Indium tin oxide (ITO) coated glass (Kintec Company) was cleaned by sonication in 2% Hellmanex III (Helma) solution (in deionised water) for 15 minutes, rinsed with deionised water and sonicated in IPA (Sigma Aldrich) for 15 minutes. The substrates were dried and cleaned further using a UV Ozone cleaner. Poly(3,4-ethylenedioxythiophene) polystyrene sulfonate (PEDOT:PSS, Ossila Al 4083) was diluted with methanol (3:1) and was deposited in ambient air by spin coating (4000 rpm, 20 seconds, 1000 rpm ramp), followed by 20 minutes annealing at 140°C. The substrates were then transferred to a nitrogen-filled glovebox for perovskite deposition. Alternatively, a 1 mM solution of (2-(9H-carbazol-9-yl)ethyl)phosphonic acid (2PACz, TCI) in anhydrous ethanol was deposited by spin coating (3000 rpm, 30 seconds)[250] on the ITO coated glass, followed by annealing at 100°C for 10 minutes. After the substrates were cooled down to room temperature, perovskite films were deposited from a precursor solution containing, FAI (1 M, Greatcell Solar Materials), PbI_2 (1.1 M, TCI), MABr (0.2 M, Greatcell Solar Materials), $PbBr_2$ (0.22 M, TCI) and CsI (0.075 M, Sigma Aldrich) in anhydrous DMF:DMSO 4:1 (v/v). The perovskite solution was spin coated in a two-step program at 1000 and 6000 rpm for 10 and 20 seconds respectively. During the

second step, 100 µL of anhydrous chlorobenzene was poured onto the spinning substrate 5 seconds prior the end of the program. The substrates were then transferred to a hotplate preheated to 100 °C and annealed for 60 minutes. Subsequently, 20 nm of C_{60} (Sigma Aldrich), 7 nm of bathocuproine (BCP, Alfa Aesar) and 120 nm of copper were deposited by thermal evaporation. Device pixel areas were defined by the evaporation mask to be 0.13 cm^2.

Two-Terminal Tandem Photodetectors – Bart Roose

Patterned ITO glass substrates (Kintec Company) were cleaned using 15 minutes of sonication in a 2% Hellmanex III (Helma) solution, followed by 5 minutes in deionised water, 15 minutes in acetone (Sigma Aldrich) and 15 minutes in IPA (Sigma Aldrich). The substrates were dried using a nitrogen stream and subjected to a 15 minute UV Ozone treatment before being transferred into a nitrogen-filled glovebox. A 1.5 mmol mL^{-1} solution of 2PACz (TCI) in anhydrous ethanol was spin coated at 3000 rpm (5 second ramp) for 30 seconds, followed by annealing for 10 minutes at 100 °C. After cooling down to room temperature, $Cs_{0.05}MA_{0.16}FA_{0.79}PbI_xBr_{3-x}$ perovskite was deposited onto the substrates by spin coating at 1000 rpm for 10 seconds (1 second ramp) and 6000 rpm for 20 seconds (3 second ramp). Anhydrous chlorobenzene was dripped onto the spinning substrate 5 seconds before the end of the program. The substrates were then annealed for 60 minutes at 100 °C. The substrates were then transferred to a thermal evaporator for deposition of 20 nm of C_{60} (Sigma-Aldrich). A 25 nm tin(IV) oxide (SnO_2) interlayer was deposited by atomic layer deposition (ALD, Picosun). Tetrakis(dimethylamino)tin(IV) (TDMASn, EpiValence) was used as precursor and H_2O as reactant. The precursor bubbler was heated to 75°C and the chamber to 100 °C, the reactant vessel was kept at room temperature. The pulsing sequence consisted of a 0.6 second pulse of TDMASn, 10 second purge, 0.1 second pulse of H_2O, 10 second purge, resulting in a growth rate of 0.1 nm per cycle. Following ALD, 1 nm of gold was deposited by thermal evaporation. The substrates were removed from the glovebox and a filtered (0.45 µm membrane) 3:1 solution of methanol (Sigma-Aldrich) and PEDOT:PSS (Clevios Heraeus Al 4083) was subsequently spin coated on top of the substrates at 4000 rpm (3.5 second ramp) for 30 seconds, followed by annealing at 140 °C for 20 minutes. After removing the substrates from the hotplate, they were immediately transferred to a nitrogen-filled glovebox. $Cs_{0.05}MA_{0.15}FA_{0.80}PbI_xBr_{3-x}$ perovskite was deposited onto the substrates by spin coating at 1000 rpm for 10 seconds (1 second ramp) and 6000 rpm for 20 seconds (3 second ramp). Anhydrous chlorobenzene (Sigma Aldrich) was dripped onto the spinning substrate 5 seconds before the end of the program. The substrates were then annealed for 60 minutes at 100 °C.

After cooling down to room temperature, 20 nm of C_{60} (Sigma Aldrich), 8 nm of BCP (Sigma Aldrich) and 120 nm of copper were deposited by thermal evaporation. Device pixel areas were defined by the evaporation mask to be 0.13 cm^2. Perovskite absorber thicknesses were varied using the precursor solution concentrations, with stock concentrations of 0.7/0.9/1.1/1.25/1/6/2.0 M producing thicknesses of ~350/450/550/650/850/1000 nm, respectively. Higher concentrations, and thicknesses, were not possible due to solubility limitations.

3.1.2 Direct X-ray Detectors

Device A: Photoconductor - Dominik Kubicki

Equimolar amounts of methylammonium iodide (MAI, Sigma Aldrich) and PbI_2 (Sigma Aldrich) powders were ground in a pestle and mortar until homogeneous (~10 minutes). A 1.3 cm dimeter mould was filled with 0.8 g of powder, and pressed in a hydraulic press (George E. Moore & Son Press) for 30 minutes. Pellets of ~1.5 mm thickness were produced, and thickness can be controlled by varying the amount of precursor powder in the press. Electrical contacts were applied using conductive silver or carbon paste over an approximate 0.5 cm x 1.0 cm area on the top and bottom face of the pellet.

Device B: Photodiode - Ganbaatar Tumen-Ulzii

To prepare a heterojunction structured device, two separate perovskite precursor solutions were prepared. First, the $FA_{0.85}Cs_{0.15}PbI_3$ solution was prepared by dissolving 1.65 M of PbI_2 (TCI), 1.4 M of FAI (Greatcell Solar Materials) and 0.25 M of CsI (Sigma Aldrich) in anhydrous DMF:DMSO 4:1 (v/v, both Sigma Aldrich). Second, a $FA_{0.85}Cs_{0.15}Pb(Br_{0.85}I_{0.15})_3$ precursor solution was prepared. 1.4 M of PbI_2 and 1.4 M of formamidinium bromide (FABr, Sigma Aldrich) were dissolved in DMF. In a separate vial, 1.25 M of CsI and 1.25 M of PbI_2 were dissolved in 1 mL DMSO. After dissolving, the two solutions were mixed to make the $FA_{0.85}Cs_{0.15}Pb(Br_{0.85}I_{0.15})_3$ precursor solution.

The nylon membranes were immersed in the $FA_{0.85}Cs_{0.15}PbI_3$ solution or $FA_{0.85}Cs_{0.15}Pb(Br_{0.85}I_{0.15})_3$ solution for 10 minutes to load the perovskite solution in the membrane, followed by annealing at 150°C for 3 hours to ensure complete solvent evaporation. Then, five layers of $FA_{0.85}Cs_{0.15}PbI_3$-filled membrane films and a layer of $FA_{0.85}Cs_{0.15}Pb(Br_{0.85}I_{0.15})_3$ filled membrane film were laminated at 130°C for 10 minutes at 1.5 MPa pressure. A manual hydraulic heated press machine (George E. Moore & Son Press) was

used for the laminating process. Then, 25 nm of C_{60} (Sigma Aldrich), 7 nm of BCP (Alfa Aesar), and 50 nm of copper were sequentially deposited on the laminated membrane film. Finally, 50 nm of gold was thermally evaporated on the other side of the membrane film to complete the device. Device pixel areas were defined by the evaporation mask to be 0.13 cm^2.

3.1.3 Cs_2ZrBr_6 Scintillators

Colloidal Synthesis of Cs_2ZrBr_6 Nanocrystal Suspensions – Anna Abfalterer

Zirconium(IV) acetylacetonate ($Zr(acac)_4$, 0.049 g, 0.10 mmol, Sigma Aldrich), caesium carbonate (Cs_2CO_3, 0.033 g, 0.10 mmol, Sigma Aldrich), 1-octadecene (ODE, 8.0 mL, Sigma Aldrich), oleylamine (OLA, 0.60 mL, Sigma Aldrich), and oleic acid (OA, 1.0 mL, Sigma Aldrich) were loaded into a 50 mL 3-neck round bottom flask and dried by refluxing under vacuum for 90 minutes while magnetically stirring at setting 4 on a magnetic stirrer (IKA® C-MAG HS 4 S000) until the precursor salts fully dissolved. Then, a dilution of benzoyl bromide (BzBr, 0.60 mL, Sigma Aldrich) diluted in dried ODE (0.90 mL) was swiftly injected at 185 °C into the stirred solution (setting 6 (increased from setting 4 shortly before injection under N_2)). 30 seconds after injection, the heating mantle was exchanged for a cold-water bath and the reaction mixture cooled to 30 °C. Subsequently, the cold-water bath was removed, the stirring discontinued, and the colloidal suspension transferred into a nitrogen filled-glovebox. Inside the glovebox, the suspension was placed into a centrifuge tube, the tube tightly closed, taken out of the glovebox, and centrifuged at 9000 rpm (rotor radius 10.4 cm) for 15 minutes. Then, the tube was taken back into the glovebox and the supernatant discarded. The precipitate was gently rinsed with 1 mL of toluene (Sigma Aldrich), the supernatant discarded, and the Cs_2ZrBr_6 nanocrystals redispersed in 2 mL of fresh toluene. Two additional washing steps: centrifuging the nanocrystal suspension at 9000 rpm for 15 minutes (rotor radius 10.4 cm), discarding the supernatant, rinsing the precipitate with 1 mL toluene, discarding the supernatant, and redispersing the nanocrystals in 2 mL toluene (2x), all were performed under exclusion of air and moisture.

Cs_2ZrBr_6 Film Deposition

Fused-quartz substrates and encapsulating slides (both UQG Optics) were cleaned by sequential 5 minute sonication steps in acetone (Sigma Aldrich), IPA (Sigma Aldrich) and deionised water. Nanocrystal suspensions of Cs_2ZrBr_6 were deposited in a nitrogen-filled glovebox onto the cleaned substrates by repeated drop casts of 50 µL of solution. Solvent was allowed to dry at room temperature (~20 minutes) before the next deposition, and a total of 10

drops were performed. Substrates were encapsulated with 0.1 mm fused-quartz slides, sealed with UV-curing glue (Bluefixx) before removing from the glovebox for measurements. Fused-quartz was required for the substrates and encapsulating slides as it did not discolour under X-ray exposure, whereby any discolouring would prevent RL light escape. 0.1 mm thickness of fused-quartz was selected to minimise any parasitic X-ray absorption.

3.1.4 Trench Substrates

Substrate Fabrication - Jack Alexander-Webber

Patterns were fabricated onto wafers using the following procedure:

Aluminium (Al, 50 nm) was sputtered onto a silicon wafer coated in 10 µm of silicon dioxide (SiO_2). Patterning of the Al hard mask was performed through electron beam lithography using UV1116 positive resist. Al under the exposed resist was etched using AZ726 MIF developer (an aqueous solution of tetramethylammonium hydroxide, TMAH) for 1 minute, followed by rinsing in deionised water and IPA (Sigma Aldrich). Following Al etching, the resist was then removed by sonicating in acetone and rinsing in IPA. CF_4 and SF_6 based reactive ion etching was chosen for patterning due to the etch rate selectivity of SiO_2 vs. Al. Various parameters were tested for etch rate and selectivity. The substrates were patterned using a 150 W CF_4 plasma, with a CF_4 flow rate of 40 sccm and a total pressure of 150 mbar for 10 minutes. This resulted in a total trench depth of 600 nm (central) and 450 nm (secondary). Note, Al remains in unetched regions hence the top section of the walls of the trenches is composed of Al (with a thickness equivalent to 50 nm – reactive ion etch). Wafers were then cut into 1 x 2 cm substrates.

Initial trench substrates were designed with a primary central trench (width = 100 µm) leading into an array (500 rows) of secondary narrower perpendicular trenches (width = 1 µm, separation = 10 µm). This substrate pattern was inherited from the previous project by Alice Dearle.[251] Using AutoCAD software, different device patterns were designed by the author of this thesis, as described in Chapter 7. These patterns were then fabricated onto substrates using the same method as above.

Perovskite Deposition

Preparation and Cleaning

Trench substrates were cleaned prior to use. Wafers were sonicated in acetone (5 minutes, Sigma Aldrich), IPA (5 minutes, Sigma Aldrich) and dried (with N_2) prior to infiltration. After

use, substrates were cleaned by dissolving the perovskite in DMF (Sigma Aldrich) and repeating the cleaning process. Figure 3.1 shows the process successfully removes any remaining perovskite.

$MAPbI_3$ precursor solutions of MAI (Sigma Aldrich) and PbI_2 (Sigma Aldrich) in DMF were prepared in a nitrogen-filled glovebox. A 0.5 M concentration stock solution was made, and any reduction in concentration performed via dilution. A concentration of 0.05 M was used as standard, unless otherwise stated. Precursor solutions were not used for more than 1 day due to concerns of stability. For DMSO depositions, DMF was replaced with DMSO, but all other parameters were identical.

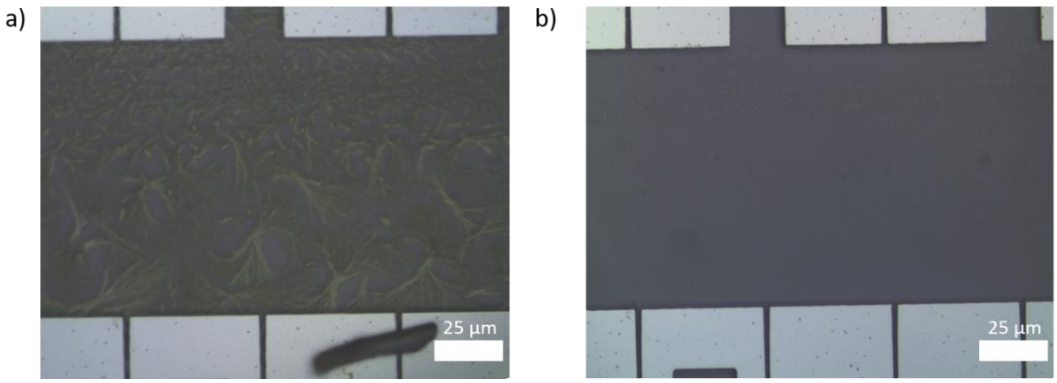

Figure 3.1: Trench Substrate Reuse After Perovskite Cleaning. *a) Trench substrates filled with perovskite. b) Trench substrates after perovskite in (a) removed by the cleaning process.*

Drop Casting Method

A 5 µL droplet of perovskite precursor solution of set concentration was drop cast onto the central large trench of a wafer using a micropipette at an angle of c.a. 45° such that the precursor solution penetrated the central trench and flowed into the secondary trenches. Infiltration was performed aerobically on the benchtop and the wafer left undisturbed until the precursor solution droplet had visibly crystallised due to the evaporation of the solvent. This method was previously developed by Alice Dearle.[251]

Spin Coating Method

Substrates were spin coated with perovskite by dropping 20 µL (0.05 or 0.1 M) of precursor solution and spinning at the quoted rpm for 40 seconds. The ramp rate was kept constant at 1000 rpm per second. Increasing the solution volume deposited onto substrates had no effect on perovskite morphology, as the excess was removed during the spinning. 3500 rpm was used

initially, but 1000 rpm displayed improved perovskite morphology. Substrates were left to dry for ~60 minutes after coating to ensure residual solvent had evaporated.

Perovskite Evaporation – Yu-Hsien Chiang

The deposition process took place in a chamber installed in a nitrogen-filled glovebox to avoid exposure of precursors and deposited films to oxygen and water during sample fabrication and handling. The clean substrates were transferred to a CreaPhys PEROvap evaporator inside an MBraun N_2 glovebox (O_2 and H_2O levels below 0.5 ppm). The chamber was pumped down to a pressure of 1-3x10^{-6} mbar for the deposition. We employed a specifically designed cooling system that maintains the evaporator walls, source shutters and shields at −20 ºC throughout the entire process. This functionality minimises re-evaporation of the precursors and cross-contamination between sources, ensuring fine control over the evaporation rates and high reproducibility. For perovskite ($FA_{0.7}Cs_{0.3}Pb(I_{0.9}Br_{0.1})_3$) deposition, FAI (GreatCell Solar), PbI_2 (TCI, >98% metal trace based purity) and CsBr (Sigma Aldrich) were filled into three different crucibles. For the organic cation, we used fresh FAI powder for every deposition. The tooling factor of each chemical was calibrated by checking the film thicknesses by profilometry inside the nitrogen-filled glovebox (DEKTAK XT profilometer). Five quartz crystal microbalances (QCMs) mounted on the top of vapour sources allows us to monitor the deposition rate of each source and control the composition. We set the rate of FAI, CsBr and PbI_2 at 1 Å s^{-1}, 0.1 Å s^{-1} and 0.8 Å s^{-1} respectively. The substrate temperature was maintained at around 18 ºC. The distance between evaporator sources and substrate holder is around 35 cm.

3.2 Perovskite Characterisation

3.2.1 Scanning Electron Microscopy

Scanning-electron microscopy (SEM) was performed using a Zeiss LEO 1550 FE-SEM with a field emission source operating at 2 kV acceleration voltage in the In-Lens mode.

3.2.2 UV-Visible Absorption – Bart Roose

Absorption measurements were carried out using a Shimadzu UV-3600 Plus double-beam spectrophotometer, with an ISR-603 integrating sphere attachment, and a step size of 1 nm. A beam splitter was used to measure the sample and reference simultaneously. Perovskite films were measured in transmission configuration and referenced to a blank ITO substrate.

3.2.3 Photoluminescence Microscopy

Photoluminescence maps of perovskites were carried out using a wide-field, hyperspectral microscope (Photon etc. IMA). Excitation was supplied by a 405 nm continuous-wave (CW) laser. Samples were imaged in the wide-field configuration with a 20× chromatic aberration-corrected objective lens. The emitted light from the sample was incident on a volume Bragg grating, which splits the light spectrally onto a charge-coupled device (CCD) camera. The grating angle was scanned relative to the incident light such that the spectrum of light coming from each point on the sample could be obtained. The detector was a 1,040 × 1,392 resolution silicon CCD camera kept at 0 °C with a thermoelectric cooler and has an operational wavelength range of 400 – 1,000 nm.

3.2.4 X-ray Diffraction – Krishanu Dey

X-ray diffractograms (XRDs) of perovskite films were obtained in Bragg–Brentano geometry using a Bruker D8 Advance X-ray diffractometer with Cu Kα radiation (λ = 1.5418 Å). All the measurements were performed with 2θ angles ranging from 10° to 50°, with a step size of 0.00214°.

3.3 Photodetector Characterisation

3.3.1 Contacting and General Considerations

Electrical contacting of fabricated devices was required to assess photodetection performance, and the contacting approach differed for each device structure. n-i-p devices were contacted using a custom device holder built in-house. p-i-n and tandem photodetectors were contacted using crocodile clips. The small area of the electrical contacts on the trench devices required a micromanipulator (LBM-7, Scientifica) with tungsten probe tips (1 μm radius, 72T Series, American Probe Tech.). Illumination areas were defined using metal masks and differed between devices.

3.3.2 IV Curves and Current vs Time

IV curve measurements were recorded with a source-measurement unit (SMU) (Keithley 2636A) controlled by a custom LabVIEW program. Light measurements were performed using various illumination sources, and the wavelength and intensity specified when used. Illumination at 1-sun (100 mW cm^{-2}, AM 1.5G reference air mass spectra), was provided by a

xenon lamp (Abet Sun 2000 Solar Simulators, AAB class), calibrated with a reference silicon diode (KG5 filter). The voltage scan range was dependent on the application using a step size of 20 mV and a dwell time of 100 ms. IV scans were performed in the reverse direction as standard.

Current-time measurements were performed using a SMU (Keithley 2450), which applied the stated bias voltage and recorded the corresponding device current.

3.3.3 Response Time

Transient Measurements were performed using a 670 nm fibre-coupled diode laser (iFLEX). The laser beam was passed through an acousto-optic modulator (IntraAction AOM-80, ME-80 driver) to ensure fast excitation and broad frequency range, outputting 100 μW at the first order diffracted beam. The photodetector current response was recorded with a FEMTO DHPCA-100 transimpedance amplifier combined with an oscilloscope (response time measurement, Tektronix TDS2024C) or a high-speed lock-in amplifier (cut-off frequency measurement, Zurich Instruments HF2LI). The gain of the DHPCA-100 was set to 10^3 V/A to maximise the bandwidth of the measurement.

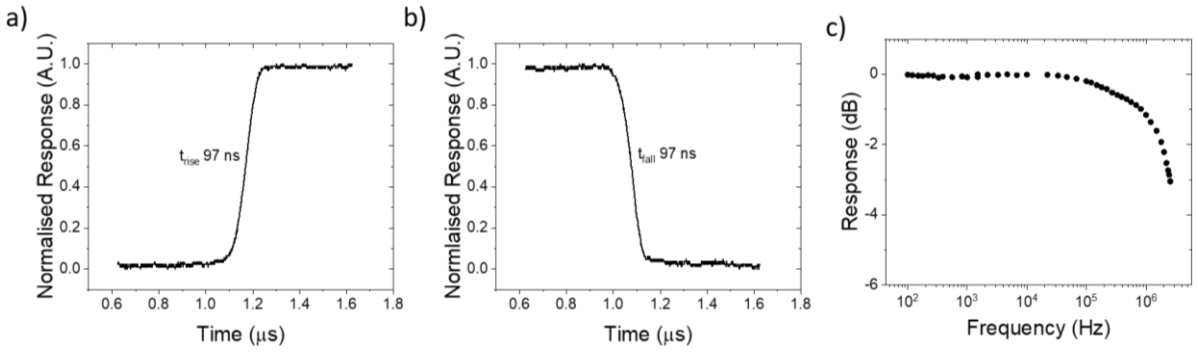

Figure 3.2: Limitations of Response Speed Measurements. *a) and b) Response time limits of the rise and fall time measuring instrument using a silicon photodiode. c) The corresponding cut-off frequency of the silicon photodiode. The limits of the system exceed the speed of the detectors measured in this thesis.*

A silicon reference photodiode (Thorlabs FDS010) was used to test the speed limitations of the measurement system. Figure 3.2 shows the limiting response speed of the system, exceeding the speed of response of all devices measured (<100 ns rise/fall times, >2 MHz cut-off frequencies). Rise and fall times were taken as the time for the signal to change from 10% to 90% of the peak response (Equation 2.10). Cut-off frequency measurements take the frequency where the response falls to −3 dB of the peak response as the device bandwidth.

3.3.4 Intensity Dependence of Photoresponse

Steady-state intensity dependent measurements were made using a 405 nm CW laser (Photon Etc 405-2W) or a fs-laser (InSight DS+ from Spectra-Physics) set to q-CW mode (120 fs pulse, 80 MHz repetition rate is significantly faster than device response times). Power was reduced using neutral density filters and calibrated using an optical power meter (PM100D, Thorlabs) with a silicon photodiode sensor (S130C, Thorlabs). The current was recorded using a Keithley 2450 SMU, and the response was calculated by subtracting the photocurrent from a dark current measured at each intensity. Taking readings of dark current at each light intensity compensates for any current drift, which can lead to errors in calculations. This is referred to as the 'dynamic' measurement procedure, and details of its development are included in Chapter 4. Pulsed intensity dependent measurements were made by adding a chopper wheel (MC2000B, Thorlabs) and recording the response with a low-noise pre-amplifier (SR570, SRS) combined with a lock-in amplifier (SR530, SRS).

The LDR, which represents the range of incident intensities between which the detector response is linear, was calculated from Equation 2.5. Photoresponses were then converted to responsivity or EQE with Equation 2.2 and 3.1:

$$EQE = \frac{(R \times h \times c)}{(\lambda \times q)} \quad (3.1),$$

where h is Planck's constant, c is the speed of light, λ is the wavelength and q the elementary charge.

3.3.5 EQE Measurements

EQEs were measured using a Bentham PVE300 system. A dual xenon short arc and quartz halogen lamp were utilised as the light source, with a swingaway mirror set to 750 nm (this is moved if it coincided with any peak of interest, e.g. narrowband peaks). A 10 x 10 cm Si reference cell was used to calibrate the power of the probe beam. Measurements in alternating current (AC) mode use an optical chopper, with a low-noise pre-amplifier and lock-in amplifier as detection electronics. Direct current (DC) measurements had a DC amplifier. External voltages were applied across the device using a Keithley 2450 SMU. Intensity reductions were made by adding neutral density filters. White bias light was applied with an in-built solar simulator in the system. Red (730 nm, M730L5 Thorlabs) and green (M530L4, Thorlabs) bias light were applied using LEDs from Thorlabs.

3.3.6 Noise

Noise spectral densities were measured in the dark using an electrically shielded box and low-noise pre-amplifier (Stanford, SR570) connected to a lock-in amplifier (Stanford, SRS830) set to measure noise. When stated, bias was supplied using the pre-amplifier. Alternatively, the dark current was measured with time (at the stated bias) using a Keithley 2450 SMU, followed by a fast-Fourier transform. The noise values obtained from both these measurements was determined to be similar (Chapter 5, Figure 5.9).

3.3.7 Pulse Train Measurement

To access the multiband detection of the tandem photodetectors, a three light source pulse train experiment was used. A CsFAMAPbIBr$_2$ / CsFAMAPbI$_3$ top and bottom sub-cell perovskite tandem photodetector (TPD) was used, to allow light sources selectively tuned to each sub-cell and at the narrowband peak of 630 nm. The three light sources were manually switched on and off, and the device response was measured using a Keithley 2450 SMU. The three light sources were a 405 nm CW laser (Photon Etc 405-2W), 630 nm xenon short arc lamp with monochromator and a 730 nm LED (M730L5 Thorlabs, combined with 665 nm long pass to minimise any excitation of top sub-cell). The reference single junction perovskite photodiode had the structure ITO/2PACz/perovskite/C60/Ag, with a CsFAMAPbI$_{2.5}$Br$_{0.5}$ absorber (~1.6 eV band gap).

3.4 Direct X-Ray Detector Characterisation

The exact details of the development of the X-ray characterisation methods are discussed in Chapter 7. A summary of the methods and equipment is included here.

3.4.1 X-Ray Source

Direct X-ray characterisation was performed using a Zeiss Xradia Versa 510 system. A propriety X-ray tube contained a tungsten anode, with variable accelerating voltage from 40-150 kV and power from 1-10 W, which was used to provide the X-ray radiation. The X-ray dose rate was varied using the source-sample distance, tube current and voltage, and filters. The X-ray tube parameters were controlled with Zeiss Scout-and-Scan software. Aluminium foil (~0.1 mm) and lead tape (3M, 0.17 mm) were used to attenuate the beam. Dose rates were recorded with a Raysafe X2 system fitted with an R/F diode sensor.

A motorised flip mount (Thorlabs), fitted with lead tape was used as a shutter for the device under test. The X-rays were modulated using a homemade chopper system, comprised of an optical chopper (Thorlabs) fitted with lead tape.

3.4.2 Electrical Measurements

Electrical contacts were provided by crocodile clips. A Keithley 2450 SMU was used to record the detector current and apply external bias. A homemade magnetic interlock was designed to enable up to 200 V external biases to be applied.

3.4.3 X-Ray Absorption Calculations

X-ray absorption efficiency and penetration depth calculations utilised attenuation coefficients calculated using the XCOM Photon Cross Sections Database from the U.S. National Institute of Standards and Technology. This program calculates the total attenuation of X-rays by an atom by summing the individual contributions from incoherent and coherent scattering, photoelectric absorption, and pair production. The attenuation of compounds is then calculated from a weighted sum of the cross sections of the atomic constituents. A noted limitation of the system is it does not account for the attenuation of secondary Compton or photoelectrons which may be produced.[19]

3.5 Indirect X-Ray Detector Characterisation

3.5.1 Radioluminescence Measurements

Radioluminescence was measured using an Edinburgh Instruments FLS1000 Photoluminescence Spectrometer combined with an XS1 system. The X-ray excited luminescence from the scintillator is collected by a liquid light guide, which delivers it to the FLS1000 where it is wavelength selected and detected. The FLS1000 was equipped with a PMT-900 detector that is sensitive from 200 − 870 nm with time-correlated single-photon counting electronics.

Radioluminescence emission was quantified by steady state irradiation with a MOXTEK MagPro X-ray source with a tungsten anode, operating at 60 kV and 100 μA. A $Bi_4Ge_3O_{12}$ (BGO) scintillator was used as a reference material to generate a relative light yield, with RL emission spectra demonstrated in Figure 3.3. By comparing the integrated emission counts under the same excitation and collection metrics, relative light yields can be produced.[237] BGO has a light yield of 8200 photons MeV^{-1}.[252] BGO was selected as a reference due to the

similarity in emission spectrum to the Cs_2ZrBr_6 sample, and the sensitivity of the photodetector was calibrated and corrected for spectral efficiency variations.

For the luminescence decay times samples were irradiated with a 40 kV Hamamatsu N5084 light excited pulsed X-ray source which was optically pumped using an Edinburgh Instruments HPL-450 pulsed diode laser.

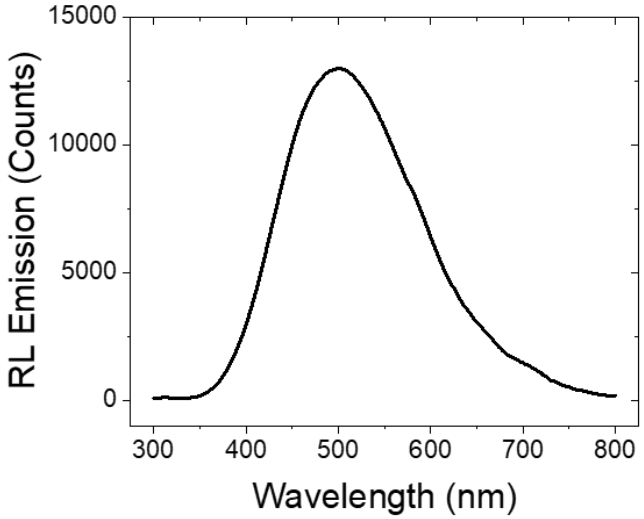

Figure 3.3: BGO Reference Scintillator Spectrum.

Chapter 4

Transient Phenomena Affecting the Characterisation of Perovskite Photodetectors

Despite their promise, perovskite photodetectors show detection behaviour that varies with time, creating inconsistent device performance. In this chapter, we link this changing behaviour to the mobile defects that migrate through perovskites. Firstly, we show that the mobile defect-induced current drift, commonly seen in perovskite detectors, makes the accurate measurement of low-light performance difficult. We propose a method to overcome these characterisation challenges, and apply it to measure the performance of perovskite photodiodes. The presence of defects can lead to photoconductive gain in detectors, and we show batch-to-batch processing variations in perovskite devices gives varying degrees of photocurrent amplification under low light intensities. Investigating the source of this gain led to the discovery that n-i-p devices have higher inherent reverse bias stability than devices with p-i-n polarity. The passivating effect oxygen exposure is utilised in aged devices to reduce the impact of defects, leading to current drifts being minimised and elimination of the gain. This work highlights the potential issues arising from mobile defects, such as inconsistent photodetector operation and even device degradation, and identifies the potential for defects to tune photodetection behaviour in perovskite photodetectors.

The content in this chapter has been adapted from O. D. I. Moseley et al., Identification and Mitigation of Transient Phenomena that Complicate the Characterisation of Halide Perovskite Photodetectors, 2022, **under review**. Photodiode fabrication and JV curve measurements were performed by Bart Roose. The author of this thesis performed all other experiments and raw data analysis.

4.1 Introduction

In less than a decade of development, perovskite photodetectors can not only outperform traditional materials,[253] with high sensitivity[37] and fast nanosecond response times,[254] but the unique material properties have advanced the functionality of detectors beyond current levels. For example, perovskite detectors offering narrow[164,165,169] and multiple spectral response bands,[174,255,256] polarisation sensitivity[151,257,258] and flexible devices[259–261] have all been demonstrated in recent years. However, despite the promise, perovskite photodetectors still face key challenges that must be overcome before commercial deployment. Foremostly, perovskite detectors have shown dynamic and variable behaviour, occurring over both short (seconds) and long (months) timescales, contributing to a constantly changing performance. In the short term, the response of perovskite detectors has been shown to drift with time, linked to ion migration in the material.[198–200] The changing performance of detectors on short time scales will be catastrophic in applications, with repeat readings from the sensor yielding different values. Moreover, this fast dynamic behaviour also makes characterising the performance of a device difficult, and representing the 'real' performance becomes a challenge. Longer-term variations in performance are also problematic as consistent performance over timescales of years is required in applications, and the stability of perovskites is an ongoing challenge.[262] The soft nature of the perovskite lattice and the dynamic behaviour of the constituent ions, leads to changes over these timescales, causing variation in device performance.[263]

An understanding of the transient variations in perovskite photodetectors over these timescales is currently lacking in the literature, despite being a widely acknowledged feature of the material.[264] Herein, the dynamic behaviour in perovskite photodetectors is presented and discussed, highlighting links to mobile defects. We begin with monitoring current drift in perovskite photodetectors, which can lead to characterisation artefacts if not properly considered. These errors wrongly exaggerate photoresponse and detectivity, and a measurement method is proposed to overcome this issue. We apply this method to measure photodiodes, and find vastly different performance between devices even with the same architecture and absorbers. A minority of devices demonstrate photoconductive gain under low light intensities, and interestingly, we correlate the devices that show the worse initial photovoltaic performance to those demonstrating the gain. Attempts to probe the mechanism of the gain led to the finding that device polarity plays a key role in reverse bias stability of perovskite devices, with p-i-n devices irreversibly degrading within tens of seconds of applying

the voltage. After storing n-i-p detectors in dry air to induce passivation of defects, devices lose both the photoconductive gain and the drifting of current, emphasising the important influence of defects on this behaviour. This work highlights the challenges caused by mobile species and defects for accurately characterising perovskite photodetectors, and highlights defect engineering as an additional lever to control device properties to meet commercial requirements.

4.2 Measurement Protocols

To characterise the photodetectors, we measured the photoresponse from the device as a function of incident light intensity. Intensity dependence measurements provide key figures of merit of a photodetector (Figure 4.1a): the linear dynamic range (LDR), responsivity (R), noise equivalent power (NEP), and specific detectivity *(D**). Combined with a separate measure of response speed, this gives an all-encompassing description of a detectors ability. The LDR can be obtained from the range of incident powers between which the response is linear. The responsivity can be found from the gradient and, if the measurement set-up is sufficiently sensitive, the NEP can be determined as the point where detector response is indistinguishable from the noise. From the NEP the detectivity can be calculated using Equation 2.9. This gives a wide picture of the performance of a photodetector, and importantly, how these change with light intensity. The relevant illumination conditions for detector operation will be application-specific, and a thorough understanding of performance across a broad intensity range will be important.

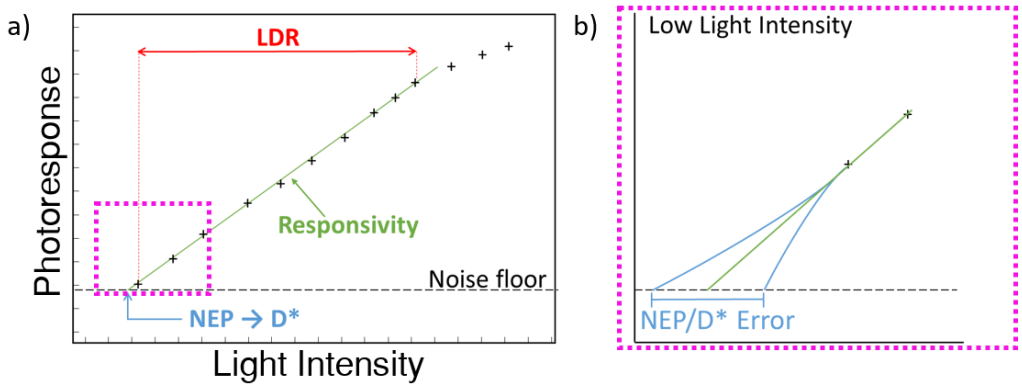

Figure 4.1: Photoresponse Intensity Dependence Measurements. *a) and b) Schematics depicting the photoresponse intensity dependence of a photodetector, revealing several figures of merit. b) The low light region of the intensity dependence (from the pink dashed region in (a)). This is important to measure as the response may not be linear to the noise floor, especially in detectors with high defect densities, which can lead to characterisation mistakes and missing of features such as gain.*

As introduced by Fang et al.,[265] ensuring the full intensity range is analysed is vital to accurately characterise a photodetector, especially the low-illumination regime where charge carrier densities approach the order of defect densities, leading to potential changes in performance. Intensity dependence measurements are sometimes performed over a small intensity range followed by a linear extrapolation to the noise level, based upon the assumption that the responsivity of the photodetector remains constant. However, this is not always the case. Responsivity has been shown to vary with light intensity, and so extrapolation would lead to potential errors in LDR, NEP and D^* values, as well as mischaracterising the performance of these devices under low light intensity (Figure 4.1b). This is particularly important for perovskite-based detectors, which like other solution processed semiconductors, possess a high density of defect states.

The shape of the photoresponse intensity dependence at low illumination provides valuable insight into the impact of defect states on detection performance. This is useful when defects contribute to photoconductive gain – the amplification of collected charge carriers in excess of those purely photogenerated and raising of EQEs above 100%. The mechanism of the gain will impact the how the light intensity impacts the detector response, and both sub- and super-linear intensity dependences have been attributed to gain in high defect density photodetectors.[104,144,266–269]

Sub-linear response can occur at low light intensities if the detector possesses a gain mechanism that requires trap states to be occupied by charges to occur. For example, charge carriers trapped in interfacial defects can cause band-bending and charge injection that enables photoconductive gain.[104,266–268] Once the light intensity is reduced, and the traps are no longer filled, this gain mechanism is lost, reducing the responsivity. Conversely, some devices only show gain at reduced light intensities, demonstrating a super-linear deviations intensity resposnse.[144,269] As light intensity is reduced, and carrier densities approach the order of defect densities, the fraction of carriers in trap states increases. Charge-selective defect states lead to an increase in lifetime of the opposite charge by reducing the likelihood of recombination. This increase in carrier lifetime, relative to their transit time through the device, enables re-circulation of carriers and gain. At lower light intensities, the deepest and longest-lived traps are filled, enhancing gain and photoresponse further. Similarly, in systems without gain but high trap densities, sub-linear deviations can also be seen at low intensities where trap-assisted non-radiative losses reduce the charge carrier collection efficiency. As a result, measurements

were performed down to the lower limits of our experimental set-up, in order to accurately report the figures of merit, and investigate any trap related phenomena that may be present.

All measurements were performed with and without reverse bias, to assess any changes in photodetector performance and any additional dynamic behaviour that may arise. Photodiodes can function without an external bias due to the in-built electric field, known as photovoltaic or self-powered mode. However, in applications they are often operated under reverse bias, known as photoconductive mode, to enhance performance.[270] Reverse bias can increase the response speed of a photodiode through two effects: increasing the drift velocity of carriers through the device, and lowering the diode capacitance by widening the depletion region. Moreover, improvements in charge dissociation and collection with an externally applied bias results in an improved linearity of response and a wider LDR.[271] However, reverse bias also raises dark current, through increased charge injection, which increases the shot noise from the device. Also, excessive reverse bias can degrade the device,[198,272] and so care must be taken to balance any improvements in performance. The amount of reverse bias was selected after analysis of the device IV curves to ensure the breakdown voltage was not met.

4.3 Defect Migration: Current Drifts and Characterisation Artefacts

The device structure used for this study was an n-i-p perovskite photodiode with an FTO/c-TiO_2/m-TiO_2/$Cs_{0.05}FA_{0.79}MA_{0.16}Pb(I_{0.84}Br_{0.16})_3$/Spiro-OMeTAD/Au architecture (Figure 4.2a). We began characterisation by measuring the dark current in the device at short circuit and under reverse bias. From IV scans, −1 V was utilised for reverse bias measurements (Figure 4.2b). Both the dark and photocurrent vary with time under reverse bias (Figure 4.2c) and short-circuit conditions (Figure 4.2d), highlighting an example of short-term dynamic behaviour. This phenomenon has been reported in the literature,[198,273] described as current drift and is particularly problematic to detection applications.[200,212,274,275] The origins of the drift have been attributed to ionic (vacancy) migration,[199,276] whereby the movement of ions opposes the applied electric field and can accumulate at interfaces to change interface energetics, which causing currents to change with time.[277] The impact on devices is a changing baseline, which lowers photodetector performance, and it also introduces characterisation challenges.

The characterisation issues from the drifting current occur when measuring the photoresponse, $I_{response} = I_{light} - I_{dark}$, required for intensity dependent measurements. A constantly varying

current means both the photocurrent (I_{light}) and dark current (I_{dark}) must be measured at each light intensity. In contrast, recording just the photocurrent, and taking a constant and independently measured dark current, brings errors into characterisation. Figure 4.2c and d shows a range of dark current values could be taken for the same device and the IV curve could also provide an additional different dark current value (which would vary depending on scan direction, step size and dwell time).

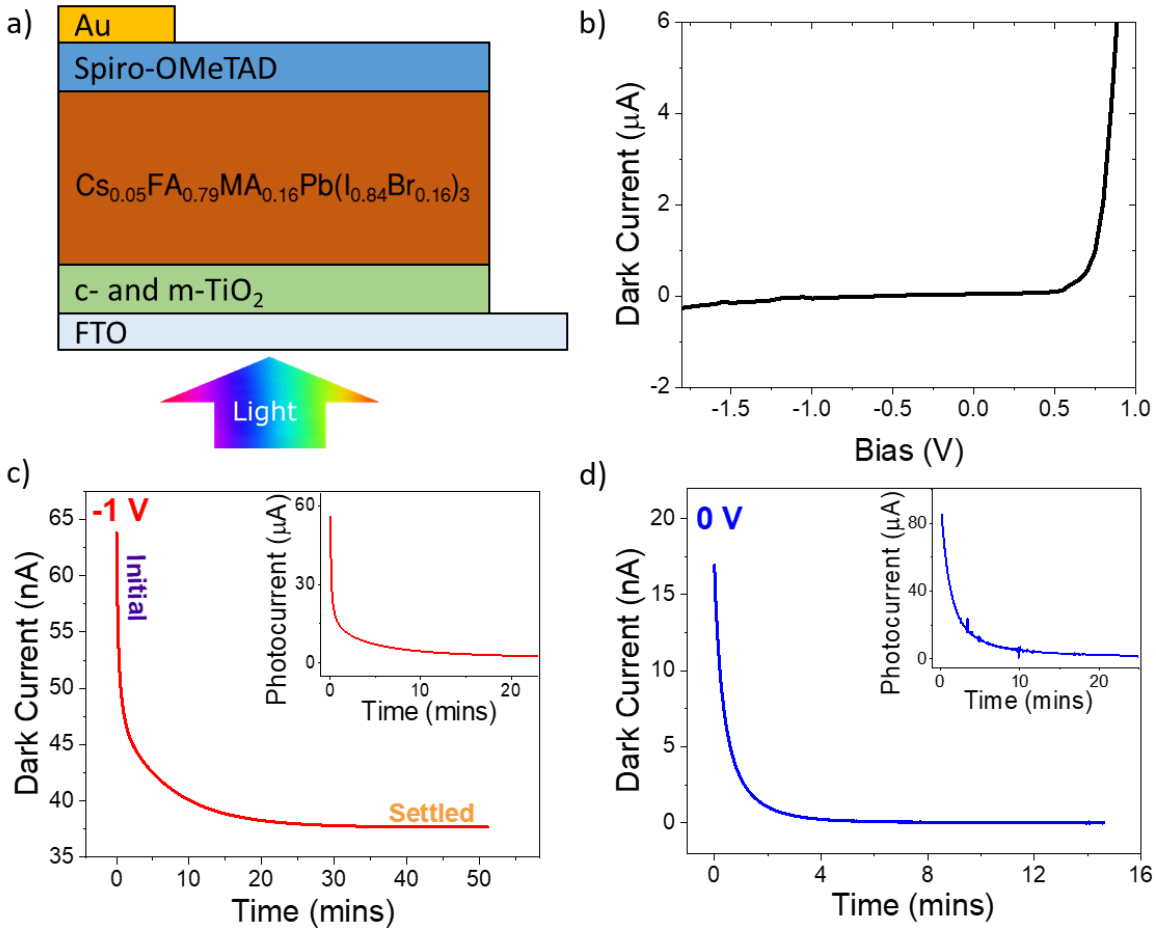

Figure 4.2 Dark Current Drift in n-i-p Photodiodes. *a) Device architecture of n-i-p photodiodes studied. b) Dark IV curves, utilised to select a suitable reverse bias value. As a result, −1 V was used as standard for the n-i-p devices. c) and d) Drift of the dark current at −1 V (c) and 0 V (d), with several minutes needed to reach settled values. Inset shows similar dynamic behaviour of the photocurrent (405 nm, 1.3 mW cm^{-2}). The initial and settled dark values are used for subsequent calculations.*

The errors from assuming a constant dark current will be particularly relevant at low illumination intensities, where the magnitude of the photocurrent and dark current become comparable. The effect of using the different possible values of the dark current on the photoresponse is emphasised in Figure 4.3a, showing the difference between using the initial (60 nA) and settled (37 nA) values, or recording a unique dark current after each corresponding

photocurrent measurement (referred to as the 'dynamic' measurement procedure). Whilst the dynamic procedure leads to a linear intensity dependence down to the limits of the experimental set-up, expected for a photodiode with transport layers preventing charge injection and any resulting gain, taking a fixed dark current value gives a considerably different result. Overestimations of dark current, taken from initial values in Figure 4.2c, lead to the appearance of sub-linearity, while the opposite is the case for taking a settled dark current value.

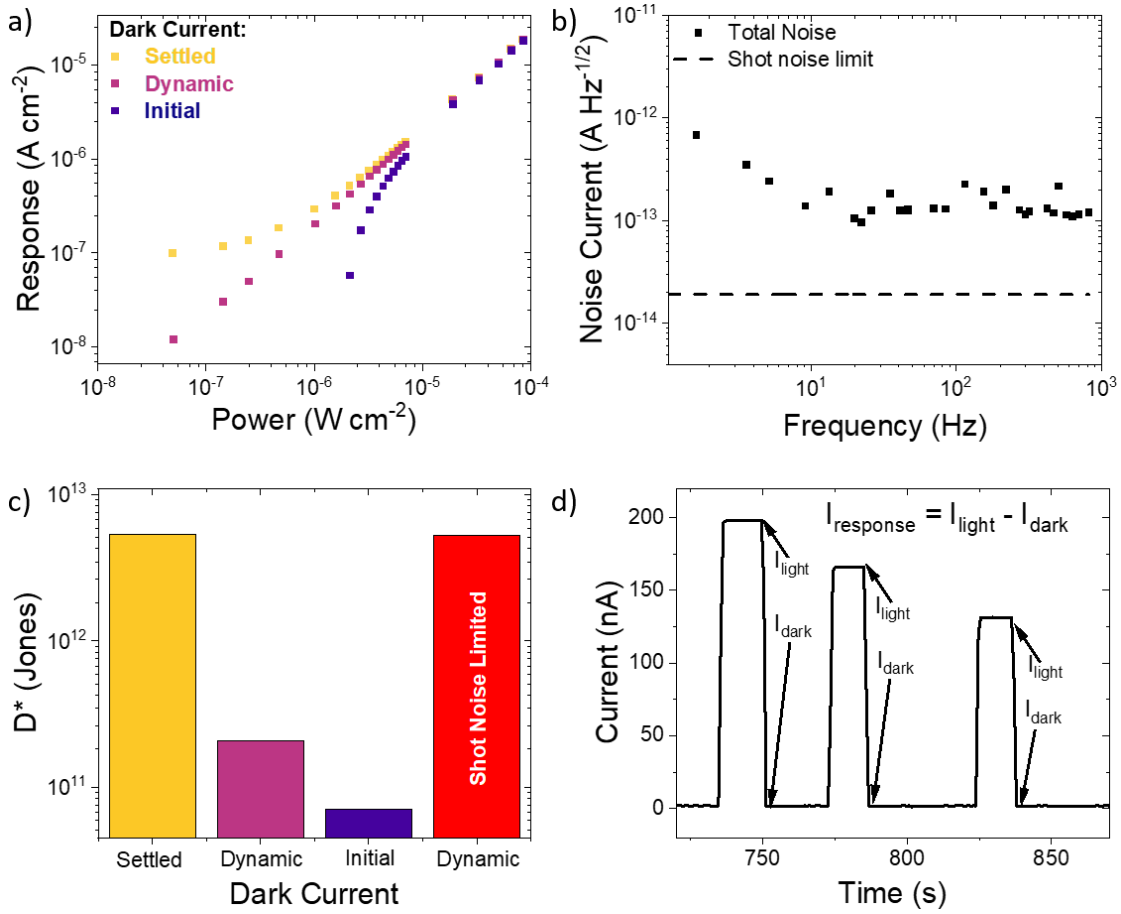

Figure 4.3: Characterisation Errors and Artefacts in Perovskite Photodetectors. *a) The impact of different dark current values in calculating the photoresponse ($I_{light} - I_{dark}$). b) The total detector noise, compared to the shot noise. c) The impact of the photocurrent variation, introduced in (a) in calculating the corresponding detectivity (using the total noise in (b)). The error in wrongly assuming the system is shot noise limited is also shown (red bar). d) The protocol for the dynamic measurement procedure, which mitigates the impact of dark current drifts on the photoresponse at low light intensities.*

The observed variation in photoresponse at low illumination intensities, arising from current drifts, is problematic when assessing the ability of a photodetector to resolve weak light signals. A measure of the low illumination detection ability is quantified by the specific detectivity, which accounts for both the photoresponse and detector noise, and the total noise spectrum of

the photodetector was measured for this calculation (Figure 4.3b). Subsequently, the photoresponse variation leads to a widespread of reported values in detectivity from the same device (Figure 4.3c), with almost two orders of magnitude difference in this example here. Using this knowledge, independent measurements of dark current were taken as standard for measurements of perovskite detectors (dynamic measurement procedure, Figure 4.3d). Reliable measurements of detectivity require not just a truly representative photoresponse measurement, but also an accurate value of the detector noise. Figure 4.3c also shows additional detectivity errors can arise when the noise current is incorrectly assumed to be shot noise limited, a common assumption in the literature,[25–30] instead of a full noise spectral measurement. Shot noise represents just a single contributing factor to the detector noise, and the actual detector noise is often higher.[37,145,153,163,278] Figure 4.3b confirms the total detector noise exceeds the shot noise in this system. Therefore, the total noise from a photodetector is required to be independently measured to accurately determine the detectivity. These points highlight the care required to correctly characterise perovskite photodetectors.

4.4 Processing Variations and Resulting Defects Lead to Gain

A total of thirty six individual n-i-p photodiodes were fabricated in two batches, all with the same parameters. As an initial assessment of the device quality, and to evaluate the light harvesting ability, current density-voltage (JV) curves in the dark and under illumination (AM1.5) were measured. Subtle variations in processing, such as solution stoichiometry and glovebox conditions, can cause differences in performance between and within batches,[279] and JV curves provide information as to what causes any variances. While the majority of devices had moderate photovoltaic performance, there were several cases of devices with lower performance, with fill-factor (FF) and short-circuit current (J_{sc}) losses. Performance can be grouped into two distinct categories with good and bad photovoltaic performance (Figure 4.4a) and typical examples of a ‘good’ and ‘bad’ device are shown in the JV curves in Figure 4.4b, referred to as Type 1 and 2 devices, respectively. The slope from 0 V to V_{mpp} (max power point) in Type 2 devices is characteristic of low shunt resistance, which usually arises from alternate current pathways through the device – a result of defects arising during fabrication – and leads to a reduction in fill-factor.[12] The semi-logarithmic plot of the dark current (Figure 4.4b inset) also highlights the difference in slope near 0 V, confirming shunt pathways.[280] The poor performing devices also suffered from J_{sc} losses and, combined with low fill-factors, the efficiencies (PCE) of the Type 2 devices are less than 10%.

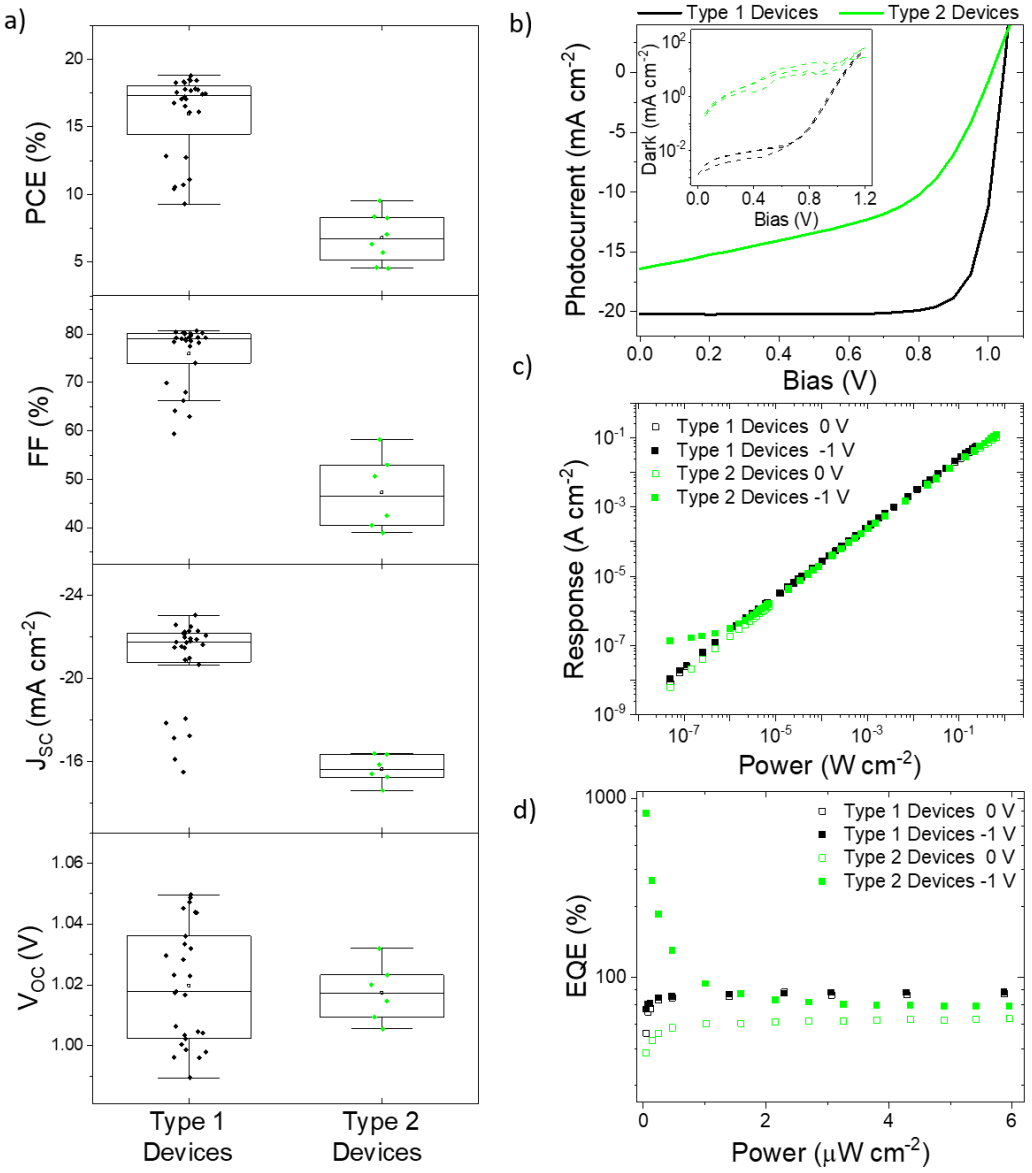

Figure 4.4: Batch-to-Batch Photovoltaic and Low-Light Photodetection Performance Variations. *Type 1 devices (black) and Type 2 devices (green) refer to devices showing good and bad initial photovoltaic performance, respectively. a) Device statistics of 36 devices, categorised as either good (Type 1, black) or bad (Low FF and J_{sc}, Type 2, green) photovoltaic performance. (V_{OC} = open-circuit voltage). b) Current-voltage curves of typical Type 1 and Type 2 devices under illumination (AM1.5, solid lines). Inset shows the dark current on a semi-logarithmic scale, highlighting the relative difference between R_{shunt} values across six devices. IV scans were performed in the reverse direction as standard. c) Intensity dependence of detector current response ($I_{photo}-I_{dark}$,) measured at 0 V (hollow data points) and −1 V (solid data points). Measurements performed using the dynamic procedure introduced above. d) The corresponding intensity dependence of EQE at low light intensities. JV measurements were performed by Bart Roose.*

The intensity dependence of Type 1 and 2 devices was measured under reverse bias and short-circuit, and clear differences between the two devices are seen (Figure 4.4c). The Type 1 devices, with superior photovoltaic performance, had a greater EQE (79% vs 59%) than the

poorer devices without applied bias at moderate light intensities. Under applied bias, there is negligible improvement for the Type 1 device, whereas Type 2 devices show an improvement in sensitivity. These findings can be expected, due to efficient collection of charge carriers in Type 1 devices, which do not require additional bias to facilitate carrier collection. Secondly, the low-light behaviour of both devices is significantly different. For Type 1, devices display the expected linearity and a wide LDR of 147 dB, while Type 2 devices deviate from linearity due to an increase in sensitivity at low light intensities. This limits the LDR of Type 2 devices to 87 dB, but amplifies the response under low-light conditions. Converting each photoresponse into the EQE at each incident intensity shows this super-linearity in more detail (Figure 4.4d) and below 1 μW cm^{-2} the EQEs begin to increase for Type 2 devices. The EQE continuously increases as light intensity decreases, exceeding 100%. This low-light behaviour is repeated across the Type 2 devices, all with poor initial photovoltaic performance. The super-linear curve is consistent with photoconductive gain originating from long-lived trap states to increase carrier lifetimes.[144,269,281]

The absence of any photoconductive gain in Type 1 devices likely stems from the lack of charge carrier injection, preventing the recirculation of charge carriers and any amplification of current beyond photogenerated contributions. This is verified by the JV behaviour seen in Figure 4.4b, indicative of good diode-like behaviour. In contrast, Type 2 devices demonstrate photoconductive gain at low light intensities when reverse biased, meaning injection from the electrodes into the perovskite likely occurs in order to generate this amplification of the photocurrent. Charge carrier injection is possible with direct electrode-perovskite contact through processing inconsistencies such as pinholes and voids in the device layers formed during fabrication. We propose that the charge injection could occur at the (i) bottom (perovskite-FTO) interface or at the (ii) top (perovskite-gold) interface. For (i), it has been shown elsewhere that the replacement of a compact TiO_2 layer with a porous TiO_2 layer reduces shunt resistance,[282,283] and FTO-perovskite contact through TiO_2 has caused photocurrent amplification in similar device structures.[144] When only porous TiO_2 was used, and direct perovskite-FTO contact is possible, photoconductive gain occurs. However, when a conformal and compact layer of TiO_2 prevents direct contact, the amplification is lost.[144] In our case, all devices use a compact layer of TiO_2, which in most cases (Type 1 devices) prevents direct contact and no amplification is observed. However, pinholes in the compact TiO_2 layer due to processing variations may allow direct contact and photoconductive gain (Type 2 devices). For (ii), thickness inconsistencies and high surface roughness in the perovskite film can lead to

incomplete hole transport layer coverage and charge injection via direct perovskite-gold contact at the top device interface. Variations in perovskite thickness can also explain the reductions in J_{sc} in Type 2 devices. Regions with excess thickness reduce current extraction through poor collection efficiency, whereas current is lost in areas with insufficient thickness from absorption losses. Further work will be required to unambiguously identify the origins of the photocurrent amplification mechanism. Overall, these findings show that two devices of the same architecture can show significant variation in their photodetection through batch-to-batch or even device-to-device differences in their processing, emphasising the importance of measuring down to low illumination levels to reveal these effects.

Further characterisation of the photodetection performance of a Type 2 device was performed, with measurements repeated under reverse bias to assess the impact of photoconductive mode operation on performance. The response to pulsed light is displayed in Figures 4.5a and b. Rise and fall times were found to be 1.6 and 2.1 μs at no applied bias, improving slightly to 1.5 and 2.0 μs under −1 V reverse bias. Similarly, slight increases in cut-off frequencies (f_{-3dB}) were seen under reverse bias, with 0.18/0.19 MHz seen at 0 and −1 V respectively. Note, the light intensity was above the regime where gain was observed due to limitations on the sensitivity of the temporal detection electronics, and so there was no detriment to response speed.[269] Improvements in response speed under reverse bias are expected when devices are limited by transit times. The observation of only slight improvements in response speed after applying bias suggests that the response speed of the device is limited by the resistance-capacitance (RC) constant, and the large capacitance related to the mesoporous TiO_2 structure. Although state-of-the-art perovskite devices have response speeds on the order of nanoseconds,[254,284] these are in highly optimised devices, with active areas as low as 0.04 mm^2.[285] Here, the device area remained larger at 10 mm^2 (as per minimum PV testing requirements) [111,286,287] and response speeds would be expected to decrease further on reduction of this area, allowing fairer comparisons.

The noise density spectra show a slight bias dependence (Figure 4.5c). Both spectra are independent of frequency above 10 Hz, but show an increase in noise at lower frequencies. Increased noise under reverse bias is expected, due to greater contributions from shot noise induced by larger dark currents. Also reverse bias has been shown to increase *1/f* noise in organic photodiodes,[288,289] and similar effects would not be unexpected in perovskite devices due to the common disorder in solution processed semiconductors. The noise measurement was combined with EQE spectra (Figure 4.5d, light intensities above 1 μW cm^{-2}) to provide

estimations of the detectivity, with peak values of 1.4 x 10^{11} Jones (−1 V) and 3.7 x 10^{11} Jones (0 V). These values compare similarly to other n-i-p devices, with state-of-the-art approaching 10^{12} Jones,[145] while commercial silicon detectors show 4 x 10^{12} Jones.[269]

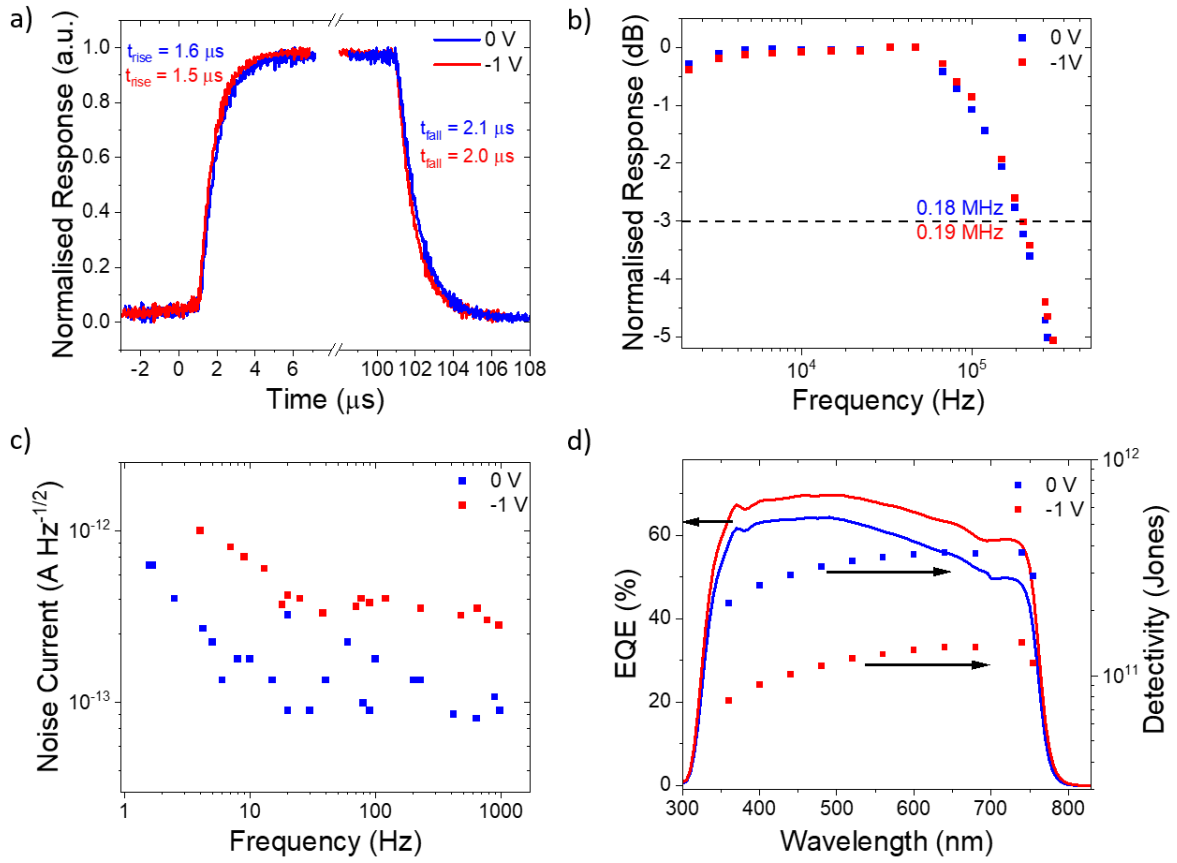

Figure 4.5: Photodetector Performance of Type 2 Photodetectors Under Reverse Bias. *Blue and red represent 0 V and −1 V performance, respectively. a) and b) show the response speed, with a) showing rise and fall times, and b) the f_{-3dB} cut-off frequency. c) Noise spectral density. d) EQE and corresponding detectivity estimations. Response speed and EQE used illumination levels above the regime where gain was observed (>10 μW cm^{-2}).*

4.5 Inverting Device Architectures Reveal p-i-n Reverse Bias Instabilities

In order to understand which interfaces were responsible for the photoconductive gain that generates the low-light performance discrepancies between Type 1 and 2 devices, we fabricated devices with alternative architectures. Photodiodes with a p-i-n structure were produced, comprised of ITO/PEDOT:PSS/$Cs_{0.05}FA_{0.79}MA_{0.16}Pb(I_{0.84}Br_{0.16})_3$/$C_{60}$/BCP/Cu (Figure 4.6a). The EQE spectrum confirms the device is sensitive to photons across the visible range (Figure 4.6b).

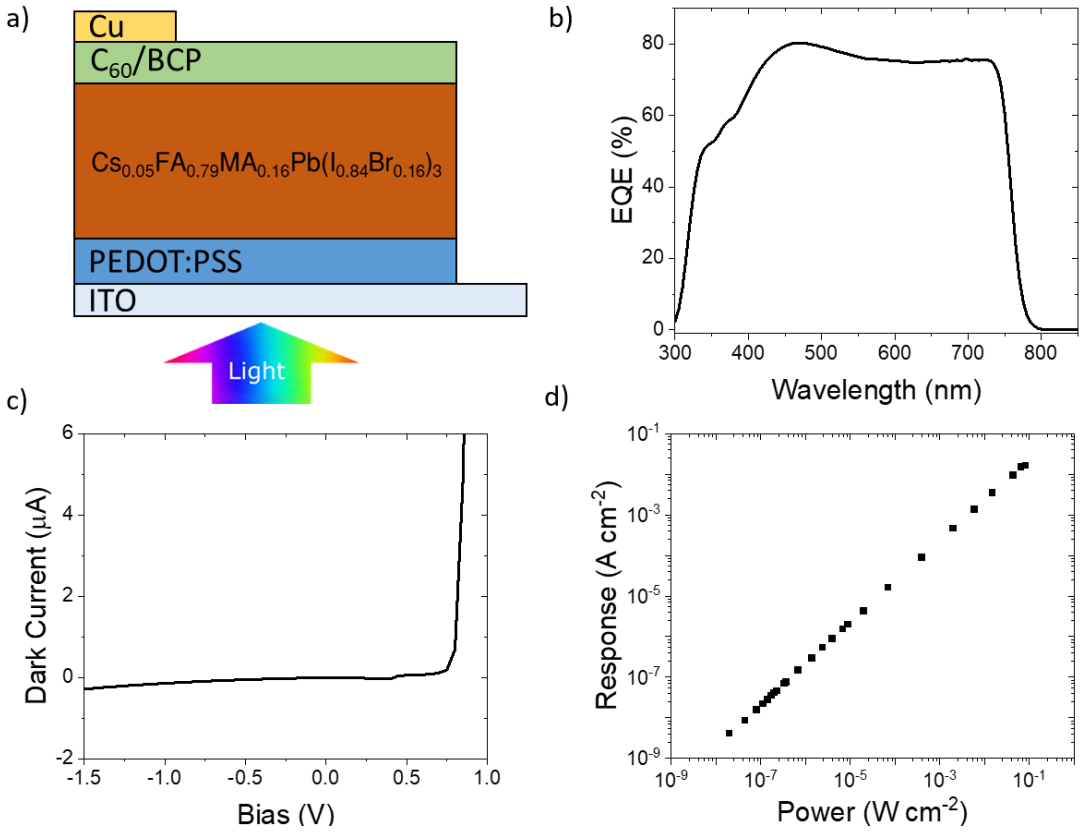

Figure 4.6: p-i-n Photodetectors. *a) Device architecture. b) EQE spectrum (0 V). c) Dark IV curve. d) The intensity dependence of the photoresponse (0 V). Measurements under reverse bias were not possible due to device instability.*

Analysis of the IV curves led to −1 V being used again for reverse bias measurements (Figure 4.6c), and the photoresponse intensity dependence was initially measured without bias (Figure 4.6d). However, attempts to characterise the p-i-n photodetectors under reverse bias were not possible, as at the selected value of −1 V, the device current irreversibly spiked shortly after applying the voltage, indicating severe instability. We investigated this further by applying smaller reverse biases and Figure 4.7a shows incrementally increasing the reverse bias in 0.1 V steps. At −0.4 V the dark current flowing through the device increases instantaneously, hitting the 20 μA compliance set on the SMU. Remeasuring the IV curve after the current spike shows the device no longer behaves as a diode, instead displaying the linear relationship expected from a resistor (Figure 4.7b). This indicates the device has formed irreversible shunt pathways through the device. We repeated this experiment across devices made in four separate batches, and all displayed an identical response, with full breakdown seen around −0.4 V after tens of seconds of exposure. The poor stability of these devices under reverse bias contrasts the n-i-p devices, which did not degrade after −1 V for one hour (Figure 4.2), and showed no long-term instability during all reverse bias measurements.

Insight into the origins of the reverse bias stability discrepancies between n-i-p and p-i-n detectors can be provided by studying the relative direction of the reverse bias in the device. The opposite polarity of the devices means the current flows in opposite directions, relative to the illumination side. In addition, the external bias is also flipped relative to the device illumination side and the mobile ions in the device will travel in opposite directions in n-i-p and p-i-n devices (Figure 4.7c). One possible mechanism for the lower reverse bias stability of p-i-n devices would result from metal ions from the top electrode migrating through the device.[290] Once electrochemically reduced, this would form a shunt pathway, giving the behaviour seen in the IV curves. It has been shown that replacing the top contact metal with transparent ITO increases reverse bias stability in p-i-n devices by preventing localised shunt formation, suggesting the metal electrode is a weak point for stability.[198] Similarly, dark lock-in thermography on p-i-n devices with a combined electrode of ITO with a gold metal frame emphasised the metal frame as the point of localised shunting.[272] However, in n-i-p devices the opposite polarity prevents this metal migration from the top electrode.

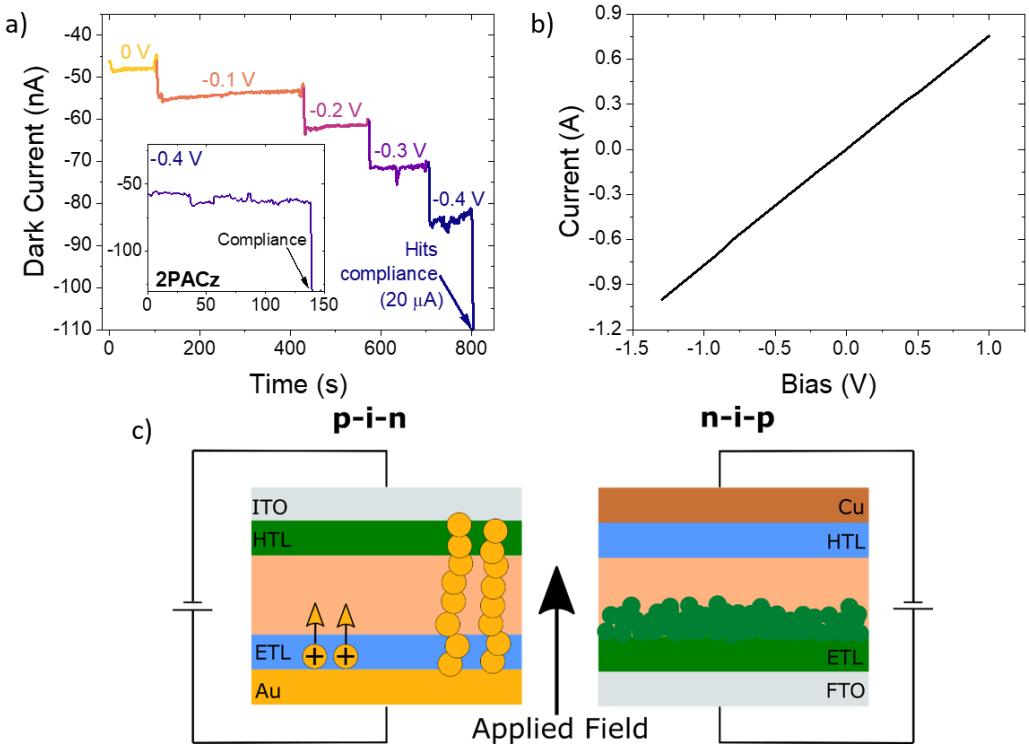

Figure 4.7: Reverse Bias Instability of p-i-n Devices. *a) Dark current measurements vs time, with bias increased in 0.1 V steps from 0 to −0.4 V. At −0.4 V the diode breaks down and the current increases to the SMU compliance (−20 µA). Similar behaviour was repeated over ten p-i-n devices made in four different batches. Inset, 2PACz HTL devices showing similar breakdown at −0.4 V (identical x-/y-axes to 4.7a) b) The dark IV curves after breakdown. c) Schematic of reverse biased p-i-n (left) and n-i-p (right) detectors, demonstrating the alternate polarities and migration of positive metal ions through the device, creating a shunt pathway. HTL and ETL = hole and electron transport layers, respectively.*

In addition, the different transport layers may also play a role in preventing or enabling the migration of ions through the device. However, no improvements in stability were seen when swapping out PEDOT:PSS for 2PACz as the hole transport layer, with identical breakdown at −0.4 V (Figure 4.7a inset). Further research into the stability discrepancy between the n-i-p and p-i-n photodiodes is required to enable long lasting devices for real-world photodetector deployment. Moreover, reverse bias stability is needed in other perovskite device applications. Direct X-ray detectors require high external biases during operation and, crucially, perovskite solar cells must be able to withstand any reverse bias stresses faced in day-to-day use.[291,292] Connecting solar cells into modules can cause individual cells to be forced into reverse bias when the structure is partially shaded, and therefore tolerance is required.[293] These findings may hint that device polarity is a key factor in this stability, and provides a base for future work. Here, the n-i-p devices were utilised for the remainder of the study due to their reverse bias stability enabling measurements.

4.6 Mitigating Transient Defects with Passivation through Ageing

After the initial measurements on photodiodes, Type 2 n-i-p devices were stored in a low-humidity desiccator for approximately one year after initial fabrication and analysis, and the impact of this storage was assessed by re-measuring the photodetector parameters. The storage was selected in order to protect the devices from moisture induced degradation.[292] Oxygen was present during ageing, which has been shown to reduce defect densities in n-i-p perovskite solar cells, and passivate trap states in triple cation films.[294–298] In addition, ion migration allows perovskite to self-heal and improve device performance upon aging.[299]

After ageing, Type 2 devices showed a significant reduction in current drifts (Figure 4.8a). Dark currents now reach stabilised values after several seconds, whereas before this would take hours, suggesting reduced ion migration in the aged samples. This finding suggests that the perovskite film has been passivated after ageing, reducing the density of trap states and mobile defects. The intensity dependence of the photoresponse in aged devices was then re-measured using the same protocols established earlier, with significant differences seen compared to the measurements on freshly made and tested Type 2 devices (Figure 4.8b). Importantly, the aged devices show a clear loss in photoconductive gain at low light intensities. The absence of gain has two possible origins: removal of shunt pathways preventing charge carrier injection under bias, or a reduction in the charge carrier lifetime (relative to carrier transit times). The

passivation of the perovskite film after ageing would be expected to increase carrier lifetimes in the low illumination regime by reducing competing trap-assisted recombination pathways.[85,294,300] Therefore, the removal of photocurrent amplification likely occurs due to the prevention of the charge injection process.

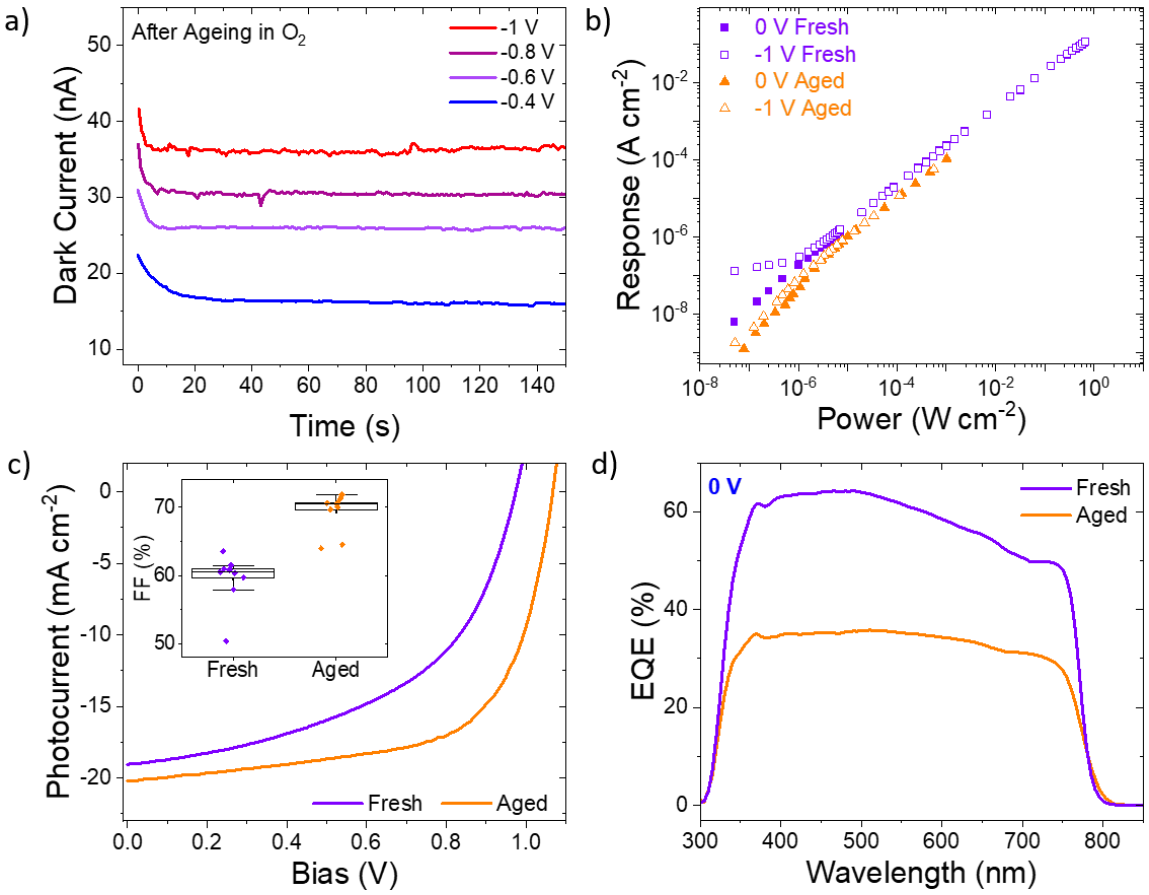

Figure 4.8: Type 2 Photodetectors After Ageing. *a) Transient behaviour of the dark current under reverse bias, no longer displaying the long settling times seen in fresh devices (tens of minutes, Figure 4.2). b) Intensity dependence of aged devices compared to the fresh performance. The responsivity has dropped with ageing, and the gain at low intensities is no longer present. c) JV Curves of fresh and aged devices, with the fill-factor statistics of 9 Type 2 devices, inset. d) EQE spectrum confirming the drop in sensitivity after long-term ageing (1 year, 0 V, ~0.5 mW cm^{-2}). JV measurements were performed by Bart Roose.*

Perovskites have been demonstrated to degrade and form by-products when aged in the presence of oxygen, such as PbI_2, PbO and Pb^0,[301–304] which could act to block the direct perovskite-electrode contact. JV curves, measured on both fresh and aged (1 week) Type 2 devices, demonstrate a clear improvement in fill-factor after oxygen ageing exposure (Figure 4.8c) suggesting that the original shunt pathways which enabled charge injection and thus gain have been greatly reduced. Ageing in the presence of oxygen has been shown to generate PbO, instead of the detrimental metallic Pb^0 that is seen when aged under vacuum, which contributes

to improvements in photoluminescence in aged films.[303] Similarly, $MAPbI_3$ perovskites have been shown to degrade in oxygen, forming PbI_2 in the reaction.[301,302] Formation of these products at the transport layer interface would generate a barrier to charge injection, and this is supported by the susceptibility of the perovskite surfaces to ageing effects.[305–308] Here, continued ageing results in a reduction of charge collection efficiency (Figure 4.8d), which could be due to the insulating nature of the degradation species limiting current extraction. This finding suggests that ageing with oxygen exposure presents a compromise between healing the processing defects and maintaining efficient charge collection in the photodetector. Work identifying the exact cause of the gain removal in Type 2 devices after ageing is ongoing. Overall, this demonstrates the ability to alter the properties of perovskite photodetectors after fabrication, through ageing and passivation.

4.7 Outlook and Conclusions

An advantage of halide perovskites in optoelectronics is their tunable properties through compositional and dimensionality engineering, allowing material optimisation to suit specific applications. The influence of defects on photodetector performance, shown here, demonstrates an additional material attribute that can act as a controllable lever on device performance. Defects and trap states contribute to generating photoconductive gain in perovskite photodetectors, by extending carrier lifetimes beyond transit times or influencing interface energetics to allow charge injection.[267,269] Defect density, position and trap state depth are three parameters which impact the magnitude and light intensity dependence, of photocurrent amplification.[309] By specific engineering of these defects, they can allow greater photoresponse in particular light intensity regimes, and be designed to suit particular applications.

However, while defects and processing variations allow photoconductive gain to amplify response, this also leads to slower transit times and small LDRs. Additionally, as shown, defects also generate current drifts that are undesirable for commercial applications and generate characterisation difficulties. Designing a fast detector with a wide linear response and stable current output can be targeted by passivation. While ageing has shown to be an effective passivating strategy here, and elsewhere,[294–297] its influence is hard to control, and it also leads to degradation of the perovskite film and reductions in detector sensitivity (Figure 4.8d). The benefits of this procedure must be balanced against its detriments, and other more targeted passivation approaches would therefore be of greater benefit to commercial detectors.

Passivation techniques are prevalent in the perovskite literature, especially for solar cell applications where trap induced recombination decreases open circuit voltage (V_{OC}) values.[128,310,311] Both the perovskite surfaces and bulk material have been specifically targeted with passivation techniques such as alkali metal ions[312] non-stoichiometric PbI_2[313] and Lewis acids[314]. Additionally, defect migration can be specifically targeted by the removal of the grain boundary channels which facilitate their transport,[315–317] through grain boundary passivation[310,318,319] or grain size engineering[315,320,321]. Reducing perovskite structural dimensionality has been used to increase the activation energies of migration[322,323] and resultantly has found use in overcoming the current drifts in direct X-ray detectors, which are particularly susceptible to this effect due to the large external biases.[208,210,324]

In summary, we have highlighted the influence of defects on the performance and characterisation of photodetectors. The presence of considerable defect densities in halide perovskite films introduces a requirement to measure performance under low light intensities, where the density of trap states is comparable to charge carrier densities and their influence on performance is significant.[265] However, defects also generate challenges when measuring performance under low light intensities, as defect migration induced current drifts are of the same magnitude as the photoresponse. Therefore, care must be taken in measuring the low-light response of perovskite photodetectors. Additionally, the migration of certain species may also be responsible for the lower reverse bias stability of p-i-n architectures, highlighting the importance of device polarity in enabling long-term detector operation. We also show that the impact of defects can be controlled through material design and fabrication, allowing an additional point of control over photodetector performance. By engineering the perovskite interfaces and trap states, photoconductive gain can be introduced and manipulated to amplify photocurrents and increase sensitivity. Similarly, passivation offers a reduction in defects and their migration, enabling photodetectors with minimal current drifts and linear responses even down to low light intensities. This enables the performance of perovskite photodetectors to be optimised for the particular requirements of commercial applications.

Chapter 5

Tunable Multiband Perovskite Tandem Photodetectors with Switchable Response

In this chapter, we exploit the band gap tunability and capability of all-perovskite tandem solar cells to demonstrate a new photodetecting device concept, realising four spectral bands of response from a single multijunction device, with fast, optically controlled switching between the bands. The response to monochromatic light is highly selective and narrowband without the need for additional filters and switches to broader response bands on applying bias light. We demonstrate proof-of-principle how the manipulation of the modular multiband detector response through light conditions enables diverse applications in optical communications with secure encryption.

The content in this chapter has been adapted from O. D. I. Moseley, B. Roose et al., Tunable Multiband Halide Perovskite Tandem Photodetectors with Switchable Response, *ACS Photonics*, 2022, **accepted**.[256] A UK patent application has been filed based upon the findings of this chapter (application number 2215731.7). Devices and perovskite thin films were fabricated by Bart Roose. UV-Visible absorption spectra and SEM images were obtained by Bart Roose. The response time measurements were recorded on a system designed by Szymon Zelewski. Intensity dependence of the narrowband photoresponse were measured on a system designed by Simon Kahmann. X-ray diffraction data was obtained by Krishanu Dey. All other measurements and analysis were performed by the author of this thesis.

5.1 Introduction

A key figure of merit for photodetectors is their spectral selectivity, defining the range of photon energies to which they respond. Whereas most detectors are classified as either narrow or broadband, a third class of devices can act in more than one spectral range. Dualband detection originally emerged for multicolour IR imaging,[170,171] requiring expensive and complicated epitaxy with inorganic semiconductors[172], thereby restricting applications primarily to military use. Reducing device costs will open up more affordable applications, and recently solution processed equivalents using quantum dots,[325] organics[326,327] and perovskites[173–176] have emerged. These devices allow switchable performance, often by applying bias[177,178,328] or illuminating different sides of the device.[179] However, so far, only two separate response bands are produced from a single device and importantly these mechanisms are yet to quantify switching times. Fast switching between detection bands has not been demonstrated and would enable optical gating of detection bands, whilst more bands of detection would enable greater colour resolution, opening up a wider range of applications.

Here, we demonstrate a multiband perovskite photodetector using a two-terminal tandem photodetector (TPD), displaying rapid and selective switching between bands using bias light sources. We exploit the unique properties of a TPD when utilising a wider band gap perovskite responsible for the colour selectivity in the top sub-cell, combined with a narrower band gap perovskite layer in the bottom sub-cell. In these devices, monochromatic excitation results in a narrowband response due to the series connection imposed by the two-terminal design and the current matching requirements of both sub-cells. However, in the presence of white incident light, or by applying specific monochromatic bias light, the behaviour shifts to broader response bands, demonstrating a unique ability to optically gate the response to certain colours of light. Four detection modes are offered in total: narrowband, top sub-cell broadband, bottom sub-cell broadband and the ultra-broadband response of both sub-cells combined, while the spectral positions of these bands can be controlled through compositional engineering of the perovskite absorber layers. We propose a model to explain the device response, and use this understanding to optimise the performance in the narrowband mode, leading to FWHMs of 16 nm, detectivities over 6.0×10^{11} Jones and < 250 ns response time, with a peak response that is tuned from 545 to 800 nm. The broadband modes are also sensitive with detectivities all exceeding 7.0×10^{11} Jones. The unique behaviour of the TPD device opens up a wide range of new applications and we propose the ultrafast switching will allow for the selective detection or rejection of certain incident light energies, useful, for example, in microscopy. The novelty

of having many response bands could also bring advantages to secure optical communications, and we show that combining pulses of monochromatic light with different wavelengths allows for encryption of information through demonstration of encoding and de-coding of a three-colour light series.

5.2 Device Structure and Mechanism

The TPD has the device architecture shown in Figure 5.1a, akin to two series-connected p-i-n photodiodes or sub-cells, each with a perovskite absorber. The same device structure is used for tandem solar cells, which exploit the two absorbing junctions to increase the maximum possible conversion efficiencies over single junction devices.[329] Here, we have optimised absorption in the perovskite layers to suit multiband photodetection. The band gap of perovskites can be tuned by changing the constituent ions, and the top sub-cell (the sub-cell through which light first enters the device), is designed to have a wider band gap than the bottom sub-cell by varying the bromide:iodide ratio. As a result, higher energy light is absorbed in the top sub-cell and lower energy light in the bottom sub-cell. The two-terminal structure connects the sub-cells in series, which limits the current generated by the TPD to the lowest current from the two sub-cells, and therefore both sub-cells need to be absorbing to generate a response from the detector.

Under broadband illumination, such as the AM1.5 solar spectrum, both sub-cells will be absorbing light and generating current. However, under monochromatic excitation, the response will differ depending on the photon energy, and is divided into three categories. Ensuring perovskite thickness exceeds absorption depths for above band gap photons, higher energy light, $hv > E_{BG}^{wide}$ will be absorbed primarily in the top sub-cell (Figure 5.1b). Similarly, light of energy $E_{BG}^{narrow} < hv < E_{BG}^{wide}$ will be absorbed solely by the bottom sub-cell (Figure 5.1d), and in both cases no response will be detected, as the output of the TPD will be limited by the non-absorbing sub-cell. However, when hv is approaching E_{BG}^{wide} the absorption of the top sub-cell begins to decrease and an increasing fraction of light is transmitted through this sub-cell to reach the bottom sub-cell (Figure 5.1c). This allows the bottom sub-cell to also absorb light, and the TPD will generate a photocurrent. The small range of monochromatic photon energies that generate current in both sub-cells corresponds to a narrow band of photon detection for the complete device (Figure 5.1e).

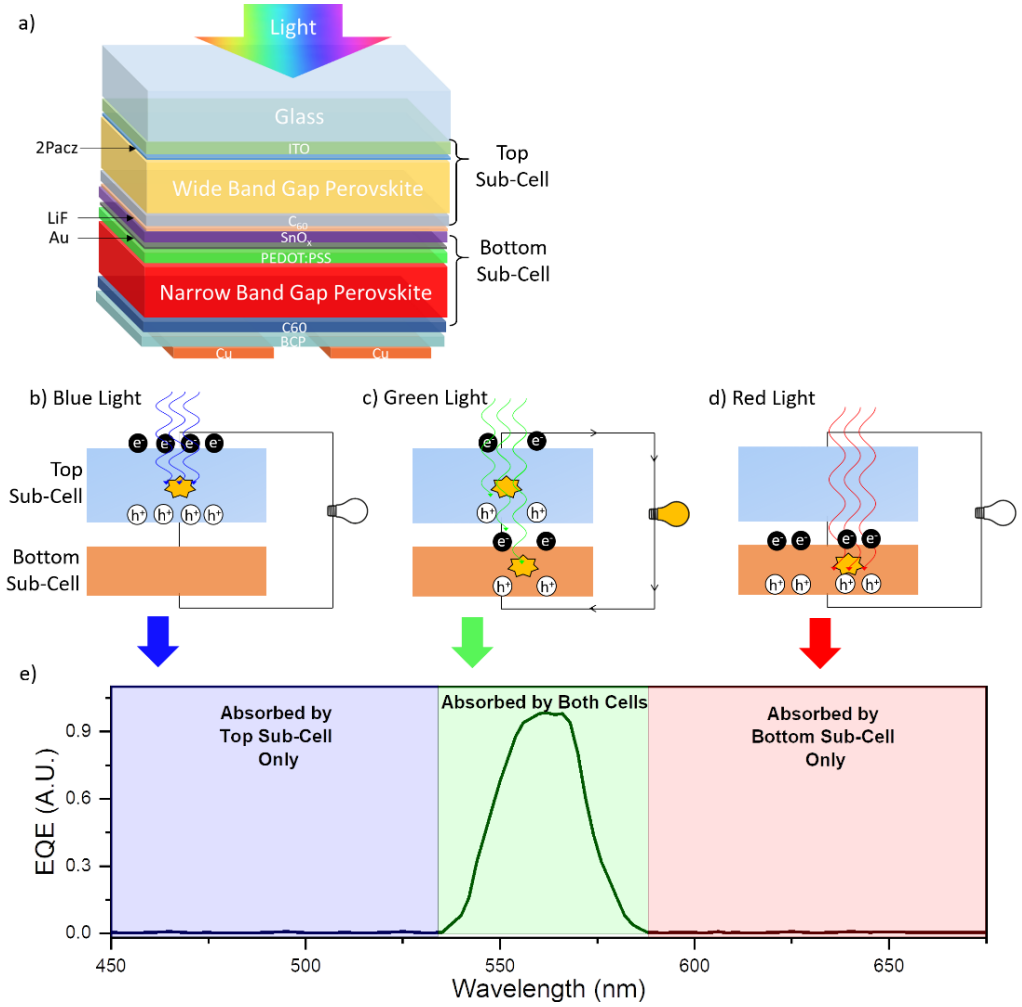

Figure 5.1: Device Structure and Narrowband Mode Detection Mechanism. *a) Schematic of the TPD device structure. b-d) Schematics of absorption in both sub-cells to monochromatic b) blue, c) green, and d) red light, with the corresponding EQE denoted in e). TPD fabrication was performed by Bart Roose.*

A narrowband response is seen when no other light sources are incident on the TPD. However, on applying continuous wave bias light the behaviour shifts back to broadband detection. The shift from narrowband to broadband detection in the presence of bias lights prevents the colour selective detection of white light; however it opens up unique multiband applications. Bias light of specific wavelengths can selectively saturate a single sub-cell (Figure 5.2a and b), and the device current will be therefore limited by the non-absorbing sub-cell. This generates two more bands of response: the first up to E_{BG}^{wide} (top sub-cell broadband) and the second from E_{BG}^{narrow} to E_{BG}^{wide} (bottom sub-cell broadband, Figure 5.2c). Similarly, two bias lights (or white bias light) can saturate both sub-cells, allowing an ultra-broadband response up to E_{BG}^{narrow}. The spectral positions of all four of these bands, including the narrowband peak, can be tuned

with perovskite band gap and exploiting the use of bias light allows the response of the device to be selectively switched between the modes.

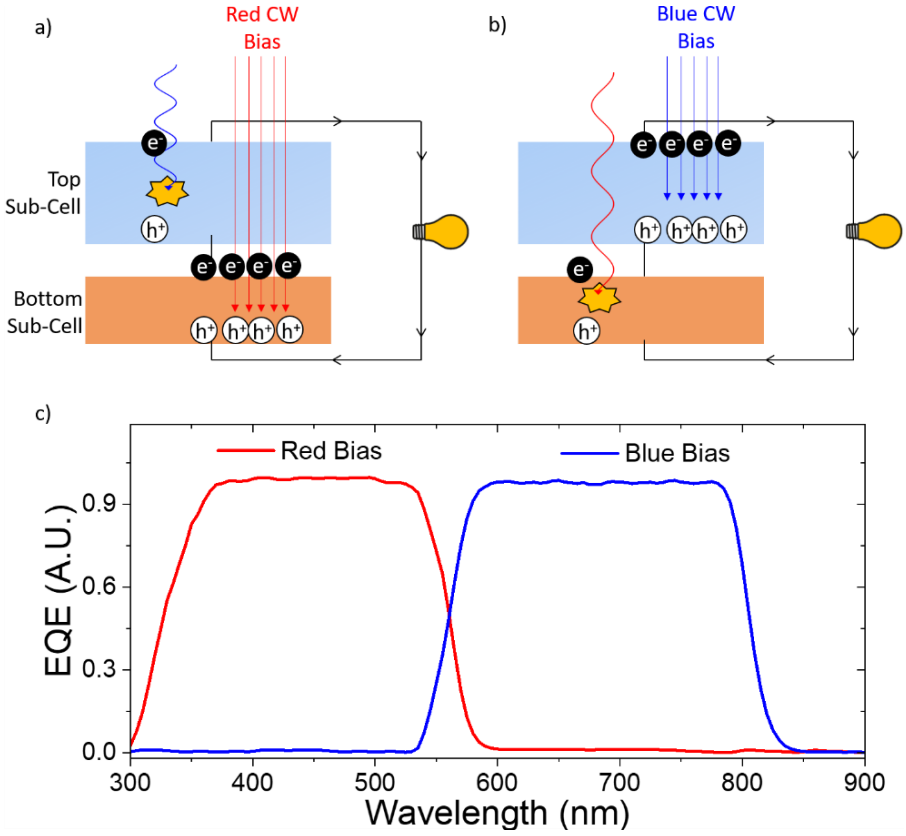

Figure 5.2: Broadband Mode Detection Mechanism. *a) and b) Schematics of pulsed monochromatic light absorption in both sub-cells, during the application of a) red and b) blue continuous wave (CW) bias light. c) The corresponding EQE with red and blue bias light. Continuous wave bias light saturates one sub-cell, allowing the chopped light to probe the response of the other, current limiting sub-cell. Switching between the narrowband response (Figure 5.1) and two broadband modes is controllable with bias light colour, generating a multiband detector.*

5.3 Modelling Device Performance

We demonstrate the optical concepts of the TPD behaviour to a monochromatic light probe by modelling the absorption and current generation in each sub-cell. Using the measured absorption spectra of perovskite films, we calculated the distribution of photon absorption between two sub-cells as a function of perovskite composition and thickness. Herein, we abbreviate the perovskite compositions to $APbI_xBr_{3-x}$ and $BPbI_xBr_{3-x}$, where *A* and *B* refer to $Cs_{0.05}FA_{0.79}MA_{0.16}$ and $FA_{0.83}MA_{0.17}$, respectively. It is noted that the poor solubility of CsBr meant compositions with higher bromide fractions have the caesium-free A-site, $BPbI_xBr_{3-x}$. XRD and SEM were initially performed on the films, to confirm the perovskite composition

was formed and the film was pinhole-free (Figure 5.3). Pinholes would otherwise reduce absorption, allowing shorter wavelength light to pass through the top sub-cell and reduce selectivity. In the model, we assume internal quantum efficiencies of 100%, implying that any absorption event would lead to charge carrier extraction in each sub-cell. The requirement of current matching between the sub-cells, imposed by the series connection of the two-terminal device, was included by taking the smaller current from both of the sub-cells as the final output of the device. We note that the impact of the other layers in the devices was not accounted for, in terms of either parasitic absorption or cavity effects, however, proof-of-principle and general trends can be obtained without these contributions.

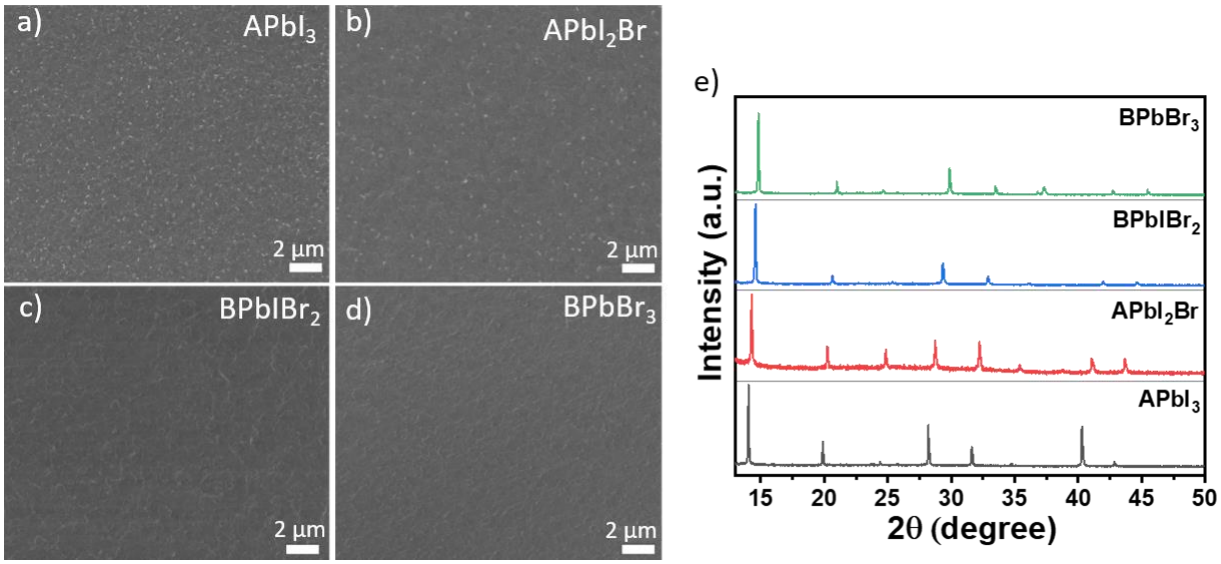

Figure 5.3: Analysis of Perovskite Thin Films with Different Compositions. *a)-d) SEM images and e) X-Ray diffractograms of the perovskite absorbers used in the model and in subsequent devices. SEM and XRD data were obtained by Bart Roose and Krishanu Dey, respectively.*

The results of the model confirms the narrowband response occurs when both sub-cells are absorbing the incident light (Figure 5.4a). By inputting absorption data from perovskite thin films of varying composition (by varying the iodide to bromide ratio) into the model demonstrates the impact of band gap on photodetection. By varying the composition of the top and bottom sub-cell perovskite (Figures 5.4b and c, respectively), we demonstrate the spectral position of the narrowband response is dictated by the top sub-cell with the wider band gap. The role of the bottom sub-cell is to absorb the light transmitted through the top sub-cell, requiring a smaller band gap, and thus it has no impact on the wavelength of narrowband response.

The spectral response after the introduction of bias lights is shown in Figure 5.4d, where saturating a sub-cell with bias light allows the response to switch to either of two broadband detection bands. The band gaps of both sub-cells dictate the onsets of these bands, demonstrating that their spectral position is also tunable. The concept thus generalises to other semiconductor materials that maintain these requirements, including other absorber materials used for multi-junction cells, and we herein continue to demonstrate the concept with halide perovskites.

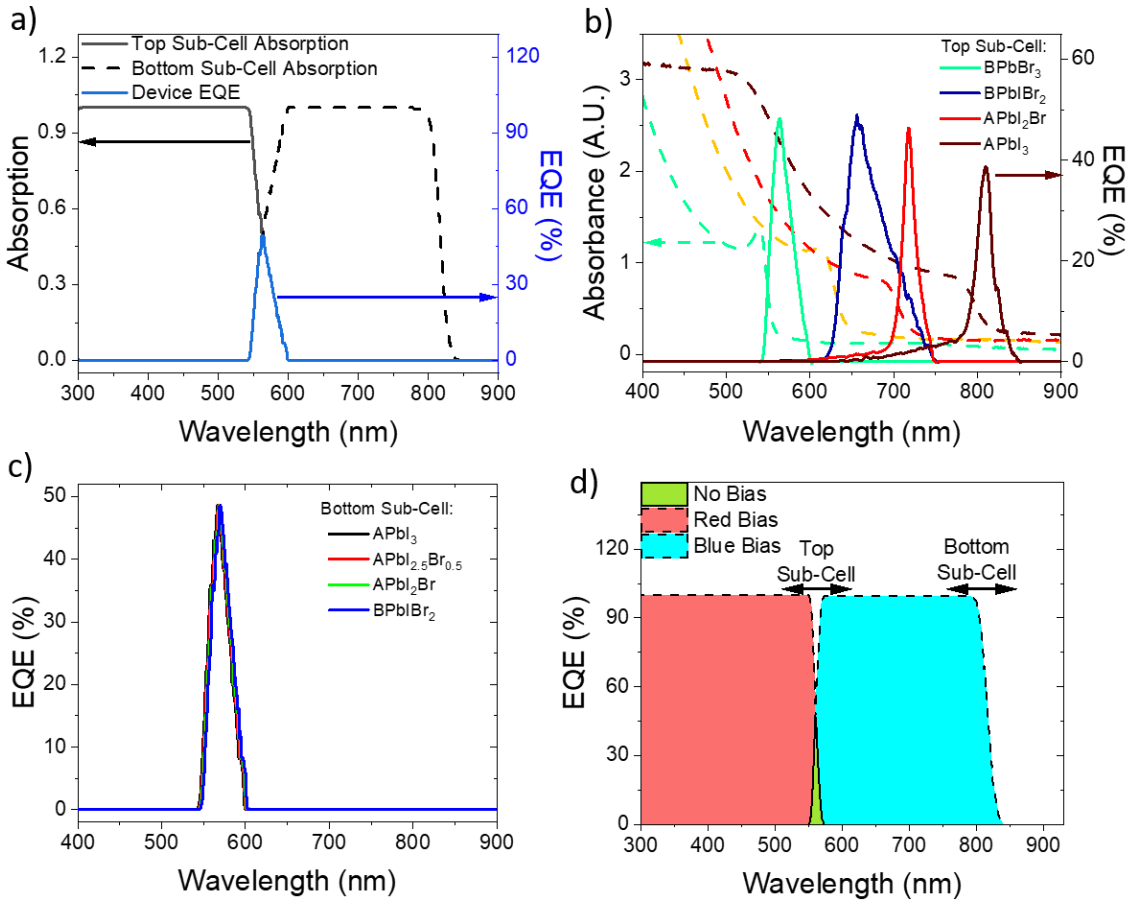

Figure 5.4: Modelling TPD Response – Spectral Tuning with Perovskite Composition. *a) Absorption (black lines) in the wide band gap ($BPbBr_3$, solid line) top sub-cell and narrow band gap bottom sub-cell ($APbI_3$, dashed line) in the TPD structure, and the corresponding modelled EQE (blue line) from the full TPD device. b) Varying the top sub-cell composition, whilst keeping the bottom sub-cell fixed. Absorption data for different perovskite thin films (dashed lines), with the modelled EQE (solid lines) when used as a 500 nm top sub-cell absorber, combined with a 500 nm $APbI_3$ bottom sub-cell. c) Varying the bottom sub-cell composition whilst keeping the top sub-cell constant ($BPbBr_3$), both with 500 nm thickness. d) TPD device EQE with no bias light (green), and red and blue bias lights, highlighting the tunability of all three bands with absorber band gap.*

The selectivity of the narrowband peak is optimised with the top sub-cell thickness (Figure 5.5a): increasing thickness reduces the transmission of photons above the energy of the

narrowband peak, decreasing the size of any side shoulders and the FWHM. While increasing the wide band gap thickness should continually improve selectivity, the sensitivity will eventually begin to drop once the required charge carrier transport length exceeds diffusion lengths of carriers, though we note that this is not included in the model due to the assumption of 100% internal quantum efficiency. A smaller band gap offset between the sub-cells, requires more top sub-cell thickness optimisation in order to produce a highly selective narrowband response. The extreme case of using the same absorber for both cells is possible (as shown for $APbI_3$ / $APbI_3$ in Figure 5.4b), and would enable narrowband detection of white light, but is prone to shoulders on the narrowband response and sensitivity losses (Figure 5.5b). The bottom sub-cell must be of suitable thickness to sufficiently harvest above-band gap photons. However, the spectral selectivity is unaffected by the bottom sub-cell thickness.

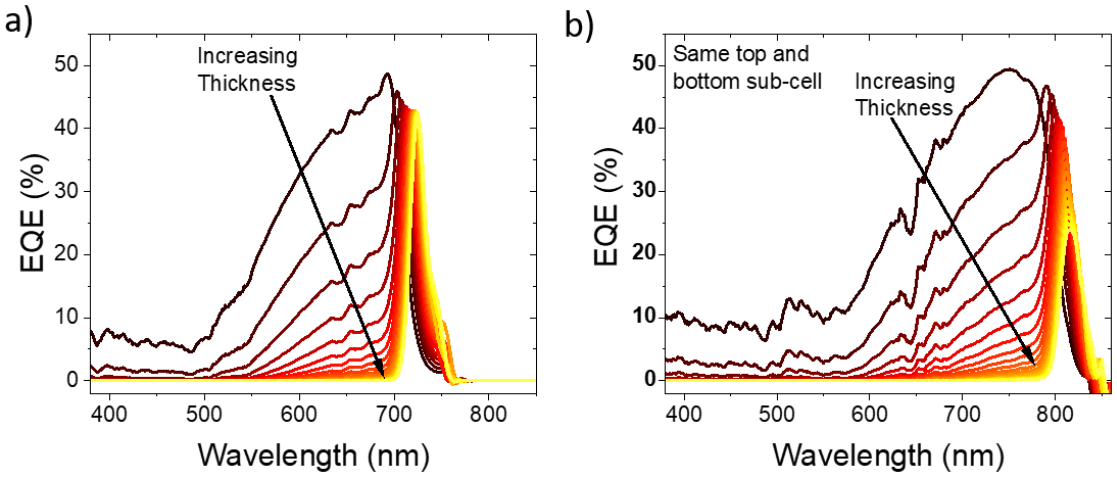

Figure 5.5: Modelling TPD Response – Perovskite Thickness. *a) Increasing thickness of $APbI_2Br$ top sub-cell from 100-1000 nm (50 nm steps), combined with an $APbI_3$ bottom (1000 nm thick) sub-cell. b) Increasing the thickness of the top sub-cell from 100-1000 nm (50 nm steps), when $APbI_3$ is used in both sub-cells.*

5.4 Narrowband Photodetector Performance

Following the results of the model, proof-of-concept devices were fabricated consisting of an $APbI_2Br$ absorber in the top sub-cell and $APbI_3$ in the bottom sub-cell. This was used as the archetypal device for the remainder of the study. We began by assessing the detection of monochromatic light, and initial EQEs displayed the expected narrowband response peak centred at 705 nm (Figure 5.6a). However, they also contained side peaks in the blue (335-450 nm) and NIR (740-825 nm) regions of the spectra. These side peaks represent photon energies where only one sub-cell will be absorbing, and therefore the response from the overall device will be coming from the current limiting non-absorbing sub-cell. Reducing the current

produced in the non-absorbing sub-cell improves selectivity, and studying the origins of this leakage current allowed narrowband performance to be optimised through applied bias and probe light intensity.

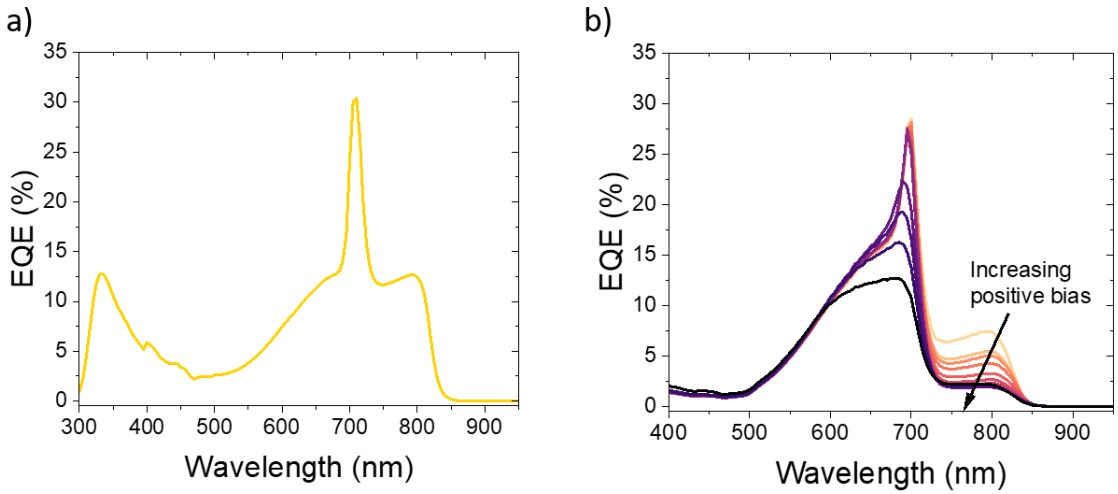

Figure 5.6: Improving Narrowband Selectivity – Applied Bias. *a) Initial EQE spectrum at 0 V applied bias, in narrowband mode (monochromatic light probe, no bias light), demonstrating side peaks which lower selectivity. b) The EQE with different external biases applied across the whole TPD device, from -0.1 to 1 V (0.1 V step).*

The current from the non-absorbing cell is comparable to the dark current of a single junction photodiode, and therefore reducing the magnitude of this current was possible with externally applied biases. Fixing the external bias across the TPD at 0 V (as performed in Figure 5.6a) and illuminating only one sub-cell drives the non-absorbing sub-cell into reverse bias, a result of the photovoltage generated in the absorbing cell.[330] More dark current is expected under reverse bias due to charge injection from the contacts,[331] contributing to larger side peaks. However, applying a positive bias across the entire device can counteract the photovoltage generated in the absorbing cell, and decrease the reverse bias applied to the non-absorbing cell. A forward bias of 0.5 V was found to be optimal for improving selectivity (Figure 5.6b).

Probe light intensity impacts the relative magnitude of the photoresponse compared to the leakage current in the non-absorbing sub-cell. As a result, side peaks are more significant at low incident intensities, where this leakage current is of a similar magnitude to the photocurrent. Therefore, greater selectivity is achieved at higher probe light intensities (Figure 5.7a). The side peaks are exaggerated in our measurement system, due to sharp lamp intensity drop offs below ~430 nm and above ~700 nm (Figure 5.7b). To gain more understanding on this effect, the side peaks were selectively probed over a wider range of intensities using 405 nm and 800 nm monochromatic light, shown in Figures 5.7c and 5.7d respectively. For 405 nm

irradiation, there are three distinct regimes: an initial increase in current, followed by a plateau and then a second rise in current. The initial rise in TPD response at low light intensities represents the region where the absorbing top sub-cell is current limiting, and the current plateaus when this top sub-cell photocurrent exceeds the leakage current in the non-absorbing narrow band gap sub-cell, around 49 μA cm^{-2}. At low light intensities the leakage current in the bottom sub-cell is higher than the top sub-cell photocurrent, due to its smaller band gap (generating more thermal carriers) and because the entire TPD cell is held at short circuit driving the non-absorbing cell into reverse bias (bias was not optimised for this measurement). Above intensities of ~3 $mWcm^{-2}$ the current begins to increase again, but the EQE continues to decrease. A possible explanation for this third regime is the onset of bimolecular recombination allowing efficient luminescent coupling between the two cells[332] and will be the subject of future investigations.

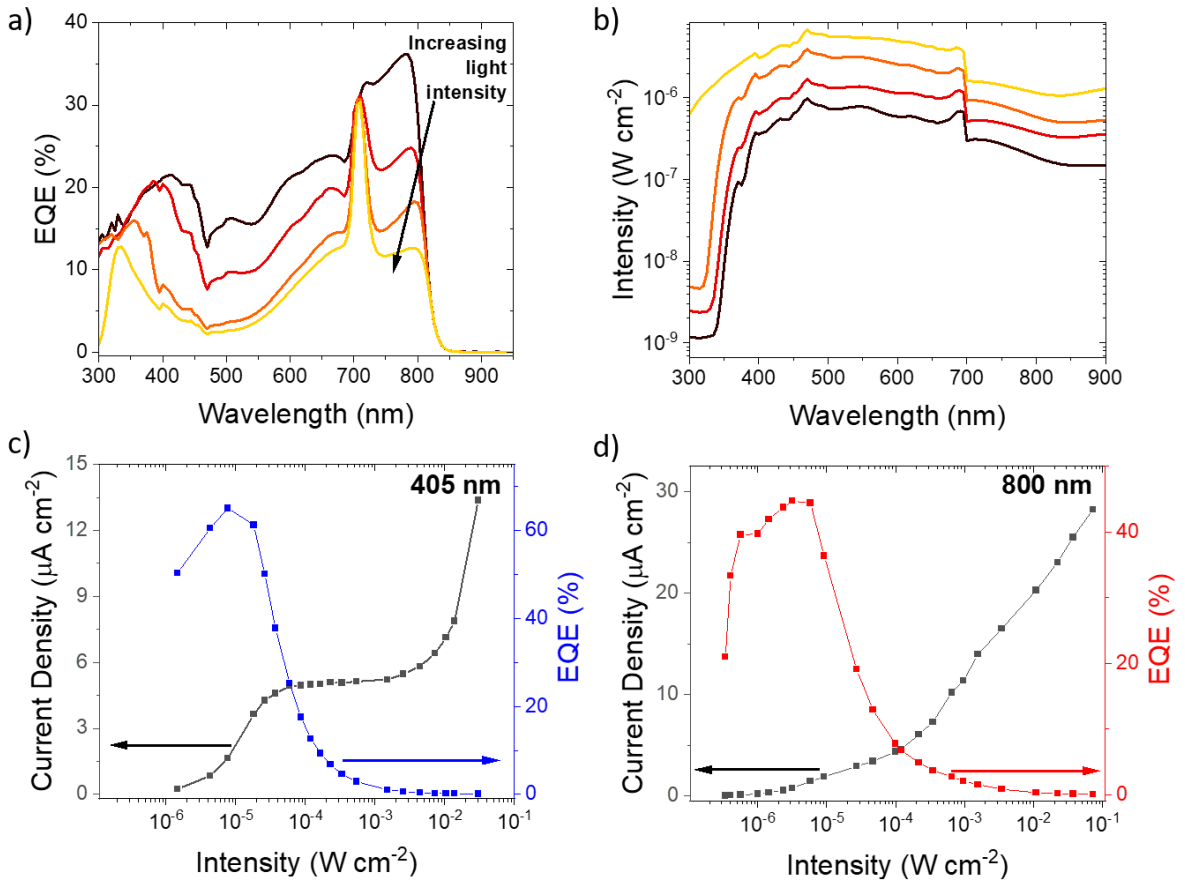

Figure 5.7: Improving Narrowband Selectivity – Probe light Intensity. *a) Intensity dependence of the EQE selectivity. Power was reduced by adding neutral density filters, with the corresponding probe light intensity shown in b). Below ~350 nm the power falls off significantly, and resultantly the leakage current of the non-absorbing narrow band gap cell is very significant in this region, leading to side peaks in the narrowband response. c) and d) Intensity dependence of side peak current and EQE in the blue (405 nm, c)) and NIR (800 nm, d)) at 0 V.*

For the side peak at 800 nm the behaviour is less understood, and the current gradually increases with intensity over the whole measured range. Luminescent coupling is unlikely in this case, as the narrower band gap of the bottom sub-cell would emit photons too low in energy to be absorbed by the top sub-cell. Again, the EQE reaches a peak value (at a similar power to the 405 nm plot, ~5 − 7 μWcm^{-2}), likely representing the switchover of limiting current from the absorbing to the non-absorbing cell, and then continually decreases. The exact mechanism will be the subject of future studies. Importantly, the size of the side peaks decreases with increasing light intensity, improving the selectivity of the narrowband peak. Both the blue and NIR side peaks drop below 1% EQE above illumination intensities of 500 μWcm^{-2}.

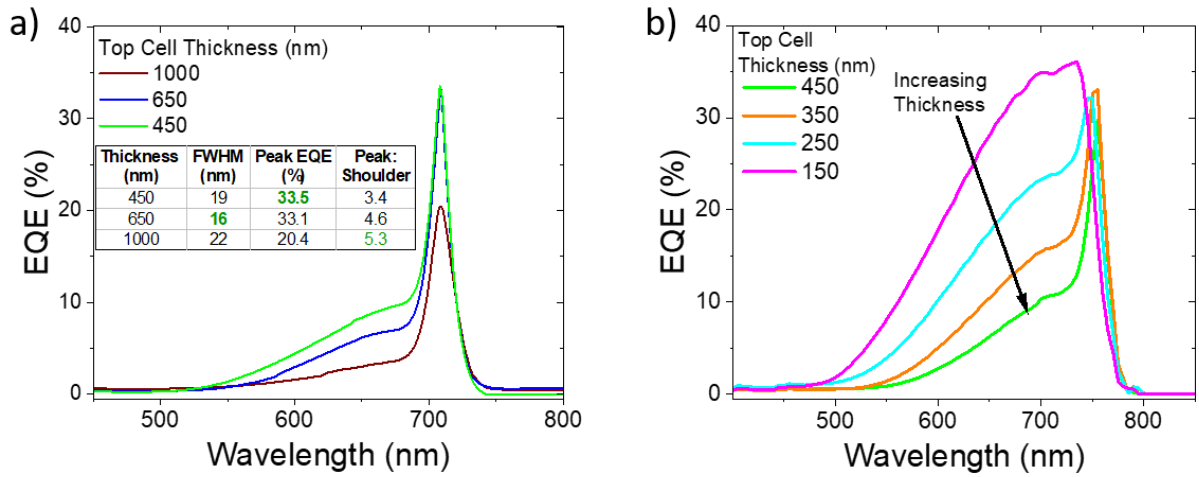

Figure 5.8: Improving Narrowband Selectivity – Perovskite Thickness. *a) $APbI_2Br$ top-cell and b) $APbI_{2.5}Br_{0.5}$ top-cell, both combined with $APbI_3$ (450 nm) bottom sub-cells. The green values in the inset table highlight the best performance for each metric.*

Following the understanding of measurement conditions on narrowband performance, the device was optimised to improve selectivity. As shown in the model (Figure 5.5), thick perovskite films in the top sub-cell are a requirement for a selective response. The thickness of the top sub-cell perovskite was varied through precursor concentration, and the effect on EQE is shown in Figure 5.8a. Increasing the thickness of the top-cell absorber reduces the shoulder of the narrowband peak by increasing the absorption of these wavelengths in this top sub-cell. The same trend is seen for a smaller band gap top sub-cell perovskite (Figure 5.8b). While increasing thickness will further improve selectivity, at thicknesses of 1000 nm the sensitivity has decreased, due to finite charge diffusion lengths leading to incomplete collection of charge carriers over such larger distances. Therefore, a trade-off exists, which can be tuned depending on the requirements of the device. EQEs of 33.5% with a 19 nm FWHM at 705 nm were achieved, which increases to 36.4% EQE and 21 nm FWHM at 755 nm for the $APbI_{2.5}Br_{0.5}$ top

sub-cell device. This represents the highest sensitivity for a filterless narrowband photodetector at low applied bias.

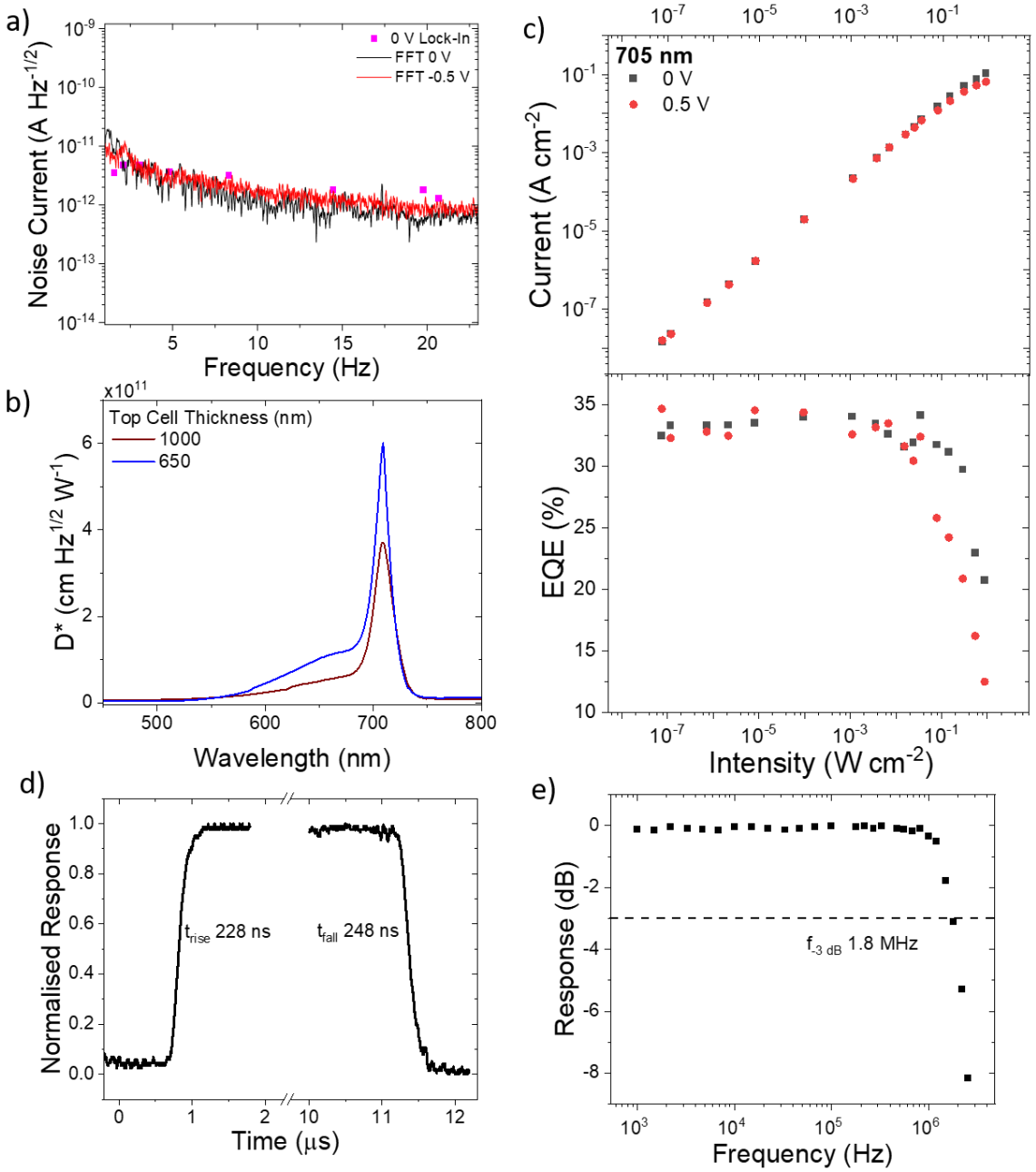

Figure 5.9: Narrowband Photodetector Characterisation. *a) Noise spectral density, measured by Fourier transform of current-time data, or using a SR510 lock-in amplifier. b) The effect of top sub-cell perovskite ($APbI_2Br$) thickness on detectivity. c) Linear dynamic range of the narrowband peak (705 nm) represented with the current density (top), and corresponding EQE (bottom) as light intensity is increased from ~10^{-7} to 10^{-1} W cm^{-2}. Note, the lowest intensity and current were set by the resolution limitations of the measurement set-up. d) Transient response to 670 nm square wave pulsed light for the TPD. Rise and fall times were taken from the time for the signal to change from 10 to 90% of the peak response. e) The corresponding cut-off frequency for the same device.*

The photodetection performance of the optimised TPD was then analysed. The frequency dependence of the noise current was recorded by applying a fast Fourier transform to the time dependence of the dark current (Figure 5.9a). The noise shows little bias dependence between 0 and 0.5 V, and gives values of 113 fA $Hz^{-1/2}$ at 20 Hz. Combined with the responsivity values of 0.19 AW^{-1} at 705 nm, this corresponds to peak narrowband detectivities of over 6.0 x 10^{11} Jones (Figure 5.9b), the highest reported value for narrowband perovskite photodetectors to date. At the narrowband wavelength of 705 nm, LDRs (measured using the 'dynamic' procedure introduced in Chapter 4) are observed to be over 113 and 126 dB at 0.5 and 0 V respectively, limited by the lower limits of the measurement set-up (Figure 7.9c). This matches the best perovskite narrowband performance from charge collection narrowing mechanisms[163,164,333], and is only bettered by broadband detectors, which can exceed 200 dB[22,23]. The response speed is another important feature of photodetection and the rise/fall times to pulsed light were measured to be 228/248 ns, respectively (Figure 5.9d), with a −3 dB cut-off frequency of 1.8 MHz (Fig 5.9e). These results compare favourably to the response speeds offered by the charge collection narrowing mechanism,[165,179,333] in that case limited by the low transit times of charges across the thick perovskite layers needed in those devices. The mechanism of switching between modes of TPD operation is controlled by bias lights, and so fast detection times correspond to fast switching times between modes, a feature not seen in previous multiband detection. Further improvements in response speed may be possible by reducing the active pixel area to reduce the RC constant of the device.

Through compositional tuning of the top sub-cell perovskite halide site with bromide and iodide, we demonstrate TPDs with narrowband response peaks between 545 and 800 nm (Figure 5.10a). We note that the perovskite thickness was kept constant at ~450 nm, and increased selectivity would be afforded with thicker depositions. Tuning the top sub-cell perovskite band gap allows a narrowband response across most of the visible and into the NIR spectral region using the TPD device structure. Similarly, this band gap also controls the switchover wavelength between the top and bottom sub-cell broadband responses. As predicted, the band gap of the bottom sub-cell has negligible influence on the narrowband peak wavelength, instead controlling the bottom sub-cell broadband spectral position (Figure 5.10b).

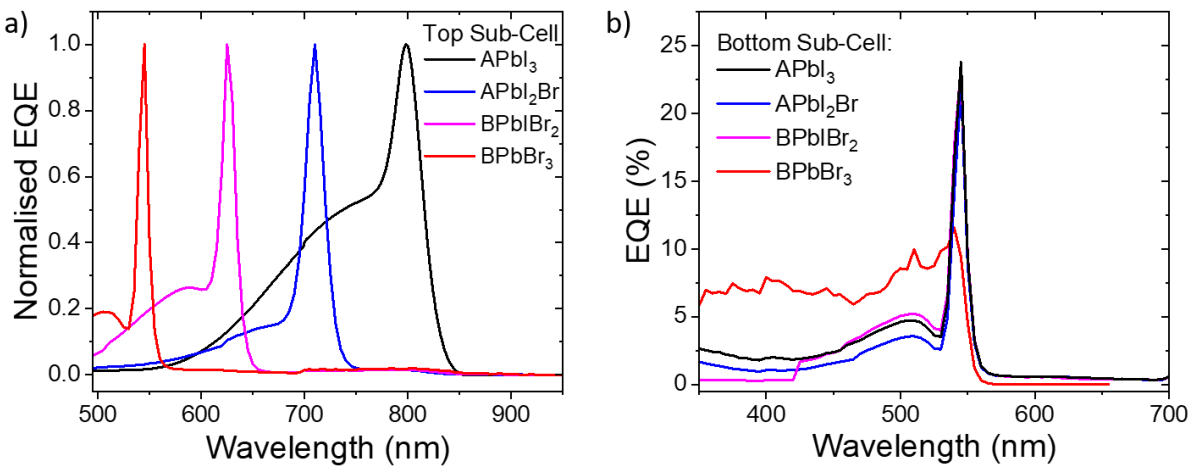

Figure 5.10: Tuning Response Bands with Perovskite Composition. *a) Varying top sub-cell composition, with constant $APbI_3$ bottom sub-cell. b) Varying the bottom sub-cell composition, with constant $BPbBr_3$ top sub-cell.*

5.5 Multiband Detection

Measuring TPDs in the dark gives a narrowband response, but the energy bandwidth of photodetection can be switched by applying bias light of different colours, demonstrating a multiband response. Saturating one or both sub-cells with charge carriers by selective continuous wave illumination will change the response of the device to a pulsed probe light. The response of a TPD when the top and bottom sub-cells are saturated with green or red bias light respectively is shown in Figure 5.11a.

Using the measured performance of the TPD, we highlight the unique response of a TPD versus a narrowband photodetector and a broadband detector of similar band gap to the bottom sub-cell using a matrix of response to two monochromatic light sources (Figure 5.11c). The detection of a 400 nm probe source by the TPD will depend on the application of a second light at 600-800 nm. Only by sending both pulses simultaneously will the TPD detect light, whereas individual pulses of light will be (electrically) rejected. In contrast, broadband detectors will detect either one or both of the individual pulses, depending on the semiconductor band gap. Combined with fast switching at above MHz bandwidths, this allows control of the detection of certain colours to be switched in-situ, and demonstrates a unique mechanism of gating the response, which may have applications in selective microscopy.

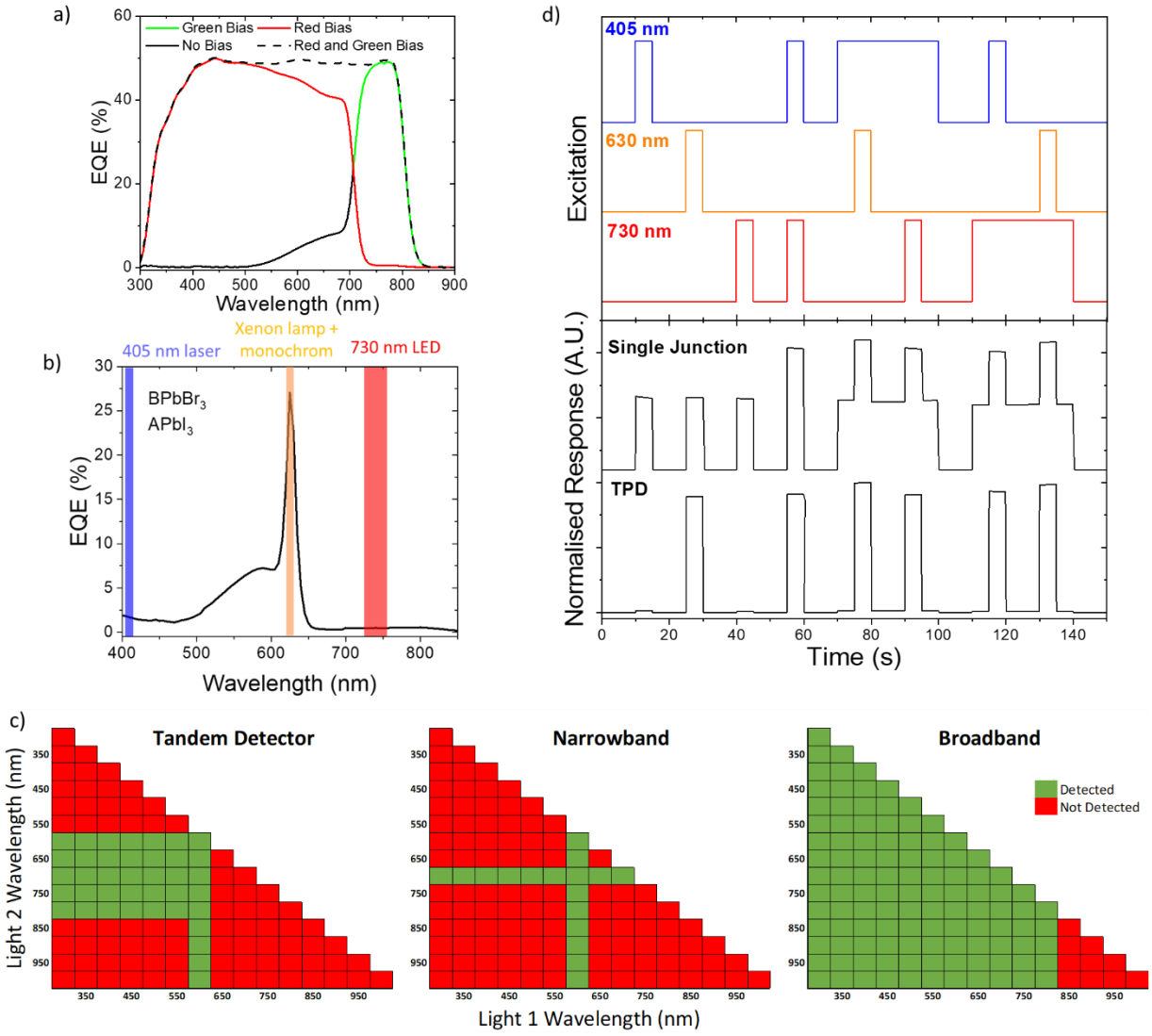

Figure 5.11: Switchable Multiband Detection for Encrypted Communications. *a) EQE spectra demonstrating all possible bands of response, depending on bias light colour. b) Pulse train experiment schematic, with the EQE of the measured $BPbBr_3$ / $APbI_3$ TPD device. This top and bottom sub-cell perovskite device was chosen as it allows us to selectively excite each sub-cell with the light sources chosen. c) Matrix of detection for a two-colour dual light excitation for three different perovskite detectors. The narrowband detector response is centred at 600 nm, and the single junction broadband detector has a band gap of ~800 nm. The symmetry of the response means only half the matrix is shown. The threshold for detection was set so that only one of the two pulses require absorbing in a single junction detector for a signal to be registered. d) The response of a perovskite TPD and single junction photodetector (~760 nm band gap) to the pulse train of three light sources, introduced in Figure 5.11b.*

We also propose that the unique multiple bands of response would be advantageous for encrypting optical information. To demonstrate this concept, we use this method to consider coded optical pulses, whose deciphering will depend on the detector. Figure 5.11d shows a pulse train of three different light sources: 405 and 730 nm, to selectively excite the top and bottom sub-cells respectively, and 630 nm which corresponds to the peak narrowband response

of the TPD device (experimental details in Figure 5.11b). The response of the TPD device is compared to a single junction perovskite photodiode, and only when either the 630 nm or both the 405 and the 730 nm probes are sent simultaneously, does the TPD afford a significant response. In contrast, the single junction cell detects each light pulse additively. Therefore, the TPD can uniquely decipher this encrypted optical information, and opens up a number of new applications as a building block in secure optical communications.

5.6 Conclusions

In summary, a tandem photodetector with rapidly switchable and tunable multiband response has been developed and demonstrated with halide perovskite device stacks. A combination of absorption modelling and empirical observations have allowed the mechanism of the behaviour to monochromatic and broadband illumination sources to be understood, with the optimum measurement conditions for selective performance uncovered. By controlling measurement conditions, narrowband selectivity is enhanced, and when combined with perovskite thickness tuning, affords narrowband detection exceeding 6.0×10^{11} Jones with FWHMs as low as 16 nm. This narrowband peak has been tuned from 545 to 800 nm by varying the iodide to bromide ratio of the perovskite absorbers, with a greater range possible through other compositions and additives including tin, chloride and 2D perovskite systems. Applying bias light to excite both sub-cells, or each sub-cell individually, affords three more detection bands, giving a multiband response that can be selectively controlled. Response speeds to light are ~250 ns, with bandwidths above 1 MHz, allowing fast optical switching between detection modes. A proof-of-concept pulse train of three different light colours was used to demonstrate the powerful potential for new applications in optical communication.

Chapter 6

Halide Perovskite Scintillators: Unique Promise and Current Limitations

Perovskites have thus far shown enormous promise as scintillating materials, demonstrating good light yields and impressively short decay times, all from low-temperature solution synthesis. In this chapter, we describe the mechanistic differences between perovskite and traditional scintillators, and use this knowledge to explain the exceptional performance already seen from this emerging material. The limitations of perovskites are discussed, and pathways to further improve the material are proposed, utilising knowledge derived from the concurrent development of other perovskite optoelectronic devices. Finally, we propose applications which would benefit from perovskite scintillators, highlighting areas where they can replace traditional materials, or offer unique properties to increase the functionality of X-ray detectors.

The content in this chapter was adapted from O. D. I. Moseley et. al, Halide Perovskite Scintillators: Unique Promise and Current Limitations, *J. Mater. Chem. C*, 2021, **9**, 11588-11604.[11] Cs_2ZrBr_6 nanocrystal solutions were provided by Anna Abfalterer. UV-visible absorption and PL spectra of Cs_2ZrBr_6 films were measured by Anna Abfalterer. Radioluminescence measurements were performed with assistance from Hayden Salway and Linjie Dai. All other experiments and data analysis were performed by the author of this thesis.

6.1 Introduction

The widespread use of X- and γ-rays in a range of sectors including healthcare, security and industrial screening is underpinned by the efficient detection of the ionising radiation. Such detector applications are dominated by indirect detectors in which a scintillating material is

combined with a photodetector. Halide perovskites have recently emerged as an interesting class of semiconductors, showing enormous promise in optoelectronic applications including solar cells, LEDs and photodetectors. Here, we discuss how the same superior semiconducting properties that have catalysed their rapid development in these devices, including high photon attenuation and fast and efficient emission properties, also make them promising as efficient and adaptable scintillator materials. By outlining the key mechanisms in their operation as scintillators, and the differences to existing materials, we show why reports of remarkable performance have already emerged. The standout performance in the literature is analysed, in order to the highlight the remaining challenges facing the commercialisation of perovskite scintillators, followed by suggestions to overcome these limitations. We describe how further learning from other perovskite optoelectronic devices will propel forward their applications as scintillators. Specifically, the importance of a Stokes shift to prevent the reabsorption of RL is highlighted, with bright scintillation measured in a Cs_2ZrBr_6 nanocrystal system. This material also displays 854/3940 ns decay time constants and negligible afterglow after 40 μs, which suit tomographic applications. Finally, we outline where these materials can make the most impact in detector applications by maximally exploiting their unique properties, leading to dramatic improvements in existing detection systems or introducing entirely new functionality.

6.2 Mechanistic Origins of Bright and Fast Emission

Perovskites have shown huge promise as a highly emissive scintillator with ultrafast decay times, and performance already exceeds commercial values. The foundation of their exceptional properties can be traced back to a differing mechanism of emission compared to traditional materials. While the exact mechanisms of RL are complex and material dependent, the general process can be simplified into three key steps: (i) generation and relaxation of excited charge carriers, (ii) transport of carriers to emission centres, and (iii) radiative recombination of carriers (Figure 6.1). A prediction for the maximum number of photons emitted (N_{ph}) is possible by looking at each of these steps in Equations 6.1 and 6.2:

$$N_{ph} = B \times S \times Q \tag{6.1},$$

$$B = \frac{E_{in}}{E_{BG} \times \beta} \tag{6.2}.$$

Here, B represents the number of carriers generated per incident photon (step i) and is a function of the incident photon energy, E_{in}, the band gap, E_{BG}, and a material dependent β term. S and Q represent the quantum efficiencies of the carrier transfer (step ii) and radiative recombination (step iii) processes, respectively. β is material-specific term and can be predicted using existing models.[14,334,335] The value of β is approximately 3 for semiconductors, whereas $2 < \beta < 3$ for ionic crystals, leading to the generation of approximately 65,000 carriers per MeV photon in CsI:Tl.[336] Carriers are then transferred to emission centres where they can emit in step iii.

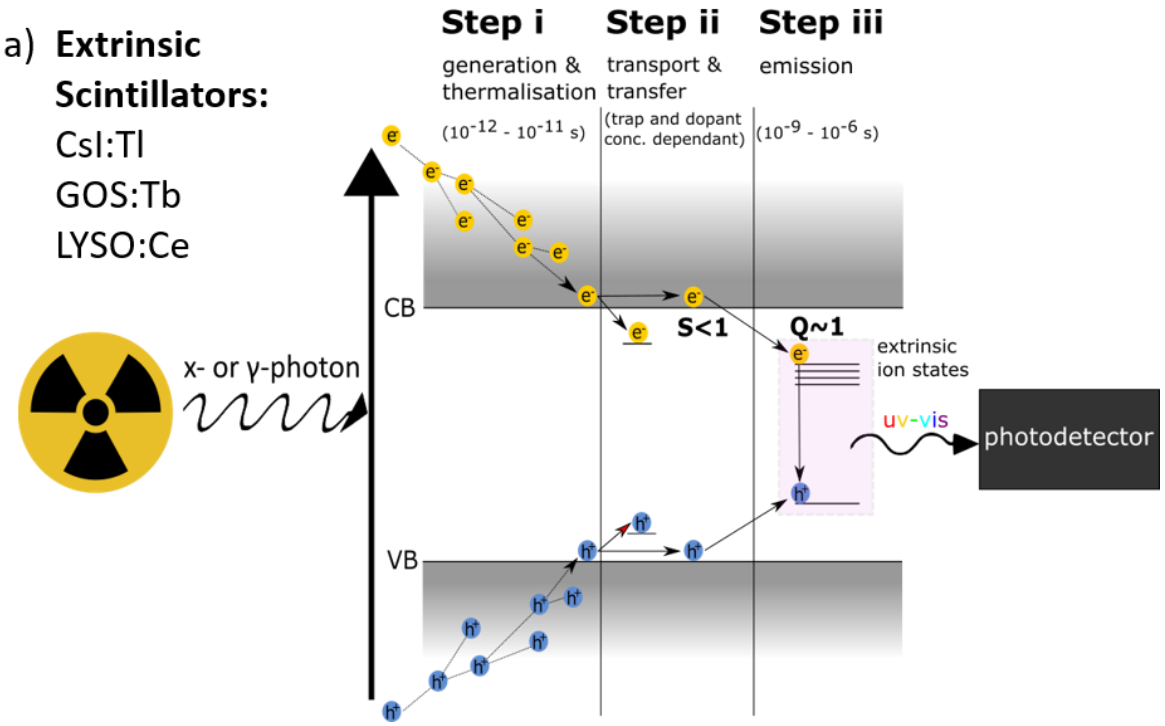

Figure 6.1: Scintillation Mechanism in Extrinsic Emitter Systems. *a) The additional transfer step to the dopant energy levels (pink box) in extrinsic emitters increases the likelihood of charge carrier trapping, causing light yield losses and afterglow.*

A key mechanistic difference between different scintillator materials is the origin of the RL being intrinsic to the material, or the result of an extrinsic dopant. Extrinsic emitters, including CsI:Tl, GOS:Tb (Gd_2O_2S), and LYSO:Ce ($Lu_{2(1-x)}Y_{2x}SiO_5$), are utilised commercially and the properties of extrinsic emission (Figure 6.1) depend on the activator ion.[56] However, limitations to extrinsic materials arise in steps i and ii in the scintillation process. Firstly, to ensure efficient charge transfer in step ii, prevent thermal repopulation of emissive states, and reduce reabsorption of the scintillated light, the matrix band gap must be wider than the band gap of the dopant emission centre. The inverse relationship between the number of charge carriers generated in the cascade and the material band gap (Equation 6.2) causes this wide band gap

host to limit the maximum number of generated emissive states. Secondly, carriers have to diffuse to reach activation sites, increasing the time of scintillation and the probability of reaching a trap state. This leads to slow responses (for example 1 μs in CsI:Tl and 3 μs in GOS:Pr)[337] and afterglow, while competing carrier trapping events can also quench carriers and reduce light yields. The efficiency of the energy migration phase, combined with the subsequent energy transfer to the activator site, is represented by the *S* term in Equation 6.1.

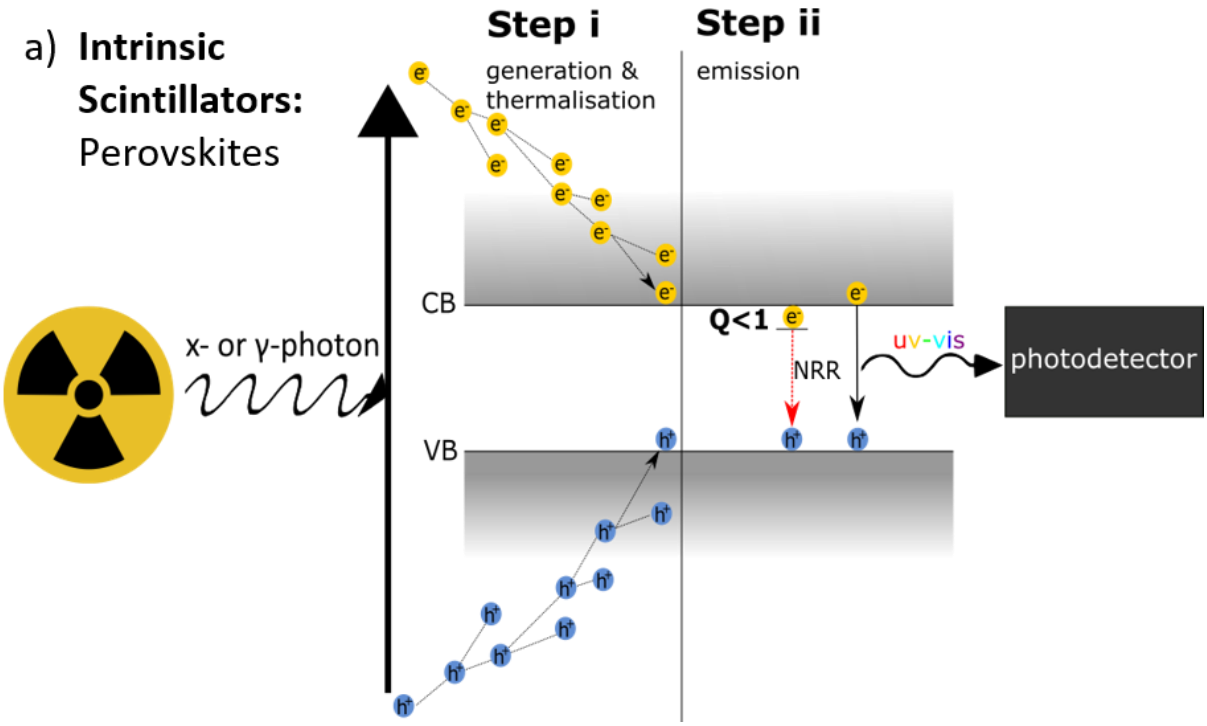

Figure 6.2: Scintillation Mechanism in Intrinsic Emitter Systems. *a) The smaller band gaps and absence of transfer step increases theoretical light yields. Perovskites are an example of a scintillator with an intrinsic emission mechanism. (NRR = non-radiative recombination).*

In contrast to existing scintillators, perovskites are direct band gap semiconductors, which allows X-ray absorption and visible light emission from the same material. This mechanism is known as intrinsic emission, with RL occurring from band-to-band or excitonic states (Figure 6.2), and is advantageous to the emission properties. Intrinsic emission allows narrower band gaps, which increases the maximum light yields. For example, $MAPbI_3$ materials can generate a theoretical maximum of ~270,000 charge carriers per MeV, over 4 times as many as CsI:Tl. The absence of a transfer step in perovskites makes scintillation timescales limited by the emission step, and parity-allowed band-to-band or excitonic decay times can be sub-nanosecond. This makes perovskites potentially brighter and faster than traditional extrinsic materials, underlining their potential for indirect detectors.

6.3 Critical Assessment of Perovskite Scintillator Performance

6.3.1 Stopping Power

Perovskites have high mass attenuation coefficients due to their high-*Z* components. As a result, at 100 keV, a relevant energy for many imaging applications, the coefficient for $MAPbI_3$ is 3.1 $cm^2\ g^{-1}$, in comparison to 2.0 $cm^2\ g^{-1}$ for CsI:Tl (Figure 6.3a). However, the stopping power of a scintillator depends on the mass density of the material, not just the mass attenuation coefficient. The attenuation of photons through a solid can be obtained using the Beer-Lambert law (Equation 6.3) which shows the dependence of the intensity of transmitted photons *I* on the material density ρ

$$I = I_0 e^{-(\frac{\mu}{\rho})\rho x} \quad (6.3),$$

where I_0 is the intensity of incident photons, μ is the linear absorption coefficient, and *x* is the material thickness. The mass attenuation coefficient, μ/ρ, is often used due to its lack of material density dependence, allowing comparisons regardless of phase or crystal structure.[13] However, the material mass densities of $PbWO_4$ and BGO exceed 7 g cm^{-3}, compared to values generally less than 4 g cm^{-3} for perovskite single crystals (Figure 6.3c). This is in part due to the large volume occupied by the halide ions, and in comparison, oxide perovskites scintillators are not as restricted ($LuAlO_3$ - 8.3 g cm^{-3}).

Although densities around the value of perovskite single crystals are observed in traditional scintillators (NaI and CsI crystals are 3.7 and 4.5 g cm^{-3}, respectively), some of the most promising perovskite materials are even less dense. For example, the highest light yields to date have been demonstrated with perovskites of reduced dimensionality. 2D materials contain alternating inorganic layers with large organic spacers, and the bulk of the organic moieties reduces density further (Figure 6.3d), with $(NH_3(CH_2)_2O(CH_2)_2O(CH_2)_2NH_3)PbCl_4$ ($(EDBE)PbCl_4$) yielding just 2.2 g cm^{-3}.[54] Similarly, despite bright RL demonstrated from perovskite nanocrystals such as $CsPbBr_3$, polymer host matrices for the nanocrystals are often used, reducing density further (Figure 6.3e). The low-*Z* organic components of the matrices increase the attenuation length, and any improvements in film quality or environmental stability provided by the polymer must be carefully balanced against the increase in penetration depth in the scintillator. The decrease in stopping power in reduced dimensionality systems can be seen in Figure 6.3b, where almost twice as much material is needed with a 2D perovskite compared to its 3D analogue to sufficiently stop the 150 keV photons utilised in medical CT

scanners. This reduces the image resolution of the detector system due to an increase in light scattering inside the detector, leading to optical crosstalk.

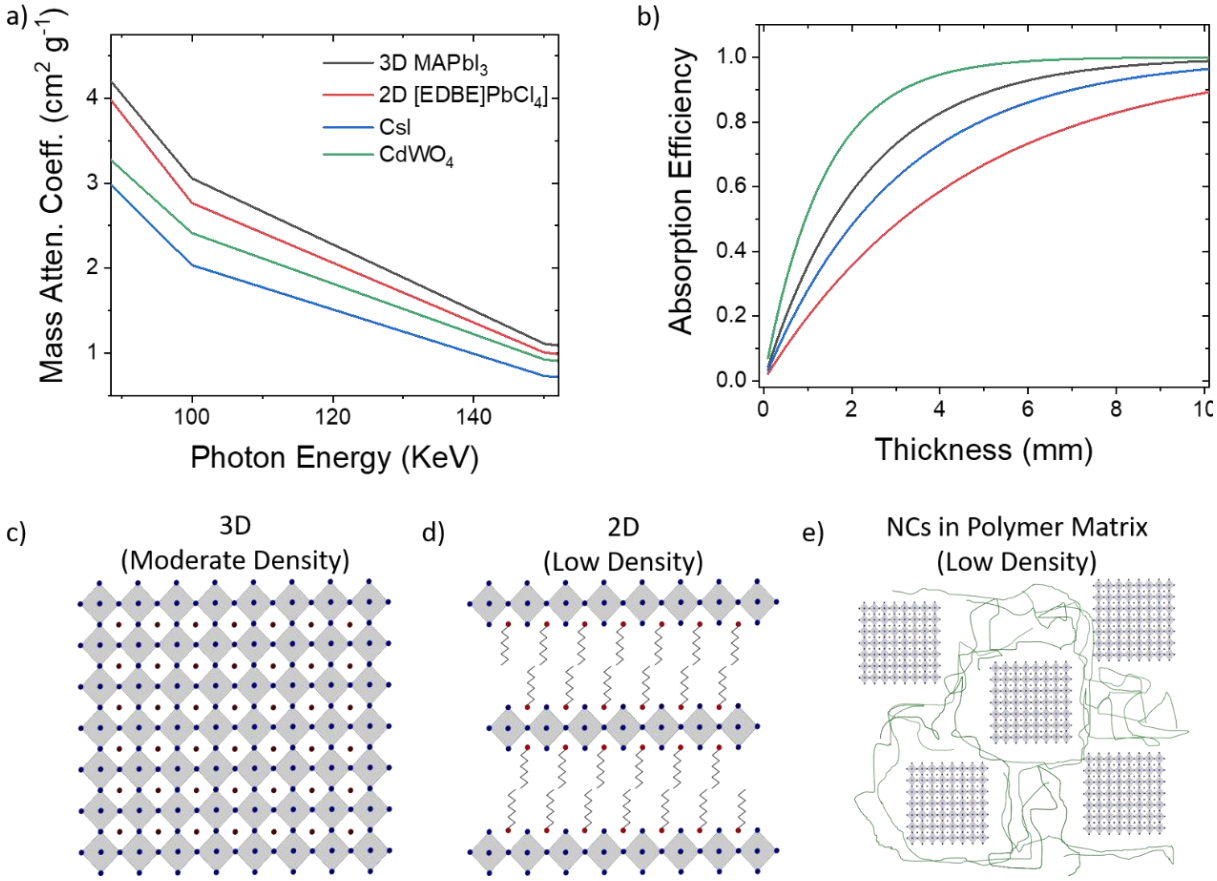

Figure 6.3: Stopping Power of Perovskite Scintillators. *a) Mass attenuation coefficient variation with photon energies relevant to medical imaging, for perovskite scintillators and commercial CsI and $CdWO_4$ materials (Calculated using data obtained from Ref. 19). b) The corresponding absorption efficiency once material density is accounted for at 150 keV. The low efficiency of 2D perovskites to attenuate the incident photons highlights the requirement of high-density materials (note, the legend is common in (a) and (b)). c-e) Crystal structure schematics demonstrating the detrimental effect of reducing perovskite dimensionality on material density by: (d) introducing low-Z organic components as A-site cations, or (e) embedding nanocrystals in a polymer matrix.*

6.3.2 Light Yields

Reports of room temperature light yields in perovskites have thus far been limited to reduced dimensionality systems, either through compositional or physical confinement, and this is proposed to be due to the increase in exciton binding energy preventing thermal quenching of the emissive states at room temperature (Figure 6.4a). 2D perovskites $(C_6H_5(CH_2)_2NH_3)_2PbBr_4$ ($(Phe)PbBr_4$) and $(EDBE)PbCl_4$ have displayed light yields of 10,000[221] and 9,000[54] photons MeV^{-1}, respectively. Similarly, all-inorganic $CsPbBr_3$ systems have displayed RL, with

nanocrystals showing 5x higher emission intensity than $YAlO_3$:Ce systems[98], and nanosheets[338] reporting 21,000 photons MeV^{-1}. In contrast, bulk 3D systems such as $MAPbBr_3$ single crystals, whose growth into large area thick layers is already well documented[253], have yet to display any appreciable scintillation at room temperature[219], with bulk $CsPbBr_3$ emission intensities around four orders of magnitudes lower than $CsPbBr_3$ nanocrystals under the same conditions.[98] The greater exciton binding energy of the nanocrystals (up to 120 meV) compared to bulk perovskite systems (< 15 meV)[339] was reasoned to prevent thermal quenching of the emissive state. A strong temperature dependence of light yield has been found in perovskite materials[340] (Figure 6.4b), allowing bright emission even from 3D systems at low temperatures.[54] Light yields of 90,000 ± 18,000 and 116,000 ± 23,000 photons MeV^{-1} at 77K and 8 K respectively have been demonstrated in $MAPbBr_3$ single crystals[220], consistent with a freezing out of the thermal dissociation of excitons, which when combined with the low trap densities (~10^{10} cm^{-3})[81] promotes efficient radiative decay.

While promising, the room temperature light yields of perovskites are suggestive of losses, and parasitic self-absorption of the emitted photons will limit external emission of the photons (i.e., RL intensities). For example, the intrinsic emission spectrum of direct band gap semiconductors with small Stokes shifts, such as perovskites, overlaps with their absorption spectra, causing significant reabsorption and limiting light yields (Figure 6.4c). Self-absorption in thick perovskite materials was originally studied under optical excitation, where Wenger et al.[341] found that increasing thickness decreases the intensity and redshifts the photoluminescence, through reabsorption particularly of the higher energy photons. The PLQE of 2 mm thick $MAPbBr_3$ crystals was reported to be 6.4% externally despite internal values calculated to be 67%, and reducing this disparity has since become a focus in the scintillator community.

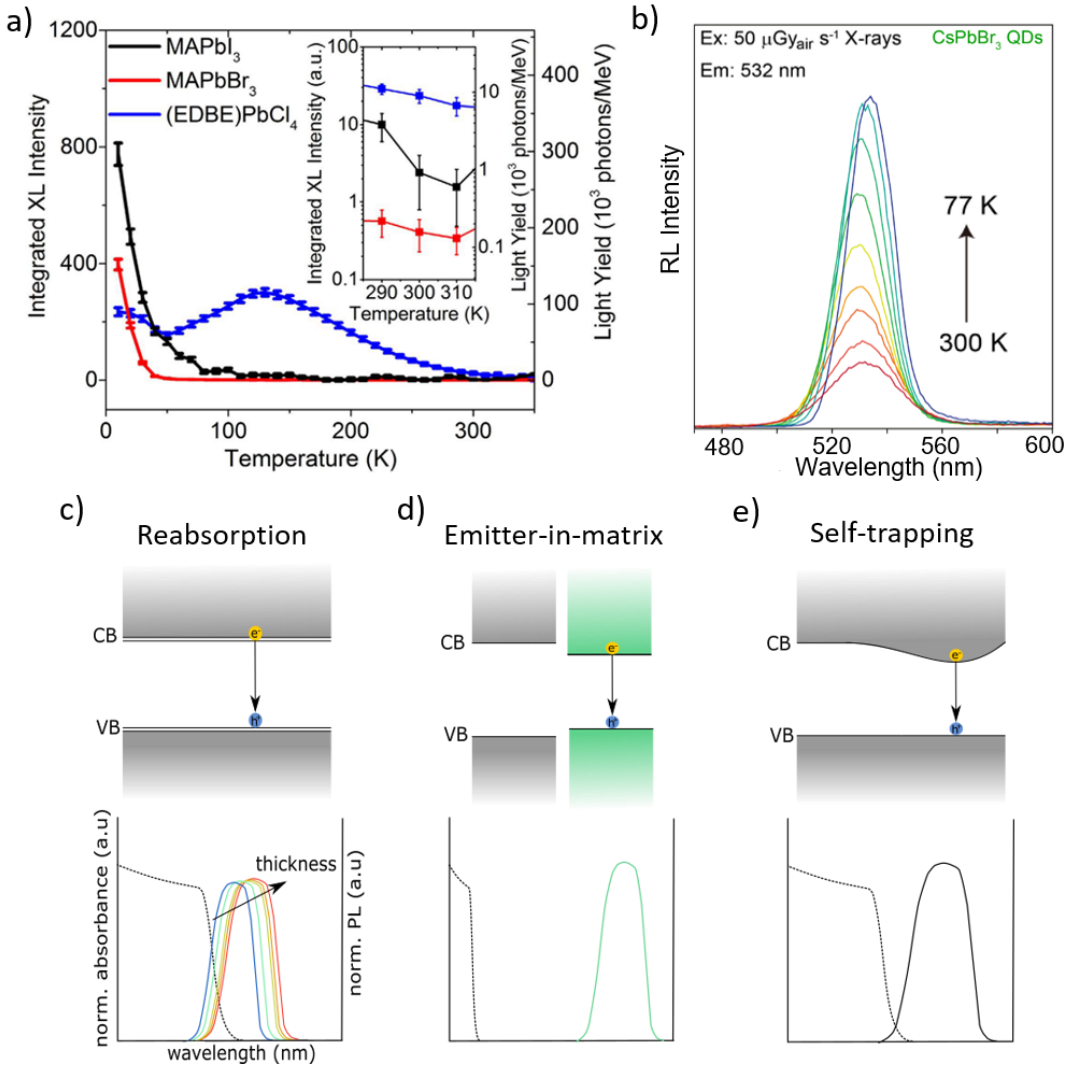

Figure 6.4: Perovskite Scintillator Performance and External Light Yield Challenges. *a) Temperature and dimensionality dependence of perovskite RL from 3D $MAPbX_3$ single crystals, and 2D $(EDBE)PbCl_4$, showing higher room temperature emission from the reduced dimensionality system. Reproduced with permission from Ref. 54. b) Temperature dependence of $CsPbBr_3$ nanocrystal RL. Reproduced with permission from Ref. 98. c-e) Schematics of energy levels and expected absorption (dashed lines) and emission spectra (solid lines), highlighting the self-absorption issue with PVKs and possible solutions. c) Band-to-band emission with significant overlap between the absorption and emission spectra. The normalised emission as thickness increases shows the expected redshift due to reabsorption of the shorter wavelengths. d) Reintroducing the extrinsic mechanism with an emitter-in-matrix system. e) Self-trapped exciton emission with large Stokes shift.*

Solutions to reduce the impact of reabsorption have exploited the embedding of the perovskite emitter within a wide band gap matrix (Figure 6.4d). This includes $CsPbBr_3$ nanocrystals contained in a wide band gap Cs_4PbBr_6 matrix, where the matrix contributes to the stopping power and helps stabilise the emission centres.[228] The strong confinement in the 0D structure yields an exciton binding energy of ~90 meV and, combined with reduced self-absorption, led

to light yields of 64,000 photons MeV^{-1} at room temperature.[229] Similarly, an organic dye with a large Stokes shift has been combined with $CsPbBr_3$ nanocrystals, where efficient sensitisation by the perovskite and emission by the organic component at longer wavelengths[236] minimises reabsorption losses. However, the final device offered only moderate RL intensity, comparable to BGO (8200 photons MeV^{-1}). A similar system was proposed by Ning et al.[342] for visible light conversion, where PbS quantum dots were fabricated within a perovskite, with the NIR emission from the quantum dots shifted well away from the perovskite absorption onset, minimising reabsorption. Localisation and relaxation of emissive species with the lattice can induce a Stokes shift, and negligible self-absorption was demonstrated in 1D structured Rb_2CuBr_3 due to self-trapping of excitons[247] (Figure 6.4e). The exceptional PLQE values of 98.6% translated to approximate light yields of 91,000 photons MeV^{-1}, the highest room temperature value from perovskite scintillators to date. Emission from self-trapped excitons was also seen in the $Cs_2Ag_{0.6}Na_{0.4}In_{1-y}Bi_yCl_6$ double perovskite[237], where the Bi^{3+} doping can be used to tune the radiation stopping power due to its high atomic number. An optimum of 15% loading produced light yields of ~39,000 photons MeV^{-1}. However, these self-trapped excitonic systems are prone to longer decay times on the order of tens of microseconds, with considerable afterglow in Rb_2CuBr_3 of 2.72% at 20 ms, and thus will be suited to fewer applications.

6.3.3 Response Speeds

Perovskite scintillation has been shown to occur very rapidly, with fast decay times presented in literature. $CsPbBr_3$ nanocrystal scintillators demonstrated a short decay time of 44.6 ns under γ-ray excitation[98]. The same material displayed a 5 ns decay time upon UV excitation, with the faster decay potentially due to avoiding the additional excitation and cascade steps in RL,[343] combined with the shorter penetration depth of UV compared to X-rays, exciting the surface. The decay time shortened to 3 ns once combined in a Cs_4PbBr_6 matrix, attributed to additional confinement affects accelerating recombination.[228] A similar $CsPbBr_3$:Cs_4PbBr_6 system has recently offered impressively short RL decays, with a 1.4 and 6.7 ns fast and slow component, showing promise for room temperature fast detection applications.[229] 2D perovskites have displayed rapid room temperature decay times, with $(EDBE)PbCl_4$ demonstrating a single decay component of 7.9 ns from UV-visible excitation[54], and $(Phe)PbBr_4$ has been measured independently to have a dominant decay time of around 10 ns[248,344], offering considerable improvement on current materials (Table 6.1). Studying the scintillation temperature dependence from $MAPbBr_3$ single crystals, Mykhaylyk et al.[220] demonstrated that above 60 K

the emission components retain impressive decay times of 0.1/1 ns respectively, which combined with increased light yields of ~90,000 photons MeV^{-1} at liquid nitrogen temperature make this a prospect for ultrafast timing precision. Similarly, RL decays from $CsPbBr_3$ single crystals reached 1 ns at 7 K, and outperformed LYSO:Ce at resolving a pulsed synchrotron beam.[345] Detector cooling is already a feature in HP-Ge direct detectors, operated at 77 K due to the small material band gap, and so is a commercial possibility for perovskites.

Table 6.1: RL Decay Times of Fast Commercial and Perovskite Scintillators.

Material	Decay Time (ns)	Refs.
CsI:Tl	1000	58
LSO:Ce	40	62
LYSO:Ce	33	223
$LaBr_3$-Ce	15	63
LuI_3-Ce	31/140/1000	346
LuAP:Ce	17	347
BGO	300	348
BaF_2 [a]	0.8/630	349
$CsPbBr_3$ NCs	44.6	98
$CsPbBr_3$ (7 K)	1 (Fast component) [b]	345
$MAPbBr_3$ (77 K)	0.1/1	220
$PhePbBr_4$	9.4	221,248,344
	9.9	
	11 (81%)/36 (18%)/236 (1%)	
$CsPbBr_3$:Cs_4PbBr_6	3 [c]	228,229
	1.4 (88%)/6.7 (12%)	

[a] Low light yields from fast crossover component and slow excitonic emission limit commercial use.

[b] Microsecond background emission component also seen below 70 K that would contribute to afterglow.

[c] Measured with UV excitation. It has been reported that the decay time measured from RL excitation is slower, due to the additional excitation and cascade steps.[343]

6.3.4 Stability

The tolerance of perovskite scintillators to X- and γ-rays has not been studied in detail, though initial results look promising. Reports have demonstrated steady RL intensity under continuous irradiation for several hours in $CsPbBr_3$ nanocrystals[98] and nanosheets (2 hours at 18 μGy s^{-1})[227]. Higher doses have also been tolerated by perovskite scintillators, with $Cs_2Ag_{0.6}Na_{0.4}In_{0.85}Bi_{0.15}Cl_6$ showing no losses after 50 hours and a 34 Gy combined dose[237], whereas 800 Gy reduced the RL intensity of $CsPbBr_3$ nanocrystals with an organic dye to just 85%.[236] Although reductions in light output begin to show at these doses[229] – tridoped $Cs_2Ag_{0.6}Na_{0.4}InCl_6$:$Yb^{3+}$/$Er^{3+}$/$Bi^{3+}$ reduced its RL to 49% after 53 Gy[350] – they still outperform traditional materials, as CsI:Tl emission dropped to 28% after the same dose. An improved understanding of the degradation mechanisms from more focussed studies correlating the effect of the high-energy radiation on both the perovskite material and the scintillation performance would benefit the field enormously. The stability of perovskites in direct detectors may also provide useful understanding in this context. A perovskite-in-polymer membrane system showed negligible current reduction after a total dose of 376.8 Gy (equivalent to 1.88 million chest X-rays)[191] while $MAPbBr_3$ single crystals irradiated with a 230 Gy dose over 10 hours displayed no losses.[351] The retention of charge transport properties would suggest no significant material degradation, which is promising for scintillators.

There are also studies on the effect of high-energy radiation on perovskite solar cells. The importance of efficiency, weight and size have made perovskites a promising prospect for space applications, and as such there is an effort to analyse the tolerance of these materials to the sources of cosmic radiation. γ-ray studies have shown small losses in J_{sc} in mixed-halide systems, due to radiation induced phase segregation[352], similar to the Hoke effect,[353] although the largest losses are due to colour centers in the glass reducing transmittance.[354] The broad quantum efficiency of most photodetectors used in combination with scintillators makes precise tuning of the band gap by alloying different halides to less important than in solar cells, as a result this phase segregation should not impact perovskite indirect detectors. A range of perovskite absorbers were tested by Boldyreva et al., with $MAPbI_3$ displaying remarkable stability after 1 MRad (equivalent to 10 kGy) of γ-ray exposure, attributed to CH_3I and NH_3 undergoing radiation-induced radical chemistry that then self-heal any generated defects.[355] Similarly, $MAPbI_3$ was tested in an energy-converter application, and devices showed no performance degradation after 57 Sv H*(10) γ-ray dose irradiation (equivalent to 57 Gy).[356] The radiation hardness of perovskites has also been shown to extend to protons and electrons,

demonstrating a similar self-healing behaviour after irradiation.[357,358] It is proposed that the lability of the constituent ions in perovskite structures allows any defects formed by the radiation to be removed, limiting and recovering from any damage. In addition, many defects in perovskites introduce only shallow states, and so any radiation induced defects may be benign to operation.[359] The moisture instability of perovskites may require encapsulation in end designs, which may further complicate outcoupling considerations. However, many current materials suffer from hygroscopicity and detector designs often guard against this.[360]

6.4 Improving Scintillator Light Yields: Lessons from Photovoltaics and LEDs

The large cascade of charge carrier generation gives perovskite scintillators high theoretical light yields, but to date recorded values are much lower. Common themes emerge to explain these losses: competing non-radiative recombination processes lowering internal light yields, and outcoupling issues, due to reabsorption preventing efficient light escape. Solutions to these challenges could be found within the field of perovskites for solar cells and LEDs, where maximising radiative efficiency and optoelectronic performance is paramount.

6.4.1 Internal Light Yields

The PLQE, the fraction of photons emitted by a sample relative to the number of photons absorbed, is a common metric used to assess the radiative efficiency of optoelectronic devices. A key difference between RL and PL is the direct excitation of the excited state in PL measurements with photons of energy comparable to the band gap, whereas RL includes the initial interaction of the high-energy ionising radiation followed by the resulting cascade and relaxation steps. As a result, losses in this initial scintillation step are not the focus of PL improvement. The spectra of perovskite emission after visible or X-ray excitation are very similar,[361] albeit typically with a redshift of the RL due to the self-absorption of the higher energy emission that is well documented in thick perovskite samples, suggesting that both PL and RL are likely to originate from the same states. However, the recombination regime and thus carrier lifetime are both strongly dependent on the charge density, therefore the relevant luminescence efficiency metric will depend on the excitation conditions relevant to the application.[362] For example, the PLQE of photovoltaic materials is typically assessed under "1-sun" illumination conditions, which generates an initial charge-carrier density of ~10^{15}–10^{16} cm^{-3} where trap-assisted recombination is the dominant non-radiative process that competes

with the radiative bimolecular component.[362] As a result, research in the solar cell fields has focused on reducing the density of trap states via passivation to improve luminescence yields. However, in operating LED devices, charge densities are typically higher, and non-radiative Auger recombination also needs consideration. In contrast, the lack of standard excitation conditions for radiation detectors, with the incident beam energy and flux depending on the application, combined with the complicated cascade of charge carrier generation for every incident photon, makes it difficult to calculate an expected carrier density regime in scintillators. Auger recombination processes will lead to non-proportional effects in energy resolved detectors at high incident energies.[44] In such cases, high mobility materials have been proposed to rapidly diffuse carriers away from high density regions and ensure radiative recombination competes sufficiently with the non-radiative Auger processes.[363] In addition, it is likely that the large material volume and high trap densities in perovskite scintillators will still allow trap-assisted recombination to contribute to emission losses in many applications. Therefore, applying techniques established to improve PLQE may have benefits in increasing the emission quantum efficiency of the final step in RL, and improve perovskite scintillator light yields.

Removing trap states via passivation is common in perovskite thin films to overcome the high defect densities[79,85], with a wide range of methods shown to raise emission efficiencies, demonstrating internal PLQEs exceeding 95%.[312] Successful approaches include adding passivating agents to the precursor solution,[312,364] chemical post treatment[311,365] and light soaking,[297,366] with species such as phosphate based molecules binding to uncoordinated lead sites,[367] 2D molecules forming well passivated quasi-2D perovskite surfaces,[368] or alkali halides binding excess halide species.[312] In thin film devices, the short penetration depth of UV-visible light and the importance of any interfaces with charge transport layers makes surface defects highly important, and often the target of passivation techniques. However, the increased thickness and deeper charge carrier generation in scintillators makes bulk trap states more important and passivation techniques targeting these bulk traps would be important. Systematic passivation approaches to perovskite scintillators are yet to be reported.

Raising PLQEs by increasing the charge carrier density into the bimolecular regime is another prevalent tactic in solar cells and LEDs. Reducing the material volume in LEDs by decreasing perovskite thickness can allow charge carrier densities to exceed trap-assisted recombination levels[369], but the necessity of thick highly attenuating materials makes this approach impractical for scintillators. An alternative method to increase carrier densities involves the use

of charge carrier funnelling to enhance radiative efficiency. Quasi-2D materials, with n (n>1) layers of PbI_6 octahedra between large organic spacers, contain a mixture of n layered phases, with carrier funnelling to the lowest band gap occurring. PLQEs above 10% at low excitation fluences of 6 mW cm^{-2} resulted from the high carrier concentrations (~ 10^{16} cm^{-3}) within these low band gap phases, translating into efficient LED devices.[370] The lower energy emission from the smallest band gap would also contribute to reduced reabsorption. However, the compositional engineering of these phases is complex, and can introduce additional defects and grain boundaries that limit radiative efficiency and require additional passivation.[367] This may add complications when scaling up to the large volume materials needed in radiation detection. A solution may come from the finding that mixed halide perovskites can self-organise into band gap gradients, an effect that can be stabilised by cation selection, to achieve similar charge carrier concentration but with greater potential for upscaling.[371] More work is needed to control such gradients and implement into scintillators.

6.4.2 Light Management and Outcoupling

Maximising the extraction of light from the scintillator is a key area of research, largely due to the parasitic self-absorption of emitted light by perovskites. Solutions are being developed, such as introducing a transfer step to a redshifted emission centre or engineering materials with large Stokes shifts by the self-trapping of emissive moieties. Reintroducing an extrinsic emitter system nullifies the inherent advantages of perovskite scintillators. Firstly, wide band gap hosts require an additional charge carrier transfer step, and secondly the light emission from the scintillator is restricted to longer wavelengths, limiting the compatibility with standard visible photodetectors. Therefore, designing perovskite scintillators with Stokes shifts should provide the more fruitful approach to retain the advantages of perovskites.

We demonstrate this by employing Cs_2ZrBr_6 nanocrystal films as scintillators. The PL absorption and emission spectra of these materials shows a large Stokes shift (Figure 6.5a), suggestive of emission from self-trapped excitons, which should enable bright scintillation without reabsorption.[372] A thick film of these nanocrystals was deposited by repeated drop castings of a colloidal suspension (Figure 6.5b), and the X-ray induced emission measured. The RL spectrum (Figure 6.5a) displays an emission peak of ~540 nm, which is optimal for pixelated silicon photodetectors for imaging applications. Importantly, there is minimal redshifting between the PL and RL spectra, indicative of a reabsorption-free scintillator.[341] This reabsorption can reduce the externally emitted light, and the absence of this effect in these Cs_2ZrBr_6 systems is favourable for obtaining high light yields. To estimate the light yields, the

emission is compared to a reference material of known output. BGO (light yield 8200 photons MeV^{-1})[252] was selected as a suitable reference, due to its spectral similarity with the perovskite emission (See Chapter 3). A relative light yield of 3700 photons MeV^{-1} was produced from the Cs_2ZrBr_6 nanocrystal scintillator films.

The response times from Cs_2ZrBr_6 nanocrystals are suited to high frame-rate imaging applications, with RL decay measurements (Figure 6.5c) revealing a faster 854 ns decay component combined with a slower component of 3940 ns. Importantly, these systems show virtually no afterglow, with 0.1% relative emission remaining 40 μs after initial excitation. Afterglow is problematic for tomographic applications, where temporal crosstalk degrades the image quality.[373] Persistent RL remaining after milliseconds is unwanted, as CT imaging rates reach up to 5 kHz.[49] The minimal afterglow in Cs_2ZrBr_6 compares favourably to other reabsorption-free perovskite scintillators in the literature, such as Rb_2CuBr_3, which have >2% emission remaining after 20 ms, as well as commercial CsI:Tl (>0.5% after 3 ms).[58,247] Overall, Cs_2ZrBr_6 nanocrystals are an ideal candidate for realising the promising theoretical performance of intrinsic perovskite scintillators.

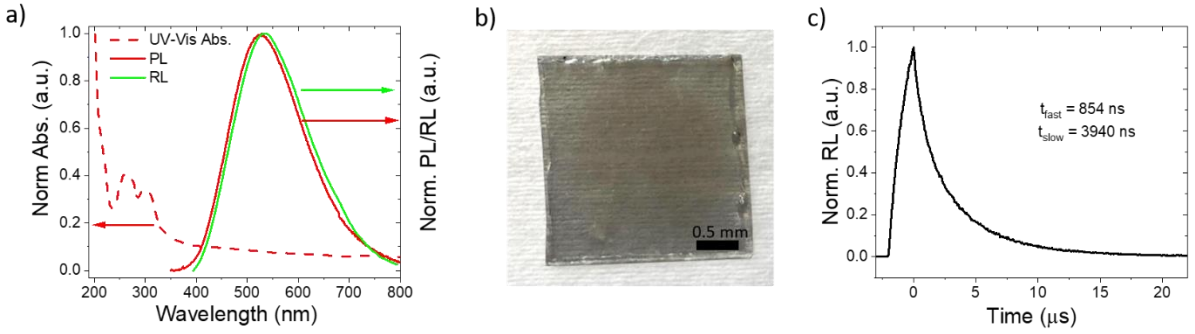

Figure* 6.5*: Performance of Cs_2ZrBr_6 Nanocrystal Scintillators. *a) UV-visible absorption (dashed) and PL/RL (solid) spectra of Cs_2ZrBr_6 films. PL was stimulated by 300 nm light, RL was stimulated by an X-ray tube operating at 60 kV tube voltage and 100 μA tube current. b) Image of a drop-casted Cs_2ZrBr_6 thick film. c) RL decay stimulated by a pulsed X-ray (2 μs pulse width, peak X-ray energy ~8 keV, maximum 40 kV). UV-visible and PL spectra obtained by Anna Abfalterer.*

The contribution of photon recycling, and the possibility of photons escaping after multiple emission and reabsorption events, has not yet been considered in perovskite scintillators. Photon recycling has been demonstrated in perovskite solar cells, allowing high excitation densities to increase quasi-fermi-level-splitting, and subsequently produce high V_{oc} values.[374] Photon recycling has also been calculated to contribute >70% of light emission in state-of-the-art perovskite LEDs[375], and is partly responsible for their outstanding EQEs, by giving photons

approaching the surface of the perovskite outside the cone of emission another chance of escape. The extreme thicknesses required in scintillating materials compared to photovoltaic and LED systems make photon recycling considerations all the more relevant. It has been shown that the number of photon recycling events increases with thickness in a solar cell operated at maximum power point, and this would increase further in a scintillator system due to the absence of charge carrier collection.[376] However, while many recycling events may occur in scintillators, extracting sufficient numbers of photons in the forward direction from samples of relevant thicknesses may still prove difficult without considerations for shifting the emission energies away from the absorption edge of the majority of the material. Even with a straight-line propagation of reemitted light, the optical extinction length of the scintillated light would require around 385 photon recycling events to travel across a 270 μm $CsPbBr_3$:Cs_4PbBr_6 film.[377] Internal PLQEs of 95% would still result in the quenching of almost all emission, even with this conservative estimation of the number of recycling events. As a result, to achieve high light yields in perovskite scintillators, preventing reabsorption is an essential design feature and this must be balanced with the desired properties of the detector systems, e.g. retaining fast emission.

While photon recycling allows additional attempts at emission, better outcoupling increases the probability of emitted photons escaping the scintillator and reaching the photodetector. This is achievable using photonic structures, which have recently emerged as a potential concept to improve the performance of existing high refractive index scintillators.[378–381] Increasing the cone of emission will improve the light yields of scintillators, with simulations suggesting 90-110% enhancements[379], and increase the timing resolution, by increasing the likelihood that light is emitted at the first instance it meets the scintillator/detector interface, increasing the light yield at early times.[378] Spatial resolution would also improve through decreased lateral distances between the point of emission and detection by the photodetector. Better optical coupling between the scintillator and detector can provide similar performance improvements, possible in perovskite devices by direct deposition onto photodetectors (discussed in Section 6.5.2) or on to fibre-optic plate structures. These performance benefits are of relevance to perovskite scintillators yet such approaches remain unexplored. There have been examples of photonic structures improving the performance of perovskite lasers[382,383] and also coloured solar cells.[384] Extending this to scintillators would be a fruitful prospect, and should prove simpler due to the absence of any additional transport layers on the surface, or by directly patterning the perovskite itself.

6.5 Applications and Opportunities

Besides the exceptional emission properties, perovskite materials also have unique features, such as band gap tunability and solution deposition, which provide further advantages over existing materials and potential opportunities for novel detector applications.

6.5.1 Tunable Emission

By varying the constituent ions and the material dimensionality during synthesis, the properties of perovskites can be tuned. This allows the band gap to be controlled, and consequently the emission wavelength can be selected to suit the required photodetector for applications. Important photodetectors are photomultiplier tubes (PMTs) and silicon photomultipliers (SiPMs) for high sensitivity and photon counting modes, and silicon detectors in imaging arrays (CCDs/CMOS). $CsPbX_3$ nanocrystals, as one example, can be optimised to each of these applications by varying the halide ion, with $CsPbCl_3$ optimised to ~400 nm for bi-alkali photocathode PMTs, while $CsPbBr_3$ would suit the peak sensitivity of silicon detectors (~550 nm). The large degree of band gap tuning offered by perovskites has other commercial applications, for example, by adding spectral information onto images with multispectral scintillators. This would be applicable to energy-selective CT scanning; where traditional CT displays a contrast image based purely on the different attenuation of materials, spectral CT collects the energy dependence of the attenuation by splitting the detector into two scintillators, a top layer optimised to soft radiation and a bottom layer for hard radiation.[385] This provides information on the atomic number of the tissues in the scan, and is especially useful when radiocontrast agents such as iodine are added. It also opens up the possibility of use in applications which traditionally use dual energy X-ray absorptivity (known as DEXA), such as bone densitometry. Utilising the range of perovskite scintillators in a multispectral system was proposed by Sytnyk et al.[386] who proposed a four-layer stack of perovskite materials, with each layer utilising a different perovskite in order to provide a greater spectral resolution. Each layer is optimised in terms of stopping power to a range of incident X-ray energies, and each emits at a different wavelength. When combined with a spectrally resolved detector, or a a-Si:H array with colour filters, this could enhance current ionising radiation imaging.

6.5.2 Low-Temperature Fabrication and Flexible Detection

A desirable feature of perovskites compared to other scintillator materials is their simple fabrication, retaining exceptional optoelectronic properties when deposited from solution.

Solution processing and low-temperature material growth simplifies film fabrication, reduces production costs and enables compatibility with a range of substrates and electronics. It allows growth directly onto photodetectors or fibre-optic plates, improving optical coupling with the emitting scintillator, with demonstrations on pixelated a-Si photodiode arrays for imaging[98] and silicon photomultipliers[249] without optical grease. Existing scintillators, such as NaI:Tl and BGO for spectroscopy applications, are grown in single crystal form at high temperatures (>1700 ^{o}C) with high production costs. CsI:Tl for imaging screens involves an expensive vacuum evaporation growth to obtain its needle-like morphology. GOS phosphors are a cheaper alternative, but at a reduced sensitivity and spatial resolution. Perovskite synthesis has shown to be easily controlled to produce the structures required for detector applications. Perovskite single crystals can be quickly grown using inverse temperature crystallisation, utilising the reduction in solubility at higher temperatures displayed in some solvents[121,387], and the growth shown to be influenced by the shape of the container.[121] This allows both large area and sub-micrometre crystals to be produced.[388–390] Furthermore, the control of perovskite morphology via different processing routes could allow for improved high-resolution imaging, and a low-cost alternative to CsI:Tl. Grain size engineering[391,392] or optimisation of nanocrystal films to further reduce light scattering and optical crosstalk may enable further advances in MTF values.

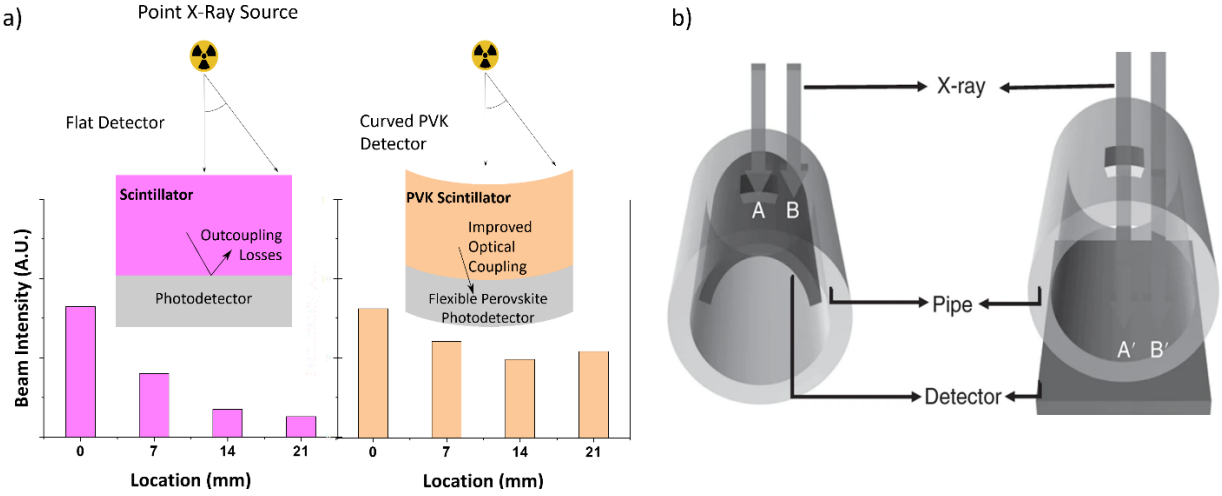

Figure 6.6: Unique Functionality with Flexible Perovskite Scintillators*. a) Overcoming uneven X-ray intensity distributions from point sources with flexible perovskite (PVK) scintillators and photodetectors. Scintillators can be combined with flexible perovskite photodetectors, which can simplify fabrication of the full indirect detector system and potentially improve light outcoupling from scintillator to photodetector. Adapted with permission from Ref. 191. b) Flexible detectors conforming to the inside of a pipe allow lower energy radiation and consequently thinner scintillators with enhanced spatial resolution. Reproduced with permission from Ref. 191.*

Low-temperature deposition also enables compatibility with flexible substrates, resulting in a detector that can conform to surfaces, useful in medical diagnostics and non-destructive testing.[393] The importance of flexible radiation detectors was well explained by Zhao et al.[191], whereby intensity differences between pixels in the centres and edges of the detector from point X-ray sources can result in imaging errors and misdiagnosis (Figure 6.6a).[394] Substrate flexibility also allows better non-destructive industrial imaging by being placed inside of objects and thus requiring softer beam energies and thinner scintillators (Figure 6.6b). Flexible perovskite devices are well developed,[260] with flexible solar cells exceeding 19% power conversion efficiency,[395] and flexible direct X-ray detectors demonstrated.[396–398] Retaining flexibility with increasing perovskite thickness is a challenge, and a perovskite in a porous nylon membrane, developed for flexible direct X-ray detection, demonstrated 2/3 mm minimum bending radii in 130/240 μm thick devices, respectively. However, unlike direct detectors and solar cells, which require charge transport considerations and compatible transport layers and electrodes,[399] scintillators are much simpler, making the prospect of developing a flexible scintillator promising. Alternate uses of flexibility could include accurately measuring dose delivery with detectors conforming to body parts. Despite lead-based perovskite scintillators being exempt from EU regulations on hazardous substances in electronic equipment (RoHS),[400] applications requiring closer contact with the human body may require less toxic analogues. Alternative metals such as copper, europium, bismuth and tin have all been integrated into perovskite-like structures and demonstrated scintillation.[237,239,245,247,401–403] Lead-free indirect detectors have demonstrated exceptional performance, and currently present the highest light yields of perovskite materials to date (Rb_2CuBr_3 ~91,000 photons MeV^{-1},[247] Cs_4EuX_6 ~78,000 photons MeV^{-1} [245]). However, the decrease in stopping power when replacing lead with a lower atomic number element must be considered.

There are significant cost reductions in the material production of perovskites compared to commercial scintillator materials, as cheap and earth-abundant precursor materials, combined with low-temperature (<150 ^oC) and ambient processing conditions, contribute to inexpensive production. An analysis was presented by Cao et al.[228] in their growth of $CsPbBr_3$:Cs_4PbBr_6, suggesting the cost of a crude ingot was similar to CsI:Tl, while considerable savings up to a factor of 2000% can be made over Ce^{3+} doped materials (LYSO, YAG, YAP used for spectroscopic applications) without the concerns on the supply and extraction of rare-earth materials.[404] High-throughput production of perovskites have also been projected to bring costs

down further in other areas, for example in photovoltaics,[405] where scalable techniques, such as slot-die coating,[406] doctor blading,[189] inkjet printing[192] and thermal evaporation[407] have all been demonstrated. It was estimated that detectors for CT, SPECT (single-photon emission computed tomography) and high-energy physics require over 70,000 kg of scintillator material annually at today's usage alone,[408] emphasising the importance on the scalability of production.

6.5.3 All-Perovskite Indirect Detectors

The considerable development of perovskite production techniques demonstrates another significant feature unique to perovskites that will suit their commercial success: the wide range of other perovskite optoelectronic devices vying for market penetration. The difficulties in advancing from material discovery to large scale production is often the largest hurdle for new scintillators, due to difficulty in large-area growth and understanding the role of defects in relation to performance.[409] It is of great advantage that perovskites share these challenges between multiple prolific fields, which should ensure rapid transition from the academic lab to commercial success. Further, the simultaneous development of perovskite photodetectors can be specifically exploited for all-perovskite indirect detectors.[410] The field of perovskite photodetectors is very active, with impressive detectivities and response times[411] and high gain factors over 10^5 [21,412,413] suiting high sensitivity requirements. Flexible perovskite photodetector arrays have already been demonstrated,[261] highlighting the potential for an all-perovskite system to offer functionality beyond that of current materials, specifically for PET detectors. From a commercial perspective, these devices would also simplify detector fabrication, and could overcome outcoupling problems with refractive index matching to reduce internally reflected RL. Self-powered photodetectors[37,150,414] would enable greater portability by avoiding the need for bulky power supplies, improving access to radiation detector systems. This is relevant in healthcare, where patients may not have access to hospitals, as well as industrial radiography and mobile security, in conjunction with small and portable radionuclide radiation sources.

6.5.4 Additional PET Functionality

An enormous performance advantage of perovskite scintillators over current materials is their rapid emission times, which can improve detector timing resolution. Fast emission is required in PET detectors, and exceeding the response times of the currently used scintillators can enable additional functionality with time-of-flight PET (TOF-PET). Traditional PET works using a radioactive tracer, designed to emit a pair of antiparallel 511 keV photons upon positron decay,

to image and monitor biological pathways in the body (Figure 6.7a). The pair of X-ray photons is then coincidently detected by a ring of scintillator detectors. The position of the two photons will then produce a line of response along which the annihilation occurred, and building up enough detection events produces an image. The desirable attributes of a PET detector are introduced in Table 2.4, and currently BGO, LSO and LYSO are commercially used in such systems. By adding additional timing information, the point of emission along the line of response can be known, which can improve the signal-to-noise ratio of the system, especially in full body scans.[415] The important parameter in TOF detectors is the timing resolution of the whole detector system, and for scintillator devices this is strongly dependent on the decay time and the light yield of the emission.[416] A timing resolution of around 10 ps FWHM is the target, as this will allow a 1.5 mm confidence window of the interaction along the line of response.[44] To achieve this, scintillator decay times below 1 ns, and a light yield of 10,000 photons ns^{-1}, are required.[417] This has already shown to be possible in cooled perovskite single crystals[220], which may enable deployment in this role (Figures 6.7b and c); additional work towards fast, room temperature emitters will be further enabling.

Perovskite based detectors can also improve the spatial resolution of PET scanners by adding depth-of-interaction (DOI) information. The penetration of 511 keV photons requires long scintillator crystals which limits the spatial resolution, and causes parallax errors from off-centre photons not approaching the scintillator perpendicularly.[418] This is particularly problematic in small ring systems. Adding depth information is possible with the wide range of perovskite scintillator materials, with layers of two or more detector materials with different decay times or emission wavelengths, which can be distinguished by the photodetector (Figure 6.7d). Alternatively, it could be possible to use the self-absorption of perovskites and the associated spectral change to determine the depth-of-interaction. With an accurate understanding of the optical properties of the crystal, the increased redshifting as a function of interaction depth would demonstrate the position of absorption, combined with a hyperspectral camera (Figure 6.7e). Overall, there is a range of possibilities for the unique properties of perovskites to improve on current PET systems, demonstrating the commercial potential of the material.

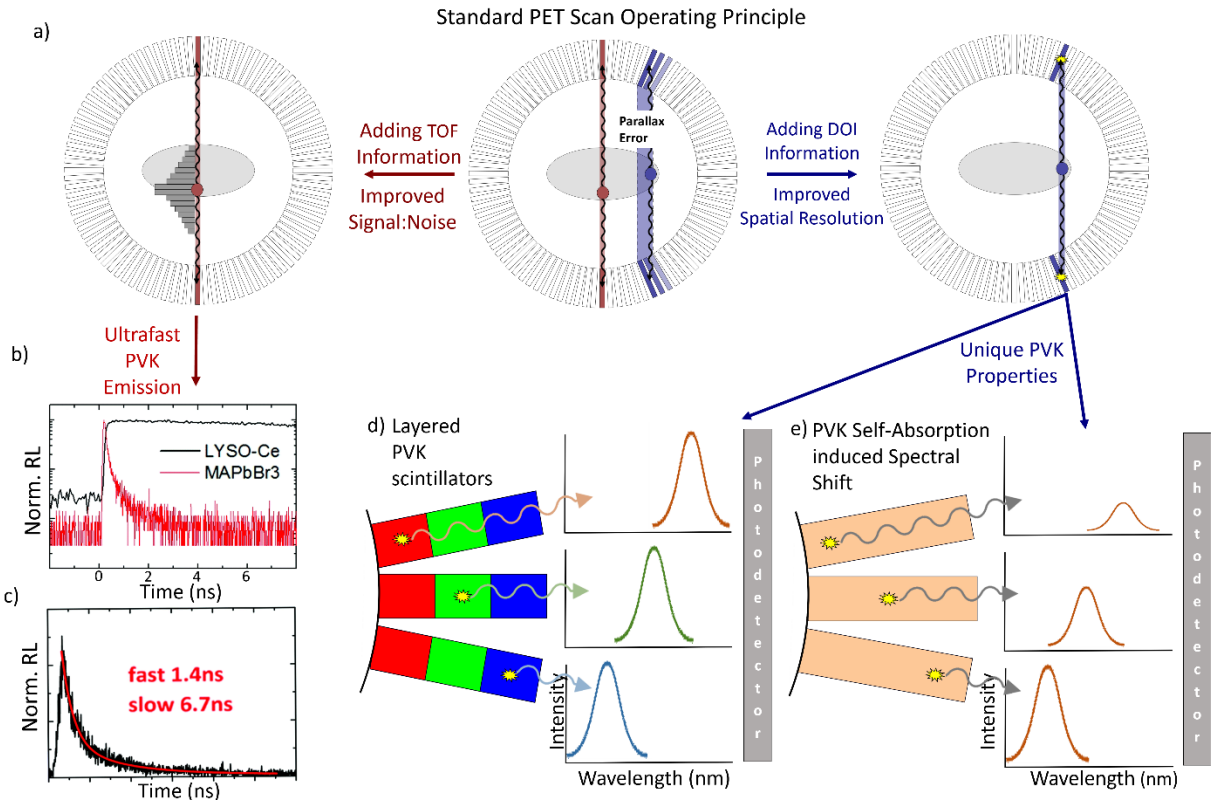

Figure 6.7: Additional PET Functionality with Perovskite Scintillators. *a) The operating principle and existing issues of PET (centre) with parallax errors from off-centre detector line of response. Adding TOF information (left) provides information on the interaction position along the line of response, and depth information (right) increases spatial resolution. b-c) Demonstrations of ultrafast perovskite (PVK) scintillation to provide TOF information. b) is reproduced from Ref. 220, published by The Royal Society of Chemistry and c) is reproduced from Ref. 229 with permission from The Royal Society of Chemistry. d-e) Utilising perovskites to add depth information by d) layering different band gap materials and e) exploiting the spectral change from RL self-absorption.*

6.6 Conclusions

Owing to their intrinsic scintillation, combined with novel material properties, perovskites have the potential to increase the functionality of indirect detectors beyond current possibilities. The exceptional reported light yields and fast emission decay times holds promise for many applications, especially TOF systems, while the unique features of perovskite materials expands the range of systems in which they can be utilised, from flexible systems to multispectral layered detectors. Furthermore, a low-cost and simple fabrication may enable cost savings over existing materials, with the considerable simultaneous research on these materials for other optoelectronic applications relaxing the expected strain of upscaling to commercial levels. Despite admirable progress in a short time, there remains enormous room to develop these materials, primarily by reducing the disparity between experimental and

maximum theoretical light yields, and the lack of application-specific degradation studies. Engineering materials with greater Stokes shifts, such as Cs_2ZrBr_6 nanocrystals, lowering trap densities and/or controlling carrier density and recombination sites will bring improvements in photon outcoupling and luminescence yields. Further advances in other perovskite light emitting applications will feedback to further improve their scintillator performance. The promising radiation hardness and even self-healing already demonstrated in preliminary studies, combined with the carefully controlled end-use environments, means the use of halide perovskites as scintillator detectors will not be far from commercial application.

Chapter 7

Perovskite Direct X-Ray Detectors: Characterisation and Unique Device Design

In this chapter, we report an approach to overcome the inherent limitations of direct X-ray detectors through the design of novel device structures. Perovskites are utilised as the X-ray sensitive material, and we demonstrate a method to pattern the perovskite during its growth. This technique generates a favourable semiconductor morphology that enables deposition directly into detector appropriate structures and arrays. Concurrently to the development of devices, an experimental set-up and characterisation procedure was designed to assess the performance of X-ray detectors.

Device A utilised perovskite pellets produced by Dominik Kubicki. Device B was fabricated by Ganbaatar Tumen-Ulzii. Optical depth trench substrates were fabricated by Jack Alexander-Webber based upon patterns designed by the author of this thesis. Trench substrates were filled with perovskites by the author of this thesis, initially using a drop casting method developed by Alice Dearle.[251] Evaporating perovskite onto trench substrates was performed by Yu-Hsien Chiang. Methods to fabricate the X-ray depth substrates were proposed by Lee Robinson, based upon structures designed by the author of this thesis. All other experiments and raw data analysis were carried out by the author of this thesis.

7.1 Introduction

The direct detection of X-rays by semiconductors utilises the X-ray induced current or voltage to sense the incident radiation, similar to the detection of visible light by photodiodes and

photoconductors. However, the long penetration depth of X-rays makes their detection more difficult than visible photons. Thick absorbers are required in X-ray detectors, often exceeding millimetres, and the collection of the X-ray generated charge carriers across these distances is highly challenging for semiconductors. Thus, the direct mechanism is only suitable before the absorption depth exceeds the distances of efficient carrier collection. As a result, direct detectors are restricted to low-energy applications, for example ~20 keV mammography photons, and higher energies are detected by an indirect system (see Chapter 6 for the progress of perovskite scintillators). The two-step mechanism of indirect detection lowers detection performance, especially image resolution, due to inefficiencies in the scintillation process. Therefore, designing direct X-ray systems which can overcome their limitations and detect high-energy X-ray photons would revolutionise the ways in which X-ray are used.

Here, an existing method to deposit perovskites from solution into patterns and form a highly crystalline material is utilised.[251] The selective perovskite growth is a result of device design, with etched regions of exposed SiO_2, referred to as trenches, controlling where the deposition occurs. The original devices, shown in Figure 7.1a-c, are adapted to produce a novel device structure for the detection of X-ray photons. The benefits of the device structure are expected to be twofold: advancing the detector performance, through a unique operating mechanism and favourable perovskite morphology, as well as improving the fabrication of devices with a fast and selective semiconductor deposition. (Figure 7.1d).

The anticipated X-ray detection performance enhancements are a result of the unique device structure (Figure 7.1e). Lateral contacts decouple the X-ray generation and charge carrier collection dimensions, ensuring the perovskite can be thick enough to absorb X-rays, without introducing constraints on the carrier transport. This was theoretically proposed by Mescher et al., who modelled improvements in detector performance in a similar structure.[215] Moreover, the absence of a top contact in this structure prevents any losses of sensitivity through parasitic absorption. The improved material quality grown in the trenches will also provide performance benefits (Figure 7.1c). The sensitivity of perovskite direct detectors is correlated with the carrier transport lengths, often quantified by the mobility-lifetime product. The absence of grain boundaries improves the carrier transport in single crystalline perovskites compared to their polycrystalline counterparts,[80,81] and as a result, single crystalline perovskites have been more successful in X-ray detectors.[78,181,184,419–421] The trench structures generate a perovskite morphology with a low density of visible grain boundaries compared to polycrystalline films, which can be exploited to enhance detector sensitivity.

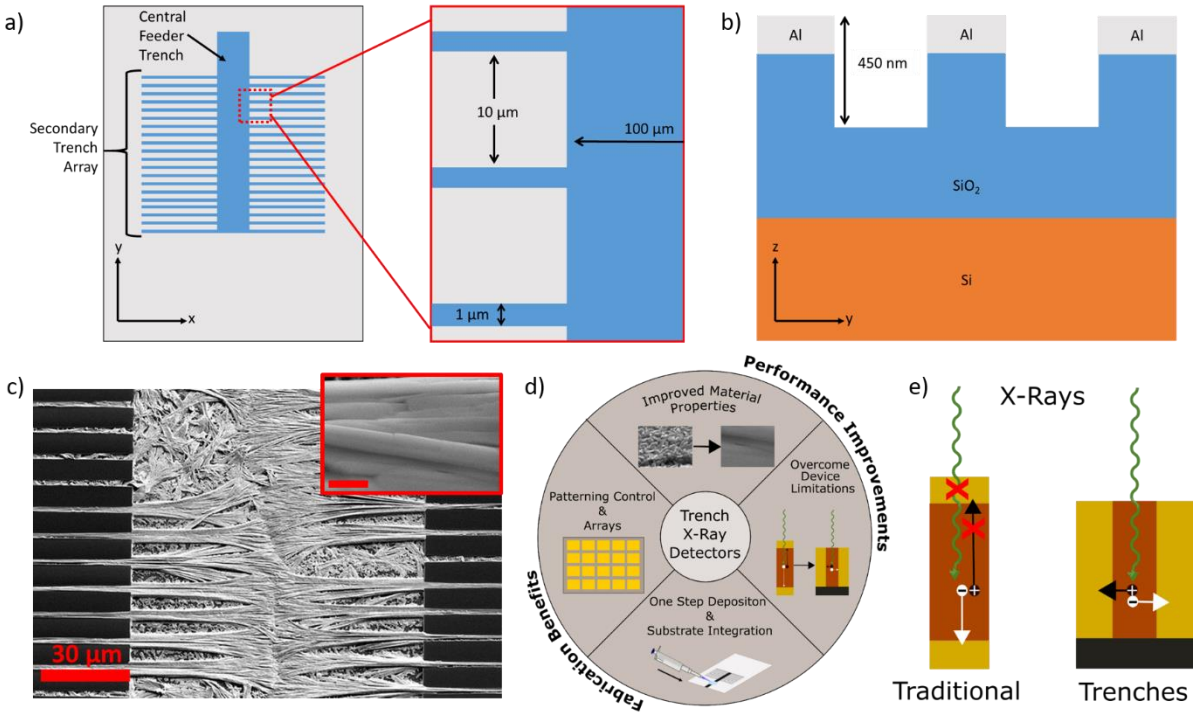

Figure 7.1: Trench Substrates and Concept. *a) and b) Schematics of the original trench substrates used at the beginning of this project. The grey represents the aluminium top surface, and the blue represents the etched out trenches, exposing the SiO_2 layer beneath. a) Top down view b) Side on view. c) The original perovskite growth in the minor trenches and the orientated growth back into the main trench. Inset shows the low density of grain boundaries (scale bar 1 µm). d) Summary of the advantages of trench based X-ray detectors, improving performance and fabrication. e) Overcoming the inherent limitations of traditional direct detectors (left), namely the long carrier transport distances and top contact parasitic absorption, with trench based lateral detectors (right). Figures a-c adapted from Ref. 251 with permission.*

The trench structures also overcome the fabrication issues currently facing the commercialisation of perovskite single crystal X-ray detectors. Growing single crystals is time consuming (requiring several hours to days), incompatible with substrates, and only makes small single pixels (up to tens of cubic centimetres).[38] The orientation and patterning of perovskites by the trench substrates offers a solution to all these issues. As growth is facilitated by solvent evaporation, and deposition is performed aerobically at room temperature, the perovskite deposition time is short (completed within minutes). Incompatibility of single crystals with substrates makes integration into devices challenging, and is overcome here by direct growth into trench substrates with electrodes prefabricated, offering a one-step deposition with no further processing. Lastly, the pattern of the trenches can be designed, allowing control of the device structures and enabling arrays of pixels that could be utilised in imagers. These reasons underpin the motivations of this project, and the proposed device

structure demonstrates a proof-of-principle to overcome the limitations currently facing direct detectors.

Alongside the development of direct devices, a characterisation set-up for the measurement of direct X-ray detectors was developed, in order to measure the devices under development. By utilising test perovskite devices, with photodiode and photoconductor structures, experimental procedures to quantify the key detector metrics were established.

7.2 Development of X-Ray Detector Characterisation Techniques

The nature of X-rays brings additional challenges to detector characterisation compared to visible light. The generation of X-rays is more difficult than optical photons, and subsequently the control over the radiation energy and intensity is more limited. Also, the damaging properties of the ionising radiation brings added safety and stability considerations for experiments. In this section, an experimental set-up specialised to quantify direct X-ray detector performance is produced. Measurement procedures to generate the key figures of merit are also proposed, accounting for any specific requirements that perovskite devices present.

7.2.1 X-Ray Source Considerations

In order to assess the X-ray detection performance of detectors, a source of X-rays is required. A key consideration of the source is its emission spectrum, and to characterise detectors, the source must generate X-rays of similar energy and intensity to that used in the planned application. There are three main sources of X-ray radiation that could be used for experiments: synchrotron radiation, radioactive isotopes and X-ray tubes. Synchrotron radiation is generated at specialised particle accelerators, whereby radiation is emitted by a particle beam accelerated through a closed loop circuit. The X-rays produced are extremely intense, highly collimated, and allow control over the beam energy. However, these are only available at central facilities, and thus would not be applicable for day-to-day testing. Radioactive isotopes, both natural and manmade, can emit energy in the form of X- and γ-rays, or alpha and beta particles. The emission energies of these sources are fixed, with the energy of some sources relevant to X-ray imaging. Some applications require the specific detection of radioisotopes, e.g. nuclear medicine, which uses the 140 kV emission of technetium-99m for single-photon emission computed tomography (SPECT). This radionuclide would be an ideal source for developing detectors for SPECT systems. However, the lack of control over the emission properties of radioisotope sources makes them unsuitable in determining the general detection capabilities

of an X-ray detector. In addition, the safety concerns of a constantly emitting radioactive source, without an existing dedicated laboratory, made the use of radionuclides impractical.

X-rays are also generated using an X-ray tube, which offers the advantages of being small and practical for in-house laboratory equipment, whilst allowing control of the X-ray energy and intensity. Importantly, X-ray tubes are the source in many X-ray applications, and so logically, detectors should be assessed by their ability to detect these radiations. Radiation is generated in an X-ray tube via the impact of high energy electrons hitting a metal anode target, and a schematic of this process is shown in Figure 7.2a. Electrons are generated from a cathode via thermionic emission, and then accelerated towards an anode target by an accelerating voltage. Although the majority of energy from the electrons is lost as heat, a small fraction is converted to X-rays. The spectrum of radiation generated by X-ray tubes is a superposition of a continuous bremsstrahlung emission spectrum (from accelerated electron – anode nuclei interactions) and characteristic emission lines (from accelerated electron – anode electron interactions, Figure 7.2b). The bremsstrahlung emission spectrum is controlled by the accelerating voltage of the tube, with a max photon energy (keV) equal to the tube voltage (kV), while the characteristic emission energies are specific to the anode material.

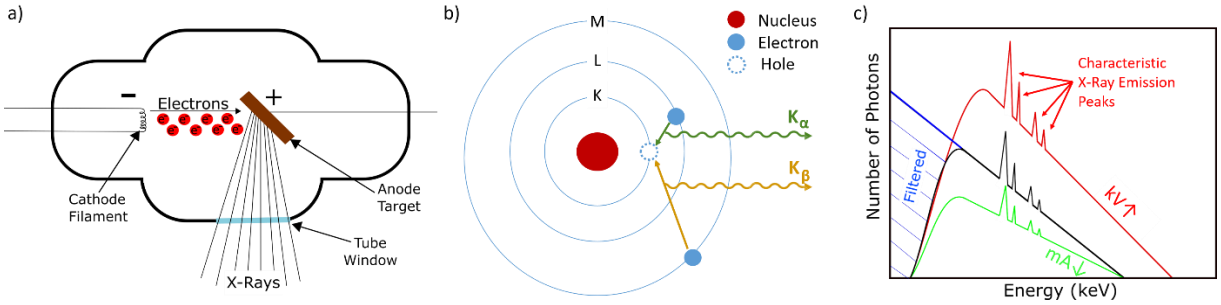

***Figure 7.2: X-Ray Tubes**. a) Schematic of X-ray tube operation. b) Origins of characteristic X-rays. Core anode electrons are emitted as photoelectrons by the accelerated electrons, and filling of the vacancy by higher shell electrons emits characteristic X-rays. The fixed transition energies for each element make the characteristic photons specific to the anode material. c) Schematic of the control over the spectrum with an X-ray tube. The spectrum is altered by increasing the accelerating voltage (kV, red) or reducing the tube current (mA, green). The low energy X-rays are filtered out by the X-ray tube itself, or with additional filtration.*

X-ray tubes provide control over the photon energy and intensity through four variables: accelerating tube voltage (kV), tube current (mA), anode target material and filtration. The influence of these parameters is shown in Figure 7.2c. This control is convenient for detector analysis, as it allows the performance to be measured under a range of X-ray conditions. Increasing the accelerating voltage raises the maximum photon energy and the beam intensity,

and changing the anode material will change the characteristic emission energies, demonstrating the control over the spectrum of X-rays. Filtration can also alter the X-ray spectrum. The X-ray tube itself (for example the anode and glass window) will absorb and filter out the lower energies, typically less than 20 kV, from the spectra. Additional filtration can also remove a greater component of the low-energy spectra, and reduce the overall intensity. Aluminium filters are commonly used, and have advantages in medical imaging as low-energy X-rays are significantly absorbed by the patient, without contributing to the image. This increases the dose administered to the patient, to no diagnostic advantage, and so removing these low-energy components reduces the corresponding risk of the procedure. In contrast, the tube current only influences the intensity of the X-ray beam.

As detectors were developed with a focus on imaging applications, an X-ray source that can generate radiation similar to that used in these scenarios was essential; spanning the 40 kV used in mammography up to ~160 kV for high-energy CT scans. Control over the tube parameters, was also required, as this allows the X-ray spectrum and intensity to be manipulated. A source that can move forwards and backwards would provide additional means to tune the X-ray intensity. X-ray tubes are a point source, making the area covered by the emission at a fixed point, and corresponding fluence, proportional to the inverse square of the distance from the source. For example, doubling the source – sample distance will quarter the intensity. Another practical consideration is for the source to have ample surrounding space to allow a device-under-test to be placed in the beam along with all the required measurement equipment. An X-ray source was found that fulfilled these requirements, contained within a Zeiss Xradia Versa 510 system otherwise used for high-resolution μ-CT imaging for materials analysis. This source enables control of the tube voltage from 40 - 150 kV, tube currents from 1 - 250 μA and source sample distance (± 21 cm), all via propriety Zeiss software.

A photograph of the X-ray source within the Zeiss Xradia is shown in Figure 7.3. Due to the risk of ionising radiation exposure, the source is required to be contained within a shielded enclosure to prevent any leakage of X-rays. In addition, the combined risk of the radiation and high-voltages within the X-ray source meant interlocks on the chamber doors are needed, to prevent accidental exposure to these hazards. These features were already in place in the system. Furthermore, the characterisation of the performance of the devices-under-test requires measuring the electrical output of the device during X-ray exposure. This means the measurement equipment, kept outside of the X-ray chamber, must be able to connect to the device inside the radiation-proof shield. The Xradia system already had a designated port for

cables, allowing electrical wires to be connected. A final safety consideration was the high external biases, up to 200 V, applied across the device for direct detection measurements. This required another interlock to prevent exposure to voltages while the device was tested. A magnetic interlock was designed in-house, to attach to the doors of the X-ray chamber, which cuts-out the bias when the doors are opened.

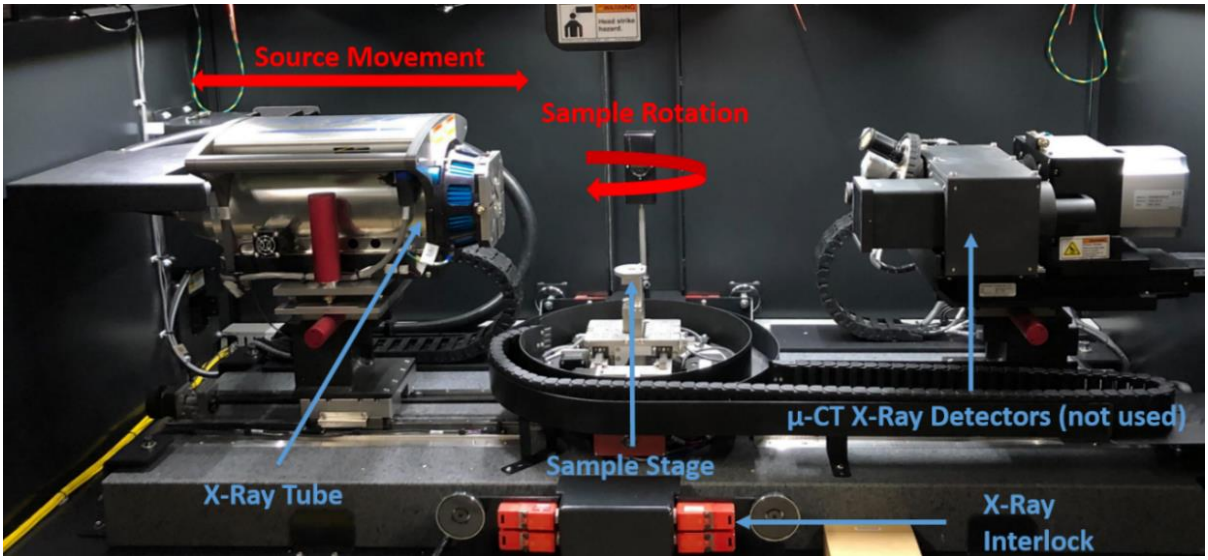

***Figure 7.3: X-Ray Characterisation Set-Up**. Inside the Zeiss Xradia Versa X-ray chamber.*

For X-rays, the amount of radiation is quantified by the absorbed dose, the energy deposited per unit mass of stated material. The unit of absorbed dose is Gray (Gy, equivalent to J kg^{-1}), used for X-rays due to the convenience with respect to biological systems. The absorbed dose is sometimes referred to as *Kerma*, the kinetic energy released to matter.[20] To quantify the X-rays incident on the device-under-test requires a dosimeter. Direct measurement of the energy and intensity is difficult, due to the penetration of X-ray photons. Two common dosimeter designs are the silicon diode and ionisation chamber, which both can determine the parameters of the beam from the carefully calibrated electronic outputs of the device. The dosimeter was required to cover the keV range from the Zeiss source (40 - 150 keV), and also the dose rates expected for measurements (1 $nGy_{air}\ s^{-1}$ up to 10 $mGy_{air}\ s^{-1}$). A Raysafe X2 R/F diode sensor was used, which covered these requirements.

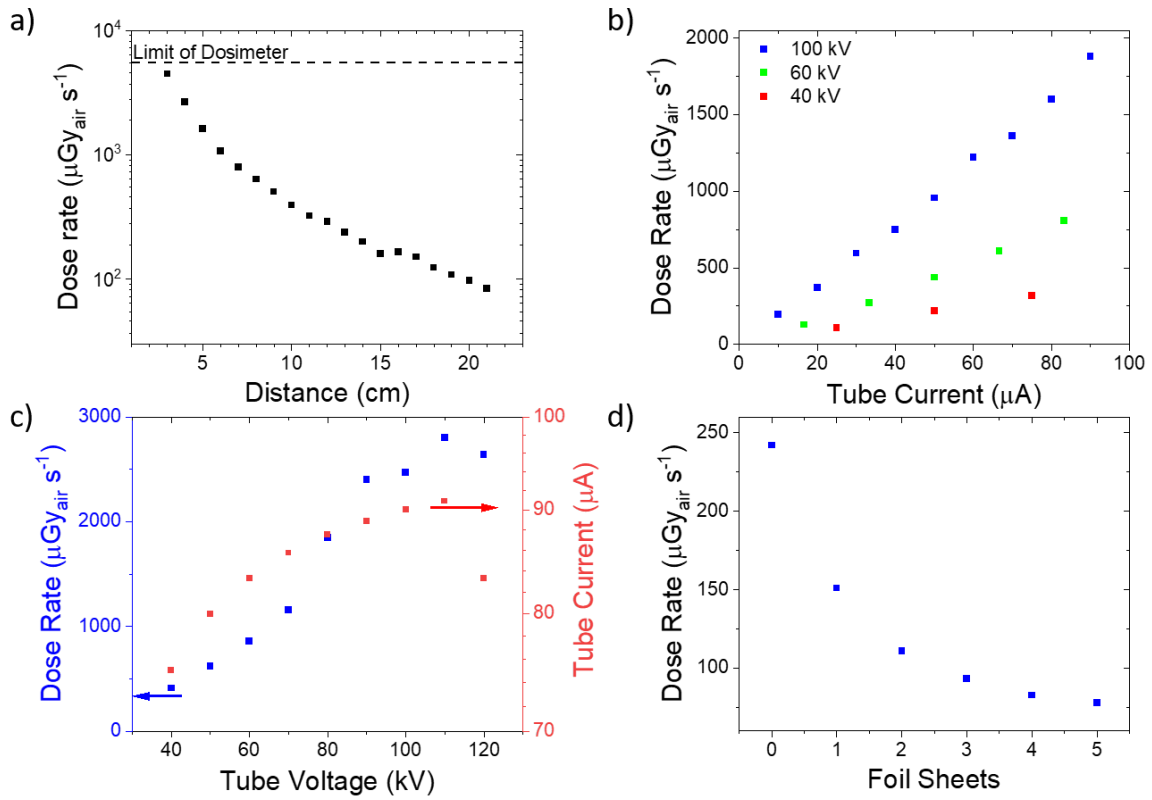

Figure 7.4: Varying X-Ray Dose. *a) Increasing source – sample distance (100 kV, 10 μA tube parameters). The dose decrease approximately follows the inverse square law. b) Tube current induced dose variations. c) Tube voltage induced dose variations. It should be noted that the software did not allow the tube current to be fixed as voltage was varied, and so the change in tube current is also shown (red, right y-axis). d) Lowering dose with aluminium foil (~0.1 mm) filters (100 kV, 10 μA tube parameters).*

Using the dosimeter, the effect of the tube parameters on the dose rate was calibrated. Within the X-ray chamber, the source has approximately 20 cm of travel to/from the device-under-test, and Figure 7.4a shows the decrease in dose rate as the source is moved away from the sample, agreeing with the expected inverse square relationship. At the selected tube parameters, the dose rate exceeded the limits of the dosimeter below 3 cm. The dose can also be reduced by lowering the tube current, as shown in Figure 7.4b, however the software which controls the tube parameters only allows a small range of fixed tube currents. Similarly, the tube voltage can vary the dose rate (Figure 7.4c), though there was also additional variation in tube current due to the limitations of the control software. Lastly, filters can reduce the X-ray dose rate, and aluminium foils demonstrate this in Figure 7.4d. It was also determined that two sheets of lead tape efficiently attenuate a 40 kV tube voltage beam (transmission <1%), which was utilised in the design of components for characterisation. Where tube current and source – sample distance solely affect the beam intensity, tube voltages and filtration also change the spectrum

of radiation. Overall, the Zeiss source allows great flexibility over the X-ray beam spectrum and intensity, suiting the characterisation of X-ray detectors.

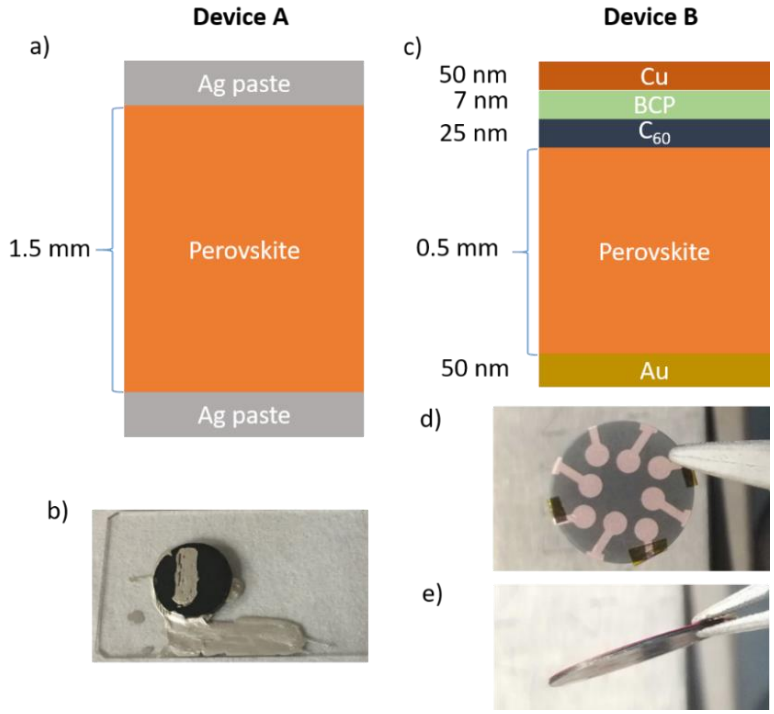

Figure 7.5: Perovskite Test Devices for Developing X-ray Detector Characterisation Techniques. *a) and b) Device A, photoconductor. Perovskite composition in Device A was* $MAPbI_3$*. The* $MAPbI_3$ *pellet was produced by Dominik Kubicki. c-e) Device B, photodiode. Perovskite composition in Device B was a* $FA_{0.85}Cs_{0.15}PbI_3$ *-* $FA_{0.85}Cs_{0.15}Pb(Br_{0.85}I_{0.15})_3$ *heterojunction. Device B was fabricated by Ganbaatar Tumen-Ulzii.*

7.2.2 Direct Detector Characterisation

Characterising the ability of a direct X-ray detector to convert X-rays into an electrical signal requires measuring several key parameters, and a combination of sensitivity, detection limit, response time and stability give a broad understanding of a device's potential. In order to develop the measurement techniques, two perovskite test devices were utilised. Device A is a photoconductor, while Device B is a photodiode, and schematics of their architectures are shown in Figure 7.5.

Sensitivity

Sensitivity measures the magnitude of a detector's signal in response to incident X-rays. A measure of sensitivity is obtained by recording the detector output as a function of dose rate. Plotting the response of the detector, $I_{on} - I_{off}$, at each X-ray dose rate then allows sensitivity to

be obtained from the gradient, and a schematic of this process is shown in Figures 7.6a and b. The units of sensitivity are $\mu C\ Gy^{-1}\ cm^{-2}$.

Several issues arose from initial measurements. The first involves the perovskite devices-under-test, which suffered from huge baseline drifts during measurements, similar to those displayed in perovskite photodetectors (see Chapter 4). An extreme example of this effect is shown in Figure 7.6c, utilising Device A. Drifting currents have been attributed to ion migration in halide perovskites,[199,276] and remain a particular problem within the detector community.[200,212,274] The requirement of external biases to collect charges over the large device thicknesses has the unwanted side effect of increasing ion migration. The powder-based synthesis in these devices generates a high grain boundary density, which act as transport channels for ion movement and increase this drift, but the effect is still prevalent in other devices. As detailed in Chapter 4, the drifting of current, and shifting of the baseline, has to be accounted for in sensitivity measurements. These measurements utilised the 'dynamic' techniques proposed from this chapter, and I_{on} and I_{off} values were measured at each dose rate, summarised by the following procedure:

1. Turn the X-ray tube on at a set dose rate
2. Record the value of I_{on}
3. Turn the X-rays source off
4. Record the value of I_{off}
5. Increase the dose rate
6. Repeat from Step 1

The dose rate was scanned from low to high, to minimise any potential light soaking effects (the changing of performance after light exposure, as reported in perovskite solar cells)[422,423] and X-ray induced degradation. A snapshot of Steps 1 to 4, for a single dose rate, is shown in Figure 7.6d. This highlights two problems with this measurement, both originating from the practicalities of the X-ray source. The first is the X-ray source has a long (>30 seconds) warm-up period. This warm-up period was confirmed to be an artefact of the X-ray source, and not from the device-under-test, by measuring the dose rate during this time, which shows an identical variation. This effect makes it difficult to distinguish any variations in the device response from the variations in X-ray production. It also increases experiment time significantly, as the source is required to be turned on and off multiple times per measurement. The second issue is the slow turn off time of the source, demonstrated by the slow tail (>2 seconds) of response from the device under test. Again, this was validated with the dosimeter

to be an artefact of the X-ray tube. This wrongly generates the impression devices are slow to respond to X-rays.

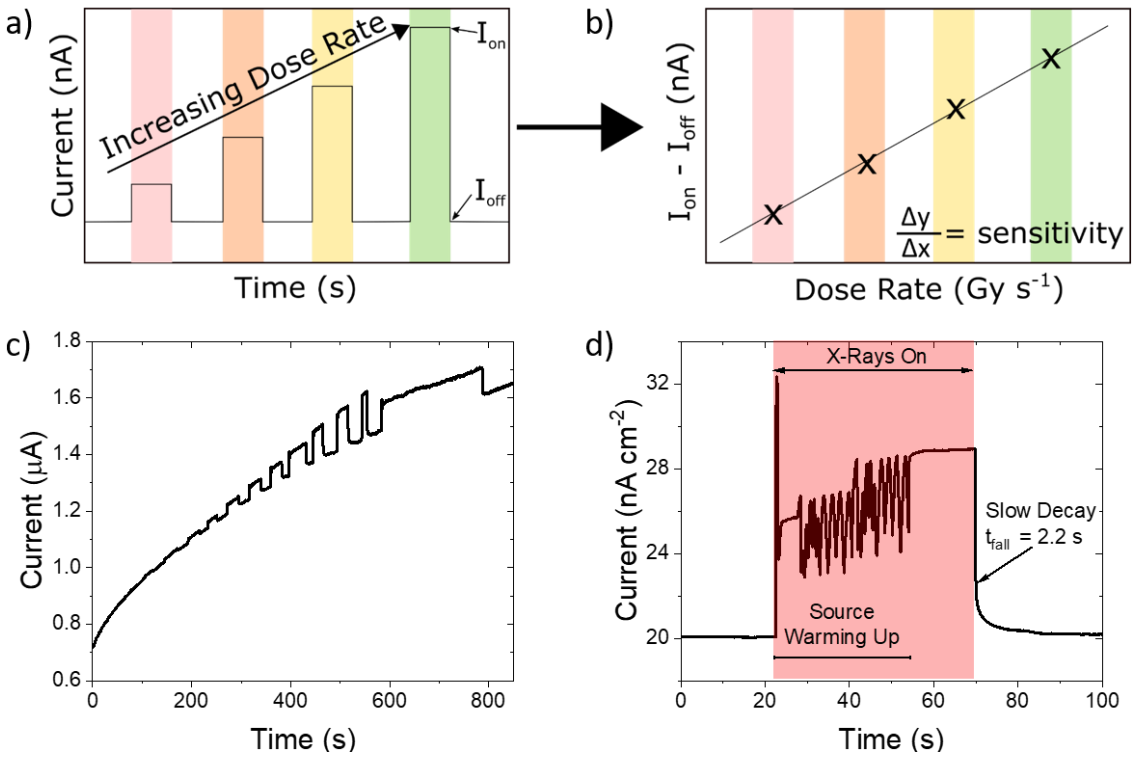

Figure 7.6: Sensitivity Measurements: Procedure and Issues. *a) and b) Schematics of sensitivity measurement procedure. Current is recorded at different dose rates (a), with the corresponding response at each point extracted in (b). c) Drifting of Device A current (−10 V external bias), while measuring the X-ray response at increasing dose rates. d) Sensitivity measurement at a single dose rate, demonstrating the source warm-up and cool down time.*

To overcome these issues, an X-ray shutter was designed to allow the source to continually run throughout a full sensitivity measurement, removing any source artefacts and speeding up the procedure. The shutter was adapted from a motorised optics flip mount, with additional lead tape to attenuate the beam. The response speed of the shutter was 500 ms. This improved the practicalities of sensitivity measurements, with the new procedure as follows:

1. Turn the X-ray tube on (ensure shutter closed)
2. Set the dose rate
3. Open the shutter
4. Record the value of I_{on}
5. Close the Shutter
6. Record the value of I_{off}
7. Increase the dose rate
8. Repeat from Step 3

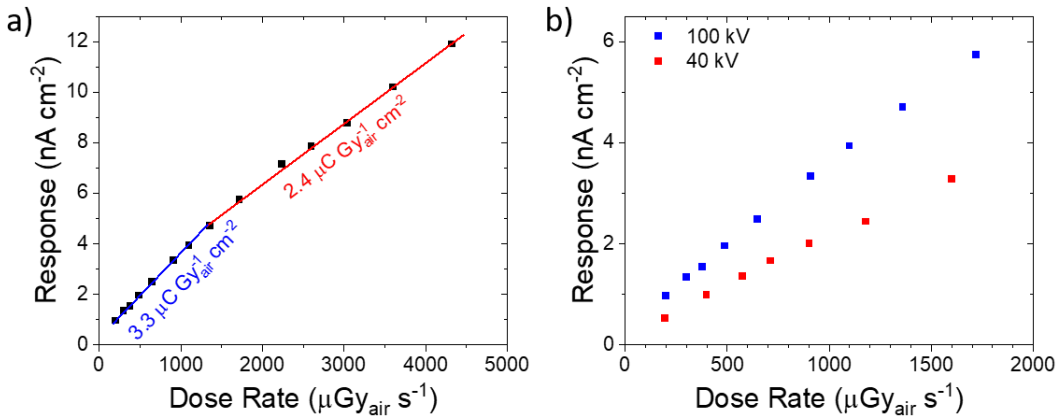

Figure 7.7: Sensitivity Variations with X-ray Beam Properties. *a) Dose rate dependence of detector sensitivity for Device B (100 kV tube voltage). b) X-ray energy dependence of detector sensitivity (Device B).*

Using this protocol, the response of Device B was measured as a function of dose rate, using a tube voltage of 100 kV (Figure 7.7a). Interestingly, the sensitivity is not constant, and the sensitivity at lower dose rates is improved by over 50% compared to higher dose rates. Variations of sensitivity with dose rate are unfavourable for imaging, where a wide linear dynamic range is required, and it will have repercussions for the detection limit calculations, as introduced later.

The effect of varying the tube voltage on detector sensitivity is shown in Figure 7.7b. The sensitivity demonstrates a clear dependence on the X-ray energy, with higher performance at 100 kV versus 40 kV (for the same dose rate). Higher X-ray energies are more penetrating, and one explanation for this energy dependence is the fact these devices were irradiated through a copper electrode, which would attenuate a greater portion of the 40 kV beam. However, while this result shows the effect of X-ray tube voltage on the same device, lower tube voltages would produce improved performance if the detector was optimised for the penetration depth. The penetration depth of 100 kV photons in $MAPbI_3$ is six times greater than 40 kV, allowing an optimised detector for 40 kV X-rays to be much thinner than for 100 kV X-rays, with shorter carrier transport requirements and higher performance.[19] Overall, the impact of dose rate and X-ray spectrum on detector sensitivity demonstrates how this result can be affected by the measurement conditions, requiring transparency when quoting the performance of a detector.

The sensitivity is further influenced by the external bias applied to a detector. External biases increase the drift length of carriers, leading to improvements in both the probability of collection and the detector sensitivity. Photoconductors, such as Device A, require a bias to generate a signal, and the response under 5, 10 and 20 V are shown in Figures 7.8a and b,

demonstrating greater responses with higher biases. Device B, due to its photodiode structure, allows self-powered detection, but sensitivity also increases with reverse bias (Figure 7.8c), improving linearly to 40 V, the limits of the voltage source in this experiment. To enable higher external biases, a voltage interlock system was designed to allow up to 200 V to be applied, and fully characterise the impact on sensitivity.

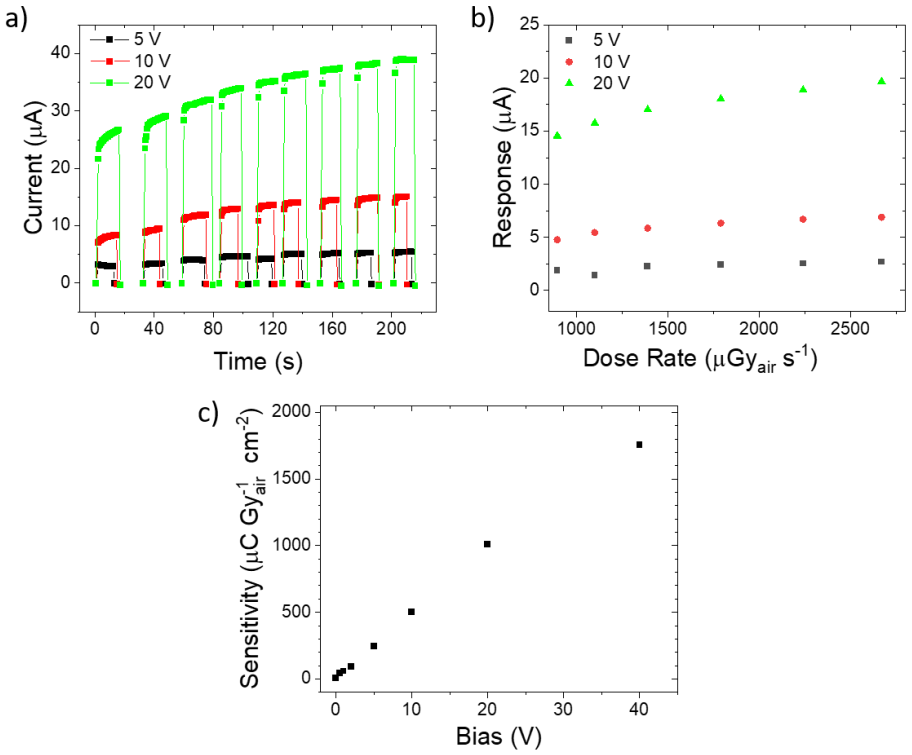

Figure 7.8: Impact of Bias on Detector Sensitivity. *a) and b) The impact of bias on Device A current (a), and the corresponding response (b). c) The impact of bias on photodiode sensitivity (Device B). 100 kV tube currents were used for all measurements.*

Detection Limits

The limit of detection (LoD) is a measure of the lowest dose rate that can be distinguished from the noise, similar to the NEP metric for photodetectors. However, there is less cohesion in the research community for how best to measure the LoD for direct X-ray detectors. The prevailing method entails an independent noise analysis of a detector, followed by measurements to find the dose rate which generates a signal-to-noise ratio of 3.[188,190,200,205,211,420,421,424,425] This is based upon the definition of detection limit used by the International Union of Pure and Applied Chemistry (IUPAC), based upon statistical analysis by Currie.[426]

As introduced above, the sensitivity of an X-ray detector is highly dependent on both the operating conditions and the device structure (i.e. photodiode or photoconductor, and semiconductor thickness), and the detection limit has similar variation. Recently, Pan et al.

developed a method to calculate LoDs values representative of an X-ray detector material, without influence of operation or achitecture.[33] In this method, detection limits are estimated based on measurements of sensitivity and dark current, offering much simpler experiments. This technique removes the requirement to measure the response of the detector down to very low incident X-ray dose rates, where errors can be introduced. In addition, it can be difficult to lower X-ray intensities to the noise level without altering the photon energy spectrum by adding filters. However, an important, and not mentioned, requirement for this method to be valid is that sensitivity must remain constant with dose rate. As introduced above, this is not the case in some detectors, which would generate errors when calculating detection limits. Instead, this method was used to provide an estimation of LoD in our characterisation procedure, and precise quantification involved measuring response down to the level of the detector noise.

Response Speed

In order to measure the response speed of an X-ray detector, the beam is required to be pulsed, allowing rise and fall times to be determined from the time taken for the signal to respond to the modulated radiation. The X-ray tube offers no options for pulsing, and so modulation had to be introduced after continuous wave X-ray production. The shutter, designed to negate the influence of the slow warm-up and cool down times of the source, generates pulses in the radiation. However, these are limited by the opening and closing times of the shutter to approximately 500 ms, and measuring faster detector responses will require quicker pulsing. A chopper adapted for X-ray measurements was designed, by including lead tape to attenuate the beam. The resulting modulated radiation is shown in Figure 7.9a, with the frequency controllable from 20 – 200 Hz (and above if alternate chopper wheels were used).

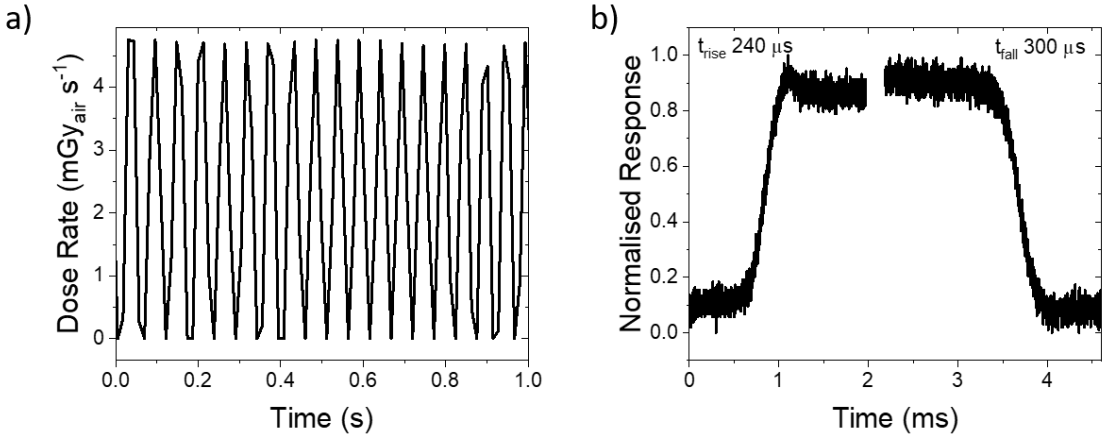

Figure 7.9: Pulsed X-rays for Response Speed Measurements. *a) Dose rate variation using a 20 Hz chopper frequency (40 kV tube voltage). b) Response time limits of the system, measured optically.*

The limiting rise and fall times of this chopper system were measured optically, using visible light and a silicon photodetector (Figure 7.9b). Rise and fall times of 240 and 300 μs, respectively, demonstrate the bounds of this system. The difficulty in modulating X-rays makes the measurement of response speed in the literature rare, despite its importance for applications. Emerging results have returned cut-off frequencies of 200 and 480 Hz, which correspond to rise and fall times slower than milliseconds.[78,183] For reference, organic semiconductor-based direct X-ray detectors also demonstrate response times above 10 milliseconds, suggesting the limits of our system should be sufficient for most detectors.[427,428] This chopper system can be combined with an oscilloscope or lock-in amplifier, to measure response speed in the time or frequency domain, respectively.

Stability

Applications require detectors with stable performance over long usage periods. However, the high energy of X-rays can damage detectors, leading to a deterioration in performance with time. It is therefore a requirement to measure the impact of radiation exposure on detection performance to assess detector stability. The irradiation of two Device B photodiodes, fabricated identically but in separate batches and measured on different days, is shown in Figure 7.10a. The initial response in Measurement 1 showed a noisy portion during the first hour. This is very similar to the X-ray tube warm-up variations shown in Figure 7.6, and so it may not be a result of device instabilities. To account for this, future measurements were performed with the dosimeter adjacent to the sample, to allow the variations in tube output and device response to be discriminated.

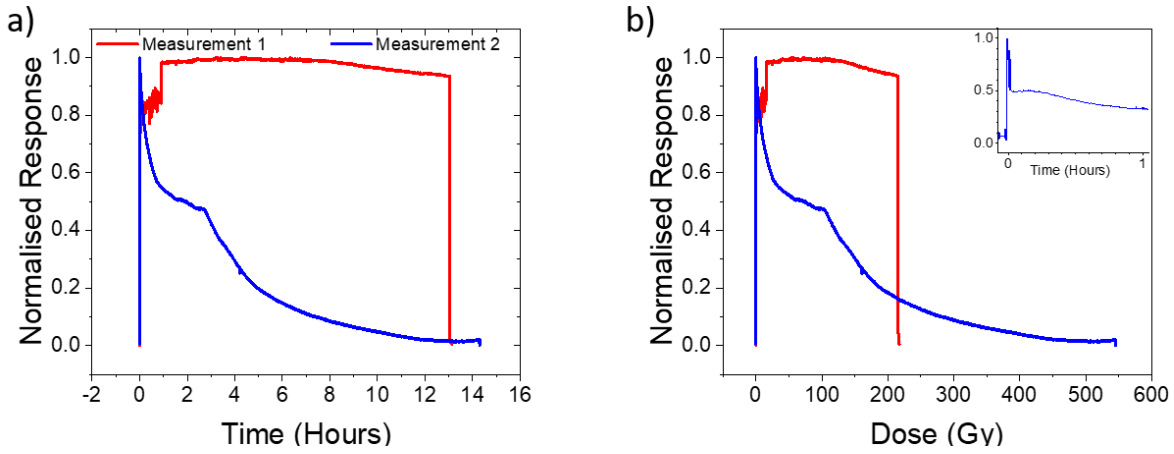

Figure 7.10: X-Ray and Bias Stability. *a) and b) The stability of Device B response (100 kV tube energy and −40 V external bias). Measurement 1 used a 4.6 mGy_{air} s^{-1} dose rate and Measurement 2 used a 10.6 mGy_{air} s^{-1} dose rate. This leads to different cumulative doses, shown in (b). b) Inset shows the variation of normalised dark current with −40 V external bias, demonstrating degradation without X-ray exposure.*

The difference in dose rate between Measurements 1 and 2 generates a difference in accumulated dose in each case. Therefore, cumulative dose is a more comparable metric than time (Figure 7.10b). Measurement 2 demonstrates a deterioration in response throughout the irradiation, approaching the initial dark current value by the end of the measurement. The difference in stability between two identical devices highlights the impact of other factors on an X-ray detectors longevity. The environment is one key factor, and the perovskite tolerance to radiation could vary with conditions, for example, humidity (measurements were performed in air on unencapsulated samples). Secondly, large biases are required for the measurements, and this has been shown to degrade perovskite solar cells.[198,272,293] As a result, the stability measurement procedure was adapted to include a reference device, exposed to the same bias and environmental conditions as the irradiated device, but without X-ray exposure. The inset of Figure 7.10b shows the normalised current of a reference device, and reverse bias likely contributed to some of the degradation in Measurement 2.

7.2.3 Device Design Implications

Throughout the development of measurement techniques to analyse X-ray detectors, various practicalities were discovered that were then fed back to improve device design. As discussed, the impact of humidity on stability of perovskites can deteriorate performance, making it difficult to isolate X-ray induced damage during stability measurements.[429,430] As a result, devices were encapsulated, using a glass cover to seal the perovskite from the environment. However, early measurements demonstrated the high instability of glass towards X-rays. Figure 7.11a shows a glass microscope slide after 2.4 Gy of radiation exposure, showing discolouration. As a result, fused silica was used for encapsulation, which have much greater radiation tolerance. A thickness of 0.1 mm was used to minimise any parasitic absorption.[354]

It was found that the top contact material has an impact on test device performance. While photodetectors are irradiated through a transparent conductive oxide deposited on glass, the instability of glass to ionising radiation, and parasitic attenuation, meant that X-ray devices are instead irradiated through a thin (<100 nm) metal contact. Interestingly, Device B consistently produced higher performance when irradiated though the copper side, rather than the gold (see Figure 7.5 for the device architecture). The transmission of both these contacts (fixed at 50 nm) is shown in Figure 7.11b. Above 10 keV, both electrodes transmit ~100% of X-ray photons, and so parasitic absorption by the metal was not the cause of this discrepancy. Instead, differences could come from within the device itself. The copper side corresponds to where C_{60} is deposited on top of perovskite. This material is known to passivate perovskites, and any

defects detrimental to performance may have been removed.[318] However, C_{60} has also been shown to introduce performance-inhibiting deep trap states,[431] and so more work is required in order to confirm this theory. Similarly, when silver was replaced with carbon paste as the top contact in Device A, it was routinely observed that silver/Perovskite/Carbon devices would show higher performance when irradiated through the silver side, despite the expected reduction in parasitic absorption from the lower atomic number of carbon. Due to these findings, devices were irradiated from both sides during measurements, in order to test for any differences.

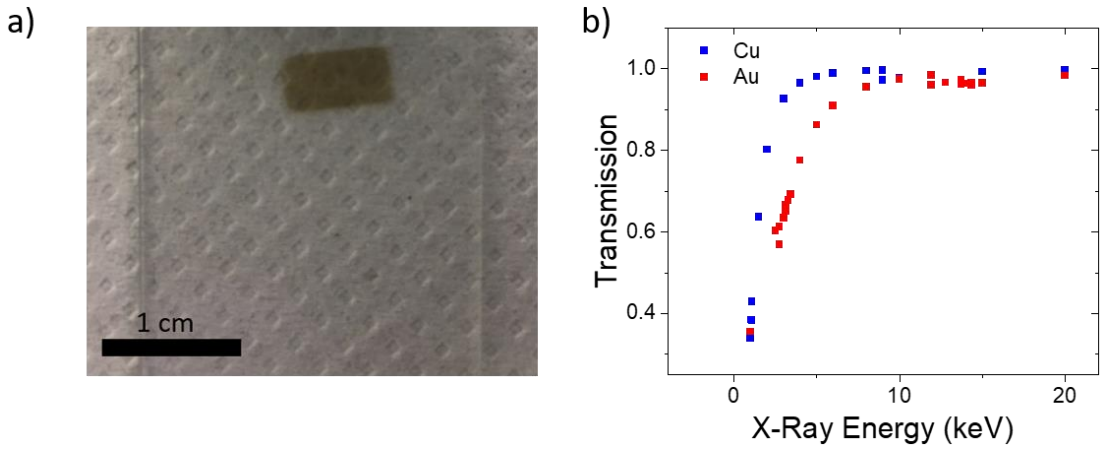

Figure 7.11: X-Ray Detector Device Design Implications. *a) Glass discolouration after 10 minutes at 4 $mGy_{air}\ s^{-1}$ (100 kV tube voltage). b) Copper and gold X-ray transmission (50 nm). Calculated using data obtained from the XCOM Database.*[19]

7.3 Using Trench Substrates to Overcome Direct X-Ray Detector Limitations

The motivation for using trench structures for direct X-ray detection was introduced in Section 7.1, and the development of perovskite-based trench detectors was split into four aspects, each investigated in turn. First, the growth of the perovskite was studied. The challenges of X-ray depth trenches (>100 μm deep), in terms of both substrate fabrication and perovskite growth, meant that the project began using trench depths relevant for visible light absorption (~450 nm). Developing an understanding of the perovskite growth mechanisms in smaller trenches enabled further improvements to deposition conditions. It will also assist the scaling-up of the growth when the trench volume increases to X-ray trenches. Once the perovskite growth was understood, the obtained knowledge was used in optimising the deposition technique, to improve the perovskite quality and suit the large areas and volumes required of X-ray devices. Following this, the trench structures were adapted for detection, allowing visible light

photodetection performance to be measured. The final step of the project was the design of X-ray depth trenches. Discussions with collaborators on the requirements of X-ray detectors, the established findings of optical trench substrates, and the limits of lithography led to the design of trench substrates to overcome the direct X-ray detector limitations.

7.3.1 Understanding Perovskite Growth in Trench Structures

By drop casting $MAPbI_3$ precursor solutions into the trench structure, a highly selective deposition occurs, only growing within the features.[251] In addition, the morphology of the perovskite produced from this method appears close to ideal, with very few grain boundaries visible under electron and optical microscopy. Initially, the origins of the growth from drop casted precursors was analysed, using the original trench design (Figure 7.1), in order to identify the requirements of the substrate and perovskite material. This knowledge will then be applicable when designing X-ray tailored substrates, and for future optimisation of the deposition to improve the perovskite properties.

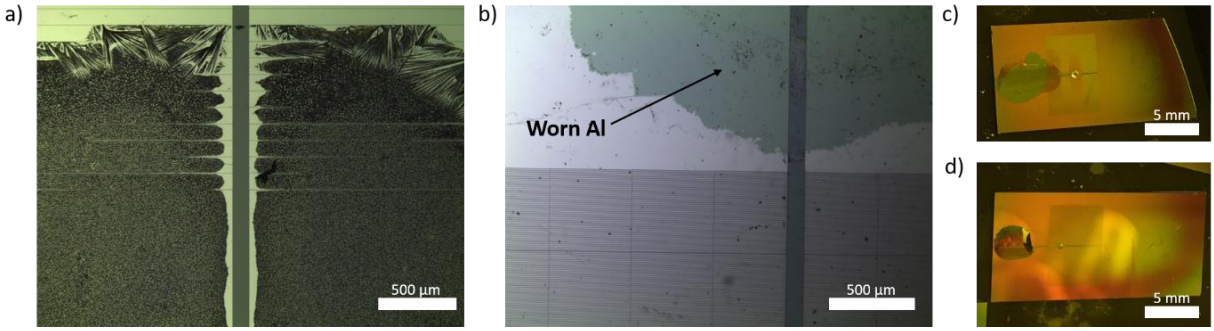

Figure 7.12: Importance of Substrate Surface for Selective Patterning. *a) Substrate with photoresist (UV1116) left as the exposed top surface, showing preferential perovskite deposition on the resist instead of in the trenches. b) Substrate with worn aluminium in the region where precursors had previously been deposited. c) and d) The difference in contact angle on a worn (c) and fresh (d) substrate. Only d) showed selective deposition.*

This selectivity of the drop cast deposition allows patterns of semiconductor that match the design of the trench structures, a highly desirable feature that allows production of detector arrays. Selectivity was thought to result from the preferential wetting of the SiO_2 trenches over the aluminium surface,[251] and once infiltrated into the trench array, the solution is drawn through the whole pattern by capillary forces, before it crystallises and grows into perovskite. This theory of the selectivity of perovskite was probed by varying the surface materials of the substrates. By replacing the aluminium surface with exposed photoresist (UV1116), the selective deposition no longer occurred (Figure 7.12a). Instead, a negative patterning was seen,

whereby the perovskite selectively grew on the surface, and not within the trenches. Further support for the importance of substrate surface energy on selectivity was seen when the precursors were deposited on old substrates, with the aluminium surface worn away (Figure 7.12b). Precursors wet the worn substrates to a much greater degree (Figure 7.12c), with the droplet having a much lower contact angle, compared to fresh devices (Figure 7.12d). As a result, the perovskite does not fill the trenches in the worn substrates, remaining on the substrate surface. These findings established the requirements of surface energy contrasts between the two surfaces for the perovskite to selectively fill the trenches and be patterned.

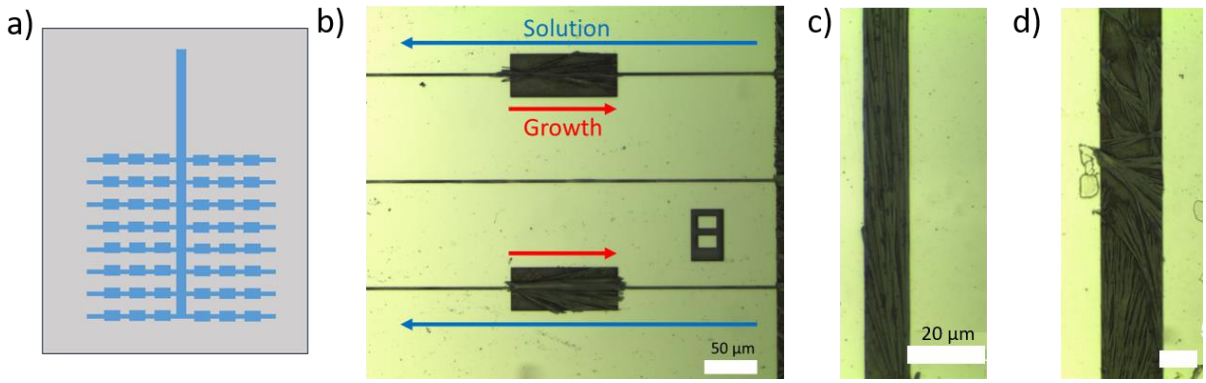

Figure 7.13: Probing Perovskite Growth Mechanisms with Substrate Design*. a) Schematic of substrates patterned with narrow and wide regions in the minor trenches. b) Images of the growth in the narrow wide substrates (main trench on right hand side), demonstrating the solution flows away from the main trench (blue arrows), and grows back towards it (red arrows). c) and d) Images of growth in a 12 and 33 µm trenches, respectively (scale bar is 20 µm in both).*

After filling of the trenches by the precursor, nucleation and growth occurs to produce the perovskite. The high orientation of perovskite growth imposed by the minor trenches (Figure 7.1c) suggests nucleation takes place in the minor trenches (~1 µm wide) before growing back towards the main trench (~100 µm wide). Further insight into how and where the nucleation events occur was obtained by designing specific trench patterns. The pattern determines both where the solution can travel and how the perovskite nucleates and grows, so carefully designed trenches can help explain these processes. By designing trenches with narrow and wide regions within the minor trenches (Figure 7.13a), it was seen that grains grow out of a minor trench and back towards the main trench (Figure 7.13b). The spatial confinement within the minor trenches encourages heterogeneous nucleation on the trench surface, increasing the chance of growth stemming from these regions. Once nucleated, the abundance of precursor material towards the main trench favours growth back in this direction.

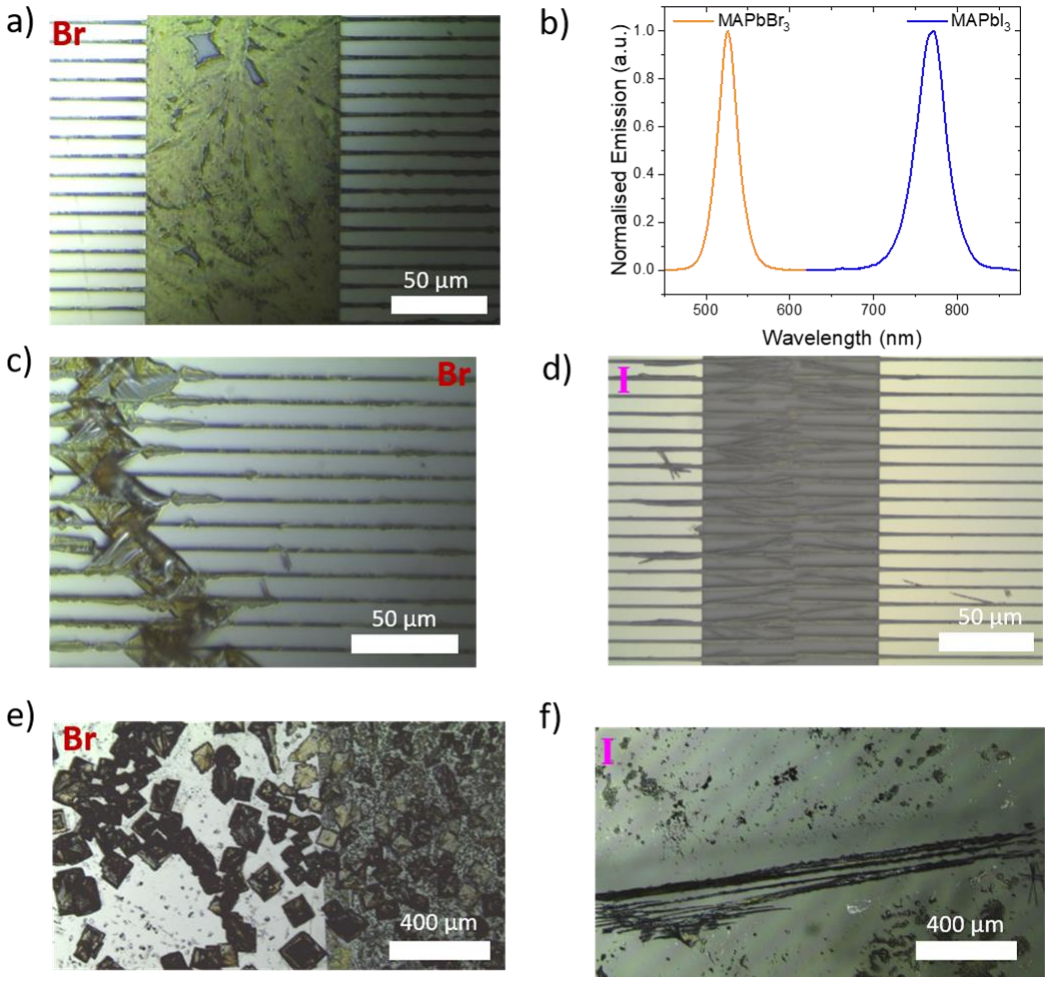

Figure 7.14: Perovskite Composition and Growth Orientation. *Left hand side - $MAPbBr_3$, right hand side - $MAPbI_3$. a) $MAPbBr_3$ displaying no preferential growth orientation. b) PL from $MAPbBr_3$ and $MAPbI_3$ from hyperspectral images. c) $MAPbBr_3$ growing out of trenches, instead of along. d) $MAPbI_3$ highly orientated growth from the minor trenches. e) and f) The differences between $MAPbBr_3$ (e) and $MAPbI_3$ (f) growth on unpatterned substrates.*

Once nucleation occurs in the minor trenches, the growth is patterned by the minor trenches, leading to orientated perovskite growth across the main trench. The requirements for this orientation were first studied by increasing the width of the minor trenches (originally 1 µm). Substrates with 200, 33 and 12 µm wide trenches were produced, and while the 12 µm retained the orientation (Figure 7.13c), albeit with several parallel grains, 33 µm and above showed little control over the growth direction (Figure 7.13d). This will have significance for X-ray structures for two reasons. Firstly, perpendicular growth can block trenches, preventing the flow of precursor solution, and limiting the area patterned by the perovskite. As discussed later, the patterning of large areas, into arrays, is an important feature for X-ray detector devices. Additionally, deeper trenches will likely have greater widths due to lithographic fabrication limitations, and this finding will help guide the device design.

This control over perovskite orientation by the trenches was elucidated further by analysing the importance of the perovskite composition. While $MAPbI_3$ precursors (in DMF), discussed thus far, demonstrate the long wire-like perovskite growth, replacing with $MAPbBr_3$ precursors (still in DMF), did not reproduce the same advantageous deposition (Figure 7.14a). Hyperspectral PL images confirm the bromide analogue was produced, emitting at the expected ~530 nm wavelength (Figure 7.14b).[341] However, $MAPbBr_3$ did not grow along the minor trenches or grow orientated material across the main trenches. Instead, $MAPbBr_3$ grows outwards from the minor trench, instead of back along the pattern, and once nucleation occurs, growth is equal in all directions with no orientation implemented by the trench structure (Figure 7.14c). The anisotropic and orientated growth of $MAPbI_3$ (Figure 7.14d) has been established elsewhere to be caused by the formation of an intermediate clathrate-phase solvatomorph, which only occurs in certain polar aprotic solvents (e.g. DMF and DMSO).[432,433] The absence of similar morphology in the bromide analogue, shown here, suggests a similar solvent-precursor structure does not form. This prevents the wire-like patterning of the perovskite, and restricts trench use to $MAPbI_3$. Growing both the iodide and bromide analogue on a non-patterned SiO_2 substrate reiterates this, with $MAPbI_3$ still growing into long wires, while $MAPbBr_3$ grows into cubes (Figure 7.14e and f). The cubic growth of $MAPbBr_3$ bulk crystals is practical for traditional direct detectors, with flat top and bottom surfaces ideal for electrodes, explaining the prevalence of this material in the literature. However, the incompatibility with the lateral patterned growth meant it was not suitable for trench detectors.[122]

7.3.2 Optimising Deposition for Detection

Through changing the substrate materials and patterns, along with the precursor salts, the requirements for the selective growth of perovskites with preferable morphology were established. This understanding was applied to improve the deposition to suit X-ray detector devices. There are different aspects of perovskite growth that make it ideal for X-ray detectors. First, is the production of perovskite with a high degree of crystallinity, with the associated advantageous transport properties that allow efficient charge carrier collection. Additionally, large-area deposition is useful, as this allows the production of commercial-scale structures and arrays. Finally, growth that would suit upscaling into the deeper trenches needed for X-ray attenuation would be beneficial. By varying the conditions and parameters of the perovskite deposition, these desirable features of perovskite deposition were targeted.

Perovskite growth in trench substrates was shown to have a morphology similar to single crystals, with very few grain boundaries visible under optical microscopy. Single crystals,

defined by their continuous crystal lattice without disruptions from grain boundaries, possess improved semiconductor properties over polycrystalline films due to the removal of the detrimental defects associated with grain boundaries.[434] Grain boundaries have been proposed to be a key factor in enabling the ion migration-induced current drifts that detract from perovskite detector performance (see Chapter 4).[199] Additionally, perovskite single crystals demonstrate high carrier mobilities and lifetimes, allowing long transport lengths.[80,435] These ideal properties for detection, make high crystallinity a goal for perovskite growth. One challenge to improving the perovskite quality was determining a method to quantify crystallinity. A combination of the substrate structure and the small size of the perovskite material makes the conventional path of diffraction analysis, either using X-rays or electrons, difficult. Instead, microscopy approaches were used, analysing the density of grain boundaries and the resulting morphology of the perovskite material as a high throughput assessment of perovskite quality.

A decrease in the number of nucleation events would produce fewer grain boundaries, removing their detrimental impact on performance. Similarly, decreasing the likelihood of nucleation would allow the solution to travel further through the trench pattern before crystallisation. Therefore, reducing the nucleation density was targeted as a means to improve the perovskite deposition. As nucleation occurs after the solvent evaporation induced supersaturation of precursors, lower concentrations would slow the emergence of nucleation events, and it was previously found that reducing the precursor solution concentration could improve the perovskite deposition within trenches.[251] Lower concentrations resulted in fewer visible grain boundaries, as well as a reduction in premature crystallisation, which can block the trenches and prevent large-area patterning. This was further explored here by replacing DMF with DMSO, a higher boiling point solvent (b.p. 153 ^{o}C and 189 ^{o}C, respectively), which would slow evaporation and resulting nucleation. DMSO is still a polar aprotic solvent, which elsewhere has been shown to allow highly orientated $MAPbI_3$ growth, suitable for trench patterns.[433] DMSO depositions displayed different morphology to the DMF attempts (Figure 7.15a and b) with little influence of growth from the minor trenches. The PL spectra of the DMSO based perovskite also displays a high-energy shoulder in its emission spectrum (Figure 7.15c), which remained after annealing at 100 ^{o}C for 30 minutes, and could originate from solvent-precursor interactions remaining after growth. The formation of perovskite from DMSO has been shown to occur via a more complicated process of intermediate formation than DMF, which could lower its suitability to the orientated growth within trenches.[436]

Improvements in morphology were not seen after trialling different solution concentrations, and so DMF remained the solvent of choice.

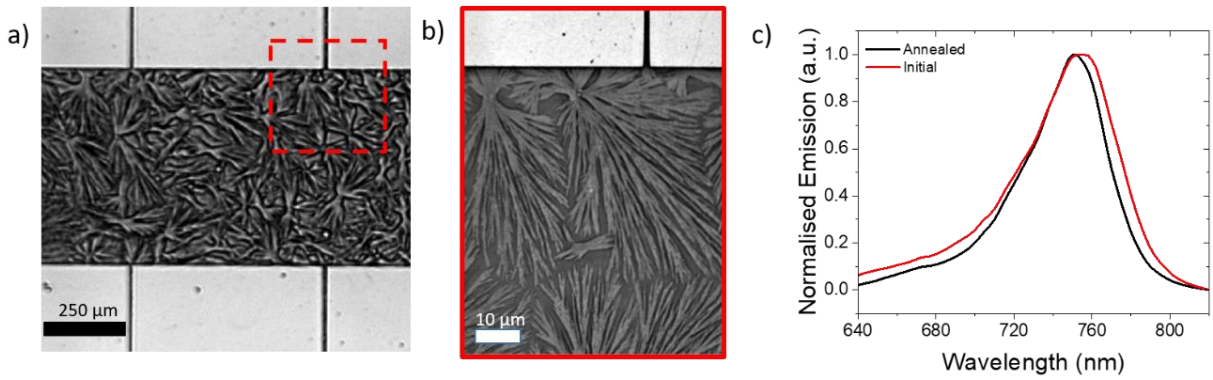

Figure 7.15: Replacing DMF with DMSO. *a) and b) Morphology of $MAPbI_3$ growth using DMSO, with (b) showing the red dashed region in more detail. c) PL spectrum from identical main trench regions before and after annealing.*

Other deposition methods were also trialled, and improving perovskite growth by spin coating the precursor solution onto the trench substrates was attempted. Spin coating was hoped to improve the coverage of perovskite, by removing the need for the solution to travel through the trench array. Initial spin coating approaches resulted in a significantly higher surface coverage, compared to the drop coating methods used previously, and Figure 7.16a shows that the perovskite reached the end of the trench pattern. However, the resulting perovskite was polycrystalline with a high density of visible grain boundaries (Figure 7.16b), and the trench pattern appeared to have no influence over the growth, with no wire-like material as seen previously. This is expected due to the high spin speeds (3500 rpm) spreading and evaporating the solvent, inducing rapid crystallisation. Optimising the solvent concentration and spin parameters allowed improvements to be made. Higher concentrations (0.1 M) and slower spin speeds (1000 rpm) improved the crystallinity, and orientated growth out of the minor trenches was seen (Figure 7.16c). The improved coverage with spin coating may be beneficial when scaling up to X-ray substrates, and the range of parameters that can be controlled when spin coating (e.g. spin speed, ramp speed, spin time) gives additional points of control when optimising for deeper trenches.

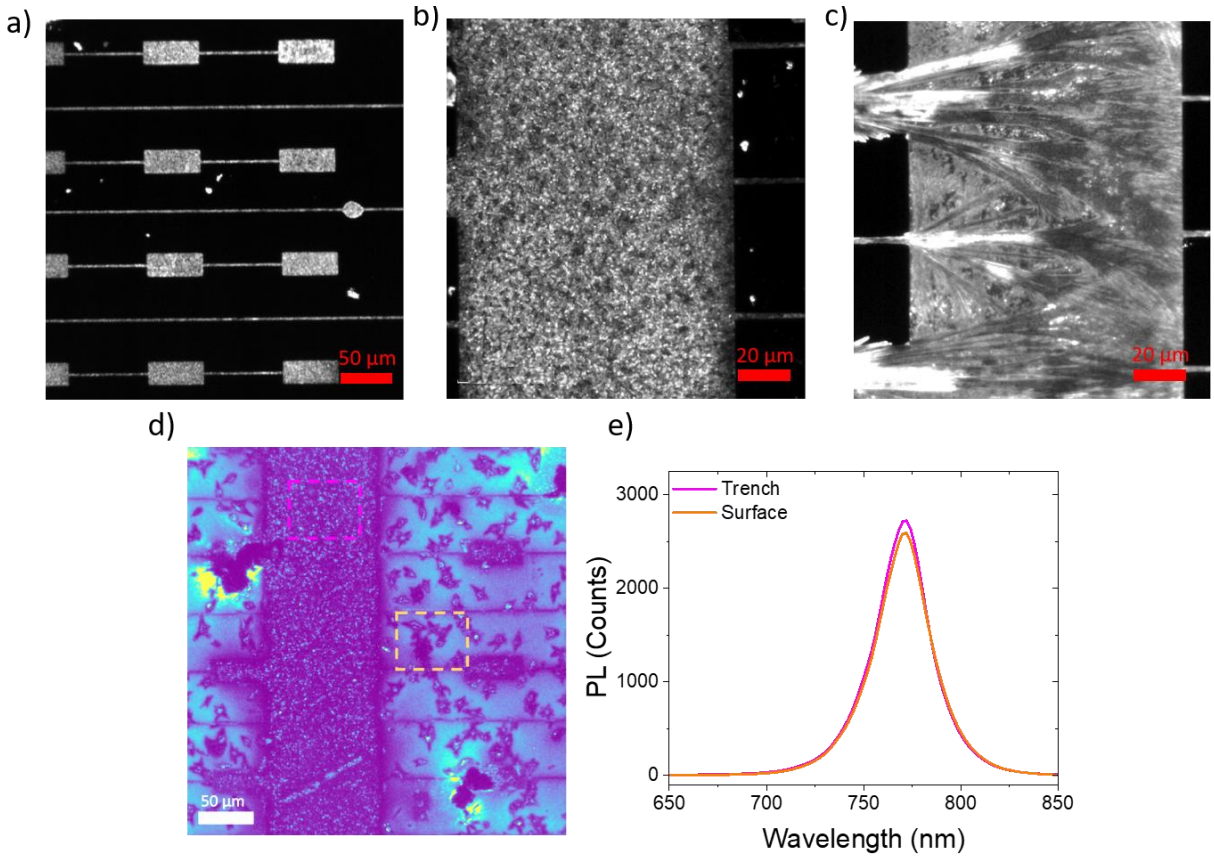

Figure 7.16: Alternative Perovskite Deposition Methods. *a)-c) Spin coating. a) Image of the edge of the trench pattern, demonstrating full coverage. b) The corresponding main trench on the same device as (a), with clear polycrystalline morphology and no orientation from the minor trenches. c) Improved morphology after optimising spin parameters. d) and e) Evaporation of perovskite. d) Hyperspectral PL image (770 nm) of solvent-free $MAPbI_3$ evaporation, highlighting unselective deposition over the whole substrate. e) Corresponding PL spectra of the main trench and aluminium surface, demonstrating similar spectra in both regions. Perovskite evaporation was performed by Yu-Hsien Chiang.*

Removing the need for solution to travel through the array when spin coating was taken further by using a solvent-free evaporation of perovskite on top of the trench structures. However, no selectivity was offered from this method, and perovskite was deposited all over the substrate (Figure 7.16d). This was confirmed with hyperspectral images, which displayed almost identical emission from the trench regions and substrate surface (Figure 7.16e). The perovskite within the trenches showed a different morphology to the surface of the substrate, likely due to the different surface energies. This finding confirmed that a solution-based deposition was required to enable selective patterning of the perovskite.

7.3.3 Photodetectors

The aluminium surface on the trench substrates is responsible for the selective perovskite deposition, as introduced in Section 7.3.1, as well as operating as the electrode material for electrical photodetection measurements. After perovskite deposition, the device operates as a lateral photoconductor that can detect visible light, and this detecting ability was assessed (Figure 7.17a). The initial trench substrates (Figure 7.1a) were not suitable for electrical measurements, as the continuous aluminium surface does not allow for measurement across the perovskite regions. Instead, two regions of aluminium are needed to be electrically isolated, and a device structure was designed for detector measurements (Figure 7.17b). In order to electrically contact across the trenches, tungsten probe tips (~5 µm width) were required to be placed on the adjacent aluminium, and designing patterns with wider aluminium contact areas increased the practicality of the measurement.

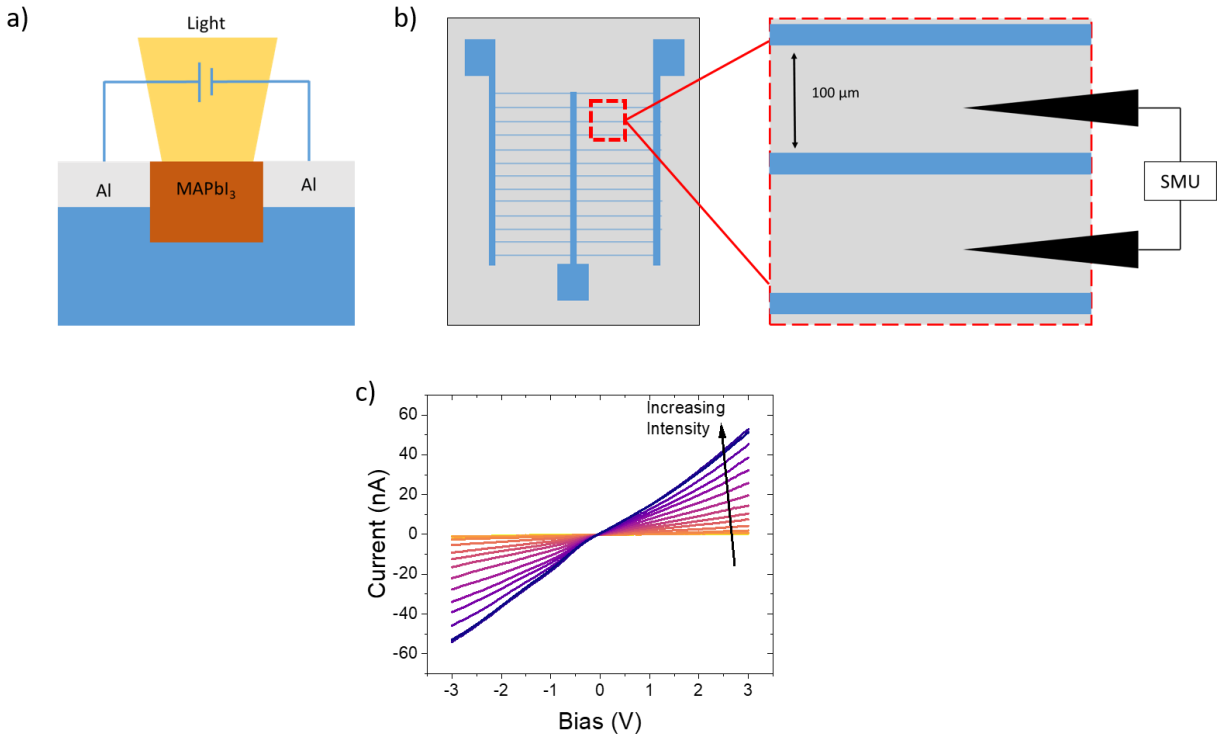

Figure 7.17: Photodetection Using Optical Depth Trenches. *a) Schematic of photodetector device structure. b) Top down schematic of photodetector device pattern. Inset shows a single pixel with the probe tips contacting across an electrically isolated trench. The electrical measurements recorded with a source measure unit (SMU). c) IV curves demonstrating light intensity dependence of photoresponse.*

The substrates were filled with $MAPbI_3$ using the original drop casting procedure, and the detection of visible light was assessed using IV curves. White light was used as the excitation

source and the performance at a range of incident intensities is shown in Figure 7.17c. The IV scans are symmetrical in forward and reverse bias, which is consistent with the symmetry of the Al/$MAPbI_3$/Al structure. The linear relationship in the IV curves suggests an ohmic metal-semiconductor contact forms with low energetic barriers to collection.[437] Higher intensity light generates a larger current response in the photodetector, displaying a clear photodetecting ability. This finding confirms that the direct deposition of perovskite into substrates prefabricated with electrodes is suitable for photodetectors. Therefore, after scaling up to account for the additional penetration depth, trench devices will enable the direct detection of X-rays.

7.3.4 X-Ray Detectors: Substrate Design

Following the understanding and optimisation of perovskite growth, and the demonstration of visible light detection in trenches of optical depth, the substrates were designed for X-ray detection. There are three significant challenges to scaling up the devices for X-ray detectors: fabricating suitable depth substrates, filling and growing perovskite in the deep trenches and analysing the detection performance under X-ray irradiation. The work in Section 7.2 on producing X-ray characterisation procedures was performed alongside the device development, in order to characterise the resulting devices. The substrates were then designed in X-ray relevant dimensions.

The design of the substrates needed a balance of the requirements for detection with the limitations of the lithography procedures. The development of a process to fabricate X-ray depth trenches was assisted by Lee Robinson (Cleanroom Process Coordinator, Dept. of Electrical Engineering, University of Cambridge) following discussions on the device applications. Increasing the depth of the trench to account for X-ray penetration depth is a challenge for lithography, as the aspect ratio (the ratio of trench depth to width) exceeds unity. This can lead to patterning errors such as undercutting and delamination. The increased trench depth also increases the volume of the trenches, which will bring challenges for scaling up the perovskite fabrication from optical trenches. As a result, initial devices were designed to be the minimum depth to still allow sufficient X-ray absorption when filled with perovskite. Using data obtained from the XCOM Photon Cross Section Database (See Chapter 3 for calculation details), the absorption efficiency of $MAPbI_3$ is shown in Figure 7.18a for increasing X-ray energies, and 93% of 33 keV X-rays are absorbed by 100 μm.[19] While monochromatic X-ray energies are displayed in Figure 7.18a, X-ray tubes used in applications generate a continuous bremsstrahlung spectra with energies up to the equivalent kV applied (see Section 7.2.1), and

the peak intensity is usually 33 - 50% of the tube accelerating voltage.[20] As a result, 33 keV would be the peak emission for ~60 - 100 kV tube voltages (relevant conditions for radiography applications). From this, 100 µm was determined to be a suitable depth to combine efficient X-ray absorption without being too challenging for fabrication and deposition.

The lateral width of the trench would also impact the trench volume and the aspect ratio. If the width is too small, relative to the depth, the quality of the trench substrate fabrication may drop. However, greater widths would increase the lateral charge transport distance and further increase the volume required to be filled with perovskite, affecting the deposition (see Figure 7.13). To find the optimum in this trade-off, a substrate was designed with a range of trench widths, from 5 µm (aspect ratio 20) to 100 µm (aspect ratio 1). Figures 7.18b and c show schematics of the initial substrate design, which will be used as guidelines for the ongoing development of trench X-ray detectors.

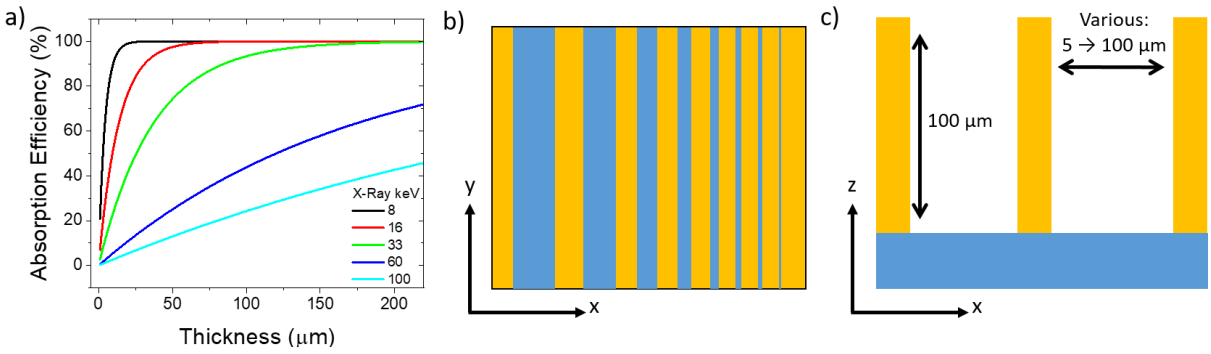

Figure 7.18: Trench Design for X-Ray Detection. *a) Absorption efficiency of $MAPbI_3$ at various X-ray energies. b) and c) Schematics of the initial X-ray trench design (b) with top down and (c) side on views.*

7.4 Conclusions

This chapter utilises a method to pattern perovskites with high-quality morphology for direct X-ray detection applications. The project was split into two parts, the first was producing a set-up capable of measuring direct X-ray detector performance, and the second focussed on the development of the novel device structures. An X-ray tube and radiation-proof chamber were adapted to enable accurate and safe X-ray detector characterisation. Using test devices, a set of measurement protocols were established to assess detector performance. These protocols accounted for the specific behaviour of perovskite devices, such as current drifts, light soaking effects and irradiation direction asymmetry, as well as taking the behaviour of the Xradia Versa X-ray tube into consideration. This enables the accurate characterisation of perovskite detector

sensitivity, limit of detection, response speed and stability, and the set-up would be applicable to measure the performance of trench structures.

The development of trench detector devices began with optical depth structures, before scaling up to the higher depths required for X-ray detection. The mechanistic origins of the perovskite growth were uncovered, stemming from a combination of the selective wetting of the trench patterns and the formation of perovskite-solvent intermediates, and this understanding was used to improve the perovskite deposition. By slowing the onset of precursor solution supersaturation and nucleation, the perovskite was manipulated to pattern larger areas of the substrate and with higher apparent crystallinity. The use of aluminium, essential to the selective deposition of the perovskite, was exploited as electrodes, and the devices were shown to be effective photodetectors.

We proposed the lateral structure of these detectors can be used to overcome the inherent issues restricting direct X-ray detectors, by decoupling the X-ray absorption and charge collection dimensions. After calculating the X-ray penetration depth, potential substrates were designed, balancing the requirements of substrate fabrication, perovskite deposition and X-ray detection. These substrates can be used as guidelines for future development of X-ray detectors. The filling of the larger volume trenches with perovskites, followed by the characterisation of the structures as X-ray detectors, would be the next steps in this project (discussed in Chapter 8). However, the knowledge already obtained on the perovskite growth, combined with the parallel development of X-ray characterisation techniques, will provide a strong foundation to approach the remaining challenges.

Chapter 8

Conclusions and Future Work

8.1 Conclusions

Current visible and X-ray detectors utilise traditional inorganic materials. However, the high-temperature fabrication and brittle mechanical properties makes novel device design with these materials difficult and expensive. In addition, the fixed properties, especially band gaps, limits the control offered over their spectral bandwidths and performance. Metal halide perovskites offer a solution to these restrictions. In this thesis, the unique properties of perovskites were exploited to improve the performance of visible light and X-ray detectors and develop devices with enhanced functionality over established technologies. However, some features of perovskites generated challenges when characterising their detection performance, and methods to accurately measure their detecting ability were described.

The outstanding optoelectronic properties of perovskites, which are retained when deposited from solution-based syntheses, enable detectors that already outcompete established materials after less than a decade of development. However, other characteristics of this material, especially the high density of mobile defects, can modify the performance of perovskite detectors over a range of timescales. This transient behaviour generates consistency issues and makes accurately characterising a detector's ability difficult. Moreover, the high and ionising energies of X-rays produce additional considerations when studying detector performance. In this work, we outlined these challenges, demonstrated the errors that can arise if not accounted for, and presented techniques to nullify their influence on measurements. These methods can be universally applied, and will be utilised for future characterisation of these materials.

The ability of perovskites to be fabricated from solution allows the design of new device structures that can advance detection. The tunable band gaps enabled multiband photodetectors to be developed, which can selectively detect specific regions of the visible spectrum. Precise control of absorption through two perovskite layers in a tandem structure provided this

functionality. The performance of this detector was optimised through the perovskite deposition and operating conditions to enable high selectivity and sensitivity, with detectivities approaching 10^{12} Jones in all modes. Importantly, the switching between these modes was rapid, with cut-off frequencies exceeding 1 MHz. This device was then used to successfully demonstrate a method to send optical information with additional security.

Direct X-ray detectors, despite their fundamental advantages over scintillator-based systems for high-resolution imaging, are a commercial rarity due to the challenge of long-distance carrier transport. By demonstrating the potential of lithographic trench structures to precisely pattern perovskites into arrays, we proposed a device structure that can overcome these limitations by decoupling the photon absorption and charge collection dimensions. The deposition of perovskites into these trenches was developed and devices were successfully deployed as photodetectors as a proof-of-concept demonstration. Patterns were designed to enable the scaling up to depths suitable for X-ray detection. These device structures, and the learnings of perovskite growth, will act as guidelines for new detector developments, offering the potential to revolutionise X-ray imaging by enabling direct detection of X-rays regardless of photon energy.

Overcoming the carrier transport limitations of direct detectors will enable efficient X-ray detection, but ultrafast performance will always require the rapid emission times of indirect detectors. Perovskite scintillators have impressed after a very short development period, currently showing light yields and response speeds in excess of existing materials. This work proposed the applications that will most benefit from these properties. We showed that PET scanning could be advanced with perovskites detectors, by exploiting the nanosecond decay times to add time-of-flight information and improve the diagnostic capabilities of this imaging technique. The ongoing steps towards perovskite scintillator commercialisation were also discussed, with solutions to the remaining limitations suggested that will allow the potential of this material to be realised. We demonstrated one of these solutions by exhibiting efficient scintillation in Cs_2ZrBr_6 nanocrystals, thanks to a large Stokes shift. The combined findings of this thesis aim to elevate perovskite detectors from a lab-scale success into a commercial reality.

8.2 Future Work

The wide scope of this thesis means there are several directions for future research, each aimed at further developing the understandings of the operating mechanisms of perovskite devices, as well as developing proof-of-concepts for real-world applications. The lessons learned on the accurate characterisation of detectors should be utilised throughout the next steps, in addition to being beneficial to the wider perovskite detector community.

8.2.1 Photodetectors

The findings in Chapter 4 suggest photodetector properties can be tuned by engineering the density, depth and distribution of defect states in perovskites. A systematic study of the low-light behaviour of identical devices, each with varying passivation techniques, would generalise the findings further and allow the detector performance to be optimised to application-specific requirements. Additional investigation into confirming the origins of the photoconductive gain in poor performing photovoltaic devices would be useful, which could later be selectively introduced in order to amplify detector responses. Photoluminescence studies would be useful here, on fresh and aged devices, to shed useful insight on the importance of carrier lifetimes to this mechanism. Lastly, the insight obtained into the influence of device polarity on reverse bias stability warrants more research, especially in aiming to identify the exact cause of this degradation. The importance of bias stability is important to many optoelectronic perovskite devices, especially solar cells, which are susceptible to this effect when modules are partially shaded. This increases the potential impact of this work. The role transport layers play in enabling or mitigating this degradation would be an additional interesting and application-relevant finding.

The unique response of multiband tandem photodetectors, developed in Chapter 5, present an opportunity for the commercialisation of a perovskite device. The encryption method already demonstrated could further display the device's credentials with the communication of real information, for example, using an encoded Morse message. Developing other applications that would benefit from the novel detection performance would be valuable, such as adding time-resolved information onto images. By optical gating the response at specified time intervals, the evolution of a signal with time can be generated. A low-cost time-resolved detector would have widespread use in microscopy and spectroscopy, and designing an experiment to display this ability would be of high importance.

8.2.2 Indirect X-Ray Detectors

The finding that Cs_2ZrBr_6 nanocrystals can overcome the low external light yields which currently restrict the potential of perovskite scintillators, whilst retaining suitable temporal performance for tomography, warrants further development of this material. The first steps would be the development of a simple deposition method that can produce thick and uniform scintillator films. This deposition method should also enable facile combination with photodetectors, to ease the integration into full indirect detector systems. The potential for functional mechanical properties, such as flexibility, should be explored during this phase.

Following this, the scintillation properties can be studied in more detail. Specifically, the absolute quantification of the light yield with pulse height spectroscopy would be advantageous, to enable comparisons to existing materials. The light yields can then be optimised using the suggestions in Chapter 6, for example, with passivation strategies and incorporation of photonic structures.

The final steps would be combining the scintillator with photodetector arrays and the demonstration of efficient X-ray detection and imaging. This will allow the spatial resolution to be measured, the results of which can be fed directly back into the device fabrication in order to optimise this metric. Incorporating the nanocrystals into a matrix, or patterned structures, could prevent light scattering and spreading from the point emission to the point of collection, and improve both the spatial resolution and imaging performance.

8.2.3 Direct X-Ray Detectors

The potential for the trench substrates to enable efficient direct detection, regardless of X-ray energy, make this a key area for future development. The findings from Chapter 7 can be used as guidelines for the next steps, utilising the design of the X-ray optimised structures. Once the designed substrates have been fabricated, the first goal would be to optimise the growth of perovskite in the large trenches. The large volumes would require more precursor solution to fill. As a result, it is expected that the drop casting method would be more suitable than spin coating, due to the large volumes of solution lost when spinning. As with the optical depth devices, constant feedback and redesigning of suitable trench patterns with the substrate fabricators would be required during this optimisation process. A potential method for the deposition of perovskite in the trenches could be inverse temperature growth of perovskite single crystals. Designing the trench features to reach the ends of the substrate, and covering the top of the substrate during deposition could allow this, similar to the space confined growth

of perovskite single crystals into thin structures. This may be a more suitable method for the large volumes, if drop casting is not sufficient.

Once fabricated, the X-ray detection ability can be assessed. The development of experimental techniques to measure X-ray detection performance was discussed in Chapter 7, and these methods should be utilised in these measurements. By measuring the key figures of merit, such as sensitivity and detection limits, the impact of different perovskite growth on X-ray detection can be evaluated. Correlating the influence of morphology on detector performance will act as a guideline for future growth developments.

Lastly, the trench substrates can be adapted for different X-ray applications. Trench depths can be tuned to a specific X-ray requirement, for example, the 140 keV X-rays utilised in CT scanners would need a different depth device to the 40 keV mammography energies. Similarly, different shapes and patterns of detector pixels would be required in applications, such as arrays for imaging detectors, which could be incorporated into future designs. Direct feedback from industrial collaborators would be useful here, as well as the lessons already learned from earlier substrate fabrication and perovskite deposition. Overall, using the high performance from optimised perovskite growth, combined with device structures that overcome the inherent issues facing existing direct detectors, perovskite-based trench devices could revolutionise the ways in which we use X-rays.

8.3 Closing Remarks

Our ability to image and communicate with the electromagnetic spectrum is limited by existing detector technology, and advancements with perovskite-based devices have the potential to transform how we use this radiation. In this thesis, we highlighted how such detectors can begin easing the strains on current communications bands, with secure visible light communications, and transform medical imaging, with improved spatial resolution and lower patient radiation risk in CT and PET scans. However, research into this material is still in its infancy, and perovskites remain an untapped resource. The findings of this thesis provide a foundation to progress this technology, and further development will continue to uncover additional applications that perovskites are uniquely placed to advance.

References

1 W. C. Röntgen, *Nature*, 1896, **53**, 274–276.

2 J. Holler, V. Tsiatsis, C. Mulligan, S. Karnouskos, S. Avesand and D. Boyle, *Internet of Things*, Academic Press, Oxford, 1st edn., 2014.

3 M. N. Ahangar, Q. Z. Ahmed, F. A. Khan and M. Hafeez, *Sensors*, 2021, **21**, 706.

4 K. Naughton, Driverless Cars' Need for Data Is Sparking a New Space Race, https://www.bloomberg.com/news/articles/2021-09-17/carmakers-look-to-satellites-for-future-of-self-driving-vehicles, (accessed 2 September 2022).

5 L. E. M. Matheus, A. B. Vieira, L. F. M. Vieira, M. A. M. Vieira and O. Gnawali, *IEEE Communications Surveys & Tutorials*, 2019, **21**, 3204–3237.

6 D. Tsonev, S. Videv and H. Haas, in *Broadband Access Communication Technologies VIII*, SPIE, 2014, vol. 9007, p. 900702.

7 P. J. Withers, C. Bouman, S. Carmignato, V. Cnudde, D. Grimaldi, C. K. Hagen, E. Maire, M. Manley, A. Du Plessis and S. R. Stock, *Nat Rev Methods Primers*, 2021, **1**, 1–21.

8 S. Dixon, *Diagnostic Imaging Dataset Annual Statistical 2016/2017 (NHS England)*, 2017.

9 R. Doll, *Br J Cancer*, 1995, **72**, 1339–1349.

10 E. J. Hall and D. J. Brenner, *The British Journal of Radiology*, 2012, **85**, 1316–1317.

11 O. D. I. Moseley, T. A. S. Doherty, R. Parmee, M. Anaya and S. D. Stranks, *J. Mater. Chem. C*, 2021, **9**, 11588–11604.

12 Jenny Nelson, *Physics of Solar Cells*, Imperial College Press, London, 1st edn., 2003.

13 P. A. Rodnyi, *Physical Processes in Inorganic Scintillators*, CRC Press, Boca Raton, 1st edn., 1997.

14 C. A. Klein, *Journal of Applied Physics*, 1968, **39**, 2029–2038.

15 D. K. Ferry, in *Semiconductors: Bonds and bands*, IOP Publishing, Bristol, 2nd edn., 2019.

16 Andrew Burrows, in *Chemistry3*, Oxford University Press, Oxford, 2nd edn., 2009, pp. 448–470.

17 T. Markvart and L. Castañer, in *Solar Cells*, ed. A. McEvoy, Elsevier, Oxford, 2nd edn., 2013, pp. 27–54.

18 M. A. Green and M. J. Keevers, *Progress in Photovoltaics: Research and Applications*, 1995, **3**, 189–192.

19 M. J. Berger, J. H. Hubbell, S. M. Seltzer, J. Chang, J. S. Coursey, R. Sukumar, D. S. Zucker and K. Olsen, XCOM: Photon Cross Sections Database, https://www.nist.gov/pml/xcom-photon-cross-sections-database (accessed July 2022).

20 P. Allisy-Roberts and J. Williams, in *Farr's Physics for Medical Imaging*, W.B. Saunders, Edinburgh, 2nd edn., 2008, pp. 1–21.

21 Z. Yang, Y. Deng, X. Zhang, S. Wang, H. Chen, S. Yang, J. Khurgin, N. X. Fang, X. Zhang and R. Ma, *Advanced Materials*, 2018, **30**, 1704333.

22 Q. Lin, A. Armin, D. M. Lyons, P. L. Burn and P. Meredith, *Advanced Materials*, 2015, **27**, 2060–2064.

23 C. Bao, Z. Chen, Y. Fang, H. Wei, Y. Deng, X. Xiao, L. Li and J. Huang, *Advanced Materials*, 2017, **29**, 1703209.

24 S. K. Saha, in *High Resolution Imaging: Detectors and Applications*, Jenny Stanford Publishing, Singapore, 2015, pp. 250–300.

25 G. Cen, Y. Liu, C. Zhao, G. Wang, Y. Fu, G. Yan, Y. Yuan, C. Su, Z. Zhao and W. Mai, *Small*, 2019, **15**, 1902135.

26 S.-F. Leung, K.-T. Ho, P.-K. Kung, V. K. S. Hsiao, H. N. Alshareef, Z. L. Wang and J.-H. He, *Advanced Materials*, 2018, **30**, 1704611.

27 T. Zou, X. Liu, R. Qiu, Y. Wang, S. Huang, C. Liu, Q. Dai and H. Zhou, *Advanced Optical Materials*, 2019, **7**, 1801812.

28 Y. H. Lee, I. Song, S. H. Kim, J. H. Park, S. O. Park, J. H. Lee, Y. Won, K. Cho, S. K. Kwak and J. H. Oh, *Advanced Materials*, 2020, **32**, 2002357.

29 D. Liu, B.-B. Yu, M. Liao, Z. Jin, L. Zhou, X. Zhang, F. Wang, H. He, T. Gatti and Z. He, *ACS Appl. Mater. Interfaces*, 2020, **12**, 30530–30537.

30 H. Sun, W. Tian, F. Cao, J. Xiong and L. Li, *Advanced Materials*, 2018, **30**, 1706986.

31 G. Li, Y. Wang, L. Huang and W. Sun, *ACS Appl. Electron. Mater.*, 2022, **4**, 1485–1505.

32 G. Simone, M. J. Dyson, C. H. L. Weijtens, S. C. J. Meskers, R. Coehoorn, R. A. J. Janssen and G. H. Gelinck, *Advanced Optical Materials*, 2020, **8**, 1901568.

33 L. Pan, S. Shrestha, N. Taylor, W. Nie and L. R. Cao, *Nat Commun*, 2021, **12**, 5258.

34 I. Clairand, J.-M. Bordy, E. Carinou, J. Daures, J. Debroas, M. Denozière, L. Donadille, M. Ginjaume, C. Itié, C. Koukorava, S. Krim, A.-L. Lebacq, P. Martin, L. Struelens, M. Sans-Merce and F. Vanhavere, *Radiation Measurements*, 2011, **46**, 1252–1257.

35 L. Basiricò, A. Ciavatti and B. Fraboni, *Advanced Materials Technologies*, 2021, **6**, 2000475.

36 E. Säckinger, in *Analysis and Design of Transimpedance Amplifiers for Optical Receivers*, John Wiley & Sons, Inc., New Jersey, USA, 1st edn., 2018, pp. 43–106.

37 L. Dou, Y. Yang, J. You, Z. Hong, W.-H. Chang, G. Li and Y. Yang, *Nat Commun*, 2014, **5**, 5404.

38 M. I. Saidaminov, V. Adinolfi, R. Comin, A. L. Abdelhady, W. Peng, I. Dursun, M. Yuan, S. Hoogland, E. H. Sargent and O. M. Bakr, *Nat Commun*, 2015, **6**, 8724.

39 B. Yang, Y.-J. Li, Y.-X. Tang, X. Mao, C. Luo, M.-S. Wang, W.-Q. Deng and K.-L. Han, *J. Phys. Chem. Lett.*, 2018, **9**, 3087–3092.

40 M. C. Nuss, D. H. Auston and F. Capasso, *Phys. Rev. Lett.*, 1987, **58**, 2355–2358.

41 A. C. Warren, J. H. Burroughes, J. M. Woodall, D. T. McInturff, R. T. Hodgson and M. R. Melloch, *IEEE Electron Device Letters*, 1991, **12**, 527–529.

42 K. J. Siebert, H. Quast, R. Leonhardt, T. Löffler, M. Thomson, T. Bauer, H. G. Roskos and S. Czasch, *Appl. Phys. Lett.*, 2002, **80**, 3003–3005.

43 L. Laperriere, O. Bubon, G. Belev, G. DeCrescenzo, O. Tousignant, A. Reznik, H. Mani, J. Greenspan, J. A. Rowlands, J. B. Frey, K. S. Karim and S. Kasap, *Sensors*, 2011, **11**, 5112–5157.

44 P. Lecoq, *Nuclear Instruments and Methods in Physics Research, Section A: Accelerators, Spectrometers, Detectors and Associated Equipment*, 2016, **809**, 130–139.

45 B. G. Lowe and R. A. Sareen, in *Semiconductor X-Ray Detectors*, CRC Press, Boca Raton, 1st edn., 2013, pp. 370–392.

46 N. Rao, B. Ament, R. Parmee, J. Cameron and M. Mayo, *Journal of Pharmaceutical Innovation*, 2018, **13**, 270–282.

47 P. M. Shikhaliev, *Phys. Med. Biol.*, 2006, **51**, 4267–4287.

48 P. M. Shikhaliev, S. G. Fritz and J. W. Chapman, *Medical Physics*, 2009, **36**, 5107–5119.

49 M. Spahn, *Nuclear Instruments and Methods in Physics Research A*, 2013, **731**, 57–63.

50 B. Zhao and W. Zhao, *Med Phys*, 2008, **35**, 1978–1987.

51 C. W. E. van Eijk, *Nuclear Instruments and Methods in Physics Research A*, 2003, **509**, 17–25.

52 C. W. E. van Eijk, *Nuclear Tracks and Radiation Measurements*, 1993, **21**, 5–10.

53 C. W. E. van Eijk, *Proceedings of SPIE - The International Society for Optical Engineering*, 1996, **2706**, 158–167.

54 M. D. Birowosuto, D. Cortecchia, W. Drozdowski, K. Brylew, W. Lachmanski, A. Bruno and C. Soci, *Scientific Reports*, 2016, **6**, 37254.

55 C. W. E. van Eijk, *Physics in Medicine and Biology*, 2002, **47**, 85–106.

56 T. Yanagida, *Proc Jpn Acad Ser B Phys Biol Sci.*, 2018, **94**, 75–97.

57 C. Celiktas, E. E. Ermis and M. Bayburt, *Journal of Radioanalytical and Nuclear Chemistry*, 2012, **293**, 377–382.

58 J. D. Valentine, W. W. Moses, S. E. Derenzo, D. K. Wehe and G. F. Knoll, *Nuclear Inst. and Methods in Physics Research, A*, 1993, **325**, 147–157.

59 C. M. Carpenter, C. Sun, G. Pratx, R. Rao and L. Xing, *Medical Physics*, 2010, **37**, 4011–4018.

60 C. Michail, V. Koukou, N. Martini, G. Saatsakis, N. Kalyvas, A. Bakas, I. Kandarakis, G. Fountos, G. Panayiotakis and I. Valais, *Crystals*, 2020, **10**, 429–429.

61 V. B. Mikhailik and H. Kraus, *Journal of Physical Studies*, 2010, **14**, 4201–4201.

62 C. L. Melcher and J. S. Schweitzer, *IEEE Transactions on Nuclear Science*, 1992, **39**, 502–505.

63 E. V. D. Van Loef, P. Dorenbos, C. W. E. Van Eijk, K. W. Krämer and H. U. Güdel, *Nuclear Inst. and Methods in Physics Research, A*, 2002, **486**, 254–258.

64 P. Lecoq, I. Dafinei, E. Auffray, M. Schneegans, M. V. Korzhik, O. V. Missevitch, V. B. Pavlenko, A. A. Fedorov, A. N. Annenkov, V. L. Kostylev and V. D. Ligun, *Nuclear Inst. and Methods in Physics Research, A*, 1995, **365**, 291–298.

65 E. Sakai, *IEEE Transactions on Nuclear Science*, 2001, **34**, 418–422.

66 L. Swiderski, M. Moszynski, A. Syntfeld-Kazuch, M. Szawlowski and T. Szczesniak, *Nuclear Inst. and Methods in Physics Research, A*, 2014, **749**, 68–73.

67 V. M. Goldschmidt, *Naturwissenschaften*, 1926, **14**, 477–485.

68 C. J. Bartel, C. Sutton, B. R. Goldsmith, R. Ouyang, C. B. Musgrave, L. M. Ghiringhelli and M. Scheffler, *Science Advances*, 2019, **5**, 1–5.

69 F. Ünlü, E. Jung, S. Öz, H. Choi, T. Fischer and S. Mathur, in *Perovskite Solar Cells*, John Wiley & Sons, Ltd, Weinheim, 2021, pp. 1–31.

70 J. Zhou and J. Huang, *Advanced Science*, 2018, **5**, 1700256.

71 S. Sun, T. Salim, N. Mathews, M. Duchamp, C. Boothroyd, G. Xing, T. C. Sum and Y. M. Lam, *Energy and Environmental Science*, 2014, **7**, 399–407.

72 G. D. Cody, *Journal of Non-Crystalline Solids*, 1992, **141**, 3–15.

73 Y. H. Chang and C. H. Park, *Journal of the Korean Physics Society*, 2004, **44**, 889–893.

74 R. Prasanna, A. Gold-Parker, T. Leijtens, B. Conings, A. Babayigit, H.-G. Boyen, M. F. Toney and M. D. McGehee, *J. Am. Chem. Soc.*, 2017, **139**, 11117–11124.

75 M. Anaya, G. Lozano, M. E. Calvo and H. Míguez, *Joule*, 2017, **1**, 769–793.

76 P. Wangyang, C. Gong, G. Rao, K. Hu, X. Wang, C. Yan, L. Dai, C. Wu and J. Xiong, *Advanced Optical Materials*, 2018, **6**, 1701302.

77 K. Galkowski, A. Mitioglu, A. Miyata, P. Plochocka, O. Portugall, G. E. Eperon, J. T.-W. Wang, T. Stergiopoulos, S. D. Stranks, H. J. Snaith and R. J. Nicholas, *Energy Environ. Sci.*, 2016, **9**, 962–970.

78 H. Wei, Y. Fang, P. Mulligan, W. Chuirazzi, H. H. Fang, C. Wang, B. R. Ecker, Y. Gao, M. A. Loi, L. Cao and J. Huang, *Nature Photonics*, 2016, **10**, 333–339.

79 R. Brenes, D. Guo, A. Osherov, N. K. Noel, C. Eames, E. M. Hutter, S. K. Pathak, F. Niroui, R. H. Friend, M. S. Islam, H. J. Snaith, V. Bulović, T. J. Savenije and S. D. Stranks, *Joule*, 2017, **1**, 155–167.

80 Q. Dong, Y. Fang, Y. Shao, P. Mulligan, J. Qiu, L. Cao and J. Huang, *Science*, 2015, **347**, 967–971.

81 D. Shi, V. Adinolfi, R. Comin, M. Yuan, E. Alarousu, A. Buin, Y. Chen, S. Hoogland, A. Rothenberger, K. Katsiev, Y. Losovyj, X. Zhang, P. A. Dowben, O. F. Mohammed, E. H. Sargent and O. M. Bakr, *Science*, 2015, **347**, 6221.

82 N. D. Arora, J. R. Hauser and D. J. Roulston, *IEEE Transactions on Electron Devices*, 1982, **29**, 292–295.

83 A. D. Wright, C. Verdi, R. L. Milot, G. E. Eperon, M. A. Pérez-Osorio, H. J. Snaith, F. Giustino, M. B. Johnston and L. M. Herz, *Nat Commun*, 2016, **7**, 11755.

84 S. D. Stranks, G. E. Eperon, G. Grancini, C. Menelaou, M. J. Alcocer, T. Leijtens, L. M. Herz, A. Petrozza and H. J. Snaith, *Science*, 2013, **342**, 341–4.

85 D. W. deQuilettes, S. Koch, S. Burke, R. K. Paranji, A. J. Shropshire, M. E. Ziffer and D. S. Ginger, *ACS Energy Lett.*, 2016, **1**, 438–444.

86 S. D. Stranks, V. M. Burlakov, T. Leijtens, J. M. Ball, A. Goriely and H. J. Snaith, *Physical Review Applied*, 2014, **2**, 1–8.

87 K. Miyata, D. Meggiolaro, M. T. Trinh, P. P. Joshi, E. Mosconi, S. C. Jones, F. De Angelis and X.-Y. Zhu, *Science Advances*, 2017, **3**, 1701217.

88 K. Frohna, T. Deshpande, J. Harter, W. Peng, B. A. Barker, J. B. Neaton, S. G. Louie, O. M. Bakr, D. Hsieh and M. Bernardi, *Nature Communications*, 2018, **9**, 1829.

89 F. Zheng, L. Z. Tan, S. Liu and A. M. Rappe, *Nano Letters*, 2015, **15**, 7794–7800.

90 G. J. Wetzelaer, M. Scheepers, A. M. Sempere, C. Momblona, J. Avila and H. J. Bolink, *Advanced materials*, 2015, **27**, 1837–41.

91 Z. Ni, C. Bao, Y. Liu, Q. Jiang, W.-Q. Wu, S. Chen, X. Dai, B. Chen, B. Hartweg, Z. Yu, Z. Holman and J. Huang, *Science*, 2020, **367**, 1352–1358.

92 M. A. Mahmud, T. Duong, Y. Yin, H. T. Pham, D. Walter, J. Peng, Y. Wu, L. Li, H. Shen, N. Wu, N. Mozaffari, G. Andersson, K. R. Catchpole, K. J. Weber and T. P. White, *Advanced Functional Materials*, 2020, **30**, 1907962.

93 J. Yuan, L. Zhang, C. Bi, M. Wang and J. Tian, *Solar RRL*, 2018, **2**, 1800188.

94 S. Yang, J. Dai, Z. Yu, Y. Shao, Y. Zhou, X. Xiao, X. C. Zeng and J. Huang, *J. Am. Chem. Soc.*, 2019, **141**, 5781–5787.

95 K. Frohna and S. D. Stranks, in *Handbook of Organic Materials for Electronic and Photonic Devices*, ed. O. Ostroverkhova, Woodhead Publishing, Cambridge, 2nd edn., 2019, pp. 211–256.

96 F. Zhang, H. Lu, J. Tong, J. J. Berry, M. C. Beard and K. Zhu, *Energy Environ. Sci.*, 2020, **13**, 1154–1186.

97 J. C. Blancon, H. Tsai, W. Nie, C. C. Stoumpos, L. Pedesseau, C. Katan, M. Kepenekian, C. M. M. Soe, K. Appavoo, M. Y. Sfeir, S. Tretiak, P. M. Ajayan, M. G. Kanatzidis, J. Even, J. J. Crochet and A. D. Mohite, *Science*, 2017, **355**, 1288–1292.

98 Q. Chen, J. Wu, X. Ou, B. Huang, J. Almutlaq, A. A. Zhumekenov, X. Guan, S. Han, L. Liang, Z. Yi, J. Li, X. Xie, Y. Wang, Y. Li, D. Fan, D. B. L. Teh, A. H. All, O. F. Mohammed, O. M. Bakr, T. Wu, M. Bettinelli, H. Yang, W. Huang and X. Liu, *Nature*, 2018, **561**, 88–93.

99 J. H. Heo, D. H. Shin, J. K. Park, D. H. Kim, S. J. Lee and S. H. Im, *Advanced Materials*, 2018, **30**, 1–6.

100 F. Yan and H. Volkan Demir, *Nanoscale*, 2019, **11**, 11402–11412.

101 A. M. Stoneham, *Reports on Progress in Physics*, 1981, **44**, 1251.

102 P. Y. Yu and M. Cardona, in *Fundamentals of Semiconductors: Physics and Materials Properties*, eds. P. Y. Yu and M. Cardona, Springer, Berlin, Heidelberg, 1996, pp. 159–202.

103 D. Banerjee and K. K. Chattopadhyay, *Hybrid Inorganic Organic Perovskites*, Elsevier, Cambridge, 2018.

104 R. Dong, Y. Fang, J. Chae, J. Dai, Z. Xiao, Q. Dong, Y. Yuan, A. Centrone, X. C. Zeng and J. Huang, *Advanced Materials*, 2015, **27**, 1912–1918.

105 J. R. Ayres, *Journal of Applied Physics*, 1993, **74**, 1787–1792.

106 R. E. Brandt, V. Stevanović, D. S. Ginley and T. Buonassisi, *MRS Communications*, 2015, **5**, 265–275.

107 W.-J. Yin, T. Shi and Y. Yan, *Appl. Phys. Lett*, 2014, **104**, 63903.

108 H. Min, D. Y. Lee, J. Kim, G. Kim, K. S. Lee, J. Kim, M. J. Paik, Y. K. Kim, K. S. Kim, M. G. Kim, T. J. Shin and S. Il Seok, *Nature*, 2021, **598**, 444–450.

109 H. Min, M. Kim, S.-U. Lee, H. Kim, G. Kim, K. Choi, J. H. Lee and S. I. Seok, *Science*, 2019, **366**, 749–753.

110 J. Jeong, M. Kim, J. Seo, H. Lu, P. Ahlawat, A. Mishra, Y. Yang, M. A. Hope, F. T. Eickemeyer, M. Kim, Y. J. Yoon, I. W. Choi, B. P. Darwich, S. J. Choi, Y. Jo, J. H. Lee, B. Walker, S. M. Zakeeruddin, L. Emsley, U. Rothlisberger, A. Hagfeldt, D. S. Kim, M. Grätzel and J. Y. Kim, *Nature*, 2021, **592**, 381–385.

111 J. J. Yoo, G. Seo, M. R. Chua, T. G. Park, Y. Lu, F. Rotermund, Y.-K. Kim, C. S. Moon, N. J. Jeon, J.-P. Correa-Baena, V. Bulović, S. S. Shin, M. G. Bawendi and J. Seo, *Nature*, 2021, **590**, 587–593.

112 E. M. Tennyson, T. A. S. Doherty and S. D. Stranks, *Nat Rev Mater*, 2019, **4**, 573–587.

113 T. A. S. Doherty, A. J. Winchester, S. Macpherson, D. N. Johnstone, V. Pareek, E. M. Tennyson, S. Kosar, F. U. Kosasih, M. Anaya, M. Abdi-Jalebi, Z. Andaji-Garmaroudi, E. L. Wong, J. Madéo, Y.-H. Chiang, J.-S. Park, Y.-K. Jung, C. E. Petoukhoff, G. Divitini, M. K. L. Man, C. Ducati, A. Walsh, P. A. Midgley, K. M. Dani and S. D. Stranks, *Nature*, 2020, **580**, 360–366.

114 G. W. P. Adhyaksa, S. Brittman, H. Āboliņš, A. Lof, X. Li, J. D. Keelor, Y. Luo, T. Duevski, R. M. A. Heeren, S. R. Ellis, D. P. Fenning and E. C. Garnett, *Advanced Materials*, 2018, **0**, 1804792.

115 A.-F. Castro-Méndez, J. Hidalgo and J.-P. Correa-Baena, *Advanced Energy Materials*, 2019, **9**, 1901489.

116 Y. Zhang, Y. Liu, Z. Xu, H. Ye, Q. Li, M. Hu, Z. Yang and S. F. Liu, *Journal of Materials Chemistry C*, 2019, **4**, 1–224.

117 D. M. Jang, K. Park, D. H. Kim, J. Park, F. Shojaei, H. S. Kang, J. P. Ahn, J. W. Lee and J. K. Song, *Nano Lett*, 2015, **15**, 5191–5199.

118 Y. Dang, Y. Liu, Y. Sun, D. Yuan, X. Liu, W. Lu, G. Liu, H. Xia and X. Tao, *CrystEngComm*, 2015, **17**, 665–670.

119 G. Grancini, A. R. Srimath Kandada, J. M. Frost, A. J. Barker, M. De Bastiani, M. Gandini, S. Marras, G. Lanzani, A. Walsh and A. Petrozza, *Nat Photonics*, 2015, **9**, 695–701.

120 J. M. Kadro, K. Nonomura, D. Gachet, M. Grätzel and A. Hagfeldt, *Sci Rep*, 2015, **5**, 11654.

121 M. I. Saidaminov, A. L. Abdelhady, B. Murali, E. Alarousu, V. M. Burlakov, W. Peng, I. Dursun, L. Wang, Y. He, G. Maculan, A. Goriely, T. Wu, O. F. Mohammed and O. M. Bakr, *Nat Commun*, 2015, **6**, 7586.

122 Y.-X. Chen, Q.-Q. Ge, Y. Shi, J. Liu, D.-J. Xue, J.-Y. Ma, J. Ding, H.-J. Yan, J.-S. Hu and L.-J. Wan, *J. Am. Chem. Soc.*, 2016, **138**, 16196–16199.

123 Y. Liu, Y. Zhang, Z. Yang, D. Yang, X. Ren, L. Pang and S. F. Liu, *Advanced Materials*, 2016, **28**, 9203–9203.

124 National Renewable Energy Labs (NREL) Efficiency Chart, https://www.nrel.gov/pv/cell-efficiency.html, (accessed 1 July 2022).

125 M. M. Lee, J. Teuscher, T. Miyasaka, T. N. Murakami and H. J. Snaith, *Science*, 2012, **338**, 643–646.

126 G. Giorgi, J. I. Fujisawa, H. Segawa and K. Yamashita, *J Phys Chem Lett*, 2013, **4**, 4213–4216.

127 W. Shockley and H. J. Queisser, *Journal of Applied Physics*, 1961, **32**, 510–519.

128 R. Lin, J. Xu, M. Wei, Y. Wang, Z. Qin, Z. Liu, J. Wu, K. Xiao, B. Chen, S. M. Park, G. Chen, H. R. Atapattu, K. R. Graham, J. Xu, J. Zhu, L. Li, C. Zhang, E. H. Sargent and H. Tan, *Nature*, 2022, **603**, 72.

129 A. Al-Ashouri, E. Köhnen, B. Li, A. Magomedov, H. Hempel, P. Caprioglio, J. A. Márquez, A. B. M. Vilches, E. Kasparavicius, J. A. Smith, N. Phung, D. Menzel, M. Grischek, L. Kegelmann, D. Skroblin, C. Gollwitzer, T. Malinauskas, M. Jošt, G. Matič, B. Rech, R. Schlatmann, M. Topič, L. Korte, A. Abate, B. Stannowski, D. Neher, M. Stolterfoht, T. Unold, V. Getautis and S. Albrecht, *Science*, 2020, **370**, 1300–1309.

130 Y.-H. Kim, S. Kim, A. Kakekhani, J. Park, J. Park, Y.-H. Lee, H. Xu, S. Nagane, R. B. Wexler, D.-H. Kim, S. H. Jo, L. Martínez-Sarti, P. Tan, A. Sadhanala, G.-S. Park, Y.-W. Kim, B. Hu, H. J. Bolink, S. Yoo, R. H. Friend, A. M. Rappe and T.-W. Lee, *Nat. Photonics*, 2021, **15**, 148–155.

131 Y. Cao, N. Wang, H. Tian, J. Guo, Y. Wei, H. Chen, Y. Miao, W. Zou, K. Pan, Y. He, H. Cao, Y. Ke, M. Xu, Y. Wang, M. Yang, K. Du, Z. Fu, D. Kong, D. Dai, Y. Jin, G. Li, H. Li, Q. Peng, J. Wang and W. Huang, *Nature*, 2018, **562**, 249–253.

132 W. Xu, Q. Hu, S. Bai, C. Bao, Y. Miao, Z. Yuan, T. Borzda, A. J. Barker, E. Tyukalova, Z. Hu, M. Kawecki, H. Wang, Z. Yan, X. Liu, X. Shi, K. Uvdal, M. Fahlman, W. Zhang, M. Duchamp, J.-M. Liu, A. Petrozza, J. Wang, L.-M. Liu, W. Huang and F. Gao, *Nature Photonics*, 2019, **13**, 418–424.

133 F. Deschler, M. Price, S. Pathak, L. E. Klintberg, D. D. Jarausch, R. Higler, S. Huttner, T. Leijtens, S. D. Stranks, H. J. Snaith, M. Atature, R. T. Phillips and R. H. Friend, *J Phys Chem Lett*, 2014, **5**, 1421–6.

134 Z. Li, J. Moon, A. Gharajeh, R. Haroldson, R. Hawkins, W. Hu, A. Zakhidov and Q. Gu, *ACS Nano*, 2018, **12**, 10968–10976.

135 S. W. Eaton, M. Lai, N. A. Gibson, A. B. Wong, L. Dou, J. Ma, L.-W. Wang, S. R. Leone and P. Yang, *Proceedings of the National Academy of Sciences*, 2016, **113**, 1993–1998.

136 Z. Xiao and J. Huang, *Advanced Electronic Materials*, 2016, **2**, 1600100.

137 K. Yan, M. Peng, X. Yu, X. Cai, S. Chen, H. Hu, B. Chen, X. Gao, B. Dong and D. Zou, *Journal of Materials Chemistry C*, 2016, **4**, 1375–1381.

138 R. A. John, N. Shah, S. K. Vishwanath, S. E. Ng, B. Febriansyah, M. Jagadeeswararao, C.-H. Chang, A. Basu and N. Mathews, *Nat Commun*, 2021, **12**, 3681.

139 T. Matsushima, F. Mathevet, B. Heinrich, S. Terakawa, T. Fujihara, C. Qin, A. S. D. Sandanayaka, J.-C. Ribierre and C. Adachi, *Appl. Phys. Lett.*, 2016, **109**, 253301.

140 Abd. R. bin Mohd. Yusoff, H. P. Kim, X. Li, J. Kim, J. Jang and M. K. Nazeeruddin, *Advanced Materials*, 2017, **29**, 1602940.

141 W. Yu, F. Li, L. Yu, M. R. Niazi, Y. Zou, D. Corzo, A. Basu, C. Ma, S. Dey, M. L. Tietze, U. Buttner, X. Wang, Z. Wang, M. N. Hedhili, C. Guo, T. Wu and A. Amassian, *Nature Communications*, 2018, **9**, 5354.

142 H. R. Xia, J. Li, W. T. Sun and L. M. Peng, *Chemical Communications*, 2014, **50**, 13695–13697.

143 X. Hu, X. Zhang, L. Liang, J. Bao, S. Li, W. Yang and Y. Xie, *Advanced Functional Materials*, 2014, **24**, 7373–7380.

144 T. Moehl, J.-H. Im, Y. H. Lee, K. Domanski, F. Giordano, S. M. Zakeeruddin, M. I. Dar, L.-P. Heiniger, M. K. Nazeeruddin, N.-G. Park and M. Grätzel, *The Journal of Physical Chemistry Letters*, 2014, **5**, 3937–3936.

145 B. R. Sutherland, A. K. Johnston, A. H. Ip, J. Xu, V. Adinolfi, P. Kanjanaboos and E. H. Sargent, *ACS Photonics*, 2015, **2**, 1117–1123.

146 Y. Fang and J. Huang, *Advanced Materials*, 2015, **27**, 2804–2810.

147 H. Deng, X. Yang, D. Dong, B. Li, D. Yang, S. Yuan, K. Qiao, Y.-B. Cheng, J. Tang and H. Song, *Nano Letters*, 2015, **15**, 7963–7969.

148 H. Sun, T. Lei, W. Tian, F. Cao, J. Xiong and L. Li, *Small*, 2017, **13**, 1701042.

149 C. Bao, W. Zhu, J. Yang, F. Li, S. Gu, Y. Wang, T. Yu, J. Zhu, Y. Zhou and Z. Zou, *ACS Applied Materials & Interfaces*, 2016, **8**, 23868–23875.

150 S. F. Leung, K. T. Ho, P. K. Kung, V. K. S. Hsiao, H. N. Alshareef, Z. L. Wang and J. H. He, *Advanced Materials*, 2018, **30**, 1704611.

151 Y. Zhan, Y. Wang, Q. Cheng, C. Li, K. Li, H. Li, J. Peng, B. Lu, Y. Wang, Y. Song, L. Jiang and M. Li, *Angewandte Chemie*, 2019, **131**, 16608–16614.

152 J. Ghosh, G. Natu and P. K. Giri, *Organic Electronics*, 2019, **71**, 175–184.

153 B. Du, W. Yang, Q. Jiang, H. Shan, D. Luo, B. Li, W. Tang, F. Lin, B. Shen, Q. Gong, X. Zhu, R. Zhu and Z. Fang, *Advanced Optical Materials*, 2018, **6**, 1701271.

154 Y. Dong, Y. Gu, Y. Zou, J. Song, L. Xu, J. Li, J. Xue, X. Li and H. Zeng, *Small*, 2016, **12**, 5622–5632.

155 W. Wang, D. Zhao, F. Zhang, L. Li, M. Du, C. Wang, Y. Yu, Q. Huang, M. Zhang, L. Li, J. Miao, Z. Lou, G. Shen, Y. Fang and Y. Yan, *Advanced Functional Materials*, 2017, **27**, 1703953.

156 N. Ma, J. Jiang, Y. Zhao, L. He, Y. Ma, H. Wang, L. Zhang, C. Shan, L. Shen and W. Hu, *Nano Energy*, 2021, **86**, 106113.

157 A. Waleed, M. M. Tavakoli, L. Gu, Z. Wang, D. Zhang, A. Manikandan, Q. Zhang, R. Zhang, Y.-L. Chueh and Z. Fan, *Nano Lett.*, 2017, **17**, 523–530.

158 Y. Guo, C. Liu, H. Tanaka and E. Nakamura, *The Journal of Physical Chemistry Letters*, 2015, **6**, 535–539.

159 C. H. Kang, I. Dursun, G. Liu, L. Sinatra, X. Sun, M. Kong, J. Pan, P. Maity, E. Ooi, T. K. Ng, O. F. Mohammed, O. M. Bakr and B. S. Ooi, *Light: Science & Applications*, 2019, **8**, 94.

160 M. Zhang, L. Wang, L. Meng, X.-G. Wu, Q. Tan, Y. Chen, W. Liang, F. Jiang, Y. Cai and H. Zhong, *Advanced Optical Materials*, 2018, **6**, 1800077.

161 J. Lu, X. Sheng, G. Tong, Z. Yu, X. Sun, L. Yu, X. Xu, J. Wang, J. Xu, Y. Shi and K. Chen, *Advanced Materials*, 2017, **29**, 1700400.

162 A. Armin, R. D. Jansen-Van Vuuren, N. Kopidakis, P. L. Burn and P. Meredith, *Nature Communications*, 2015, **6**, 6343–6343.

163 J. Xue, Z. Zhu, X. Xu, Y. Gu, S. Wang, L. Xu, Y. Zou, J. Song, H. Zeng and Q. Chen, *Nano Letters*, 2018, **18**, 7628–7634.

164 Q. Lin, A. Armin, P. L. Burn and P. Meredith, *Nature Photonics*, 2015, **9**, 687–694.

165 Y. Fang, Q. Dong, Y. Shao, Y. Yuan and J. Huang, *Nature Photonics*, 2015, **9**, 679–686.

166 J. Zhou, J. Luo, X. Rong, P. Wei, M. S. Molokeev, Y. Huang, J. Zhao, Q. Liu, X. Zhang, J. Tang and Z. Xia, *Advanced Optical Materials*, 2019, **7**, 1900139.

167 J. Wang, S. Xiao, W. Qian, K. Zhang, J. Yu, X. Xu, G. Wang, S. Zheng and S. Yang, *Advanced Materials*, 2021, **33**, 2005557.

168 J. Li, J. Wang, J. Ma, H. Shen, L. Li, X. Duan and D. Li, *Nature Communications*, 2019, **10**, 806–806.

169 L. Li, Y. Deng, C. Bao, Y. Fang, H. Wei, S. Tang, F. Zhang and J. Huang, *Advanced Optical Materials*, 2017, **5**, 1700672–1700672.

170 R. Rehm, M. Walther, J. Schmitz, J. Fleißner, J. Ziegler, W. Cabanski and R. Breiter, *Electronics Letters*, 2006, **42**, 577–578.

171 R. Rehm, M. Walther, J. Schmitz, F. Rutz, A. Wörl, R. Scheibner and J. Ziegler, in *Infrared Technology and Applications XXXVI*, SPIE, 2010, vol. 7660, pp. 456–467.

172 A. Srinivasan, S. Murtaza, J. C. Campbell and B. G. Streetman, *Appl. Phys. Lett.*, 1995, **66**, 535–537.

173 H. Kim, W. Kim, Y. Pak, T. J. Yoo, H.-W. Lee, B. H. Lee, S. Kwon and G. Y. Jung, *Laser & Photonics Reviews*, 2020, **14**, 2000305.

174 B. Huang, J. Liu, Z. Han, Y. Gu, D. Yu, X. Xu and Y. Zou, *ACS Appl. Mater. Interfaces*, 2020, **12**, 48765–48772.

175 J. Song, Q. Cui, J. Li, X. Jiayue, Y. Wang, L. Xu, J. Xue, Y. Dong, T. Tian, H. Sun and H. Zeng, *Advanced Optical Materials*, 2017, **5**, 1700157.

176 J. Liu, Y. Zou, B. Huang, Y. Gu, Y. Yang, Z. Han, Y. Zhang, X. Xu and H. Zeng, *Nanoscale*, 2020, **12**, 20386–20395.

177 L. Li, H. Chen, Z. Fang, X. Meng, C. Zuo, M. Lv, Y. Tian, Y. Fang, Z. Xiao, C. Shan, Z. Xiao, Z. Jin, G. Shen, L. Shen and L. Ding, *Advanced Materials*, 2020, **32**, 1907257.

178 Z. Lan, Y. Lei, W. K. E. Chan, S. Chen, D. Luo and F. Zhu, *Science Advances*, 2020, **6**, 1–9.

179 M. I. Saidaminov, M. A. Haque, M. Savoie, A. L. Abdelhady, N. Cho, I. Dursun, U. Buttner, E. Alarousu, T. Wu and O. M. Bakr, *Adv Mater*, 2016, **28**, 8144–8149.

180 C. C. Stoumpos, C. D. Malliakas, J. A. Peters, Z. Liu, M. Sebastian, J. Im, T. C. Chasapis, A. C. Wibowo, D. Y. Chung, A. J. Freeman, B. W. Wessels and M. G. Kanatzidis, *Crystal Growth and Design*, 2013, **13**, 2722–2727.

181 H. Wei, D. DeSantis, W. Wei, Y. Deng, D. Guo, T. J. Savenije, L. Cao and J. Huang, *Nature Mater*, 2017, **16**, 826–833.

182 Y. He, L. Matei, H. Joon Jung, K. M. McCall, M. Chen, C. C. Stoumpos, Z. Liu, J. A. Peters, D. Young Chung, B. W. Wessels, M. R. Wasielewski, V. P. Dravid, A. Burger and M. G. Kanatzidis, *Nature Communications*, 2018, **10**, 293–295.

183 S. Yakunin, D. N. Dirin, Y. Shynkarenko, V. Morad, I. Cherniukh, O. Nazarenko, D. Kreil, T. Nauser and M. V. Kovalenko, *Nature Photonics*, 2016, **10**, 585–589.

184 W. Wei, Y. Zhang, Q. Xu, H. Wei, Y. Fang, Q. Wang, Y. Deng, T. Li, A. Gruverman, L. Cao and J. Huang, *Nature Photonics*, 2017, **11**, 315–321.

185 S. Shrestha, R. Fischer, G. J. Matt, P. Feldner, T. Michel, A. Osvet, I. Levchuk, B. Merle, S. Golkar, H. Chen, S. F. Tedde, O. Schmidt, R. Hock, M. Rührig, M. Göken, W. Heiss, G. Anton and C. J. Brabec, *Nature Photon*, 2017, **11**, 436–440.

186 G. J. Matt, I. Levchuk, J. Knüttel, J. Dallmann, A. Osvet, M. Sytnyk, X. Tang, J. Elia, R. Hock, W. Heiss and C. J. Brabec, *Advanced Materials Interfaces*, 2020, **7**, 1901575.

187 M. Hu, S. Jia, Y. Liu, J. Cui, Y. Zhang, H. Su, S. Cao, L. Mo, D. Chu, G. Zhao, K. Zhao, Z. Yang and S. F. Liu, *ACS Appl. Mater. Interfaces*, 2020, **12**, 16592–16600.

188 S. Tie, W. Zhao, D. Xin, M. Zhang, J. Long, Q. Chen, X. Zheng, J. Zhu and W. H. Zhang, *Advanced Materials*, 2020, **32**, 1–7.

189 Y. C. Kim, K. H. Kim, D. Y. Son, D. N. Jeong, J. Y. Seo, Y. S. Choi, I. T. Han, S. Y. Lee and N. G. Park, *Nature*, 2017, **550**, 87–91.

190 W. Pan, B. Yang, G. Niu, K. Xue, X. Du, L. Yin, M. Zhang, H. Wu, X. Miao and J. Tang, *Advanced Materials*, 2019, **31**, 1904405.

191 J. Zhao, L. Zhao, Y. Deng, X. Xiao, Z. Ni, S. Xu and J. Huang, *Nature Photonics*, 2020, **14**, 612–617.

192 H. Mescher, F. Schackmar, H. Eggers, T. Abzieher, M. Zuber, E. Hamann, T. Baumbach, B. S. Richards, G. Hernandez-Sosa, U. W. Paetzold and U. Lemmer, *ACS Applied Materials & Interfaces*, 2020, **12**, 15774–15784.

193 H. Wei and J. Huang, *Nature Communications*, 2019, **10**, 1066–1066.

194 Y. He, C. C. Stoumpos, I. Hadar, Z. Luo, K. M. McCall, Z. Liu, D. Y. Chung, B. W. Wessels and M. G. Kanatzidis, *J. Am. Chem. Soc.*, 2021, **143**, 2068–2077.

195 Z. Zhang, D. Cao, Z. Huang, E. O. Danilov, C.-C. Chung, D. Sun and G. Yang, *Advanced Optical Materials*, 2021, **9**, 2001575.

196 L. Pan, Y. Feng, P. Kandlakunta, J. Huang and L. R. Cao, *IEEE Transactions on Nuclear Science*, 2020, **67**, 443–449.

197 Y. He, M. Petryk, Z. Liu, D. G. Chica, I. Hadar, C. Leak, W. Ke, I. Spanopoulos, W. Lin, D. Y. Chung, B. W. Wessels, Z. He and M. G. Kanatzidis, *Nature Photonics*, 2020, **15**, 36–42.

198 A. R. Bowring, L. Bertoluzzi, B. C. O'Regan and M. D. McGehee, *Advanced Energy Materials*, 2018, **8**, 1702365.

199 Y. Yuan and J. Huang, *Acc. Chem. Res.*, 2016, **49**, 286–293.

200 M. Xia, J.-H. Yuan, G. Niu, X. Du, L. Yin, W. Pan, J. Luo, Z. Li, H. Zhao, K.-H. Xue, X. Miao and J. Tang, *Advanced Functional Materials*, 2020, **30**, 1910648.

201 P. Calado, A. M. Telford, D. Bryant, X. Li, J. Nelson, B. C. O'Regan and P. R. F. Barnes, *Nature Communications*, 2016, **7**, 1–10.

202 P. Vashishtha and J. E. Halpert, *Chem. Mater.*, 2017, **29**, 5965–5973.

203 K. C. Kwon, K. Hong, Q. Van Le, S. Y. Lee, J. Choi, K.-B. Kim, S. Y. Kim and H. W. Jang, *Advanced Functional Materials*, 2016, **26**, 4213–4222.

204 B. Yang, W. Pan, H. Wu, G. Niu, J.-H. Yuan, K.-H. Xue, L. Yin, X. Du, X.-S. Miao, X. Yang, Q. Xie and J. Tang, *Nature Communications*, 2019, **10**, 1989.

205 Y. Huang, L. Qiao, Y. Jiang, T. He, R. Long, F. Yang, L. Wang, X. Lei, M. Yuan and J. Chen, *Angewandte Chemie - International Edition*, 2019, **58**, 17834–17842.

206 L. Basiricò, S. P. Senanayak, A. Ciavatti, M. Abdi-Jalebi, B. Fraboni and H. Sirringhaus, *Advanced Functional Materials*, 2019, **29**, 1902346–1902346.

207 S. Yakunin, M. Sytnyk, D. Kriegner, S. Shrestha, M. Richter, G. J. Matt, H. Azimi, C. J. Brabec, J. Stangl, M. V. Kovalenko and W. Heiss, *Nat Photon*, 2015, **9**, 444–449.

208 H. Tsai, F. Liu, S. Shrestha, K. Fernando, S. Tretiak, B. Scott, D. T. Vo, J. Strzalka and W. Nie, *Science Advances*, 2020, **6**, 1–8.

209 B. Bin Zhang, X. Liu, B. Xiao, A. Ben Hafsia, K. Gao, Y. Xu, J. Zhou and Y. Chen, *Journal of Physical Chemistry Letters*, 2020, **11**, 432–437.

210 H. Li, J. Song, W. Pan, D. Xu, W. Zhu, H. Wei and B. Yang, *Adv. Mater.*, 2020, **32**, 2003790.

211 R. Zhuang, X. Wang, W. Ma, Y. Wu, X. Chen, L. Tang, H. Zhu, J. Liu, L. Wu, W. Zhou, X. Liu and Y. Yang, *Nat. Photonics*, 2019, **13**, 602–608.

212 X. He, M. Xia, H. Wu, X. Du, Z. Song, S. Zhao, X. Chen, G. Niu and J. Tang, *Advanced Functional Materials*, 2022, **32**, 2109458.

213 Y. He, W. Pan, C. Guo, H. Zhang, H. Wei and B. Yang, *Advanced Functional Materials*, 2021, **31**, 2104880.

214 L. Basiricò, A. Ciavatti, T. Cramer, P. Cosseddu, A. Bonfiglio and B. Fraboni, *Nat Commun*, 2016, **7**, 13063.

215 H. Mescher, E. Hamann and U. Lemmer, *Sci Rep*, 2019, **9**, 5231.

216 A. N. Belsky, P. Chevallier, P. Dhez, P. Martin, C. Pédrini and A. N. Vasil'ev, *Nuclear Inst. and Methods in Physics Research, A*, 1995, **361**, 384–387.

217 A. N. Belsky, P. Chevallier, E. N. Mel'chakov, C. Pédrini, P. A. Rodnyi and A. N. Vasil'ev, *Chemical Physics Letters*, 1997, **278**, 369–372.

218 K. Shibuya, M. Koshimizu, Y. Takeoka and K. Asai, *Nuclear Instruments and Methods in Physics Research, Section B: Beam Interactions with Materials and Atoms*, 2002, **194**, 207–212.

219 K. Shibuya, M. Koshimizu, K. Asai and H. Shibata, *Applied Physics Letters*, 2004, **84**, 4370–4372.

220 V. B. Mykhaylyk, H. Kraus and M. Saliba, *Materials Horizons*, 2019, **6**, 1740–1747.

221 C. W. E. van Eijk, J. T. M. De Haas, P. A. Rodnyi, I. V. Khodyuk, K. Shibuya, F. Nishikido and M. Koshimizu, *IEEE Nuclear Science Symposium Conference Record*, 2008, 3525–3528.

222 A. Xie, F. Maddalena, M. E. Witkowski, M. Makowski, B. Mahler, W. Drozdowski, S. V. Springham, P. Coquet, C. Dujardin, M. D. Birowosuto and C. Dang, *Chem. Mater.*, 2020, **32**, 8530–8539.

223 C. M. Pepin, P. Bérard, A. L. Perrot, C. Pépin, D. Houde, R. Lecomte, C. L. Melcher and H. Dautet, *IEEE Transactions on Nuclear Science*, 2004, **51**, 789–795.

224 A. Xie, C. Hettiarachchi, F. Maddalena, M. E. Witkowski, M. Makowski, W. Drozdowski, A. Arramel, A. T. S. Wee, S. V. Springham, P. Q. Vuong, H. J. Kim, C. Dujardin, P. Coquet, M. D. Birowosuto and C. Dang, *Communications Materials*, 2020, **1**, 1–10.

225 F. Maddalena, A. Xie, Arramel, M. E. Witkowski, M. Makowski, B. Mahler, W. Drozdowski, T. Mariyappan, S. V. Springham, P. Coquet, C. Dujardin, M. D. Birowosuto and C. Dang, *J. Mater. Chem. C*, 2021, **9**, 2504–2512.

226 R. Cala', I. Frank, F. Pagano, F. Maddalena, C. Dang, M. D. Birowosuto and E. Auffray, *Appl. Phys. Lett.*, 2022, **120**, 241901.

227 Y. Zhang, R. Sun, X. Ou, K. Fu, Q. Chen, Y. Ding, L.-J. Xu, L. Liu, Y. Han, A. V. Malko, X. Liu, H. Yang, O. M. Bakr, H. Liu and O. F. Mohammed, *ACS Nano*, 2019, **13**, 2520–2525.

228 F. Cao, D. Yu, W. Ma, X. Xu, B. Cai, Y. M. Yang, S. Liu, L. He, Y. Ke, S. Lan, K. L. Choy and H. Zeng, *ACS Nano*, 2019, **14**, 5183–5193.

229 Q. Xu, J. Wang, W. Shao, X. Ouyang, X. Wang, X. Zhang, Y. Guo and X. Ouyang, *Nanoscale*, 2020, **12**, 9727–9732.

230 W. Chen, M. Zhou, Y. Liu, X. Yu, C. Pi, Z. Yang, H. Zhang, Z. Liu, T. Wang, J. Qiu, S. F. Yu, Y. (Michael) Yang and X. Xu, *Advanced Functional Materials*, 2022, **32**, 2107424.

231 B. Wang, J. Peng, X. Yang, W. Cai, H. Xiao, S. Zhao, Q. Lin and Z. Zang, *Laser & Photonics Reviews*, 2022, **16**, 2100736.

232 H. Zhang, Z. Yang, M. Zhou, L. Zhao, T. Jiang, H. Yang, X. Yu, J. Qiu, Y. (Michael) Yang and X. Xu, *Advanced Materials*, 2021, **33**, 2102529.

233 W. Ma, T. Jiang, Z. Yang, H. Zhang, Y. Su, Z. Chen, X. Chen, Y. Ma, W. Zhu, X. Yu, H. Zhu, J. Qiu, X. Liu, X. Xu and Y. (Michael) Yang, *Advanced Science*, 2021, **8**, 2003728.

234 Q. Xu, S. Zhou, J. Huang, X. Ouyang, J. Liu, Y. Guo, J. Wang, J. Nie, X. Zhang, X. Ouyang and W. Jia, *Materials Today Physics*, 2021, **18**, 100390.

235 J.-X. Wang, X. Wang, J. Yin, L. Gutiérrez-Arzaluz, T. He, C. Chen, Y. Han, Y. Zhang, O. M. Bakr, M. Eddaoudi and O. F. Mohammed, *ACS Energy Lett.*, 2022, **7**, 10–16.

236 M. Gandini, I. Villa, M. Beretta, C. Gotti, M. Imran, F. Carulli, E. Fantuzzi, M. Sassi, M. Zaffalon, C. Brofferio, L. Manna, L. Beverina, A. Vedda, M. Fasoli, L. Gironi and S. Brovelli, *Nature Nanotechnology*, 2020, **15**, 462–468.

237 W. Zhu, W. Ma, Y. Su, Z. Chen, X. Chen, Y. Ma, L. Bai, W. Xiao, T. Liu, H. Zhu, X. Liu, H. Liu, X. Liu and Y. Yang, *Light: Science and Applications*, 2020, **9**, 0–9.

238 Z. Wang, X. Xu, S. Wang, H. Xu, W. Xu, Q. Zeng, G. Deng, Y. Jiang and S. Wu, *Chemistry – A European Journal*, 2021, **27**, 9071–9076.

239 Q. Hu, Z. Deng, M. Hu, A. Zhao, Y. Zhang, Z. Tan, G. Niu, H. Wu and J. Tang, *Science China Chemistry*, 2018, **61**, 1581–1586.

240 L. Lian, M. Zheng, W. Zhang, L. Yin, X. Du, P. Zhang, X. Zhang, J. Gao, D. Zhang, L. Gao, G. Niu, H. Song, R. Chen, X. Lan, J. Tang and J. Zhang, *Adv. Sci.*, 2020, **7**, 2000195.

241 S. Cheng, M. Nikl, A. Beitlerova, R. Kucerkova, X. Du, G. Niu, Y. Jia, J. Tang, G. Ren and Y. Wu, *Advanced Optical Materials*, 2021, **9**, 1–7.

242 S. Cheng, A. Beitlerova, R. Kucerkova, M. Nikl, G. Ren and Y. Wu, *physica status solidi (RRL) – Rapid Research Letters*, 2020, **14**, 2000374.

243 J. Zhou, K. An, P. He, J. Yang, C. Zhou, Y. Luo, W. Kang, W. Hu, P. Feng, M. Zhou and X. Tang, *Advanced Optical Materials*, 2021, **9**, 2002144.

244 Y. Zhou, X. Wang, T. He, H. Yang, C. Yang, B. Shao, L. Gutiérrez-Arzaluz, O. M. Bakr, Y. Zhang and O. F. Mohammed, *ACS Energy Lett.*, 2022, **7**, 844–846.

245 Y. Wu, D. Han, B. C. Chakoumakos, H. Shi, S. Chen, M. H. Du, I. Greeley, M. Loyd, D. J. Rutstrom, L. Stand, M. Koschan and C. L. Melcher, *Journal of Materials Chemistry C*, 2018, **6**, 6647–6655.

246 L.-J. Xu, X. Lin, Q. He, M. Worku and B. Ma, *Nat Commun*, 2020, **11**, 4329.

247 B. Yang, L. Yin, G. Niu, J. H. Yuan, K. H. Xue, Z. Tan, X. S. Miao, M. Niu, X. Du, H. Song, E. Lifshitz and J. Tang, *Advanced Materials*, 2019, **31**, 1–8.

248 N. Kawano, M. Koshimizu, G. Okada, Y. Fujimoto, N. Kawaguchi, T. Yanagida and K. Asai, *Scientific Reports*, 2017, **7**, 1–8.

249 Q. Xu, W. Shao, J. Liu, Z. Zhu, X. Ouyang, J. Cai, B. Liu, B. Liang, Z. Wu and X. Ouyang, *ACS Applied Materials and Interfaces*, 2019, **11**, 47485–47490.

250 A. Al-Ashouri, A. Magomedov, M. Roß, M. Jošt, M. Talaikis, G. Chistiakova, T. Bertram, J. A. Márquez, E. Köhnen, E. Kasparavičius, S. Levcenco, L. Gil-Escrig, C. J. Hages, R. Schlatmann, B. Rech, T. Malinauskas, T. Unold, C. A. Kaufmann, L. Korte, G. Niaura, V. Getautis and S. Albrecht, *Energy Environ. Sci.*, 2019, **12**, 3356–3369.

251 A. Dearle, Nano DTC Mini-Report, University of Cambridge, 2019.

252 G. F. Knoll, *Radiation Detection and Measurement*, Wiley, New York, 4th edn., 2010.

253 Y. Liu, Y. Zhang, K. Zhao, Z. Yang, J. Feng, X. Zhang, K. Wang, L. Meng, H. Ye, M. Liu and S. (Frank) Liu, *Advanced Materials*, 2018, **30**, 1707314.

254 C. Li, H. Wang, F. Wang, T. Li, M. Xu, H. Wang, Z. Wang, X. Zhan, W. Hu and L. Shen, *Light Sci Appl*, 2020, **9**, 31.

255 F. Cao, T. Yan, Z. Li, L. Wu and X. Fang, *Advanced Optical Materials*, 2022, **10**, 2200786.

256 O. D. I. Moseley, B. Roose, S. J. Zelewski, S. Kahmann, K. Dey and S. D. Stranks, *ACS Photonics*, 2022, accepted.

257 C. Chen, L. Gao, W. Gao, C. Ge, X. Du, Z. Li, Y. Yang, G. Niu and J. Tang, *Nature Communications*, 2019, **10**, 1927–1927.

258 L. Li, X. Liu, Y. Li, Z. Xu, Z. Wu, S. Han, K. Tao, M. Hong, J. Luo and Z. Sun, *Journal of the American Chemical Society*, 2019, **141**, 2623–2629.

259 S. Chen, C. Teng, M. Zhang, Y. Li, D. Xie and G. Shi, *Advanced Materials*, 2016, **28**, 5969–5974.

260 H. S. Jung, G. S. Han, N.-G. Park and M. J. Ko, *Joule*, 2019, **3**, 1850–1880.

261 W. Wu, X. Wang, X. Han, Z. Yang, G. Gao, Y. Zhang, J. Hu, Y. Tan, A. Pan and C. Pan, *Advanced Materials*, 2019, **31**, 1805913.

262 Y. Cheng and L. Ding, *Energy & Environmental Science*, 2021, **14**, 3233–3255.

263 B. Roose, A. Ummadisingu, J.-P. Correa-Baena, M. Saliba, A. Hagfeldt, M. Graetzel, U. Steiner and A. Abate, *Nano Energy*, 2017, **39**, 24–29.

264 J. Peng, Y. Xu, F. Yao and Q. Lin, *Nanoscale*, 2022, **14**, 9636–9647.

265 Y. Fang, A. Armin, P. Meredith and J. Huang, *Nature Photonics*, 2019, **13**, 1–4.

266 D. Zhang, C. Liu, K. Li, W. Guo, F. Gao, J. Zhou, X. Zhang and S. Ruan, *Advanced Optical Materials*, 2018, **6**, 1701189.

267 F. Guo, Y. Bin, Y. Yuan, Z. Chen, Q. Dong, Y. Bi and J. Huang, *Nature Nanotechnology*, 2012, **7**, 798–802.

268 L. Shen, Y. Zhang, Y. Bai, X. Zheng, Q. Wang and J. Huang, *Nanoscale*, 2016, **8**, 12990–12997.

269 G. Konstantatos, J. Clifford, L. Levina and E. H. Sargent, *Nature Photonics*, 2007, **1**, 531–534.

270 P. Fay, in *Encyclopedia of Materials: Science and Technology*, Elsevier Ltd., Cambridge, 1st edn., 2001, pp. 6909–6923.

271 D. Yang and D. Ma, *Advanced Optical Materials*, 2019, **7**, 1800522–1800522.

272 R. A. Z. Razera, D. A. Jacobs, F. Fu, P. Fiala, M. Dussouillez, F. Sahli, T. C. J. Yang, L. Ding, A. Walter, A. F. Feil, H. I. Boudinov, S. Nicolay, C. Ballif and Q. Jeangros, *J. Mater. Chem. A*, 2019, **8**, 242–250.

273 S. E. J. O'Kane, G. Richardson, A. Pockett, R. G. Niemann, J. M. Cave, N. Sakai, G. E. Eperon, H. J. Snaith, J. M. Foster, P. J. Cameron and A. B. Walker, *J. Mater. Chem. C*, 2017, **5**, 452–462.

274 Y. Liu, Z. Xu, Z. Yang, Y. Zhang, J. Cui, Y. He, H. Ye, K. Zhao, H. Sun, R. Lu, M. Liu, M. G. Kanatzidis and S. (Frank) Liu, *Matter*, 2020, **3**, 180–196.

275 M. Xia, Z. Song, H. Wu, X. Du, X. He, J. Pang, H. Luo, L. Jin, G. Li, G. Niu and J. Tang, *Advanced Functional Materials*, 2022, **32**, 2110729.

276 C. Eames, J. M. Frost, P. R. Barnes, B. C. O'Regan, A. Walsh and M. S. Islam, *Nature communications*, 2015, **6**, 7497.

277 Y. Zhang, M. Z. Liu, G. E. Eperon, T. C. Leijtens, D. McMeekin, M. Saliba, W. Zhang, M. de Bastiani, A. Petrozza, L. M. Herz, M. B. Johnston, H. Lin and H. J. Snaith, *Mater Horiz*, 2015, **2**, 315–322.

278 H. Jing, R. Peng, R.-M. Ma, J. He, Y. Zhou, Z. Yang, C.-Y. Li, Y. Liu, X. Guo, Y. Zhu, D. Wang, J. Su, C. Sun, W. Bao and M. Wang, *Nano Lett.*, 2020, **20**, 7144–7151.

279 P. Fassl, V. Lami, A. Bausch, Z. Wang, M. T. Klug, H. J. Snaith and Y. Vaynzof, *Energy & Environmental Science*, 2018, **11**, 3380–3391.

280 K. Ramalingam and C. Indulkar, in *Distributed Generation Systems*, eds. G. B. Gharehpetian and S. M. Mousavi Agah, Butterworth-Heinemann, Oxford, 1st edn., 2017, pp. 69–147.

281 A. Maulu, J. Navarro-Arenas, P. J. Rodríguez-Cantó, J. F. Sánchez-Royo, R. Abargues, I. Suárez and J. P. Martínez-Pastor, *Nanomaterials*, 2018, **8**, 677.

282 D. Glowienka and Y. Galagan, *Advanced Materials*, 2022, **34**, 2105920.

283 R. Singh, S. Sandhu and J.-J. Lee, *Solar Energy*, 2019, **193**, 956–961.

284 C. Li, J. Lu, Y. Zhao, L. Sun, G. Wang, Y. Ma, S. Zhang, J. Zhou, L. Shen and W. Huang, *Small*, 2019, **15**, 1903599.

285 L. Shen, Y. Fang, D. Wang, Y. Bai, Y. Deng, M. Wang, Y. Lu and J. Huang, *Advanced Materials*, 2016, **28**, 10794–10800.

286 G. Yang, Z. Ren, K. Liu, M. Qin, W. Deng, H. Zhang, H. Wang, J. Liang, F. Ye, Q. Liang, H. Yin, Y. Chen, Y. Zhuang, S. Li, B. Gao, J. Wang, T. Shi, X. Wang, X. Lu, H. Wu, J. Hou, D. Lei, S. K. So, Y. Yang, G. Fang and G. Li, *Nat. Photon.*, 2021, **15**, 681–689.

287 M. Jeong, I. W. Choi, E. M. Go, Y. Cho, M. Kim, B. Lee, S. Jeong, Y. Jo, H. W. Choi, J. Lee, J.-H. Bae, S. K. Kwak, D. S. Kim and C. Yang, *Science*, 2020, **369**, 1615–1620.

288 L. Shen, Y. Fang, Q. Dong, Z. Xiao and J. Huang, *Appl. Phys. Lett.*, 2015, **106**, 023301.

289 I. K. Kim, X. Li, M. Ullah, P. E. Shaw, R. Wawrzinek, E. B. Namdas and S.-C. Lo, *Advanced Materials*, 2015, **27**, 6390–6395.

290 K. Domanski, J.-P. Correa-Baena, N. Mine, M. K. Nazeeruddin, A. Abate, M. Saliba, W. Tress, A. Hagfeldt and M. Grätzel, *ACS Nano*, 2016, **10**, 6306–6314.

291 L. Bertoluzzi, J. B. Patel, K. A. Bush, C. C. Boyd, R. A. Kerner, B. C. O'Regan and M. D. McGehee, *Advanced Energy Materials*, 2021, **11**, 2002614.

292 C. C. Boyd, R. Cheacharoen, T. Leijtens and M. D. McGehee, *Chemical Reviews*, 2019, **119**, 3418–3451.

293 E. J. Wolf, I. E. Gould, L. B. Bliss, J. J. Berry and M. D. McGehee, *Solar RRL*, 2022, **6**, 2100239.

294 Y. Cho, H. D. Kim, J. Zheng, J. Bing, Y. Li, M. Zhang, M. A. Green, A. Wakamiya, S. Huang, H. Ohkita and A. W. Y. Ho-Baillie, *ACS Energy Lett.*, 2021, **6**, 925–933.

295 A. Szemjonov, K. Galkowski, M. Anaya, Z. Andaji-Garmaroudi, T. K. Baikie, S. Mackowski, I. D. Baikie, S. D. Stranks and M. S. Islam, *ACS Materials Lett.*, 2019, **1**, 506–510.

296 Y. Zhang, Y. Zhu, M. Hu, N. Pai, T. Qin, Y.-B. Cheng, U. Bach, A. N. Simonov and J. Lu, *J. Phys. Chem. Lett.*, 2022, **13**, 2792–2799.

297 Z. Andaji-Garmaroudi, M. Anaya, A. J. Pearson and S. D. Stranks, *Advanced Energy Materials*, 2020, **10**, 1903109.

298 C. Fei and H. Wang, *Organic Electronics*, 2019, **68**, 143–150.

299 B. Roose, *RSC Adv.*, 2021, **11**, 12095–12101.

300 X. Zheng, B. Chen, J. Dai, Y. Fang, Y. Bai, Y. Lin, H. Wei, X. C. Zeng and J. Huang, *Nat Energy*, 2017, **2**, 1–9.

301 N. Aristidou, C. Eames, I. Sanchez-Molina, X. Bu, J. Kosco, M. S. Islam and S. A. Haque, *Nat Commun*, 2017, **8**, 15218.

302 A. Senocrate, T. Acartürk, G. Y. Kim, R. Merkle, U. Starke, M. Grätzel and J. Maier, *J. Mater. Chem. A*, 2018, **6**, 10847–10855.

303 S. Macpherson, T. A. S. Doherty, A. J. Winchester, S. Kosar, D. N. Johnstone, Y.-H. Chiang, K. Galkowski, M. Anaya, K. Frohna, A. N. Iqbal, S. Nagane, B. Roose, Z. Andaji-Garmaroudi, K. W. P. Orr, J. E. Parker, P. A. Midgley, K. M. Dani and S. D. Stranks, *Nature*, 2022, **607**, 294–300.

304 A. J. Pearson, G. E. Eperon, P. E. Hopkinson, S. N. Habisreutinger, J. T.-W. Wang, H. J. Snaith and N. C. Greenham, *Advanced Energy Materials*, 2016, **6**, 1600014.

305 Z. Ahmad, A. Mishra, S. M. Abdulrahim, D. Taguchi, P. Sanghyun, F. Aziz, M. Iwamoto, T. Manaka, J. Bhadra, N. J. Al-Thani, M. K. Nazeeruddin, F. Touati, A. Belaidi and S. A. Al-Muhtaseb, *Sci Rep*, 2021, **11**, 33.

306 M. Ozaki, Y. Ishikura, M. A. Truong, J. Liu, I. Okada, T. Tanabe, S. Sekimoto, T. Ohtsuki, Y. Murata, R. Murdey and A. Wakamiya, *J. Mater. Chem. A*, 2019, **7**, 16947–16953.

307 Q. Jiang, Z. Chu, P. Wang, X. Yang, H. Liu, Y. Wang, Z. Yin, J. Wu, X. Zhang and J. You, *Advanced Materials*, 2017, **29**, 1703852.

308 Y. Ouyang, Y. Li, P. Zhu, Q. Li, Y. Gao, J. Tong, L. Shi, Q. Zhou, C. Ling, Q. Chen, Z. Deng, H. Tan, W. Deng and J. Wang, *Journal of Materials Chemistry A*, 2019, **7**, 2275–2282.

309 Q. Zhao, W. Wang, F. Carrascoso-Plana, W. Jie, T. Wang, A. Castellanos-Gomez and R. Frisenda, *Materials Horizons*, 2020, **7**, 252–262.

310 T. Niu, J. Lu, R. Munir, J. Li, D. Barrit, X. Zhang, H. Hu, Z. Yang, A. Amassian, K. Zhao and S. (Frank) Liu, *Advanced Materials*, 2018, **30**, 1706576.

311 Q. Jiang, Y. Zhao, X. Zhang, X. Yang, Y. Chen, Z. Chu, Q. Ye, X. Li, Z. Yin and J. You, *Nature Photonics*, 2019, **13**, 460–466.

312 M. Abdi-Jalebi, Z. Andaji-Garmaroudi, S. Cacovich, C. Stavrakas, B. Philippe, J. M. Richter, M. Alsari, E. P. Booker, E. M. Hutter, A. J. Pearson, S. Lilliu, T. J. Savenije, H. Rensmo, G. Divitini, C. Ducati, R. H. Friend and S. D. Stranks, *Nature*, 2018, **555**, 497–501.

313 Q. Chen, H. Zhou, T. B. Song, S. Luo, Z. Hong, H. S. Duan, L. Dou, Y. Liu and Y. Yang, *Nano Lett*, 2014, **14**, 4158–63.

314 J.-W. Lee, H.-S. Kim and N.-G. Park, *Accounts of Chemical Research*, 2016, **49**, 311–319.

315 Y. Shao, Y. Fang, T. Li, Q. Wang, Q. Dong, Y. Deng, Y. Yuan, H. Wei, M. Wang, A. Gruverman, J. Shield and J. Huang, *Energy Environ. Sci.*, 2016, **9**, 1752–1759.

316 J. S. Yun, J. Seidel, J. Kim, A. M. Soufiani, S. Huang, J. Lau, N. J. Jeon, S. I. Seok, M. A. Green and A. Ho-Baillie, *Adv. Energy Mater.*, 2016, **6**, 1600330.

317 L. McGovern, I. Koschany, G. Grimaldi, L. A. Muscarella and B. Ehrler, *J. Phys. Chem. Lett.*, 2021, **12**, 2423–2428.

318 Y. Shao, Z. Xiao, C. Bi, Y. Yuan and J. Huang, *Nature communications*, 2014, **5**, 5784.

319 D. Wei, F. Ma, R. Wang, S. Dou, P. Cui, H. Huang, J. Ji, E. Jia, X. Jia, S. Sajid, A. M. Elseman, L. Chu, Y. Li, B. Jiang, J. Qiao, Y. Yuan and M. Li, *Advanced Materials*, 2018, **30**, 1707583.

320 S. Bag and M. F. Durstock, *ACS Appl. Mater. Interfaces*, 2016, **8**, 5053–5057.

321 J.-P. Correa-Baena, M. Anaya, G. Lozano, W. Tress, K. Domanski, M. Saliba, T. Matsui, T. J. Jacobsson, M. E. Calvo, A. Abate, M. Grätzel, H. Míguez and A. Hagfeldt, *Advanced Materials*, 2016, **28**, 5031–5037.

322 Y. Lin, Y. Bai, Y. Fang, Q. Wang, Y. Deng and J. Huang, *ACS Energy Lett.*, 2017, **2**, 1571–1572.

323 J.-W. Lee, Z. Dai, T.-H. Han, C. Choi, S.-Y. Chang, S.-J. Lee, N. De Marco, H. Zhao, P. Sun, Y. Huang and Y. Yang, *Nat Commun*, 2018, **9**, 3021.

324 X. Xu, W. Qian, J. Wang, J. Yang, J. Chen, S. Xiao, Y. Ge and S. Yang, *Advanced Science*, 2021, **8**, 2102730.

325 X. Tang, M. M. Ackerman, M. Chen and P. Guyot-Sionnest, *Nat. Photonics*, 2019, **13**, 277–282.

326 Z. Lan and F. Zhu, *ACS Nano*, 2021, **15**, 13674–13682.

327 J. Miao, F. Zhang, M. Du, W. Wang and Y. Fang, *Advanced Optical Materials*, 2018, **6**, 1800001.

328 J. Zhao, X. Wang, W. Lei, Y. Xu, Y. Pan, Y. Li, J. Chen and Q. Li, *ACS Appl. Mater. Interfaces*, 2022, **14**, 25824–25833.

329 H. Li and W. Zhang, *Chem. Rev.*, 2020, **120**, 9835–9950.

330 M. Meusel, C. Baur, G. Létay, A. W. Bett, W. Warta and E. Fernandez, *Progress in Photovoltaics: Research and Applications*, 2003, **11**, 499–514.

331 W. Tian, H. Zhou and L. Li, *Small*, 2017, **13**, 1702107.

332 A. R. Bowman, F. Lang, Y.-H. Chiang, A. Jiménez-Solano, K. Frohna, G. E. Eperon, E. Ruggeri, M. Abdi-Jalebi, M. Anaya, B. V. Lotsch and S. D. Stranks, *ACS Energy Lett.*, 2021, **6**, 612–620.

333 H. Rao, W.-G. Li, B.-X. Chen, D.-B. Kuang and C.-Y. Su, *Advanced Materials*, 2017, **29**, 1602639.

334 W. Van Roosbroeck, *Physical Review*, 1965, **139**, 1702–1716.

335 A. Rothwarf, *Journal of Applied Physics*, 1973, **44**, 752–756.

336 P. A. Rodnyi, P. Dorenbos and C. W. E. van Eijk, *Physica Status Solidi (B)*, 1995, **187**, 15–29.

337 F. Maddalena, L. Tjahjana, A. Xie, A. Arramel, S. Zeng, H. Wang, P. Coquet, W. Drozdowski, C. Dujardin, C. Dang and M. Birowosuto, *Crystals*, 2019, **9**, 88–97.

338 L. Wang, K. Fu, R. Sun, H. Lian, X. Hu and Y. Zhang, *Nano-Micro Letters*, 2019, **11**, 52.

339 A. Miyata, A. Mitioglu, P. Plochocka, O. Portugall, J. Tse-wei, S. D. Stranks, H. J. Snaith and R. J. Nicholas, *Nature Physics*, 2015, **11**, 582–587.

340 A. Xie, T. H. Nguyen, C. Hettiarachchi, M. E. Witkowski, W. Drozdowski, M. D. Birowosuto, H. Wang and C. Dang, *The Journal of Physical Chemistry C*, 2018, **122**, 16265–16273.

341 B. Wenger, P. K. Nayak, X. Wen, S. V. Kesava, N. K. Noel and H. J. Snaith, *Nature Communications*, 2017, **8**, 1–9.

342 Z. Ning, X. Gong, R. Comin, G. Walters, F. Fan, O. Voznyy, E. Yassitepe, A. Buin, S. Hoogland and E. H. Sargent, *Nature*, 2015, **523**, 324–328.

343 T. Yanagida, G. Okada, T. Kato, D. Nakauchi and S. Yanagida, *Applied Physics Express*, 2016, **9**, 042601.

344 S. Kishimoto, K. Shibuya, F. Nishikido, M. Koshimizu, R. Haruki and Y. Yoda, *Applied Physics Letters*, 2008, **93**, 261901.

345 V. B. Mykhaylyk, H. Kraus, V. Kapustianyk, H. J. Kim, P. Mercere, M. Rudko, P. Da Silva, O. Antonyak and M. Dendebera, *Scientific Reports*, 2020, **10**, 1–11.

346 K. S. Shah, J. Glodo, M. Klugerman, W. Higgins, T. Gupta, P. Wong, W. W. Moses, S. E. Derenzo, M. J. Weber and P. Dorenbos, *IEEE Transactions on Nuclear Science*, 2008, **51**, 891–894.

347 M. Moszyński, D. Wolski, T. Ludziejewski, M. Kapusta, A. Lempicki, C. Brecher, D. Wiśniewski and A. J. Wojtowicz, *Nuclear Inst. and Methods in Physics Research, A*, 1997, **385**, 123–131.

348 M. Moszynski, C. Gresset, J. Vacher and R. Odru, *Nuclear Inst. and Methods in Physics Research, A*, 1981, **188**, 403–409.

349 M. Laval, M. Moszyński, R. Allemand, E. Cormoreche, P. Guinet, R. Odru and J. Vacher, *Nuclear Inst. and Methods in Physics Research, A*, 1983, **206**, 169–176.

350 Z. Zeng, B. Huang, X. Wang, L. Lu, Q. Lu, M. Sun, T. Wu, T. Ma, J. Xu, Y. Xu, S. Wang, Y. Du and C. H. Yan, *Advanced Materials*, 2020, **2004506**, 1–10.

351 P. Andričević, P. Frajtag, V. P. Lamirand, A. Pautz, M. Kollár, B. Náfrádi, A. Sienkiewicz, T. Garma, L. Forró and E. Horváth, *Advanced Science*, 2020, **8**, 2001882.

352 A. G. Boldyreva, A. F. Akbulatov, S. A. Tsarev, S. Y. Luchkin, I. S. Zhidkov, E. Z. Kurmaev, K. J. Stevenson, V. G. Petrov and P. A. Troshin, *Journal of Physical Chemistry Letters*, 2019, **10**, 813–818.

353 E. T. Hoke, D. J. Slotcavage, E. R. Dohner, A. R. Bowring, H. I. Karunadasa and M. D. McGehee, *Chemical Science*, 2015, **6**, 613–617.

354 S. Yang, Z. Xu, S. Xue, P. Kandlakunta, L. Cao and J. Huang, *Advanced Materials*, 2019, **31**, 1–7.

355 A. G. Boldyreva, L. A. Frolova, I. S. Zhidkov, L. G. Gutsev, E. Z. Kurmaev, B. R. Ramachandran, V. G. Petrov, K. J. Stevenson, S. M. Aldoshin and P. A. Troshin, *The Journal of Physical Chemistry Letters*, 2020, **11**, 2630–2636.

356 G. Náfrádi, E. Horváth, M. Kollár, A. Horváth, P. Andričević, A. Sienkiewicz, L. Forró and B. Náfrádi, *Energy Conversion and Management*, 2020, **205**, 2001882.

357 S. Kanaya, G. M. Kim, M. Ikegami, T. Miyasaka, K. Suzuki, Y. Miyazawa, H. Toyota, K. Osonoe, T. Yamamoto and K. Hirose, *Journal of Physical Chemistry Letters*, 2019, **10**, 6990–6995.

358 F. Lang, N. H. Nickel, J. Bundesmann, S. Seidel, A. Denker, S. Albrecht, V. V Brus, J. Rappich, B. Rech, G. Landi and H. C. Neitzert, *Advanced Materials*, 2016, **28**, 8726–8731.

359 J. M. Ball and A. Petrozza, *Nature Energy*, 2016, **1**, 16149.

360 M. Zhuravleva, L. Stand, H. Wei, C. Hobbs, L. A. Boatner, J. O. Ramey, K. Shah, A. Burger, E. Rowe, P. Bhattacharya, E. Tupitsyn and C. L. Melcher, in *IEEE Nuclear Science Symposium Conference Record*, IEEE, 2013, pp. 1–5.

361 Y. Li, W. Shao, X. Ouyang, Z. Zhu, H. Zhang, X. Ouyang, B. Liu and Q. Xu, *The Journal of Physical Chemistry C*, 2019, **123**, 17449–17453.

362 D. W. Dequilettes, K. Frohna, D. Emin, T. Kirchartz, V. Bulovic, D. S. Ginger and S. D. Stranks, *Chemical Reviews*, 2019, **119**, 11007–11019.

363 J. Singh, *Journal of Applied Physics*, 2011, **110**, 024503.

364 M. Abdi-Jalebi, Z. Andaji-Garmaroudi, A. J. Pearson, G. Divitini, S. Cacovich, B. Philippe, H. Rensmo, C. Ducati, R. H. Friend and S. D. Stranks, *ACS Energy Letters*, 2018, **3**, 2671–2678.

365 N. K. Noel, A. Abate, S. D. Stranks, E. S. Parrott, V. M. Burlakov, A. Goriely and H. J. Snaith, *ACS Nano*, 2014, **8**, 9815–9821.

366 D. W. DeQuilettes, W. Zhang, V. M. Burlakov, D. J. Graham, T. Leijtens, A. Osherov, V. Bulović, H. J. Snaith, D. S. Ginger and S. D. Stranks, *Nature Communications*, 2016, **7**, 11683.

367 X. Yang, X. Zhang, J. Deng, Z. Chu, Q. Jiang, J. Meng, P. Wang, L. Zhang, Z. Yin and J. You, *Nature Communications*, 2018, **9**, 2–9.

368 J. W. Lee, Z. Dai, T. H. Han, C. Choi, S. Y. Chang, S. J. Lee, N. De Marco, H. Zhao, P. Sun, Y. Huang and Y. Yang, *Nature Communications*, 2018, **9**, 1–10.

369 Z. K. Tan, R. S. Moghaddam, M. L. Lai, P. Docampo, R. Higler, F. Deschler, M. Price, A. Sadhanala, L. M. Pazos, D. Credgington, F. Hanusch, T. Bein, H. J. Snaith and R. H. Friend, *Nature Nanotechnology*, 2014, **9**, 687–692.

370 M. Yuan, L. N. Quan, R. Comin, G. Walters, R. Sabatini, O. Voznyy, S. Hoogland, Y. Zhao, E. M. Beauregard, P. Kanjanaboos, Z. Lu, D. H. Kim and E. H. Sargent, *Nature Nanotechnology*, 2016, **11**, 872–877.

371 S. Feldmann, S. Macpherson, S. P. Senanayak, M. Abdi-Jalebi, J. P. H. Rivett, G. Nan, G. D. Tainter, T. A. S. Doherty, K. Frohna, E. Ringe, R. H. Friend, H. Sirringhaus, M. Saliba, D. Beljonne, S. D. Stranks and F. Deschler, *Nature Photonics*, 2020, **14**, 123–128.

372 A. Abfalterer, J. Shamsi, D. J. Kubicki, C. N. Savory, J. Xiao, G. Divitini, W. Li, S. Macpherson, K. Gałkowski, J. L. MacManus-Driscoll, D. O. Scanlon and S. D. Stranks, *ACS Materials Lett.*, 2020, **2**, 1644–1652.

373 M. Nikl, *Measurement Science and Technology*, 2006, **17**, 1–10.

374 L. M. Pazos-Outón, M. Szumilo, R. Lamboll, J. M. Richter, M. Crespo-Quesada, M. Abdi-Jalebi, H. J. Beeson, M. Vrućinić, M. Alsari, H. J. Snaith, B. Ehrler, R. H. Friend and F. Deschler, *Science*, 2016, **351**, 1430–1433.

375 C. Cho, B. Zhao, G. D. Tainter, J. Y. Lee, R. H. Friend, D. Di, F. Deschler and N. C. Greenham, *Nature Communications*, 2020, **11**, 1–8.

376 A. R. Bowman, M. Anaya, N. C. Greenham and S. D. Stranks, *Physical Review Letters*, 2020, **125**, 67401.

377 R. T. Williams, W. W. Wolszczak, X. Yan and D. L. Carroll, *ACS Nano*, 2020, **14**, 5161–5169.

378 P. Lecoq, E. Auffray and A. Knapitsch, *IEEE Nuclear Science Symposium Conference Record*, 2012, **60**, 4071–4075.

379 A. Knapitsch, E. Auffray, C. W. Fabjan, J. L. Leclercq, P. Lecoq, X. Letartre and C. Seassal, *Nuclear Instruments and Methods in Physics Research A*, 2011, **628**, 385–388.

380 M. Kronberger, E. Auffray and P. Lecoq, *IEEE Transactions on Nuclear Science*, 2008, **55**, 1102–1106.

381 Y. Kurman, A. Shultzman, O. Segal, A. Pick and I. Kaminer, *Physical Review Letters*, 2020, **125**, 040801.

382 S. Schünemann, S. Brittman, K. Chen, E. C. Garnett and H. Tüysüz, *ACS Photonics*, 2017, **4**, 2522–2528.

383 S. Chen, K. Roh, J. Lee, W. K. Chong, Y. Lu, N. Mathews, T. C. Sum and A. Nurmikko, *ACS Nano*, 2016, **10**, 3959–3967.

384 Y. Deng, Q. Wang, Y. Yuan and J. Huang, *Materials Horizons*, 2015, **2**, 578–583.

385 E. Shefer, A. Altman, R. Behling, R. Goshen, L. Gregorian, Y. Roterman, I. Uman, N. Wainer, Y. Yagil and O. Zarchin, *Current Radiology Reports*, 2013, **1**, 76–91.

386 M. Sytnyk, S. Deumel, S. F. Tedde, G. J. Matt and W. Heiss, *Applied Physics Letters*, 2019, **115**, 19051.

387 M. I. Saidaminov, A. L. Abdelhady, G. Maculan and O. M. Bakr, *Chemical Communications*, 2015, **51**, 17658–17661.

388 H. S. Rao, W. G. Li, B. X. Chen, D. Bin Kuang and C. Y. Su, *Advanced Materials*, 2017, **29**, 1602639.

389 Y. X. Chen, Q. Q. Ge, Y. Shi, J. Liu, D. J. Xue, J. Y. Ma, J. Ding, H. J. Yan, J. S. Hu and L. J. Wan, *Journal of the American Chemical Society*, 2016, **138**, 16196–16199.

390 L. Lee, J. Baek, K. S. Park, Y. E. K. Lee, N. K. Shrestha and M. M. Sung, *Nature Communications*, 2017, **8**, 15882.

391 H. Do Kim, H. Ohkita, H. Benten and S. Ito, *Advanced Materials*, 2016, **28**, 917–922.

392 W. Nie, H. Tsai, R. Asadpour, A. J. Neukirch, G. Gupta, J. J. Crochet, M. Chhowalla, S. Tretiak, M. A. Alam and H. Wang, *Science*, 2015, **347**, 522–526.

393 H. M. Thirimanne, K. D. G. I. Jayawardena, A. J. Parnell, R. M. I. Bandara, A. Karalasingam, S. Pani, J. E. Huerdler, D. G. Lidzey, S. F. Tedde, A. Nisbet, C. A. Mills and S. R. P. Silva, *Nature Communications*, 2018, **9**, 2926.

394 A. Verghese, B. Charlton, J. P. Kassirer, M. Ramsey and J. P. A. Ioannidis, *American Journal of Medicine*, 2015, **128**, 1322–1324.

395 K. Huang, Y. Peng, Y. Gao, J. Shi, H. Li, X. Mo, H. Huang, Y. Gao, L. Ding and J. Yang, *Advanced Energy Materials*, 2019, **9**, 1901419.

396 J. Liu, B. Shabbir, C. Wang, T. Wan, Q. Ou, P. Yu, A. Tadich, X. Jiao, D. Chu, D. Qi, D. Li, R. Kan, Y. Huang, Y. Dong, J. Jasieniak, Y. Zhang and Q. Bao, *Advanced Materials*, 2019, **31**, 1901644.

397 H. S. Gill, B. Elshahat, A. Kokil, L. Li, R. Mosurkal, P. Zygmanski, E. Sajo and J. Kumar, *Physics in Medicine*, 2018, **5**, 20–23.

398 H. Li, X. Shan, J. N. Neu, T. Geske, M. Davis, P. Mao, K. Xiao, T. Siegrist and Z. Yu, *Journal of Materials Chemistry C*, 2018, **6**, 11961–11967.

399 H. M. Thirimanne, K. D. G. I. Jayawardena, A. Nisbet, Y. Shen, R. M. I. Bandara, C. A. Mills, G. Shao and S. R. P. Silva, *IEEE Transactions on Nuclear Science*, 2020, **67**, 2238–2245.

400 *Directive 2011/83/EU of the European Parliament and of the Council on the restriction of the use of certain hazardous substances in electrical and electronic equipment*, 2011.

401 L. J. Xu, X. Lin, Q. He, M. Worku and B. Ma, *Nature Communications*, 2020, **11**, 1–7.

402 V. Morad, Y. Shynkarenko, S. Yakunin, A. Brumberg, R. D. Schaller and M. V. Kovalenko, *Journal of the American Chemical Society*, 2019, **141**, 9764–9768.

403 J. Cao, Z. Guo, S. Zhu, Y. Fu, H. Zhang, Q. Wang and Z. Gu, *ACS Applied Materials and Interfaces*, 2020, **12**, 19797–19804.

404 British Geographical Survey, Risk List 2012, https://www.bgs.ac.uk/mineralsuk/statistics/riskList.htm (accessed July 2020).

405 M. Cai, Y. Wu, H. Chen, X. Yang, Y. Qiang and L. Han, *Advanced Science*, 2017, **4**, 1600269.

406 Y. Galagan, F. Di Giacomo, H. Gorter, G. Kirchner, I. de Vries, R. Andriessen and P. Groen, *Advanced Energy Materials*, 2018, **8**, 1–7.

407 Y.-H. Chiang, M. Anaya and S. D. Stranks, *ACS Energy Letters*, 2020, **5**, 2498–2504.

408 C. L. Melcher, *Nuclear Instruments and Methods in Physics Research A*, 2005, **537**, 6–14.

409 C. Dujardin, E. Auffray, E. Bourret-Courchesne, P. Dorenbos, P. Lecoq, M. Nikl, A. N. Vasil'Ev, A. Yoshikawa and R. Y. Zhu, *IEEE Transactions on Nuclear Science*, 2018, **65**, 1977–1997.

410 X. Li, C. Meng, B. Huang, D. Yang, X. Xu and H. Zeng, *Advanced Optical Materials*, 2020, **8**, 1–8.

411 J. Ding, Y. Liu, H. Fang, Y. Wang, Q. Li, J. L. Sun and Q. Yan, *ACS Photonics*, 2018, **5**, 3172–3178.

412 Z. Lian, Q. Yan, Q. Lv, Y. Wang, L. Liu, L. Zhang, S. Pan, Q. Li, L. Wang and J. L. Sun, *Scientific Reports*, 2015, **5**, 16563.

413 B. Yang, F. Zhang, J. Chen, S. Yang, X. Xia, T. Pullerits, W. Deng and K. Han, *Advanced Materials*, 2017, **29**, 1703758.

414 J. Ding, H. Fang, Z. Lian, J. Li, Q. Lv, L. Wang, J. L. Sun and Q. Yan, *CrystEngComm*, 2016, **18**, 4405–4411.

415 T. K. Lewellen, *Phys Med Biol*, 2010, **53**, 1–46.

416 P. Lecoq, E. Auffray, S. Brunner, H. Hillemanns, P. Jarron, A. Knapitsch, T. Meyer and F. Powolny, *IEEE Transactions on Nuclear Science*, 2010, **57**, 2411–2416.

417 S. E. Derenzo, W. S. Choong and W. W. Moses, *Physics in Medicine and Biology*, 2014, **59**, 3261–3286.

418 M. Pizzichemi, G. Stringhini, T. Niknejad, Z. Liu, P. Lecoq, S. Tavernier, J. Varela, M. Paganoni and E. Auffray, *Physics in Medicine and Biology*, 2016, **61**, 4679–4698.

419 P. Zhang, Y. Hua, Y. Xu, Q. Sun, X. Li, F. Cui, L. Liu, Y. Bi, G. Zhang and X. Tao, *Advanced Materials*, 2022, **34**, 2106562.

420 J. Jiang, M. Xiong, K. Fan, C. Bao, D. Xin, Z. Pan, L. Fei, H. Huang, L. Zhou, K. Yao, X. Zheng, L. Shen and F. Gao, *Nat. Photon.*, 2022, **16**, 575–581.

421 W. Pan, H. Wu, J. Luo, Z. Deng, C. Ge, C. Chen, X. Jiang, W. J. Yin, G. Niu, L. Zhu, L. Yin, Y. Zhou, Q. Xie, X. Ke, M. Sui and J. Tang, *Nature Photonics*, 2017, **11**, 726–732.

422 H. R. Byun, D. Y. Park, H. M. Oh, G. Namkoong and M. S. Jeong, *ACS Photonics*, 2017, **4**, 2813–2820.

423 C. Zhao, B. Chen, X. Qiao, L. Luan, K. Lu and B. Hu, *Advanced Energy Materials*, 2015, **5**, 1500279.

424 Y. Zhang, Y. Liu, Z. Xu, H. Ye, Z. Yang, J. You, M. Liu, Y. He, M. G. Kanatzidis and S. (Frank) Liu, *Nature Communications*, 2020, **11**, 1–11.

425 B. B. Zhang, X. Liu, B. Xiao, A. B. Hafsia, K. Gao, Y. Xu, J. Zhou and Y. Chen, *Journal of Physical Chemistry Letters*, 2020, **11**, 432–437.

426 L. A. Currie, *Anal. Chem.*, 1968, **40**, 586–593.

427 B. Fraboni, A. Ciavatti, F. Merlo, L. Pasquini, A. Cavallini, A. Quaranta, A. Bonfiglio and A. Fraleoni-Morgera, *Advanced Materials*, 2012, **24**, 2289–2293.

428 L. Basiricò, A. Ciavatti, M. Sibilia, A. Fraleoni-Morgera, S. Trabattoni, A. Sassella and B. Fraboni, *IEEE Transactions on Nuclear Science*, 2015, **62**, 1791–1797.

429 B. Chen, S. Wang, Y. Song, C. Li and F. Hao, *Chemical Engineering Journal*, 2022, **430**, 132701.

430 J. S. Yun, J. Kim, T. Young, R. J. Patterson, D. Kim, J. Seidel, S. Lim, M. A. Green, S. Huang and A. Ho-Baillie, *Advanced Functional Materials*, 2018, **28**, 1705363.

431 J. Warby, F. Zu, S. Zeiske, E. Gutierrez-Partida, L. Frohloff, S. Kahmann, K. Frohna, E. Mosconi, E. Radicchi, F. Lang, S. Shah, F. Peña-Camargo, H. Hempel, T. Unold, N. Koch, A. Armin, F. De Angelis, S. D. Stranks, D. Neher and M. Stolterfoht, *Advanced Energy Materials*, 2022, **12**, 2103567.

432 E. Horváth, M. Spina, Z. Szekrényes, K. Kamarás, R. Gaal, D. Gachet and L. Forró, *Nano Letters*, 2014, **14**, 6761–6766.

433 M. Spina, E. Bonvin, A. Sienkiewicz, L. Forró and E. Horváth, *Scientific Reports*, 2016, **6**, 1–8.

434 R. Fornari, in *Single Crystals of Electronic Materials*, Woodhead Publishing, Oxford, 1st edn., 2019, pp. 17–20.

435 W. G. Li, H. S. Rao, B. X. Chen, X. D. Wang and D. B. Kuang, *Journal of Materials Chemistry A*, 2017, **5**, 19431–19438.

436 M. Jung, S.-G. Ji, G. Kim and S. Il Seok, *Chemical Society Reviews*, 2019, **48**, 2011–2038.

437 M. A. Najeeb, Z. Ahmad, R. A. Shakoor, A. Alashraf, J. Bhadra, N. J. Al-Thani, S. A. Al-Muhtaseb and A. M. A. Mohamed, *Optical Materials*, 2017, **73**, 50–55.